Climate simulations of hot Jupiters:

Developing and applying an accurate radiation scheme

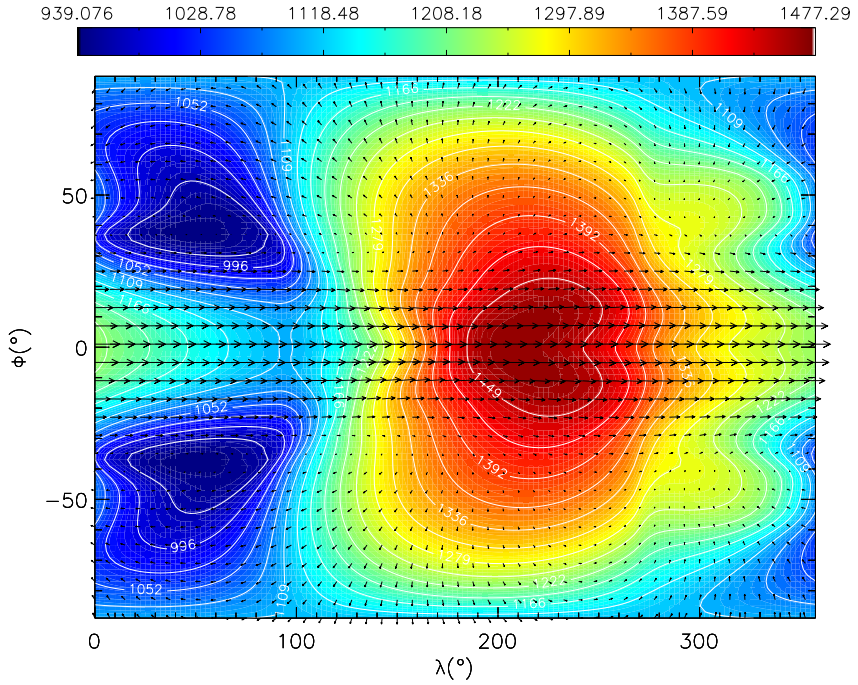

David Skålid Amundsen

Submitted by David Skålid Amundsen to the University of Exeter as a thesis for the degree of Doctor of Philosophy in Physics, February 2015.

Signed: .....
David Skålid Amundsen

Date: .....

Front page picture (Fig. 6.9): The horizontal wind velocity as arrows and temperature [K] as colours and contours at 3×10^3 Pa after 600 d for our global circulation model of HD 209458b. For more details see Chapter 6.

Abstract

To date more than 1500 exoplanets have been discovered. A large number of these are hot Jupiters, Jupiter-sized planets orbiting < 0.1 au from their parent stars, due to limitations in observational techniques making them easier to detect than smaller planets in wider orbits. This is also, for the same reasons, the class of exoplanets with the most observational constraints. Due to the very large interaction between these planets and their parent stars they are believed to be tidally locked, causing a large temperature contrast between the permanently hot day side and colder night side.

There are still many open questions about these planets. Many are observed to have inflated radii, i.e. the observed radius is larger for a given mass than evolutionary models predict. A mechanism that can transport some of the stellar heating into the interior of the planet may be able to explain this. The presence of hazes or clouds has been inferred on some planets, but their composition and distribution remain unknown. According to chemical equilibrium models TiO and VO should be present on the day side of the hottest of these planets, but these molecules have not yet been detected. Cold traps, where these molecules condense out on the night side, have been suggested to explain this. The efficiency of the heat redistribution from the day side to the night side has been found to vary significantly between different planets; the mechanism behind this is still unknown.

To begin to answer many of these questions we need models capturing the three-dimensional nature of the atmospheres of these planets. General circulation models (GCMs) do this by solving the equations of fluid dynamics for the atmosphere coupled to a radiative transfer scheme. GCMs have previously been applied to several exoplanets, but many solve simplified fluid equations (shallow water or primitive equations) or highly parametrised radiation schemes (temperature-forcing, gray or band-averaged opacities). We here present an adaptation of the Met Office Unified Model (UM), a GCM used for weather predictions and climate studies for the Earth, to hot Jupiters. The UM solves the full 3D Euler equations for the fluid, and the radiation scheme uses the two-stream approximation and correlated-k method, which are state of the art for both Earth and exoplanet GCMs. This makes it ideally suited for the study of hot Jupiters.

An important part of this work is devoted to the adaptation of the radiation scheme of the UM to hot Jupiters. This includes calculation of opacities for the main absorbers in these

atmospheres from state-of-the-art high temperature line lists, the calculation of k-coefficients from these opacities, and making sure all aspects of the scheme perform satisfactorily at high temperatures and pressures. We have tested approximations made in previous works such as the two-stream approximation, use of band-averaged opacities and different treatments of gaseous overlap. Uncertainties in current models, such as the lack of high temperature line broadening parameters for these atmospheres, are discussed.

We couple the adapted radiation scheme to the UM dynamical core, which has been tested independently. Our first application is devoted to one of the most well-observed hot Jupiters, HD 209458b. Differences between previous modelling works and our model are discussed, and we compare results from the full coupled model with results obtained using a temperature-forcing scheme.

We have also developed a tool to calculate synthetic phase curves, and emission and transmission spectra from the output of our 3D model. This enables us to directly compare our model results to observations and test the effect of various parameters and model choices on observable quantities.

Contents

List of Figures

List of Tables

Declaration

The majority of the research presented here was performed by myself, in collaboration with Isabelle Baraffe, Pascal Tremblin, Nathan Mayne and James Manners. Here I provide a chapter-by-chapter list of contributions to this work:

Chapter 3

Calculation of opacities was performed by myself using my own code for speed and ability to handle many different line list formats. Opacities for sodium and potassium were calculated using code and tables provided by Derek Homeier, adapted by me to be used in my own opacity calculation code. k-coefficients were calculated by myself using the offline Edwards–Slingo (ES) radiation code.

Chapter 4

Adaptation of the ES radiation scheme was done by me. The tests were performed by myself using the offline ES radiation code and the k-coefficients calculated in Chapter 3. Line-by-line discrete ordinate results were obtained by Pascal Tremblin using the 1D atmosphere code `ATMO`.

Chapter 5

James Manners incorporated the changes I had made to the offline ES radiation scheme into the UM. He also helped in the coupling, making sure Earth-specific physical schemes were switched off. I implemented abundance calculations suitable for hot Jupiter atmospheres, implemented the lower boundary condition and modified the implementation of the upper boundary condition. Implementation of the uniform radiation mode and subsequent testing of the coupled UM was done by me. James Manners assisted in a consulting role.

Chapter 6

The temperature-forced model was set up by Nathan Mayne and run by me. The results from the coupled model applied to HD 209458b were obtained by me. Plots of winds and temperatures were made using a plotting tool written by Nathan Mayne. I implemented the possibility to calculate phase curves, emission and transmission spectra within the framework of Atmo from UM output, and used it to calculate the synthetic observations presented here.

All results were analysed by myself, with contributions from Isabelle Baraffe, Pascal Tremblin, Nathan Mayne and James Manners.

Acknowledgements

There are many people I would like to thank. First I would like to thank Isabelle Baraffe and Nathan Mayne for many interesting discussions and their guidance and supervision from the very beginning. I would also like to thank Pascal Tremblin for help and discussions, particularly for the results in Chapter 4, and Ben Drummond for help with running Atmo.

The ES radiation scheme was provided by James Manners, and he has helped me calculate k-coefficients, incorporate changes I made to the offline ES radiation scheme into the UM, and couple the adapted radiation scheme to the UM dynamical core. For this I am very grateful. I would also like to extend my thanks to Travis Barman, Derek Homeier and Alex Pettitt for insightful discussions, and Derek in particular for also providing sodium and potassium line profiles. I am thankful for the great discussions about observations I have had with Hannah Wakeford and Tom Evans, and extend my thanks to Andrew McLeod, Tom Goffrey, Felix Sainsbury-Martinez and Tom Wilson for reading and providing comments on this thesis.

Last but not least, thanks to my family for always believing in me. It means the world to me.

The calculations in this work were performed on the University of Exeter Supercomputer, a DiRAC Facility jointly funded by STFC, the Large Facilities Capital Fund of BIS, and the University of Exeter. This work is supported by the European Research Council under the European Community's Seventh Framework Programme (FP7/2007-2013 Grant Agreement No. 247060). This research has also made use of the Exoplanet Orbit Database and the Exoplanet Data Explorer at `exoplanets.org`.

David Skålid Amundsen
Exeter, 7th May 2015

Chapter 1

Introduction

The first extrasolar planet, or exoplanet for brevity, discovered orbiting a Sun-like star was 51 Pegasi b orbiting 51 Pegasi (Mayor & Queloz 1995). The field of exoplanet research has since become one of the major fields in astronomy. To date, more than 1500 exoplanets have been confirmed[1], and a large fraction of these are, due to observational bias, very large planets orbiting very close to their parent star. We call these planets "hot Jupiters", since they are about the size of Jupiter, but are much hotter due to their close orbital distance, less than 0.1 au from their parent star. These planets are thought to have tidally locked circular orbits due to strong tidal interactions between the planets and their parent stars (for a review see Baraffe et al. 2010), and experience intense irradiation yielding a significant temperature contrast between the (permanent) day side and night side. Winds in the atmosphere of these planets are therefore expected to transport heat from the day side to the night side.

This thesis is devoted to developing a numerical tool to study the climates of hot Jupiters. As a starting point we use Met Office Unified Model (UM), a 3D global circulation model (GCM) developed by the UK Met Office for weather prediction and climate research for the Earth. Significant adaptation was needed in order to apply the UM to hot Jupiters. Most of this thesis details the adaptation and subsequent testing of the UM radiation scheme, responsible for calculating how much of the stellar irradiation is converted into heat in the atmosphere, and how much is re-emitted as thermal radiation. We apply our adapted hot Jupiter climate model to the hot Jupiter HD 209458b in Chapter 6.

Here we introduce the field of exoplanet atmosphere characterisation. We begin by discussing how observations of these very remote planets are made and how constraints on their atmospheres are obtained. Modelling of these atmospheres is discussed, with a particular emphasis on dynamical modelling, the topic of this work. Next we discuss open questions in the field and goals of the current work. Lastly, a chapter overview is provided with a statement of contribution to co-authored papers.

[1] `http://exoplanets.org` (27/02/2015)

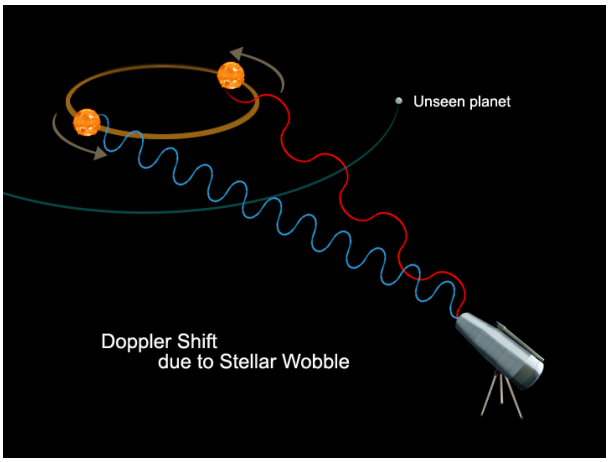

Figure 1.1: Schematic illustration of the radial velocity method used to detect and characterise exoplanets. The orbital motion of the orbiting planet causes a varying Doppler shift in the stellar light observed at the Earth. Image credit: NASA/JPL-Caltech[a].

[a] `http://www.nasa.gov/audience/formedia/telecon-20071106/4.html` (17/04/2015)

1.1 Hot Jupiter detection methods

Many different techniques are used to detect and characterise exoplanets (Wright & Gaudi 2013). The two most common methods used to detect hot Jupiters are the radial velocity method (e.g. Mayor & Queloz 1995), which measures the Doppler shift in the stellar light caused by one or more orbiting planets, and the transit method, where the planet transits in front of the star, as seen from Earth, causing an apparent reduction of the brightness of the star (e.g. Charbonneau et al. 2000; Henry et al. 2000). Both of these methods are most sensitive to massive or large planets orbiting close to their parent star, and we will discuss these methods in more detail in Sections 1.1.1 and 1.1.2.

Other exoplanet detection methods include direct imaging and gravitational microlensing. Direct imaging, as the method's name suggests, directly images planets by masking out the star (e.g. Marois et al. 2008) and is consequently most sensitive to large young (warm) planets orbiting $> 10\,\mathrm{au}$ from low-mass stars. When a star passes in front of a background star, as seen from Earth, the gravitational field of the foreground star can act as a lens magnifying the background star. If the foreground star has a planetary companion it will further distort the light for a short time. This technique is called gravitational microlensing (e.g. Beaulieu et al. 2006). It is most sensitive to planets orbiting within $1\,\mathrm{au}$ to $10\,\mathrm{au}$ of their parent star. We restrict the discussion here to the radial velocity and transit methods as hot Jupiter detections are dominated by these two techniques.

1.1.1 The radial velocity method

The first exoplanet orbiting a Sun-like star, 51 Peg b, was detected using the radial velocity method (Mayor & Queloz 1995). The motion of a star caused by orbiting planets causes a Doppler shift of the light emitted by the star. After accounting for the absolute velocity of the system relative to the Earth, as the star moves towards the Earth the light will be blue-shifted, while if it moves away from the Earth the light will be red-shifted. This is illustrated in Fig. 1.1.

By observing individual atomic lines in the stellar spectrum it is possible to measure how much the stellar light has been shifted and consequently the relative velocity of the star. The orbital period can be obtained from the period of the radial velocity signal, while the amplitude of the radial velocity depends on the planet mass $M_{\rm p}$. Since only the component of the star velocity directed towards the Earth can be measured, however, only a lower estimate can be obtained for the total velocity of the star. Consequently, only a lower constraint on the planet mass can be obtained. The mass measured with the radial velocity method is $M_{\rm p} \sin i$, where i is the inclination defined as the angle between the normal to the orbital plane of the star and the line of sight between the Earth and the star. If $i = 90°$ the star moves perpendicular to the plane of the sky, while for $i = 0°$ the star moves parallel to the plane of the sky. The actual mass of the planet can therefore only be determined if the inclination is known. Fortunately it is possible to measure the inclination in some cases; we return to this in Section 1.1.2.

Many planets have been detected using the radial velocity method (see e.g. Bonfils et al. 2013), and even multi-planet systems have been discovered using this method (Butler et al. 1999; Fischer et al. 2003). Its true power becomes evident when combined with the transit method discussed below, where the inclination can be constrained.

1.1.2 The transit method

If the orbital inclination i is close to 90° then the planet will transit in front of its parent star as seen from Earth, causing a slight, regular, reduction in the stellar brightness. If this reduction is large enough, i.e. if the star is small and/or the planet is large, this dip in brightness can be observed. We illustrate this in Fig. 1.2. The bigger the reduction in stellar brightness, the easier the planet is to detect, and consequently this method is most sensitive to large planets orbiting small stars. The dip in brightness is proportional to the area of the stellar disk blocked out by the planet relative to the total area of the stellar disk, i.e. $R_{\rm p}^2/R_*^2$. Here, $R_{\rm p}$ is the apparent radius of the planet and R_* is the radius of the parent star. Provided R_* is known it is possible to derive a radius for the planet. In addition, the inclination i discussed above can be derived since it greatly affects the light curve, the observed stellar brightness as a function of time.

The first planet detected with the transit method was HD 209458b (Charbonneau et al. 2000; Henry et al. 2000). Since then a large number of planets has been found through both ground-based projects like WASP (Pollacco et al. 2006) and the space-based NASA Kepler mission (Borucki et al. 2010). Combined with the radial velocity method, it becomes possible to obtain both the mass and radius of an exoplanet, which in turns yields a bulk density (see e.g. Charbonneau et al. 2000; Henry et al. 2000; Mazeh et al. 2000). The orbital period can be constrained from the radial velocity curve and the transit frequency, and if the planet is tidally locked this also yields the rotation period of the planet. In summary, combined these detection methods give us planet mass, radius, bulk density, orbital period, and potentially rotation period, providing initial constraints on the compositions of these planets.

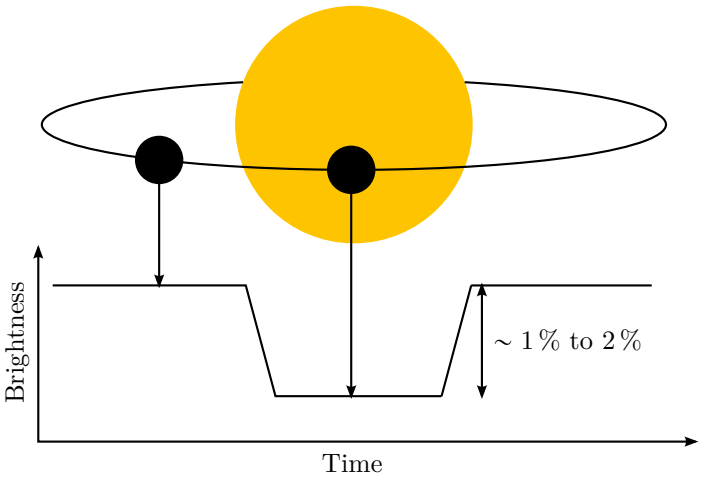

Figure 1.2: Illustration of the transit method. As the planet transits in front of its star, as seen from Earth, the apparent brightness of the star will be reduced.

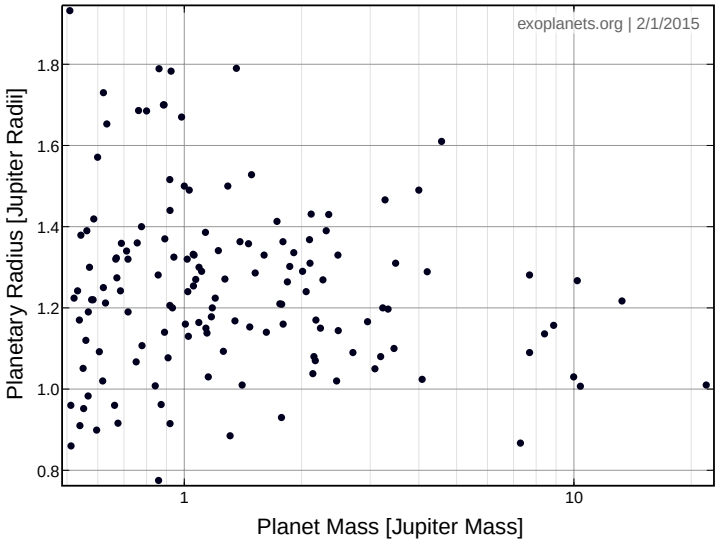

Figure 1.3: Observed mass vs radius for hot Jupiters (Han et al. 2014) showing many planets that are about the same mass as Jupiter but have much larger radii.

Intriguingly, many hot Jupiters have been found to be very inflated. In Fig. 1.3 we show the planet radius as a function of mass, which clearly shows that many planets, even though they are about the mass of Jupiter, can have a radius almost twice that of Jupiter. The amount of inflation appears to be correlated with the amount of irradiation received by the planet from its parent star (Weiss et al. 2013), but taking this intense irradiation into account in evolutionary models has been found to be insufficient to explain these large radii (Baraffe et al. 2010). The mechanism by which the inflation is supported remains elusive, though many theories exist such as vertical transport of kinetic energy, tidal dissipation, and Ohmic dissipation (Baraffe et al. 2010; Batygin & Stevenson 2010).

1.2 Observational constraints of hot Jupiter atmospheres

In this section we discuss how hot Jupiter atmospheres are characterised and what we can infer about their atmospheres from observations. We keep the review here focused on hot Jupiter

atmospheres. For general reviews of exoplanet atmospheres see e.g. Madhusudhan et al. (2014) and Seager & Deming (2010).

1.2.1 Transmission and emission spectra

The transit method discussed in Section 1.1.2 not only allows for the detection of exoplanets, but also characterisation of their atmospheres. The first detection of an exoplanet atmosphere was made by Charbonneau et al. (2002) by observing the change in R_p^2/R_*^2 during a transit as a function of wavelength for HD 209458b. If a transiting planet has an atmosphere, some of the stellar light will be absorbed or scattered by particles in the atmosphere. The amount of absorbed and scattered light will depend on which particles are present in the atmosphere. Each particle's behaviour is a function of wavelength, and they will therefore imprint their signature on the light received at Earth as changes in R_p^2/R_*^2 with wavelength. This technique is called transmission spectroscopy.

Thus the transit method gives us a way to determine the composition of exoplanet atmospheres. By comparing to atmosphere models it is possible to get estimates for temperatures as well, but it is important to note that transmission spectroscopy only probes the limb of the planet. Also, these objects are not spatially resolved in the sky so only an average of the conditions around the limb can be obtained. Despite this, transmission spectroscopy has been proved extremely valuable in the characterisation of exoplanet atmospheres.

Charbonneau et al. (2002) found an absorption peak around a wavelength of 589.3 nm, which is the wavelength of a sodium absorption doublet, as predicted to be observable by Seager & Sasselov (2000). This sparked an explosion in the field of exoplanet atmosphere characterisation. Suddenly it was possible to begin to characterise the atmospheres of planets outside our own solar system. Sodium and potassium have been detected on many hot Jupiters (Redfield et al. 2008; Sing et al. 2011, 2012, 2015; Snellen et al. 2008). These alkali metals have very strong absorption features in narrow wavelength regions and are therefore detectable even though less abundant than other gases. We show an example transmission spectrum in Fig. 1.4, obtained by Sing et al. (2015), for WASP-31b showing absorption by potassium and possibly sodium.

Water has been detected in the atmosphere of HD 209458b (Deming et al. 2013), HAT-P-1b (Wakeford et al. 2013) and HD 189733b (McCullough et al. 2014) using transmission spectroscopy. Tinetti et al. (2007) originally claimed detection of water absorption in the transmission spectrum of HD 189733b, but this was later debated (Désert et al. 2009; Sing et al. 2009), and it should be noted that the original detection was only based on three data points with large uncertainties.

These atmospheres are, from chemical equilibrium calculations assuming solar elemental abundances, expected to be composed mainly of H_2 and He. As discussed in Section 3.1.4 these are very weak absorbers, causing the heating budget to be dominated by trace gases such as H_2O, CO, CH_4, NH_3, Na and K (Burrows & Sharp 1999). As these species are strong absorbers the above mentioned detections are in agreement with expectations from models.

Another event that provides information about the planet's atmosphere is when the planet is eclipsed by the star. It then becomes possible to disentangle the amount of light emitted by the star, and the reflected and emitted light by the planet atmosphere, enabling the measurement of planet brightness temperatures. This was first done by Deming et al. (2005), who measured the infrared radiation emitted by HD 209458b immediately before secondary transit, making it possible to obtain a brightness temperature for the day side of this planet. In principle it is possible to detect molecular signatures from day side emission spectra. The reduction of brightness during secondary transit is very small, about an order of magnitude smaller than during primary transit, making high precision measurements difficult. Many of the claimed detections of molecular absorption or emission in day side emission spectra from broad-band photometry (see e.g. Swain et al. 2009) have later been disputed (Hansen et al. 2014). Even so, molecular signatures have been detected in the atmospheres of some planets using high resolution secondary eclipse measurements (see e.g. Birkby et al. 2013; Brogi et al. 2012).

The presence of clouds (used interchangeably with haze, dust and aerosols in the literature) was first inferred on HD 189733b from transmission spectroscopy through a strong increase in the apparent radius at small wavelengths (Pont et al. 2008, 2013). The behaviour is similar to that expected by Rayleigh scattering, which indicates small particle sizes. Clouds have also been invoked for other exoplanets in order to explain observations of featureless spectra (Gibson et al. 2013), muted molecular absorption features (Deming et al. 2013), or Rayleigh scattering-like slopes (Sing et al. 2013) in transmission spectra. The transmission spectrum in Fig. 1.4 shows such a Rayleigh scattering-like slope at short wavelengths. Understanding clouds in exoplanet atmospheres is very much in its infancy as composition and distribution remain unknown.

Measuring the day side emission of HD 209458b between 3.6 µm to 8.0 µm, Knutson et al. (2008) found that standard atmosphere models did not fit the data particularly well and suggested the presence of a thermal inversion layer (increasing temperature with height). TiO and VO was suggested as a potential cause of this inversion as they are strong absorbers of visible radiation and, according to equilibrium chemistry, should be present at temperatures $\gtrsim 1800$ K. However, a reanalysis of all available Spitzer secondary-eclipse data performed by Diamond-Lowe et al. (2014) found that it was unnecessary to introduce a temperature inversion in order to fit the day side emission data to models. TiO and VO have yet to be detected in the atmospheres of these planets (Hoeijmakers et al. 2014; Huitson et al. 2013; Sing et al. 2013). We will come back to this discussion in Section 1.4.4.

1.2.2 Phase curves

As a planet orbits its parent star, the part of the planet disk illuminated by the parent star as seen from Earth will vary. At primary transit the night side of the planet faces the Earth while at secondary transit only the day side is visible. Since these planets are believed to be tidally locked (Baraffe et al. 2010) temperature, and therefore the planet brightness, is expected

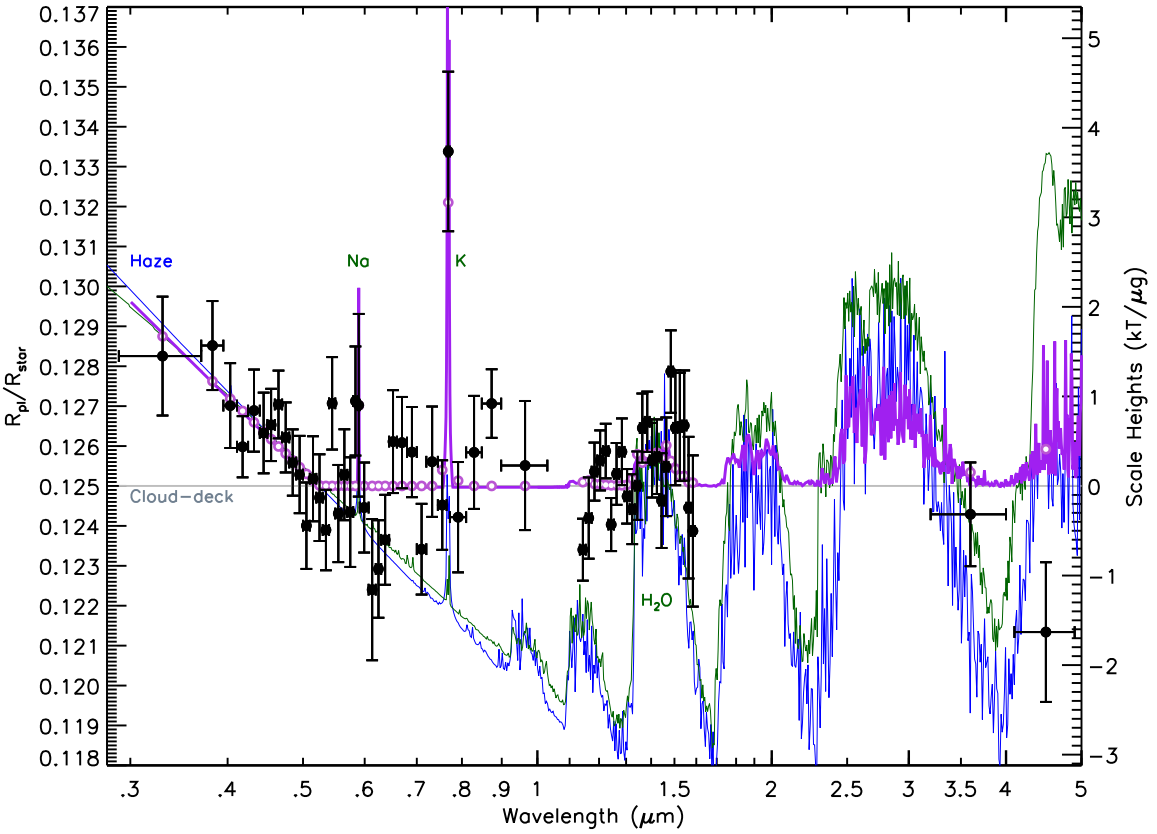

Figure 1.4: Transmission spectrum of WASP-31b showing potassium and possibly sodium absorption and a Rayleigh scattering-like slope at short wavelengths. The vertical axis is the apparent planet to star radius, which has been converted to atmospheric scale heights $H = kT/\mu g$ on the right where k is Boltzmann's constant, T is the temperature, μ is the mean molecular weight and g is the gravity. Peaks in the planet to star radius correspond to absorption maxima caused by atoms, molecules or clouds in the atmosphere. The drawn lines are model predictions discussed in more detail in Section 1.3.1. From Sing et al. (2015): Sing, D. K.; Wakeford, H. R.; Showman, A. P. et al.: HST hot-Jupiter transmission spectral survey: detection of potassium in WASP-31b along with a cloud deck and Rayleigh scattering, MNRAS, 2015, 446, 2428–2443, Fig. 12.

to vary significantly between the day and night side. By observing the evolution of the planet brightness between primary and secondary transit, called the phase curve, it is possible to obtain an estimate of the temperature distribution on these planets. This was first done by Knutson et al. (2007a) for HD 189733b, and later generalised to obtain a two-dimensional temperature map of the same planet by Majeau et al. (2012). As an example we show the phase curve from Knutson et al. (2007a) in Fig. 1.5. The observed brightness is seen to increase towards an orbital phase of 0.5, the position of secondary eclipse, as the planet day side comes into view.

Phase curves are extremely valuable in order to constrain the amount of heat redistribution between the day and night side of these planets. These measurements are unfortunately difficult and expensive to obtain since they require continuous observation of the same target for several days and also require a high level of signal-to-noise. Despite this, phase curves have now

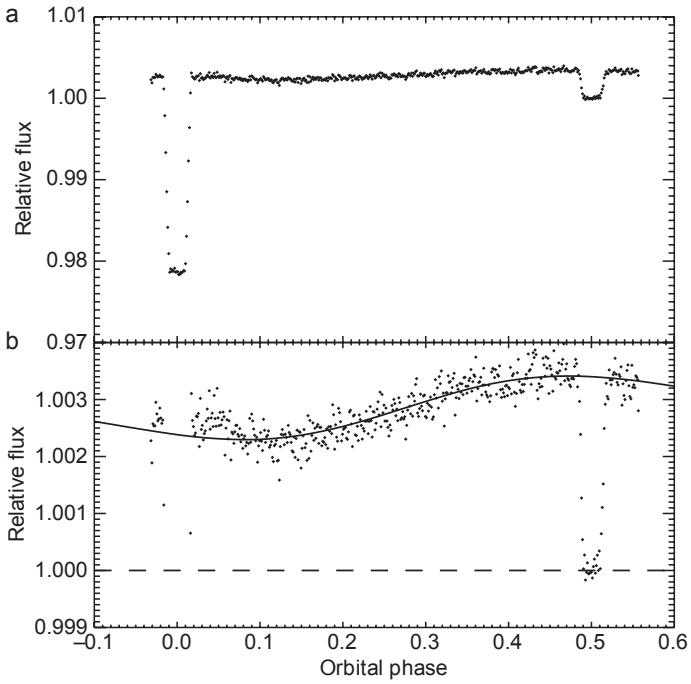

Figure 1.5: 8 µm phase curve for HD 189733b. The primary and secondary transits are located at orbital phase 0 and 0.5, respectively. Brightness increases towards secondary eclipse as the planet day side comes into view. From Knutson et al. (2007a): Knutson, H. A.; Charbonneau, D.; Allen, L. E. et al.: A map of the day-night contrast of the extrasolar planet HD 189733b, Nature, 2007, 447, 183–186, Fig. 1. Reprinted with permission from NPG.

been obtained for multiple planets. Knutson et al. (2007a) obtained a longitudinal brightness temperature map of HD 189733b, which we reproduce in Fig. 1.6, from the 8 µm phase curve. They found a hotspot shifted slightly eastward, $(16 \pm 6)°$, of the substellar point (the middle of the temperature map), which is taken as an indication of winds transporting heat from the day side to the night side of this planet. This was further supported by the modest temperature contrast. They estimate a minimum and maximum brightness temperature of (793 ± 33) K and (1212 ± 11) K, much lower than what is expected without redistribution for a tidally locked planet. The phase curve for HD 189733b at other wavelengths has also been obtained (Knutson et al. 2009, 2012), confirming the findings of a modest day-night temperature contrast.

Other planets with measured phase curves are WASP-18b (Maxted et al. 2013), Kepler-7b (Demory et al. 2013), Kepler-13Ab (Shporer et al. 2014), HD 209458b (Zellem et al. 2014) and WASP-43b (Stevenson et al. 2014). Generally, the hotspot is found to be shifted eastward of the substellar point at infrared wavelengths, but the degree of offset, brightness temperatures and temperature contrasts vary. For example, contrary to HD 189744b, WASP-18b seems to have little redistribution of heat between its day and night side with a day side brightness temperature at infrared wavelengths of over 3000 K (Nymeyer et al. 2011). For Kepler-7b and Kepler-13Ab phase curves are available at visible wavelengths, and a westward shift of the brightest point in the atmosphere is found (Demory et al. 2013; Shporer et al. 2014). This is interpreted as the presence of high-altitude reflective clouds on the day side located westward of the substellar point. The composition of these clouds is, however, not known.

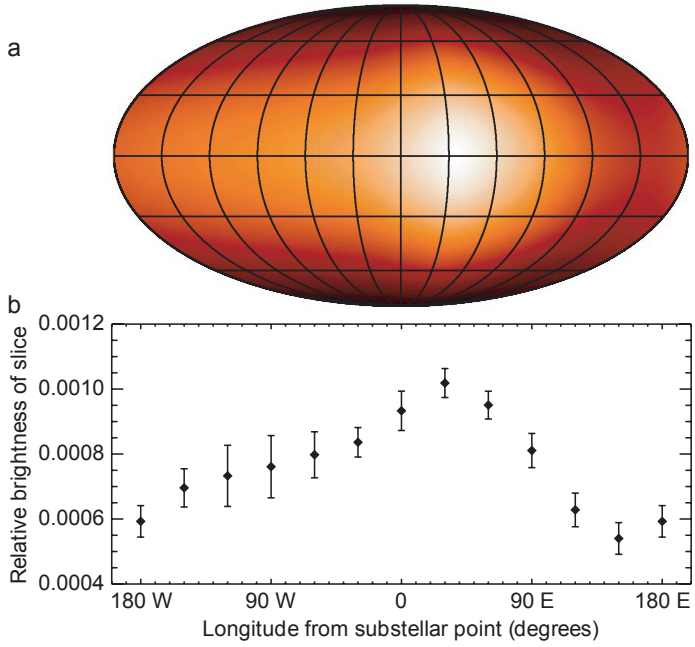

Figure 1.6: Brightness temperature map for HD 189733b derived from the phase curve in Fig. 1.5. They calculate a day side brightness temperature of (1205.1 ± 9.3) K, with the night side about 250 K colder. From Knutson et al. (2007a): Knutson, H. A.; Charbonneau, D.; Allen, L. E. et al.: A map of the day-night contrast of the extrasolar planet HD 189733b, Nature, 2007, 447, 183–186, Fig. 3. Reprinted with permission from NPG.

1.2.3 The planet radial velocity signal

The traditional radial velocity method discussed in Section 1.1.1 relies on observing the Doppler shift in the stellar light due to the presence of an orbiting planet. It is also possible to measure the radial velocity shift of molecular lines in the atmospheres of some planets. Snellen et al. (2010) measured the Doppler shift of CO lines in the transmission spectrum of HD 209458b and found a blue-shift of the signal of 2 km/s, which they interpreted as an indication of a strong wind flowing from the day side to the night side of the planet. To date this is the only measurement of a wind velocity on an exoplanet.

In summary, hot Jupiters have been found to be very diverse. Some are hotter than others, many of them may have clouds of unknown composition, and some of them are inflated while others are not. Observations give us detections of absorbers and temperature maps, and atmosphere models are needed in order to understand these observations. A large number of models with varying complexity has been developed. In the next sections we discuss some of these models, with a particular emphasis on dynamical models as this is the topic of the current work.

1.3 One-dimensional models of hot Jupiter atmospheres

Here we will review some of the modelling work that has been done in order to understand hot Jupiter atmospheres. We begin by discussing one-dimensional (1D) radiative-convective equilibrium models: the first models that were applied to hot Jupiters. These models have sophisticated treatments of radiation and chemistry, but approximate the atmosphere as static,

i.e. in radiative-convective equilibrium. For reviews on 1D atmosphere modelling see Burrows & Orton (2009) and Marley & Robinson (2014). Retrieval models, where information about a planet's atmosphere is obtained by fitting observations through an error minimization algorithm, have also been applied to hot Jupiters. We discuss these models in more detail below.

1.3.1 Equilibrium models

Planets are thought to form through gravitational collapse, where material in the planet forming disk around the parent star is slowly trapped by the increasing mass of planetary bodies. Consequently, hot Jupiters are thought to have hot interiors where the gravitational energy from the planet's formation has been transformed into thermal energy. This energy is transported outwards from the interior of the planet through convection. The stellar flux is absorbed in the atmospheres of these planets where energy transport is dominated by radiation. The thermal energy transported through convection is converted into radiation as it reaches the atmosphere and is subsequently emitted to space. In equilibrium all these processes equate to zero net heating, i.e. stellar heating, thermal emission and convective heat transport balance.

The first group of models we will discuss are radiative-convective equilibrium models. These models assume that the atmosphere is spherically symmetric and can be represented by a single radial column. They solve the radiative transfer equation combined with both a chemical equilibrium scheme for abundances, and mixing length theory to account for convection. The opacity databases used in these models are extensive, with several tens of absorbers. The first synthetic transmission spectrum was obtained using such a model (Seager & Sasselov 2000).

At present there are two main groups whose 1D atmospheric models are used extensively in the literature to interpret observations. One is that of Adam Burrows (Burrows et al. 2006; Sudarsky et al. 2003), while the other is that of Jonathan Fortney (Fortney et al. 2005, 2008b). Their models are quite similar as they make the same overall assumptions, but slightly different opacity databases are used. The models of Burrows use the database described in Sharp & Burrows (2007), while the models of Fortney use the database of Freedman et al. (2008). Since these models are 1D, they incorporate a redistribution parameter f to reduce the stellar irradiation. Only the planet disk, with area $\pi R_{\rm p}^2$, receives the stellar irradiation. The day side of the planet has an area of $2\pi R_{\rm p}^2$, and the entire planet an area of $4\pi R_{\rm p}^2$. The value of the parameter f needed to match observations is often used to interpret the efficiency of heat redistribution between the day and night side of hot Jupiters as discussed in Section 1.2.

As mentioned above, many planets seem to have spectroscopic features similar to those expected of clouds. This is not surprising as clouds have been shown to be crucial when modelling brown dwarfs (Marley et al. 2013) and solar system planets (Rossow 1978). Models applied to hot Jupiters have, however, so far been mostly cloud free, and in order to fit observations additional opacity is added to the models in ad-hoc ways (see e.g. Deming et al. 2013; Nikolov et al. 2014). This clearly illustrates the need to investigate the effect of clouds in these atmospheres.

Cloud modelling is, however, a tricky subject that introduces many new unconstrained model parameters. In this work we do not consider the effect of clouds.

In order to study phase dependent variables such as day-night contrasts with 1D models Barman et al. (2005) applied the 1D atmosphere code Phoenix (Barman et al. 2001; Hauschildt & Baron 1999) to atmospheric columns in a longitude-latitude grid for the planet HD 209458b. They found that significant redistribution of heat was required to reproduce observations. Iro et al. (2005) used a time-dependent 1D atmosphere code to study HD 209458b and derived radiative timescales. They also mimicked atmospheric circulation by adding solid body rotation and studied the longitudinal variation in the temperature structure of the planet.

Naturally, hot Jupiters are inherently three-dimensional (3D) time-dependent objects. The attempts to take 3D time-dependent effects into account in static 1D atmosphere models clearly illustrates the need for the development of proper 3D dynamical models. We discuss the development of these models in some detail in Section 1.4.

1.3.2 Non-equilibrium models

As mentioned above, hot Jupiters orbit extremely close to their parent star and will therefore receive a large amount of stellar irradiation. High energy photons may start to have an impact on the chemistry in the upper atmospheres of these systems. In addition, vertical mixing of absorbers may cause significant deviations from equilibrium abundances. Several studies of non-equilibrium effects in hot Jupiter atmospheres have been performed (see e.g. Liang et al. 2003; Line et al. 2010; Zahnle et al. 2009), the most comprehensive of which is Moses et al. (2011), who developed a 1D photochemical, thermochemical kinetics and diffusion model. The non-equilibrium scheme was applied to fixed P–T profiles derived from either GCM simulations or radiative-convective models of HD 189733b and HD 209458b, both of which assume chemical equilibrium, to see if vertical mixing and photochemistry could noticeably change abundances. They found that these processes can indeed modify abundances enough to produce observable spectral signatures, particularly for the colder planet HD 189733b.

Venot et al. (2012) also developed a chemical network suitable to hot Jupiters, including vertical mixing and photochemistry, and applied it to HD 189733b and HD 209458b using the same P–T profiles as Moses et al. (2011). Qualitatively results are similar to those of Moses et al., but some quantitative differences are found highlighting uncertainties in these chemical schemes. The feedback on the thermal structure of these planets is still an open issue, but work is underway to couple non-equilibrium chemistry schemes with 1D and 3D models.

Another equilibrium assumption used in all the above models is that of local thermodynamic equilibrium (LTE). This greatly simplifies calculation of opacities and radiative transfer, as we will discuss more in Chapters 2 and 3. Non-LTE effects could be important in the upper part of irradiated planet atmospheres. Indeed some observational works invoke non-LTE effects to explain the detection of strong emission features in hot Jupiters (see e.g. Waldmann et al. 2012),

and there has been some work on modelling non-LTE effects in these atmospheres (Barman et al. 2002; Schweitzer & Hauschildt 2004). The significance of these effects still needs to be proven, and it is beyond the scope of the present work to consider non-LTE effects.

1.3.3 Retrieval models

Another branch of 1D atmosphere models are based on retrieval techniques. These codes do not normally solve for radiative-convective and chemical equilibrium, but use observational data to constrain abundances and temperatures directly by minimising the error in synthetic spectra. One example of such a code is NEMESIS (Irwin et al. 2008), which has been applied to both solar system planets (e.g. Barstow et al. 2012) and exoplanets (e.g. Barstow et al. 2014; Lee et al. 2012, 2014). The retrieval model by Madhusudhan & Seager (2009) is slightly more restrictive in that they require energy balance at the top of the atmosphere and a constant deviation from chemical equilibrium. Line et al. (2013) compared different retrieval methods and found that they generally agree for high signal-to-noise observations, but deviations were found performing retrieval on low signal-to-noise data. We do not go into more details about retrieval schemes here, but refer to the above mentioned publications for more details.

1.4 Dynamical models applied to hot Jupiter atmospheres

Hot Jupiters are dynamic, three-dimensional objects. Observations are beginning to probe this as phase curves and wind velocities become accessible. One-dimensional models have sophisticated radiation and chemistry schemes, but their treatments of dynamical processes and horizontal temperature variations are crude. To interpret observations, investigate the accuracy of assumptions in 1D equilibrium models and gain a better understanding of the atmospheres of these planets, 3D dynamical atmosphere models have been developed. These models are called global circulation models (GCMs), and are used for weather prediction and climate research for the Earth, and have also been applied to other solar system planets such as Jupiter, Saturn, Mars and Venus (see e.g. Hollingsworth & Kahre 2010; Lebonnois et al. 2011; Müller-Wodarg et al. 2006; Yamazaki et al. 2004, respectively). These models have less sophisticated radiation and chemistry schemes than 1D models, but solve for the atmospheric flow explicitly, resolving both horizontal and vertical dimensions.

GCMs include a dynamical core which solves an approximated version of the Navier-Stokes equations, and a radiation scheme that calculates the radiative heating rate. The atmosphere is discretised, often on a latitude-longitude grid, and the radiative transfer equation is solved for vertical columns in the atmosphere.

The approximated version of the Navier–Stokes equations solved vary between different models. Most GCMs applied to hot Jupiters solve the primitive equations (Heng et al. 2011; Menou & Rauscher 2009; Showman et al. 2009; Showman & Guillot 2002; Thrastarson & Cho

2010), where it is assumed that the atmosphere is (i) in hydrostatic equilibrium with constant gravity and (ii) shallow compared to the radius of the planet (Vallis 2006). Some terms in the horizontal momentum equations are also neglected in the primitive equations to ensure the conservation of energy and momentum, this is called the traditional approximation (Vallis 2006). The exception is Dobbs-Dixon & Lin (2008) and Dobbs-Dixon & Agol (2013), who solve the full Navier–Stokes equations, and Mayne et al. (2014a) who solve the full Euler equations (the same as the Navier–Stokes equations but without the viscosity term), with a height-varying gravity. For inflated hot Jupiters (e.g. HD 209458b), the vertical extent of the atmosphere can be about 10 % of the planet radius, and it is therefore not certain if the primitive equations can be applied to these atmospheres. The validity of these approximations to hot Jupiter atmospheres was investigated in Mayne et al. (2014a), who found that deviations can occur especially for the deeper atmosphere on long timescales (> 1200 d, where 1 d is an Earth day). For reviews of GCMs applied to hot Jupiters see Showman et al. (2011) and Heng & Showman (2014).

The focus of this work is adapting the radiation scheme of an Earth GCM to hot Jupiter-like atmospheres. Below we discuss the varying radiation schemes used in GCMs previously applied to hot Jupiters.

1.4.1 Temperature-forcing

Showman & Guillot (2002) was the first to apply a GCM to a hot Jupiter atmosphere. The radiation was parametrised by a simple temperature-forcing scheme. In such a scheme the temperature is relaxed directly towards assumed equilibrium P–T profiles $T_{\rm eq}$ on a radiative time scale $\tau_{\rm rad}$. The P–T profiles and timescales used were estimated from simple analytical arguments. They found that a broad eastward equatorial jet developed transporting heat from the day side to the night side, with peak wind speeds of about 1.5 km/s.

They also proposed what has become one of the main theories behind why many hot Jupiters are inflated. A downward transport of kinetic energy, about 1 % of the absorbed stellar flux, was observed. This would be enough to affect the radius of the planet if deposited in the interior, and we come back to this issue in Section 1.6.

Their study was extended in Cooper & Showman (2005) by introducing equilibrium P–T profiles and radiative timescales from Iro et al. (2005). They again found a broad eastward equatorial jet with wind velocities exceeding 4 km/s, and perhaps more importantly, they found an eastward shift of the hottest point in the atmosphere, as later observed in the hot Jupiter HD 189733b (Knutson et al. 2007a). We reproduce a plot in Fig. 1.7 showing the equatorial jet and hotspot offset.

Fortney et al. (2006a) used the results from Cooper & Showman (2005) to calculate synthetic emission spectra and phase curves. They made several predictions for phase variations and offsets, but in terms of absolute fluxes they found significant disagreement with observational data available. This led Showman et al. (2008) to improve their model of HD 209458b and

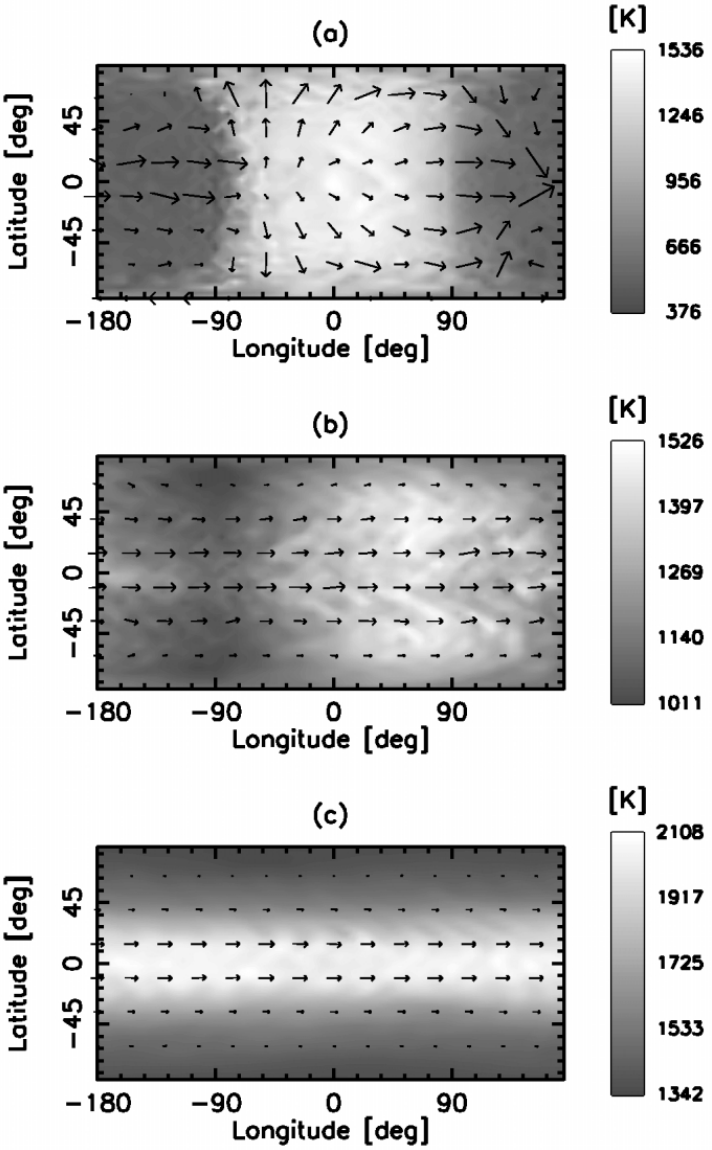

Figure 1.7: Temperatures (gray scale, light is hot and dark is cold) and winds (arrows) from a temperature-forced GCM simulation of HD 209458b at 2.5 mbar, 220 mbar and 19.6 bar (from top to bottom) after 5000 d (Earth days) of simulation time. The substellar point is at zero latitude, zero longitude. From Cooper & Showman (2005): Cooper, C. S. & Showman, A. P.: Dynamic Meteorology at the Photosphere of HD 209458b, ApJL, 2005, 629, L45–L48, Fig. 1. © AAS. Reproduced with permission.

HD 189733b by calculating horizontal variations in equilibrium P–T profiles and radiative timescales with the 1D atmosphere code by Fortney et al. (2005, 2008b) not included in the profiles by Iro et al. (2005). Comparison with available data was performed as in Fortney et al. (2006a) by calculating synthetic emission spectra and phase curves. Agreement generally improved, but large differences in the predicted and observed day side emission was found. At most wavelengths their model underestimated emission at infrared wavelengths. For HD 189733b, comparison was made with the 8 µm phase curve from Knutson et al. (2007a) and their model was found to have a similar offset and maximum, but the minimum was underestimated by about a factor of four.

Other groups have also applied GCMs to study atmospheric circulation on hot Jupiters. The study of Cho et al. (2003, 2008) differ from those discussed above in that they use a 2D one-layer model and initialise it with small-scale turbulence without direct forcing. They find polar vortices and zonal jets with relatively small wind velocities compared to those found in e.g. Showman et al. (2008). This difference is attributed to the forcing and initial condition, which may be considered less realistic than those in Showman et al. (2008). We refer to the referred papers for a more thorough discussion.

Menou & Rauscher (2009) and Rauscher & Menou (2010) presented two test cases designed for intercomparison of hot Jupiter GCMs, which were later combined into a series of benchmark tests (Heng et al. 2011). The setup in Rauscher & Menou (2010) is almost identical to that in Cooper & Showman (2005), but a different GCM is used. General agreement is found, but small differences do occur, which the authors suggest may be due to shocks, which are not properly treated in any of these models. Polichtchouk et al. (2014) performed an intercomparison of five GCMs used to study hot Jupiter atmospheres using temperature-forcing schemes and found that all models performed qualitatively similarly, but there were some quantitative differences.

There is debate in the literature about whether or not initial conditions play a role in these simulations. The general agreement is that these systems are so strongly forced that any information about the initial condition will be lost after some time, but this is still under debate. We refer to Liu & Showman (2013) and Thrastarson & Cho (2010) for a more detailed discussion.

1.4.2 Diffusive, grey and average opacity schemes

Dobbs-Dixon & Lin (2008) studied the effect of opacity on atmospheric flows on hot Jupiters. Their radiation scheme is based on flux-limited diffusion combined with Rosseland mean opacities and an imposed spatially varying temperature at the upper boundary. The diffusion approximation is essentially the first order correction to a pure black-body flux, and is only valid at large optical depths. Flux-limited diffusion is a slight variant of this designed to treat the optically thin and thick limits correctly. They find that generally atmospheres with a large opacity will exhibit larger day night temperature contrasts. Their flow patterns were similar to that of Showman et al. (2008), which indicates that general flow patterns are not very sensitive

to the exact model formulation.

Temporal variability of the atmospheric circulation on HD 209458b was studied in Dobbs-Dixon et al. (2010). Their radiation scheme was improved over that in Dobbs-Dixon & Lin (2008) by separating it into a stellar and thermal component and explicitly taking the irradiation into account, still using flux-limited diffusion. They found that the night side is much more prone to variability than the day side due to the very strong forcing. The coldest point in the atmosphere can change by about 15 % and shift in position by about 20°. The accuracy of the radiation schemes in Dobbs-Dixon et al. (2010); Dobbs-Dixon & Lin (2008) applied to hot Jupiter atmospheres have never been tested.

Dobbs-Dixon & Agol (2013) study the atmospheric circulation on HD 189733b, again with an updated radiation scheme. Mean opacities have been replaced with band-averaged opacities tabulated as a function of temperature and pressure, where the spectrum between 0.26 µm to 300 µm has been divided into 30 bands. The diffusion approximation has been replaced by the two-stream approximation, which is a very common approximation in GCMs and discussed in more detail in Chapter 2. Due to the inference of clouds in the atmosphere of HD 189733b they also supplemented their frequency dependent opacity by a grey component and a strong Rayleigh scattering-like component. It is important to note that this extra opacity was included as absorption even though it is believed to be of a scattering nature. Synthetic emission and transmission spectra, in addition to phase curves, were calculated and compared to observations. Reasonably good agreement was found, though as with Showman et al. (2008) they underestimate the 8 µm night side flux, while their day side fluxes are generally overestimated. In Chapter 4 we test the accuracy of this radiation scheme.

Rauscher & Menou (2012) introduce a double-grey radiation scheme, one component for the irradiation and one for thermal emission, and combine this with the two-stream approximation. Their model of HD 209458b has flow patterns similar to that seen in other GCMs, but no quantitative comparison is performed.

1.4.3 The two-stream approximation and the correlated-k method

To date the most sophisticated opacity treatment applied in a hot Jupiter GCM is the correlated-k method, which we discuss in more detail in Section 3.4. Showman et al. (2009) combines it with the delta-discrete ordinate method, a variant of the two-stream approximation, for the stellar component and the two-stream source function technique (Toon et al. 1989) for the thermal component, similar to the two-stream approximation but designed to be exact in the no scattering limit. This radiation scheme is state-of-the art for the Earth, and solar system and extrasolar planets. Showman et al. (2009) applied this new GCM, named the SPARC/MITgcm, to HD 189733b and HD 209458b, and it has later been applied to a wide variety of exoplanets (Kataria et al. 2014a,b, 2013; Lewis et al. 2010). These look at the effects of eccentric orbits, composition and gravity. Here we briefly discuss the results from Showman

et al. (2009) as they apply their GCM to HD 209458b, the same planet as we do in Chapter 6.

The model of HD 209458b presented in Showman et al. (2009) assumes solar metallicity and allows TiO and VO to form. Consequently their day side develops a temperature inversion around the sub-stellar point, but towards the limb of the planet the inversion disappears as temperatures are too low for gas phase TiO and VO to exist. The day side is much hotter than the temperature-forced models as they do not include effects of TiO and VO. Otherwise models are qualitatively similar to the temperature-forced models with a broad equatorial jet. Some deviations are seen in the day side emission spectrum when comparing to observations. Generally the planet flux is overestimated, except at 4.5 µm and 5.8 µm, where the flux is underestimated. It should be noted, however, that this comparison was made before the revision of the data by Diamond-Lowe et al. (2014). Accounting for this, the 4.5 µm and 5.8 µm fluxes are in much better agreement with observations.

Models of HD 189733b are also presented using solar and five times solar metallicity, but do not include TiO and VO. For this planet phase curves were also available at the time of publication, and consequently a more detailed comparison with observations is made. Increasing the metallicity generally increases the day-night temperature contrast and consequently infrared phase curve amplitudes. The five times solar metallicity model generally matches observations better than the solar metallicity model. The night side 8 µm flux is, however, underestimated in both cases, but much less so than in the temperature-forced models from Showman et al. (2008) discussed above. Generally models with sophisticated radiation schemes (Showman et al. 2009) compare better to observations than those obtained using temperature-forcing schemes (Showman et al. 2008).

1.4.4 The presence of TiO and VO

One of the more controversial topics is whether or not TiO and VO are present in the atmospheres of these planets. These molecules are strong absorbers of stellar irradiation and, if present, can cause a temperature inversion in the atmospheres of these planets as discussed above. The discussion started with observations of HD 209458b by Knutson et al. (2008) that seemed to indicate a temperature inversion on the planet's day side from its emission spectrum. This led Fortney et al. (2008a) to classify hot Jupiters into two groups: those hot enough to have TiO and VO and consequently a temperature inversion, and those that are not.

The revision of the emission spectrum from Knutson et al. (2008) by Diamond-Lowe et al. (2014) removing the need for a temperature inversion in the atmosphere of HD 209458b to explain the observations. In addition, the lack of a detection of TiO and VO (Hoeijmakers et al. 2014; Huitson et al. 2013; Sing et al. 2013) caused Parmentier et al. (2013) to investigate if TiO and VO could be depleted due to cold traps. TiO and VO may condense and gravitationally settle on the night side of these planets, which can cause the day side to become depleted of TiO and VO. This mechanism can, however, be counteracted by atmospheric circulation. Parmentier

et al. (2013) used the SPARC/MITgcm to investigate whether this cold trap could deplete TiO from the atmosphere of HD 209458b. They found that if TiO condenses into particles larger than a few microns gravitational settling can occur on the night side, keeping it from being present on the day side.

The results of Showman et al. (2009) seem to suggest that the limb of HD 209458b is too cold for TiO and VO to exist, and consequently they would not be observed in transmission spectra. However, Fortney et al. (2010) find, using the results of Showman et al. (2009), that the limb of the planet is still too hot, leading to a significantly overestimated opacity at visible wavelengths.

Whether or not HD 209458b or other hot Jupiters have TiO and VO in their atmospheres is still very much an open question. In Chapter 6 we run models of HD 209458b where we both do and do not allow TiO and VO to form.

1.4.5 Ohmic dissipation and inflated hot Jupiters

Due to the very large temperatures in the atmospheres of hot Jupiters alkali metals can become partly ionised, while at larger depths hydrogen ionisation will overtake that of alkali metals. Similar to Jupiter in our own solar system these planets may have magnetic fields that interact with the atmosphere, particularly the strong zonal jet, through the Lorentz force. Ions carried by this zonal jet may induce an inwards electrical current, which in turn may dissipate energy by ohmic dissipation at depths large enough to affect the radius of the planet. This was first proposed by Batygin & Stevenson (2010), and has been investigated in some detail (Heng 2012; Huang & Cumming 2012; Rauscher & Menou 2013; Rogers & Komacek 2014; Rogers & Showman 2014; Wu & Lithwick 2013).

It is still unclear if ohmic heating can explain the inflated radii of hot Jupiters, the problem being the presence of a magnetic field slowing down the zonal jet due to magnetic drag lowering the inward electrical current. The consideration of magnetic effects is beyond the scope of this work and we refer to Heng & Showman (2014) and the above cited papers for a more detailed discussion.

1.5 Open questions in the field

As the discussion in this chapter indicates there are many features of hot Jupiter atmospheres that are poorly understood. Whether or not some hot Jupiters have a temperature inversion in their atmosphere is not clear. If they do not, then the absence of TiO and VO, which would cause an inversion, must be explained.

How the heat redistribution efficiency varies between different planets, and how it is affected by different parameters, is not known. As more observations of hot Jupiter atmospheres are obtained statistical analysis becomes meaningful, and comparison with models will enable

conclusions to made about the processes governing the redistribution. This will also be linked to the offset of the hotspot from the substellar point and wind speeds.

The importance of non-equilibrium effects such as non-equilibrium chemistry and non-local thermodynamic equilibrium (NLTE) has only just begun to be investigated. Similarly, the understanding of clouds on hot Jupiters is in its infancy, and as yet clouds have not been implemented in a GCM applied to hot Jupiters.

Models usually assume solar elemental abundances, but the metallicity is known to vary between planets in the solar system and between stars (Baraffe et al. 2010). The metallicity can therefore be expected to vary between hot Jupiters, which will have an impact on their atmospheres as e.g. increased metallicity generally results in increased opacity.

One of the most long-standing issues is the inflation problem discussed in Section 1.1.2. The amount of inflation seems to correlate with stellar irradiation, but the physical mechanism through which inflation is sustained is not known. Several theories exist, some of them invoking interaction between the planet interior and atmosphere. Further studies of this interaction are required to resolve this issue.

Observations have so far not been of a sufficient quality to study the time variability of hot Jupiters. Variability is taken as evidence for patchy clouds on brown dwarfs (Crossfield et al. 2014), and they may be expected to have similar effects on hot Jupiters.

These are only some of the many open questions about hot Jupiter atmospheres, but it is clear that many of these cannot be answered by using 1D models. Atmospheric circulation is inherently a 3D time-varying phenomenon that requires 3D time-dependent models to investigate. Consequently, the need for GCMs applied to hot Jupiters has emerged. It is important to emphasise that since these models are complicated results can be difficult to understand in detail. A hierarchy of models, from 1D equilibrium to 3D dynamical models, will be needed in order to improve our understanding of both hot Jupiter atmospheres and planetary atmospheres in general.

1.6 Goals of the current work and impact

Here we present the adaptation of the UK Met Office GCM, the Unified Model (UM), to hot Jupiters. This model is used for both weather prediction and climate research for the Earth, and an earlier version of the one adopted here has been successfully applied to Jupiter (Yamazaki et al. 2004) and Venus (Lee et al. 2005). The current version solves the full 3D Euler equations with a height-varying gravity, i.e. the shallow atmosphere approximation has not been made (see Section 5.1 for more details). It also allows for the shallow atmosphere and constant gravity assumptions to be made by using logical switches. The UM will therefore be able to test these assumptions for hot Jupiter-like atmospheres. In addition it incorporates a state-of-the-art radiation scheme, the Edwards–Slingo (ES) radiation scheme, utilising the two-stream approximation and the correlated-k method. This makes it ideally suited to study atmospheric

circulation on hot Jupiters, but it has required significant adaptation as the Earth's atmosphere is very different from that of a hot Jupiter.

We have presented the adaptation of the dynamical core to hot Jupiter-like conditions in Mayne et al. (2014a,b) using a temperature-forcing scheme and discuss some of these results briefly in Chapter 6. There are several reasons for why we would like an accurate treatment of radiation transport in our GCM over a temperature-forcing scheme: (i) The equilibrium P–T profiles used in the forcing may have a limited accuracy; (ii) radiative timescales may also have a limited accuracy and will vary in a non-trivial way as a function of latitude, longitude and depth; (iii) the forcing parametrisation itself may not be physically realistic, though the use of time-averaged equilibrium states when analysing model results may make this less of an issue; and (iv) the model flexibility is poor since for each new planet modelled, the forcing must be changed. As discussed in Section 1.4, the difference between temperature-forced models and models with a sophisticated treatment of radiation can be large. The topic of the current work is the adaptation of the radiation scheme, and in the last chapter we present results from the hot Jupiter UM with the adapted radiation scheme.

One of the basic inputs to a radiation scheme is opacities. These opacities, which vary as a function of pressure, temperature and wavelength, provide information about how much of the radiation is converted into heat and how much is emitted thermally. The compositions of hot Jupiters are thought to be molecular hydrogen and helium based, different from the oxygen and nitrogen based atmosphere of the Earth. Consequently, the dominant atmospheric absorbers will be different, causing the need to calculate opacities for the main absorbers in hot Jupiter atmospheres. In addition, the temperatures are significantly higher on hot Jupiters than on the Earth, which means that the databases of molecular absorption lines (line lists) used for the Earth cannot be used for hot Jupiters as they are only valid up to about 400 K.

We present our calculation of opacities for the dominant absorbers in hot Jupiter atmospheres from high temperature line lists in Chapter 3. This poses challenges since these line lists are extremely large, and the ability to handle these large line lists without loss of significant data becomes important. We present a way to speed up this calculation by using an adaptive cutoff in the line list and show that the loss of accuracy is negligible while the speedup is about a factor of 100. Additionally, parallelising our opacity calculation code using OpenMP and MPI makes us capable of calculating opacities in a reasonable amount of time even for the largest line lists available.

To calculate opacities, pressure broadened line widths are needed for a H_2 and He dominated atmosphere. How this is done is often not clear in the literature, and we present our sources of pressure-broadened line widths and adaptation of them in detail. Using van der Waals broadening theory to calculate line widths is shown to be inaccurate and we consequently adopt data mainly collected from experiments performed at room temperature and pressure. We highlight the large uncertainty in this data and the need to extrapolate line widths by an order of magnitude in temperature and by a factor of three to four in rotational quantum number.

In order to treat the complicated wavelength dependence of the opacities accurately in GCMs, approximations must be made to reduce computation times. The correlated-k method mentioned above provides a framework of doing this, and we discuss this method in more detail in Section 3.4. The angular dependence of the radiative transfer equation must be simplified, which is usually done by applying the two-stream approximation discussed in Chapter 2. Both the two-stream approximation and the correlated-k method are widely used in GCM simulations of the Earth (see e.g. Thomas & Stamnes 2002), and the literature on the methods' applicability to the Earth atmosphere and their accuracy is extensive (see e.g. Goody et al. 1989; Lacis & Oinas 1991; Meador & Weaver 1980; Mlawer et al. 1997; Toon et al. 1989; Zdunkowski et al. 1980). They have both been found to yield results with satisfactory accuracy when comparing to more accurate solutions obtained from e.g. discrete ordinate (DO), line-by-line (LbL) calculations and when different schemes are compared through intercomparison projects (Collins et al. 2006; Ellingson et al. 1991; Oreopoulos et al. 2012). They are, however, still under investigation (Goldblatt et al. 2009) and are still one of the limiting factors of the accuracy of both weather prediction and climate modelling.

The correlated-k method has also been used for retrieval analysis and characterisation of hot Jupiter atmospheres (Irwin et al. 2008), and applied in model brown dwarf atmospheres (Burrows et al. 1997). Brown dwarf atmospheres have many similarities with hot Jupiter atmospheres (e.g. temperature range and composition), but local conditions are very different due to the strong irradiation from the parent stars on hot Jupiters. There is a notable lack of analysis of the accuracy of these schemes when applied to hot Jupiter-like atmospheres. This, and the frequent lack of details on opacity calculations are serious shortcomings in a field of research which develops quickly and will deliver more and more accurate data requiring reliable tools for their interpretation. For this reason, as we adapt the UM radiation scheme we perform a series of tests to verify the validity of our adapted scheme by comparing to more accurate line-by-line and discrete ordinate calculations performed with our radiative convective code `ATMO`, where both the frequency dependence of the opacity and angular dependence of the radiation is treated more accurately. These results are presented in Chapter 4.

Observations of absorbing and scattering species in hot Jupiter atmospheres have so far been limited to the detection of molecular absorbers (Huitson et al. 2013; Wakeford et al. 2013), with some observations suggesting Rayleigh/Mie scattering clouds (Pont et al. 2008; Sing et al. 2013). Due to the large uncertainties related to scatterers in hot Jupiter atmospheres and the complexity it adds to radiation transport, we limit the discussions in this work to purely absorbing atmospheres and postpone the inclusion of scattering to future work. We do, however, include Rayleigh scattering by H_2 and He in our final adapted radiation scheme.

Having verified the adapted radiation scheme's applicability to hot Jupiter atmospheres we couple it to the dynamical core of the UM. We change both the upper and lower boundary condition. The upper boundary condition takes into account radiation absorbed above the dynamical domain, and the new lower boundary condition allows us to set an intrinsic temperature

of the planet, considered more realistic than a fixed temperature surface as adopted by e.g. Showman et al. (2009). To verify the UM with the adapted radiation scheme, hereafter called "the coupled UM" or "the coupled model", we implement a uniform irradiation mode to the radiation scheme, effectively turning the UM into a 1D radiative equilibrium code, and compare resulting equilibrium P–T profiles obtained with the UM to equilibrium profiles obtained with `ATMO`. These results are presented in Chapter 5.

We apply the coupled UM to the hot Jupiter HD 209458b in Chapter 6. As discussed in Section 1.2, HD 209458b is a well-studied hot Jupiter with secondary eclipse, transmission spectrum and phase curve measurements available. The functionality of `ATMO` has been extended to be able to calculate phase curves, transmission and emission spectra from UM output, which enables us to make comparisons with observations. The hot Jupiter benchmark described in Rauscher & Menou (2010) and Heng et al. (2011) was designed to be representative of the atmosphere of HD 209458b, allowing us to directly compare the coupled model to the temperature-forced model. In addition we can compare our results to those in Showman et al. (2009), for the first time making a direct comparison of two state-of-the-art hot Jupiter GCMs with sophisticated radiation schemes possible. Consequently we can also estimate the impact of model uncertainties on observables as the setups are chosen to be as similar as possible.

1.7 Chapter overview

In Chapter 2 we discuss the theory of radiative transfer relevant to the UM radiation scheme including the derivation of the two-stream approximation. Next, in Chapter 3, we go through the calculation of opacities from high temperature line lists, and discuss the correlated-k method and the calculation of k-coefficients from these opacities. Our adopted abundance calculations, which assume chemical equilibrium, are also discussed. Details on changes made to the ES radiation scheme are provided in Chapter 4 before we present a series of tests of the adapted radiation scheme. In Chapter 5 we detail the coupling of the radiation scheme to the dynamical core, presenting the equations of motion solved by the UM dynamical core and the thermodynamic equation which couples it to the radiation scheme. Discussion and verification of our boundary conditions can be found here. We also go through the details of calculating synthetic phase curves, transmission and emission spectra from UM output. Finally, in Chapter 6, we apply the coupled UM to the hot Jupiter HD 209458b, comparing results to the temperature-forced model, the results in Showman et al. (2009) and observations. Chapter 7 ends this thesis with conclusions and some notes on the future of the project.

1.8 Statement of contribution to co-authored papers

Some of the results presented in Chapters 3 and 4 were published in Amundsen et al. (2014). Results were obtained by myself and Pascal Tremblin. I analysed the results, with contributions

from Isabelle Baraffe, Pascal Tremblin, Nathan Mayne and James Manners, and wrote the manuscript.

I am a co-author of Mayne et al. (2014a,b). I was involved in the discussions of the results presented; the work was done by Nathan Mayne. The model presented in Mayne et al. (2014a) is discussed in Section 6.2.1 to ease comparison with results obtained with the coupled hot Jupiter UM in Chapter 6.

I have also co-authored Tremblin et al. (2015). I was involved in the model development, and the paper uses the opacity database discussed in Chapter 3. Results from this paper are not presented here.

Chapter 2

Radiation transport in planetary atmospheres

The primary task of a GCM radiation scheme is to calculate radiative fluxes and heating rates. Radiation is governed by Maxwell's equations, which describe the evolution of the electromagnetic field as a function of time given the material properties and boundary conditions. In our case the magnetic field can generally be ignored and the speed of light can be considered infinite since it is much bigger than all other velocities considered. Consequently we use a simpler framework to describe radiation in planetary atmospheres, the fundamental equation being the radiative transfer equation.

The radiative transfer equation is, essentially, an energy conservation equation. The fundamental quantity is the intensity, from which all other quantities can be derived. In this chapter we go through the fundamentals of radiative transfer needed to calculate fluxes and heating rates in planetary atmospheres. We derive the two-stream approximated radiative transfer equation, which is the equation solved by the Edwards–Slingo (ES) radiation scheme used by the UM.

The theory presented here will be useful for interpreting results presented in later chapters. A more in-depth discussion is readily available in the literature; see e.g. Thomas & Stamnes (2002), Edwards & Slingo (1996), Edwards (1996) and Edwards et al. (2012).

2.1 Definitions

We begin by defining various important concepts in radiation transport. The intensity I is defined, and the Planck function, absorption, emission and scattering processes are discussed. We finally discuss the heating rate and how it can be derived from the intensity.

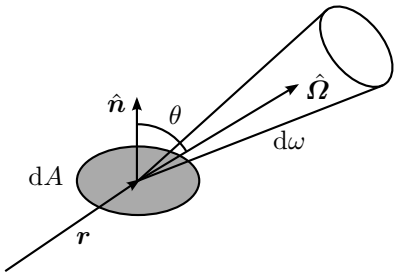

Figure 2.1: Schematic illustrating the radiative energy carried by a beam at $\boldsymbol{r}$ in the direction $\hat{\boldsymbol{\Omega}}$ per solid angle dω through a surface element dA, where θ is the angle between surface normal $\hat{\boldsymbol{n}}$ and $\hat{\boldsymbol{\Omega}}$.

2.1.1 Intensity and flux

In radiative transfer, the intensity $I_{\tilde{\nu}}$ is the fundamental quantity. It is defined as the ratio

$$I_{\tilde{\nu}}(\boldsymbol{r}, \hat{\boldsymbol{\Omega}}, \tilde{\nu}, t) = \frac{\mathrm{d}^4 E}{\cos\theta \, \mathrm{d}A \, \mathrm{d}t \, \mathrm{d}\omega \, \mathrm{d}\tilde{\nu}}, \tag{2.1}$$

where $\mathrm{d}^4 E$ is the energy that has passed through a surface element of area dA, whose normal $\hat{\boldsymbol{n}}$ is oriented at an angle θ compared to the direction of propagation $\hat{\boldsymbol{\Omega}} = (\theta, \phi)$, within a solid angle d$\omega$ around $\hat{\boldsymbol{\Omega}}$ in the time interval dt in the wavenumber interval d$\tilde{\nu}$. We illustrate this in Fig. 2.1. This energy per unit area, per unit solid angle, per unit wavenumber and per unit time is defined as the spectral intensity $I_{\tilde{\boldsymbol{\nu}}}$. The intensity is therefore a function of spatial position $\boldsymbol{r}$, direction $\hat{\boldsymbol{\Omega}}$, time t and wavenumber $\tilde{\nu}$.

The wavenumber is defined as the inverse of the wavelength of the radiation:

$$\tilde{\nu} = \frac{1}{\lambda} = \frac{\nu}{c}, \tag{2.2}$$

where λ is the wavelength, ν is the frequency and c is the speed of light.

The flux is defined as the energy per unit time per unit area passing through a surface. It is related to the intensity by

$$F_{\tilde{\nu}} \equiv \int_{4\pi} \mathrm{d}\omega \, \cos\theta \, I_{\tilde{\nu}} = \int_0^{2\pi} \mathrm{d}\phi \int_{-1}^{1} \mathrm{d}\mu \, \mu I_{\tilde{\nu}}, \tag{2.3}$$

where θ is the angle between the surface normal $\hat{\boldsymbol{n}}$ and the direction of the intensity $\hat{\boldsymbol{\Omega}}$, and $\mu = |\cos\theta|$. If $I_{\tilde{\nu}}$ is independent of $\hat{\boldsymbol{\Omega}}$, i.e. the radiation is isotropic, this yields $F_{\tilde{\nu}} = 0$ as there is no net energy transport through the surface.

2.1.2 Planck function

To introduce the Planck function we must first introduce the concept of a black-body. A black-body is an object at some temperature T that absorbs all incident radiation while at the same time emitting thermally. It is in thermal equilibrium with the environment, meaning that the amount of radiation absorbed equals the emitted radiation. The intensity of the radiation

escaping such a body is solely a function of temperature and wavenumber, and is described by the Planck function. We do not derive the Planck function here as it can be found in the literature (e.g. Thomas & Stamnes 2002).

The end result is that a black-body at temperature T emits radiation with the intensity

$$I_{\tilde{\nu}}^{\mathrm{BB}} \equiv B_{\tilde{\nu}}(T) = \frac{2hc^2\tilde{\nu}^3}{e^{hc\tilde{\nu}/k_{\mathrm{B}}T} - 1}, \tag{2.4}$$

$$I_{\lambda}^{\mathrm{BB}} \equiv B_{\lambda}(T) = \frac{2hc^2}{\lambda^5}\frac{1}{e^{hc/(\lambda k_{\mathrm{B}}T)} - 1}, \tag{2.5}$$

$$I_{\nu}^{\mathrm{BB}} \equiv B_{\nu}(T) = \frac{2h\nu^3}{c^2}\frac{1}{e^{h\nu/k_{\mathrm{B}}T} - 1}, \tag{2.6}$$

where h is Planck's constant, c is the speed of light and k_{B} is Boltzmann's constant.

The hemispheric flux is given by

$$F_{\tilde{\nu}}^{\mathrm{BB}}(T) = \int_0^{2\pi} \mathrm{d}\phi \int_0^1 \mathrm{d}\mu\, \mu B_{\tilde{\nu}}(T) = \pi B_{\tilde{\nu}}(T), \tag{2.7}$$

and equivalently for $B_{\nu}(T)$ and $B_{\lambda}(T)$.

2.1.3 Absorption

Radiation will interact with the medium it propagates through, and some of the radiation will be absorbed. The absorption coefficient describes how much of the intensity is absorbed per unit length, and is defined by

$$\mathrm{d}I_{\tilde{\nu}}^{\mathrm{abs}} = -\alpha(\tilde{\nu}) I_{\tilde{\nu}}\, \mathrm{d}s, \tag{2.8}$$

where $\mathrm{d}I_{\tilde{\nu}}^{\mathrm{abs}}$ is the change in intensity due to absorption over the distance $\mathrm{d}s$, and $\alpha(\tilde{\nu})$ is the absorption coefficient. $\alpha(\tilde{\nu})$ is often written per unit number density $\alpha_n = \alpha/n$ or per unit mass density $\alpha_\rho = \alpha/\rho$, where n and ρ are the number and mass density, respectively. α_n is usually called the absorption cross-section, as it has the unit of area, while α_ρ is the mass absorption coefficient or opacity.

2.1.4 Emission: Kirchoff's law

An atmosphere will also emit radiation thermally, contributing to an increase of the intensity. We define the change in intensity due to emission as

$$\mathrm{d}I_{\tilde{\nu}}^{\mathrm{em}} = j_{\tilde{\nu}}\, \mathrm{d}s, \tag{2.9}$$

where $j_{\tilde{\nu}}$ is the energy emitted per unit volume per unit wavenumber per unit solid angle per unit time, i.e. similar to the definition of $I_{\tilde{\nu}}$. The emission coefficient $\varepsilon(\tilde{\nu})$ is the ratio of emitted

intensity to that emitted by a perfect black-body:

$$\varepsilon(\tilde{\nu}) = \frac{\mathrm{d}I_{\tilde{\nu}}^{\mathrm{em}}}{B_{\tilde{\nu}}(T)\,\mathrm{d}s} = \frac{j_{\tilde{\nu}}}{B_{\tilde{\nu}}(T)}. \tag{2.10}$$

Kirchoff's law for thermal radiation (Thomas & Stamnes 2002) states that, in thermal equilibrium, we will have $\varepsilon(\tilde{\nu}) = \alpha(\tilde{\nu})$, and consequently

$$\mathrm{d}I_{\tilde{\nu}}^{\mathrm{em}} = \alpha(\tilde{\nu})B_{\tilde{\nu}}(T)\,\mathrm{d}s. \tag{2.11}$$

The assumption of thermal equilibrium is very restrictive, and should be relaxed. We do this by invoking the assumption of local thermodynamic equilibrium (LTE), where the medium emits according to Eq. (2.11) using the local temperature of the medium, T. This assumption is only valid if the collisional excitation and de-excitation rates are much larger than the corresponding radiative loss rates, i.e. the radiation field itself has a negligible impact on the population of quantum mechanical states of atoms and molecules in the atmosphere. This assumption breaks down if the density is low or the photon energies become high. For thermal radiation the assumption of LTE is usually acceptable (Thomas & Stamnes 2002).

2.1.5 Scattering coefficient and phase function

The scattering coefficient $\sigma(\tilde{\nu})$ is defined as the relative loss of intensity per unit length due to radiation scattered away from the beam:

$$\mathrm{d}I_{\tilde{\nu}}^{\mathrm{scat}} = -\sigma(\tilde{\nu})I_{\tilde{\nu}}\,\mathrm{d}s. \tag{2.12}$$

$\sigma_n(\tilde{\nu})$ and $\sigma_\rho(\tilde{\nu})$ are defined similarly to $\alpha_n(\tilde{\nu})$ and $\alpha_\rho(\tilde{\nu})$, respectively. Combining both absorption and scattering, we have

$$\mathrm{d}I_{\tilde{\nu}}^{\mathrm{ext}} = -\alpha(\tilde{\nu})I_{\tilde{\nu}}\,\mathrm{d}s - \sigma(\tilde{\nu})I_{\tilde{\nu}}\,\mathrm{d}s = -\left(\alpha(\tilde{\nu}) + \sigma(\tilde{\nu})\right) I_{\tilde{\nu}}\,\mathrm{d}s \equiv -k(\tilde{\nu})I_{\tilde{\nu}}\,\mathrm{d}s, \tag{2.13}$$

where we have introduced the extinction coefficient $k \equiv \alpha(\tilde{\nu}) + \sigma(\tilde{\nu})$.

The scattering phase function, $p(\hat{\boldsymbol{\Omega}}', \hat{\boldsymbol{\Omega}})$, describes the angular distribution of the scattered radiation, i.e. given a scattering event it is the probability of radiation propagating in the $\hat{\boldsymbol{\Omega}}'$ direction being scattered into the direction $\hat{\boldsymbol{\Omega}}$. The result is an increase in the intensity in the $\hat{\boldsymbol{\Omega}}$ direction given by

$$\mathrm{d}I_{\tilde{\nu}}^{\mathrm{scat},p}(\boldsymbol{\Omega}) = \frac{\sigma(\tilde{\nu})}{4\pi}\left[\int_{4\pi} \mathrm{d}\omega' I(\hat{\boldsymbol{\Omega}}')p(\hat{\boldsymbol{\Omega}}', \hat{\boldsymbol{\Omega}})\right] \mathrm{d}s \tag{2.14}$$

where $\mathrm{d}I_{\tilde{\nu}}^{\mathrm{scat},p}$ is the gain in intensity due to scattered radiation from all directions. The phase function is usually written in terms of the angle between the incoming and outgoing directions, $p(\hat{\boldsymbol{\Omega}}', \hat{\boldsymbol{\Omega}}) = p(\cos\Theta)$, where $\cos\Theta = \hat{\boldsymbol{\Omega}}' \cdot \hat{\boldsymbol{\Omega}}$ and Θ is the angle between $\hat{\boldsymbol{\Omega}}'$ and $\hat{\boldsymbol{\Omega}}$. Using the

spherical law of cosines, we have

$$\hat{\boldsymbol{\Omega}}' \cdot \hat{\boldsymbol{\Omega}} = \cos\Theta = \cos\theta' \cos\theta + \sin\theta' \sin\theta \cos(\phi' - \phi). \tag{2.15}$$

The phase function is normalised, i.e.

$$\frac{1}{4\pi} \int_{4\pi} p(\cos\Theta)\, \mathrm{d}\omega = 1, \tag{2.16}$$

and given a scattering event, the probability of scattering into the solid angle $\mathrm{d}\omega$ about $\hat{\boldsymbol{\Omega}}$ from $\hat{\boldsymbol{\Omega}}'$ is $p(\cos\Theta)\,\mathrm{d}\omega/4\pi$. The scattering phase function is often assumed to be azimuthally independent, which is a good approximation when averaging over all orientations of scatterers.

Different scatterers have different scattering coefficients and phase functions. For spherical particles with homogeneous properties the scattering phase function and cross section has been derived analytically from Maxwell's equations; this is called Mie scattering. This form of scattering is valid for all particle sizes, but certain approximations can be made in the small and large particle size limits. For particles much larger than the wavelength of the radiation geometric optics can be applied, while the limit where particles are much smaller than the wavelength of the radiation yields Rayleigh scattering.

In the current work we do not include clouds or hazes, but we do include scattering by the two most abundant particles in hot Jupiter atmospheres: molecular hydrogen and helium. Since these particles are much smaller than the relevant wavelengths Rayleigh scattering can be applied. For this reason we do not discuss Mie scattering further, but provide more details on Rayleigh scattering below.

The asymmetry factor and backscattering coefficient

Instead of using the azimuthally averaged phase function $p(u', u)$, where $u = \cos\theta$ and θ is the zenith angle of the beam direction, it is common to expand it into Legendre polynomials $P_l(u)$:

$$p(u', u) = \sum_{l=0}^{\infty} (2l+1) \chi_l P_l(u') P_l(u) \tag{2.17}$$

where the moments are given by

$$\chi_l = \frac{1}{2} \int_{-1}^{1} \mathrm{d}u'\, p(u', u) P_l(u'). \tag{2.18}$$

The first three Legendre polynomials are $P_0(u) = 1$, $P_1(u) = u$ and $P_2(u) = (3u^2 - 1)/2$. The asymmetry factor g is defined as the first moment χ_1:

$$g \equiv \chi_1 = \frac{1}{2} \int_{-1}^{1} \mathrm{d}u'\, p(u', u) u', \tag{2.19}$$

which means that

$g < 0$ backward scattering,
$g = 0$ isotropic scattering or symmetric about $\cos\Theta = 0$,
$g > 0$ forward scattering.

Due to the normalisation of the phase function $\chi_0 = 1$, which yields

$$p(u', u) = 1 + 3gu'u, \tag{2.20}$$

retaining only the two first terms in the expansion.

Another useful quantity is the backscattering coefficient, defined as

$$b(\mu) \equiv \frac{1}{2}\int_0^1 \mathrm{d}\mu'\, p(-\mu', \mu) = \frac{1}{2}\int_0^1 \mathrm{d}\mu'\, p(\mu', -\mu). \tag{2.21}$$

Rayleigh scattering

Rayleigh scattering is derived by assuming the particles are homogeneous, isotropic and spherical with a radius much smaller than the wavelength of the radiation, which is assumed to be unpolarised. The Rayleigh scattering cross section and phase function are then given by (Liou 1980)

$$\sigma_n^{\mathrm{RAY}} = \frac{8\pi^3(m_\mathrm{r}^2 - 1)^2}{3\lambda^4 n^2} f(\rho_n), \tag{2.22}$$

$$p^{\mathrm{RAY}}(\Theta) = \frac{3}{4}\left(1 + \cos^2\Theta\right), \tag{2.23}$$

where m_r is the (real) refractive index and n the number density. A correction factor $f(\rho_n)$,

$$f(\rho_n) = \frac{6 + 3\rho_n}{6 - 7\rho_n}, \tag{2.24}$$

where ρ_n is the depolarisation factor, is applied to take into consideration the anisotropy of the scattering particles.

Converting the above scattering cross section into a mass scattering coefficient by dividing by the mean molecular mass (in kg/particle), we get

$$\sigma_\rho^{\mathrm{RAY}} = \frac{\sigma_n^{\mathrm{RAY}}}{\bar{M}} = \frac{8\pi^3(m_\mathrm{r}^2 - 1)^2}{3\lambda^4 n^2}\frac{1}{\bar{M}} f(\rho_n) \tag{2.25}$$

$$= \frac{8\pi^3(m_\mathrm{r}^2 - 1)^2}{3\lambda^4}\frac{1}{\bar{M}}\frac{1}{\rho^2/\bar{M}^2} f(\rho_n) = \frac{8\pi^3(m_\mathrm{r}^2 - 1)^2}{3\lambda^4}\frac{\bar{M}}{\rho^2} f(\rho_n) \tag{2.26}$$

$$= \frac{8\pi^3(m_\mathrm{r}^2 - 1)^2}{3\lambda^4}\frac{\bar{m}}{N_\mathrm{A}\rho^2} f(\rho_n), \tag{2.27}$$

where $\bar{M}$ is the mean molecular weight in kg/particle, $\bar{m}$ is the mean molecular weight in kg/mol and N_{A} is Avogradro's number.

The Rayleigh scattering phase function can be expanded in terms of Legendre polynomials. By substituting Eq. (2.15) into Eq. (2.23), and averaging over ϕ it is possible to show that

$$p^{\mathrm{RAY}}(u', u) = 1 + \frac{1}{2} P_2(u) P_2(u'), \tag{2.28}$$

which using Eq. (2.19) yields

$$g^{\mathrm{RAY}} = \frac{1}{2} \int_{-1}^{1} \mathrm{d}u'\, u' p^{\mathrm{RAY}}(u', u) = \frac{1}{2} \int_{-1}^{1} \mathrm{d}u'\, P_1(u') \left[P_0(u') + \frac{1}{2} P_2(u) P_2(u') \right] = 0 \tag{2.29}$$

due to the orthogonality of the Legendre polynomials. This can be shown to be true for any even function of $\cos\Theta$, i.e. all phase functions symmetric about $\cos\Theta = 0$.

2.1.6 Hydrostatic equilibrium

For a stable atmosphere at rest, the pressure P at some height z must support the weight of the atmosphere above it. This situation is called hydrostatic equilibrium. In plane-parallel geometry the weight of a slab of atmosphere is given by $\mathrm{d}M = \rho \mathrm{d}V = \rho \mathrm{d}A \mathrm{d}z$, where ρ is the mass density, $\mathrm{d}V$ is the volume, $\mathrm{d}A$ is the cross-section and $\mathrm{d}z$ is the height of the slab. The pressure P is simply the force per surface area, so the top of the slab feels downward force $-P(z)\mathrm{d}A$, while the bottom feels an upwards force of $P(z+\mathrm{d}z)\mathrm{d}A$, i.e. a total force $P(z+\mathrm{d}z)\mathrm{d}A - P(z)\mathrm{d}A = -\mathrm{d}P\mathrm{d}A$, where $\mathrm{d}P = P(z) - P(z+\mathrm{d}z)$. In equilibrium this force supports the gravitational force acting on the slab, and we have

$$-\,\mathrm{d}P\,\mathrm{d}A = g\,\mathrm{d}M = g\rho\,\mathrm{d}A\,\mathrm{d}z, \tag{2.30}$$

which yields the equation of hydrostatic equilibrium:

$$\mathrm{d}P = -g\rho\,\mathrm{d}z. \tag{2.31}$$

The approximation of a plane-parallel atmosphere used above is used throughout the radiation scheme of the UM; see Section 2.2.1.

2.1.7 Heating rate

The heating rate, i.e. the rate at which the radiation exchanges energy with matter, is what couples the radiative transfer scheme to the dynamical core of the UM. From Eq. (2.1), the energy loss due to a reduced intensity over the distance $\mathrm{d}s$ is given by

$$\delta(\mathrm{d}^4 E) = \mathrm{d}I_{\tilde{\nu}} \cos\theta\, \mathrm{d}A\, \mathrm{d}t\, \mathrm{d}\omega\, \mathrm{d}\tilde{\nu}, \tag{2.32}$$

where $\mathrm{d}I_{\tilde{\nu}}$ is the change in intensity. The spectral heating rate is defined as minus the change in radiation energy per volume $\mathrm{d}V = \cos\theta\,\mathrm{d}A\mathrm{d}s$ per wavenumber $\mathrm{d}\tilde{\nu}$ per time $\mathrm{d}t$. The rate of change in the solid angle $\mathrm{d}\omega$ is then

$$\mathrm{d}\mathcal{H}_{\tilde{\nu}} \equiv -\frac{\delta(\mathrm{d}^4 E)}{\mathrm{d}V\,\mathrm{d}\tilde{\nu}\mathrm{d}t} = -\frac{\mathrm{d}I_{\tilde{\nu}}\cos\theta\,\mathrm{d}A\,\mathrm{d}t\,\mathrm{d}\omega\,\mathrm{d}\tilde{\nu}}{\cos\theta\,\mathrm{d}A\mathrm{d}s\mathrm{d}\tilde{\nu}\mathrm{d}t} = -\frac{\mathrm{d}I_{\tilde{\nu}}}{\mathrm{d}s}\mathrm{d}\omega, \tag{2.33}$$

and integrating over all angles we get

$$\mathcal{H}_{\tilde{\nu}} = -\int_{4\pi}\mathrm{d}\omega\,\frac{\mathrm{d}I_{\tilde{\nu}}}{\mathrm{d}s}. \tag{2.34}$$

The radiative heating rate is this quantity integrated over all wavenumbers:

$$\mathcal{H} = -\int_0^\infty \mathrm{d}\tilde{\nu}\,\mathcal{H}_{\tilde{\nu}} = -\int_0^\infty \mathrm{d}\tilde{\nu}\int_{4\pi}\mathrm{d}\omega\,\frac{\mathrm{d}I_{\tilde{\nu}}}{\mathrm{d}s}, \tag{2.35}$$

which in a 1D plane-parallel geometry ($\mathrm{d}z = \mathrm{d}s\cos\theta$) becomes

$$\mathcal{H} = -\int_0^\infty \mathrm{d}\tilde{\nu}\int_{4\pi}\mathrm{d}\omega\,\cos\theta\,\frac{\mathrm{d}I_{\tilde{\nu}}}{\mathrm{d}z} = -\int_0^\infty \mathrm{d}\tilde{\nu}\,\frac{\mathrm{d}}{\mathrm{d}z}\left(\int_{4\pi}\mathrm{d}\omega\,\cos\theta\,I_{\tilde{\nu}}\right) \tag{2.36}$$

since θ is independent of z. Using Eq. (2.3) for the flux we get an expression for the heating rate per unit volume:

$$\mathcal{H} = -\int_0^\infty \mathrm{d}\tilde{\nu}\,\frac{\mathrm{d}F_{\tilde{\nu}}}{\mathrm{d}z} = -\frac{\mathrm{d}F}{\mathrm{d}z}. \tag{2.37}$$

If assuming hydrostatic equilibrium, $\mathrm{d}P = -g\rho\mathrm{d}z$, where g is the gravity and ρ is the mass density, and using the ideal gas equation $P = \rho k_\mathrm{B}T/\bar{m}$, where $\bar{m}$ is the mean molecular weight, we have

$$\mathrm{d}P = -\frac{gP\bar{m}}{k_\mathrm{B}T}\mathrm{d}z, \tag{2.38}$$

and Eq. (2.37) can be written in terms of pressure:

$$\mathcal{H} = \frac{gP\bar{m}}{k_\mathrm{B}T}\frac{\mathrm{d}F}{\mathrm{d}P}. \tag{2.39}$$

2.2 The radiative transfer equation

Combining absorption, scattering and emission, Eqs. (2.11), (2.13) and (2.14), the total intensity change is given by

$$\mathrm{d}I_{\tilde{\nu}} = -k(\tilde{\nu})I_{\tilde{\nu}}\,\mathrm{d}s + \alpha(\tilde{\nu})B_{\tilde{\nu}}(T)\,\mathrm{d}s + \frac{\sigma(\tilde{\nu})}{4\pi}\left[\int_{4\pi}\mathrm{d}\omega' I(\hat{\boldsymbol{\Omega}}')p(\hat{\boldsymbol{\Omega}}',\hat{\boldsymbol{\Omega}})\right]\mathrm{d}s, \tag{2.40}$$

and dividing this equation by $k(\tilde{\nu})\,\mathrm{d}s$, we get the radiative transfer equation:

$$\frac{\mathrm{d}I_{\tilde{\nu}}}{\mathrm{d}\tau_{\mathrm{s}}} = -I_{\tilde{\nu}} + [1 - a(\tilde{\nu})]\,B_{\tilde{\nu}}(T) + \frac{a(\tilde{\nu})}{4\pi}\int_{4\pi}\mathrm{d}\omega'\,p(\hat{\boldsymbol{\Omega}}', \hat{\boldsymbol{\Omega}})I_{\tilde{\nu}}(\hat{\boldsymbol{\Omega}}), \tag{2.41}$$

where $a(\tilde{\nu}) = \sigma(\tilde{\nu})/k(\tilde{\nu})$ is the single scattering albedo and τ_{s} is the extinction optical depth:

$$\mathrm{d}\tau_{\mathrm{s}} = k(\tilde{\nu})\,\mathrm{d}s. \tag{2.42}$$

$a(\tilde{\nu})$ is the probability of a scattering event given that an extinction event occurs. The two last terms on the right-hand side of Eq. (2.41) are usually combined into the source function, $S_{\tilde{\nu}}$:

$$S_{\tilde{\nu}} = [1 - a(\tilde{\nu})]\,B_{\tilde{\nu}}(T) + \frac{a(\tilde{\nu})}{4\pi}\int_{4\pi}\mathrm{d}\omega'\,p(\hat{\boldsymbol{\Omega}}', \hat{\boldsymbol{\Omega}})I_{\tilde{\nu}}(\hat{\boldsymbol{\Omega}}). \tag{2.43}$$

2.2.1 Plane-parallel geometry

In a 1D plane-parallel vertical geometry the horizontal variations in the atmospheric properties are assumed to be negligible. Consequently, we can replace the slant optical depth τ_s with the vertical optical depth τ defined by

$$\mathrm{d}\tau = -\mathrm{d}\tau_s\,\cos\theta = -\mathrm{d}\tau_s\,u. \tag{2.44}$$

We illustrate the relationship between the slant and vertical optical depths in Fig. 2.2. The vertical optical depth is therefore given by

$$\mathrm{d}\tau = -k(z)\,\mathrm{d}z = -k_\rho(z)\rho(z)\,\mathrm{d}z = -\sum_i \zeta_i(z)k_\rho^i(z)\rho(z)\,\mathrm{d}z, \tag{2.45}$$

or in integrated form, assuming hydrostatic equilibrium:

$$\tau = \sum_i \tau_i = \sum_i \int_z^\infty \mathrm{d}z'\,\zeta_i(z')k_\rho^i(z')\rho(z') \tag{2.46}$$

$$= \frac{1}{g}\sum_i \int_0^P \mathrm{d}P'\,\zeta_i(P')k_\rho^i(P'), \tag{2.47}$$

where k_ρ^i and ζ_i are the mass extinction coefficient and mass mixing ratio of species i, respectively. The total mass extinction coefficient is $k_\rho(z)$, and the total extinction coefficient is $k(z) = k_\rho(z)\rho(z)$.

Substituting Eq. (2.44) into Eq. (2.41) we get the radiative transfer equation in plane parallel geometry:

$$u\frac{\mathrm{d}I_{\tilde{\nu}}(\tau, \hat{\boldsymbol{\Omega}})}{\mathrm{d}\tau} = I_{\tilde{\nu}}(\tau, \hat{\boldsymbol{\Omega}}) - [1 - a(\tilde{\nu})]\,B_{\tilde{\nu}}(T) - \frac{a(\tilde{\nu})}{4\pi}\int_{4\pi}\mathrm{d}\omega'\,p(\hat{\boldsymbol{\Omega}}', \hat{\boldsymbol{\Omega}})I_{\tilde{\nu}}(\tau, \hat{\boldsymbol{\Omega}}'). \tag{2.48}$$

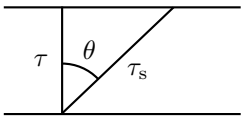

Figure 2.2: Illustration of the relationship between the slant optical depth τ_s and the (vertical) optical depth τ.

2.2.2 Hemispheric intensities and diffuse and direct components

It is customary to separate the total intensity into up-welling (+) and down-welling (−) intensities defined by

$$I^+_{\tilde{\nu}}(\tau, \hat{\boldsymbol{\Omega}}) = I^+_{\tilde{\nu}}(\tau, \theta, \phi) \equiv I_{\tilde{\nu}}(\tau, \theta \leqslant \pi/2, \phi), \tag{2.49}$$

$$I^-_{\tilde{\nu}}(\tau, \hat{\boldsymbol{\Omega}}) = I^-_{\tilde{\nu}}(\tau, \theta, \phi) \equiv I_{\tilde{\nu}}(\tau, \theta > \pi/2, \phi). \tag{2.50}$$

We introduce $\mu \equiv |\cos\theta| = |u|$ and replace all occurrences of u with μ:

$$I^+_{\tilde{\nu}}(\tau, \mu, \phi) \equiv I_{\tilde{\nu}}(\tau, \mu, \phi), \tag{2.51}$$

$$I^-_{\tilde{\nu}}(\tau, \mu, \phi) \equiv I_{\tilde{\nu}}(\tau, -\mu, \phi). \tag{2.52}$$

Substituting $I_{\tilde{\nu}} = I^+_{\tilde{\nu}} + I^-_{\tilde{\nu}}$ into Eq. (2.48) and separating the two hemispheres yields

$$\pm\,\mu \frac{\mathrm{d}I^\pm_{\tilde{\nu}}(\tau, \hat{\boldsymbol{\Omega}})}{\mathrm{d}\tau} = I^\pm_{\tilde{\nu}}(\tau, \hat{\boldsymbol{\Omega}}) - S^\pm_{\tilde{\nu}}(\tau, \hat{\boldsymbol{\Omega}}), \tag{2.53}$$

where

$$\begin{aligned} S^\pm_{\tilde{\nu}}(\tau, \Omega) = {} & [1 - a(\tilde{\nu})]\, B_{\tilde{\nu}}(T) + \frac{a(\tilde{\nu})}{4\pi} \int_\pm \mathrm{d}\omega'\, p(\hat{\boldsymbol{\Omega}}', \hat{\boldsymbol{\Omega}}) I^\pm_{\tilde{\nu}}(\tau, \hat{\boldsymbol{\Omega}}') \\ & + \frac{a(\tilde{\nu})}{4\pi} \int_\mp \mathrm{d}\omega'\, p(\hat{\boldsymbol{\Omega}}', \hat{\boldsymbol{\Omega}}) I^\mp_{\tilde{\nu}}(\tau, \hat{\boldsymbol{\Omega}}'). \end{aligned} \tag{2.54}$$

It is common to separate the non-scattered stellar irradiation from the intensity into a direct component, $I^\pm_\mathrm{s}$, with the remaining intensity $I^\pm_\mathrm{d}$ called the diffuse component. Note that by definition $I^+_\mathrm{s} = 0$ and that we have dropped the wavenumber subscript for convenience. The total intensity becomes

$$I^\pm_{\tilde{\nu}} = I^\pm_\mathrm{s} + I^\pm_\mathrm{d}. \tag{2.55}$$

Since the direct component does not contain any scattered radiation it can easily be expressed by using the simple extinction law:

$$-\frac{\mathrm{d}I^\pm_\mathrm{s}(\tau, \hat{\boldsymbol{\Omega}})}{\mathrm{d}\tau} = I^-_\mathrm{s}(\tau, \hat{\boldsymbol{\Omega}}) \quad \Rightarrow \quad I^-_\mathrm{s}(\tau, \hat{\boldsymbol{\Omega}}) = F_\mathrm{s} e^{-\tau/\mu_0} \delta(\hat{\boldsymbol{\Omega}} - \hat{\boldsymbol{\Omega}}_0), \tag{2.56}$$

where $\hat{\boldsymbol{\Omega}}_0 = (\theta_0, \phi_0)$ is the direction of the incident sunlight and F_s is the stellar flux at the top of the atmosphere. For reference, the direct component of the flux is given by

$$F_\mathrm{s}(\tau) = \int_0^{2\pi} \mathrm{d}\phi \int_0^{\pi} \mathrm{d}\theta \, \cos\theta I_\mathrm{s}^-(\tau, \theta, \phi) = F_\mathrm{s}\mu_0 e^{-\tau/\mu_0}, \tag{2.57}$$

where $\mu_0 = \cos\theta_0$, called the stellar zenith angle. To proceed we insert Eq. (2.55) into Eq. (2.53), first for the down-welling direction:

$$\begin{aligned} -\mu\frac{\mathrm{d}I_\mathrm{s}^-(\tau,\hat{\boldsymbol{\Omega}})}{\mathrm{d}\tau} - \mu\frac{\mathrm{d}I_\mathrm{d}^-(\tau,\hat{\boldsymbol{\Omega}})}{\mathrm{d}\tau} &= I_\mathrm{s}^-(\tau,\hat{\boldsymbol{\Omega}}) + I_\mathrm{d}^-(\tau,\hat{\boldsymbol{\Omega}}) - [1-a(\tilde{\nu})]\, B_{\tilde{\nu}}(T) \\ &\quad - \frac{a(\tilde{\nu})}{4\pi}\int_- \mathrm{d}\omega'\, p(\hat{\boldsymbol{\Omega}}', \hat{\boldsymbol{\Omega}}) \left[I_\mathrm{s}^-(\tau,\hat{\boldsymbol{\Omega}}') + I_\mathrm{d}^-(\tau,\hat{\boldsymbol{\Omega}}') \right] \\ &\quad - \frac{a(\tilde{\nu})}{4\pi}\int_+ \mathrm{d}\omega'\, p(\hat{\boldsymbol{\Omega}}', \hat{\boldsymbol{\Omega}}) I_\mathrm{d}^+(\tau,\hat{\boldsymbol{\Omega}}'), \end{aligned} \tag{2.58}$$

which using Eq. (2.56) yields

$$-\mu\frac{\mathrm{d}I_\mathrm{d}^-(\tau,\hat{\boldsymbol{\Omega}})}{\mathrm{d}\tau} = I_\mathrm{d}^-(\tau,\hat{\boldsymbol{\Omega}}) - [1-a(\tilde{\nu})]\, B_{\tilde{\nu}}(T) - S_\mathrm{s}^- - S_\mathrm{d}^-, \tag{2.59}$$

where

$$S_\mathrm{s}^-(\tau,\hat{\boldsymbol{\Omega}}) = \frac{a(\tilde{\nu})}{4\pi} p(\hat{\boldsymbol{\Omega}}_0, \hat{\boldsymbol{\Omega}}) F^\mathrm{s} e^{-\tau/\mu_0} \tag{2.60}$$

$$S_\mathrm{d}^-(\tau,\hat{\boldsymbol{\Omega}}) = \frac{a(\tilde{\nu})}{4\pi}\int_+ \mathrm{d}\omega'\, p(\hat{\boldsymbol{\Omega}}', \hat{\boldsymbol{\Omega}}) I_\mathrm{d}^+(\tau,\hat{\boldsymbol{\Omega}}) + \frac{a(\tilde{\nu})}{4\pi}\int_- \mathrm{d}\omega'\, p(\hat{\boldsymbol{\Omega}}', \hat{\boldsymbol{\Omega}}) I_\mathrm{d}^-(\tau,\hat{\boldsymbol{\Omega}}'). \tag{2.61}$$

We do the equivalent for the up-welling directions, and get

$$\begin{aligned} \mu\frac{\mathrm{d}I_\mathrm{d}^+(\tau,\hat{\boldsymbol{\Omega}})}{\mathrm{d}\tau} &= I_\mathrm{d}^+(\tau,\hat{\boldsymbol{\Omega}}) - [1-a(\tilde{\nu})]\, B_{\tilde{\nu}}(T) \\ &\quad - \frac{a(\tilde{\nu})}{4\pi}\int_+ \mathrm{d}\omega'\, p(\hat{\boldsymbol{\Omega}}', \hat{\boldsymbol{\Omega}}) I_\mathrm{d}^+(\tau,\hat{\boldsymbol{\Omega}}') - \frac{a(\tilde{\nu})}{4\pi}\int_- \mathrm{d}\omega'\, p(\hat{\boldsymbol{\Omega}}', \hat{\boldsymbol{\Omega}}) \left[I_\mathrm{s}^-(\tau,\hat{\boldsymbol{\Omega}}') + I_\mathrm{d}^-(\tau,\hat{\boldsymbol{\Omega}}') \right] \end{aligned} \tag{2.62}$$

which simplifies to

$$\mu\frac{\mathrm{d}I_\mathrm{d}^+(\tau,\hat{\boldsymbol{\Omega}})}{\mathrm{d}\tau} = I_\mathrm{d}^+(\tau,\hat{\boldsymbol{\Omega}}) - [1-a(\tilde{\nu})]\, B_{\tilde{\nu}}(T) - S_\mathrm{s}^+(\tau,\hat{\boldsymbol{\Omega}}) - S_\mathrm{d}^+(\tau,\hat{\boldsymbol{\Omega}}), \tag{2.63}$$

where

$$S_\mathrm{s}^+(\tau,\hat{\boldsymbol{\Omega}}) = \frac{a(\tilde{\nu})}{4\pi} p(\hat{\boldsymbol{\Omega}}_0, \hat{\boldsymbol{\Omega}}) F^\mathrm{s} e^{-\tau/\mu_0}, \tag{2.64}$$

$$S_\mathrm{d}^+(\tau,\hat{\boldsymbol{\Omega}}) = \frac{a(\tilde{\nu})}{4\pi}\int_+ \mathrm{d}\omega'\, p(\hat{\boldsymbol{\Omega}}', \hat{\boldsymbol{\Omega}}) I_\mathrm{d}^+(\tau,\hat{\boldsymbol{\Omega}}') + \frac{a(\tilde{\nu})}{4\pi}\int_- \mathrm{d}\omega'\, p(\hat{\boldsymbol{\Omega}}', \hat{\boldsymbol{\Omega}}) I_\mathrm{d}^-(\tau,\hat{\boldsymbol{\Omega}}). \tag{2.65}$$

Combining Eqs. (2.59) and (2.63) we get the radiative transfer equation using half-range intensities:

$$\pm\,\mu\frac{\mathrm{d}I_{\mathrm{d}}^{\pm}(\tau,\hat{\boldsymbol{\Omega}})}{\mathrm{d}\tau} = I_{\mathrm{d}}^{\pm}(\tau,\hat{\boldsymbol{\Omega}}) - [1-a(\tilde{\nu})]\,B_{\tilde{\nu}}(T) - S_{\mathrm{s}}^{\pm}(\tau,\hat{\boldsymbol{\Omega}}) - S_{\mathrm{d}}^{\pm}(\tau,\hat{\boldsymbol{\Omega}}), \tag{2.66}$$

where

$$S_{\mathrm{s}}^{\pm}(\tau,\hat{\boldsymbol{\Omega}}) = \frac{a(\tilde{\nu})}{4\pi}p(\hat{\boldsymbol{\Omega}}_0,\hat{\boldsymbol{\Omega}})F^{\mathrm{s}}e^{-\tau/\mu_0}, \tag{2.67}$$

$$S_{\mathrm{d}}^{\pm}(\tau,\hat{\boldsymbol{\Omega}}) = \frac{a(\tilde{\nu})}{4\pi}\int_{+}\mathrm{d}\omega'\,p(\hat{\boldsymbol{\Omega}}',\hat{\boldsymbol{\Omega}})I_{\mathrm{d}}^{+}(\tau,\hat{\boldsymbol{\Omega}}') + \frac{a(\tilde{\nu})}{4\pi}\int_{-}\mathrm{d}\omega'\,p(\hat{\boldsymbol{\Omega}}',\hat{\boldsymbol{\Omega}})I_{\mathrm{d}}^{-}(\tau,\hat{\boldsymbol{\Omega}}). \tag{2.68}$$

The interpretation of the different terms in Eq. (2.66) is straight forward: $S_{\mathrm{s}}^{\pm}$ is the source function due to scattering of the direct stellar component and $S_{\mathrm{d}}^{\pm}(\tau,\hat{\boldsymbol{\Omega}})$ is the source function due to scattering of the diffuse field. It is important to remember that when calculating the total fluxes and heating rates, the total intensity must be used, not just the diffuse components $I_{\mathrm{d}}^{\pm}$.

2.2.3 Azimuthal independence of flux and heating rate

Since we are only interested in the heating rate, which is flux dependent, it is possible to remove the azimuthal dependence in the radiative transfer equation. The first step in proving this is to average Eqs. (2.66) to (2.68) with respect to ϕ. We first look at the source terms S, starting with $S_{\mathrm{d}}^{\pm}$:

$$\begin{aligned}
S_{\mathrm{d}}^{\pm}(\tau,\mu) &= \frac{1}{2\pi}\int_0^{2\pi}\mathrm{d}\phi\,S_{\mathrm{d}}^{\pm}(\tau,\mu,\phi)\\
&= \frac{a(\tilde{\nu})}{4\pi}\int_0^1\mathrm{d}\mu'\int_0^{2\pi}\mathrm{d}\phi'\,I_{\mathrm{d}}^{+}(\tau,\mu',\phi')\frac{1}{2\pi}\int_0^{2\pi}\mathrm{d}\phi\,p(\mu',\phi',\pm\mu,\phi)\\
&\quad+\frac{a(\tilde{\nu})}{4\pi}\int_0^1\mathrm{d}\mu'\int_0^{2\pi}\mathrm{d}\phi'\,I_{\mathrm{d}}^{-}(\tau,\mu',\phi')\frac{1}{2\pi}\int_0^{2\pi}\mathrm{d}\phi\,p(-\mu',\phi',\pm\mu,\phi)\\
&= \frac{a(\tilde{\nu})}{4\pi}\int_0^1\mathrm{d}\mu'\int_0^{2\pi}\mathrm{d}\phi'\,I_{\mathrm{d}}^{+}(\tau,\mu',\phi')p(\mu',\pm\mu)\\
&\quad+\frac{a(\tilde{\nu})}{4\pi}\int_0^1\mathrm{d}\mu'\int_0^{2\pi}\mathrm{d}\phi'\,I_{\mathrm{d}}^{-}(\tau,\mu',\phi')p(-\mu',\pm\mu),\\
&= \frac{a(\tilde{\nu})}{2}\int_0^1\mathrm{d}\mu'\,I_{\mathrm{d}}^{+}(\tau,\mu')p(\mu',\pm\mu) + \frac{a(\tilde{\nu})}{2}\int_0^1\mathrm{d}\mu'\,I_{\mathrm{d}}^{-}(\tau,\mu')p(-\mu',\pm\mu),
\end{aligned} \tag{2.69}$$

where we have defined

$$I_{\mathrm{d}}^{\pm}(\tau,\mu) = \frac{1}{2\pi}\int_0^{2\pi}\mathrm{d}\phi\,I_{\mathrm{d}}^{\pm}(\tau,\mu,\phi), \tag{2.70}$$

$$p(\pm\mu',\pm\mu) = \frac{1}{2\pi}\int_0^{2\pi}\mathrm{d}\phi\,p(\pm\mu',\phi',\pm\mu,\phi). \tag{2.71}$$

The phase function loses its dependence on both ϕ and ϕ' because it is usually taken to be a function of the angle between the incoming and outgoing directions; see Section 2.1.5.

Similarly for $S_{\rm s}^{\pm}$:

$$\begin{aligned} S_{\rm s}^{\pm}(\tau,\mu) &= \frac{1}{2\pi}\int_0^{2\pi} \mathrm{d}\phi\, S_{\rm s}^{\pm}(\tau,\mu,\phi) = \frac{a(\tilde{\nu})}{4\pi} F^{\rm s} e^{-\tau/\mu_0} \frac{1}{2\pi}\int_0^{2\pi} \mathrm{d}\phi\, p(-\mu_0,\phi_0,\pm\mu,\phi), \\ &= \frac{a(\tilde{\nu})}{4\pi} F^{\rm s} e^{-\tau/\mu_0} p(-\mu_0,\pm\mu). \end{aligned} \tag{2.72}$$

Averaging the thermal source function in Eq. (2.66) over all azimuth angles is straightforward since the Planck function is isotropic. Consequently, the azimuthally independent radiative transfer equation is given by

$$\pm\,\mu \frac{\mathrm{d}I_{\rm d}^{\pm}(\tau,\mu)}{\mathrm{d}\tau} = I_{\rm d}^{\pm}(\tau,\mu) - \left[1-a(\tilde{\nu})\right] B_{\tilde{\nu}}(T) - S_{\rm s}^{\pm}(\tau,\mu) - S_{\rm d}^{\pm}(\tau,\mu), \tag{2.73}$$

where

$$S_{\rm s}^{\pm}(\tau,\mu) = \frac{a(\tilde{\nu})}{4\pi} F^{\rm s} e^{-\tau/\mu_0} p(-\mu_0,\pm\mu), \tag{2.74}$$

$$S_{\rm d}^{\pm}(\tau,\mu) = \frac{a(\tilde{\nu})}{2}\int_0^1 \mathrm{d}\mu'\, I_{\rm d}^{+}(\tau,\mu') p(\mu',\pm\mu) + \frac{a(\tilde{\nu})}{2}\int_0^1 \mathrm{d}\mu'\, I_{\rm d}^{-}(\tau,\mu') p(-\mu',\pm\mu). \tag{2.75}$$

2.2.4 Splitting into stellar and thermal components

The diffuse intensity can be thought of as consisting of two parts: a stellar part originating from the host star and a thermal part originating from the planet's thermal emission. When the planet's effective temperature is much smaller than the host star's effective temperature these are also separated in wavelength. The stellar part is often called the short-wave region, while the thermal part is called the long-wave region. This separation in wavelength is well-suited for the Earth, but less so for hot Jupiters, where temperatures can reach up to 3000 K.

Nonetheless, since Eq. (2.73) is linear with intensity the diffuse intensity can still be decomposed into a stellar part and a thermal part, often misleadingly called short- and long-wave components, respectively. From Eqs. (2.73) to (2.75) we get the radiative transfer equation for the diffuse stellar component, $I_{\rm d,s}^{\pm}$, and the diffuse thermal component $I_{\rm d,t}^{\pm}$:

$$\pm\mu \frac{\mathrm{d}I_{\rm d,s}^{\pm}(\tau,\mu)}{\mathrm{d}\tau} = I_{\rm d,s}^{\pm}(\tau,\mu) - S_{\rm s}^{\pm}(\tau,\mu) - S_{\rm d,s}^{\pm}(\tau,\mu), \tag{2.76}$$

$$\pm\mu \frac{\mathrm{d}I_{\rm d,t}^{\pm}(\tau,\mu)}{\mathrm{d}\tau} = I_{\rm d,t}^{\pm}(\tau,\mu) - \left[1-a(\tilde{\nu})\right] B_{\tilde{\nu}}(T) - S_{\rm d,t}^{\pm}(\tau,\mu), \tag{2.77}$$

where the source function $S_{{\rm d},c}^{\pm}$ for component c is given by

$$S_{\rm d,s}^{\pm}(\tau,\mu) = \frac{a(\tilde{\nu})}{2}\int_0^1 \mathrm{d}\mu'\, I_{\rm d,s}^{+}(\tau,\mu') p(\mu',\pm\mu) + \frac{a(\tilde{\nu})}{2}\int_0^1 \mathrm{d}\mu'\, I_{\rm d,s}^{-}(\tau,\mu') p(-\mu',\pm\mu), \tag{2.78}$$

and $S_{\rm s}$ is given by Eq. (2.74).

2.2.5 The two-stream approximation

The angular dependence in Eqs. (2.76) and (2.77) makes it rather difficult to solve if scattering is included even though the azimuthal dependence has been removed. In the two-stream approximation this angular dependence is reduced to two discrete angles, labelled "up" and "down". This decreases the computation time required to solve the radiative transfer equation significantly, but it does reduce the accuracy of the solution. We test the accuracy of the two-stream approximation for hot Jupiter-like atmospheres in Chapter 4.

The two-stream approximation involves applying the operator $\int_0^1 {\rm d}\mu$ to each side of Eqs. (2.76) and (2.77). We begin with the stellar component:

$$\pm \int_0^1 {\rm d}\mu\, \mu \frac{{\rm d}I^{\pm}_{\rm d,s}(\tau,\mu)}{{\rm d}\tau} = \int_0^1 {\rm d}\mu\, \left[I^{\pm}_{\rm d,s}(\tau,\mu) - S^{\pm}_{\rm s}(\tau,\mu) - S^{\pm}_{\rm d,s}(\tau,\mu) \right]. \tag{2.79}$$

In the two-stream equation, we replace explicit appearances of μ by some average $\bar{\mu}$ and the integrated intensity in each hemisphere by the integrated value:

$$I^{\pm}_{\rm d}(\tau) = \int_0^1 {\rm d}\mu\, I^{\pm}_{\rm d}(\tau,\mu), \qquad \int_0^1 {\rm d}\mu\, \mu I^{\pm}_{\rm d}(\tau,\mu) \approx \bar{\mu} I^{\pm}_{\rm d}(\tau), \qquad \bar{\mu} = \frac{\int_0^1 {\rm d}\mu\, \mu I^{\pm}_{\rm d}(\tau,\mu)}{\int_0^1 {\rm d}\mu\, I^{\pm}_{\rm d}(\tau,\mu)}. \tag{2.80}$$

Using Eq. (2.3), the flux $F_{\tilde{\nu}}$ becomes in the two-stream approximation

$$\begin{aligned} F_{\tilde{\nu}}(\tau) &= 2\pi \int_0^1 {\rm d}\mu\, \mu \left[I^{+}_{\tilde{\nu}}(\tau,\mu) - I^{-}_{\tilde{\nu}}(\tau,\mu) \right] \\ &\approx 2\pi \left[\bar{\mu} I^{+}_{\tilde{\nu}}(\tau) - \bar{\mu} I^{-}_{\tilde{\nu}}(\tau) \right] = F^{+}_{\tilde{\nu}}(\tau) - F^{-}_{\tilde{\nu}}(\tau). \end{aligned} \tag{2.81}$$

The source term $S^{\pm}_{\rm s}$ in Eq. (2.79), given Eq. (2.74), becomes

$$S^{+}_{\rm s}(\tau) = \int_0^1 {\rm d}\mu\, S^{+}_{\rm s}(\tau,\mu) = \frac{a(\tilde{\nu})}{4\pi} F^{\rm s} e^{-\tau/\mu_0} \int_0^1 {\rm d}\mu\, p(-\mu_0,+\mu) = \frac{a(\tilde{\nu})}{2\pi} F^{\rm s} b(\mu_0) e^{-\tau/\mu_0}, \tag{2.82}$$

$$S^{-}_{\rm s}(\tau) = \int_0^1 {\rm d}\mu\, S^{-}_{\rm s}(\tau,\mu) = \frac{a(\tilde{\nu})}{2\pi} F^{\rm s} \left[1 - b(\mu_0) \right] e^{-\tau/\mu_0}, \tag{2.83}$$

where the backscattering coefficient $b(\mu)$ is as defined in Eq. (2.21). The diffuse source term,

$S^{\pm}_{\rm d,s}$ in Eq. (2.79) and given by Eq. (2.78) becomes:

$$\begin{aligned}
S^{\pm}_{\rm d,s}(\tau) &= \int_0^1 {\rm d}\mu\, S^{\pm}_{\rm d,s}(\tau,\mu) \\
&= \frac{a(\tilde{\nu})}{2}\int_0^1 {\rm d}\mu'\, I^{+}_{\rm d,s}(\tau,\mu')\int_0^1 {\rm d}\mu\, p(\mu',\pm\mu) + \frac{a(\tilde{\nu})}{2}\int_0^1 {\rm d}\mu'\, I^{-}_{\rm d,s}(\tau,\mu')\int_0^1 {\rm d}\mu\, p(-\mu',\pm\mu) \\
&= a(\tilde{\nu})\int_0^1 {\rm d}\mu'\, I^{\pm}_{\rm d,s}(\tau,\mu')\left[1-b(\mu')\right] + a(\tilde{\nu})\int_0^1 {\rm d}\mu'\, I^{\mp}_{\rm d,s}(\tau,\mu')b(\mu') \\
&\approx a(\tilde{\nu})I^{\pm}_{\rm d,s}(\tau)\left[1-b\right] + a(\tilde{\nu})I^{\mp}_{\rm d,s}(\tau)b, \qquad (2.84)
\end{aligned}$$

where

$$b = \frac{\int_0^1 {\rm d}\mu'\, I^{\pm}_{\rm d}(\tau,\mu')b(\mu')}{\int_0^1 {\rm d}\mu\, I^{\pm}_{\rm d}(\tau,\mu)}. \qquad (2.85)$$

Combining all of this, we get the two-stream equations

$$\pm\,\bar{\mu}\frac{{\rm d}I^{\pm}_{\rm d,s}(\tau)}{{\rm d}\tau} = I^{\pm}_{\rm d,s}(\tau) - S^{\pm}_{\rm s}(\tau) - S^{\pm}_{\rm d,s}(\tau), \qquad (2.86)$$

with

$$S^{+}_{\rm s}(\tau) = \frac{a(\tilde{\nu})}{2\pi}F^{\rm s}b(\mu_0)e^{-\tau/\mu_0}, \qquad (2.87)$$

$$S^{-}_{\rm s}(\tau) = \frac{a(\tilde{\nu})}{2\pi}F^{\rm s}\left[1-b(\mu_0)\right]e^{-\tau/\mu_0}, \qquad (2.88)$$

$$S^{\pm}_{\rm d,s}(\tau) = a(\tilde{\nu})I^{\pm}_{\rm d}(\tau)\left[1-b\right] + a(\tilde{\nu})I^{\mp}_{\rm d}(\tau)b. \qquad (2.89)$$

The derivation above is easily repeated for the thermal component as the Planck function is isotropic. The result is

$$\pm\,\bar{\mu}\frac{{\rm d}I^{\pm}_{\rm d,t}(\tau)}{{\rm d}\tau} = I^{\pm}_{\rm d,t}(\tau) - \left[1-a(\tilde{\nu})\right]B_{\tilde{\nu}}(T) - S^{\pm}_{\rm d,t}(\tau), \qquad (2.90)$$

with

$$S^{\pm}_{\rm d,t}(\tau) = a(\tilde{\nu})I^{\pm}_{\rm d,t}(\tau)\left[1-b\right] + a(\tilde{\nu})I^{\mp}_{\rm d,t}(\tau)b. \qquad (2.91)$$

2.2.6 Two-stream flux equations

Using Eq. (2.81), it is possible to write the two-stream approximated radiative transfer equation in terms of fluxes. We have $F^{\pm}_{\rm d}(\tau) = 2\pi\bar{\mu}I^{\pm}_{\rm d}(\tau)$, or $I^{\pm}_{\rm d}(\tau) = F^{\pm}_{\rm d}(\tau)/(2\pi\bar{\mu})$ where the frequency

dependence has again been dropped for convenience. Equations (2.86) and (2.90) then become

$$\frac{\mathrm{d}F_{\mathrm{d}}^{+}(\tau)}{\mathrm{d}\tau} = \gamma_1 F_{\mathrm{d}}^{+}(\tau) - \gamma_2 F_{\mathrm{d}}^{-}(\tau) - Q^{+}, \tag{2.92a}$$

$$\frac{\mathrm{d}F_{\mathrm{d}}^{-}(\tau)}{\mathrm{d}\tau} = \gamma_2 F_{\mathrm{d}}^{+}(\tau) - \gamma_1 F_{\mathrm{d}}^{-}(\tau) + Q^{-}, \tag{2.92b}$$

where

$$Q^{+} = \begin{cases} \gamma_3 a F^{\mathrm{s}} e^{-\tau/\mu_0} & \text{for the stellar component,} \\ 2\pi \left[1-a\right] B_{\tilde{\nu}}(T) & \text{for the thermal component,} \end{cases} \tag{2.93a}$$

$$Q^{-} = \begin{cases} \left[1-\gamma_3\right] a F^{\mathrm{s}} e^{-\tau/\mu_0} & \text{for the stellar component,} \\ 2\pi \left[1-a\right] B_{\tilde{\nu}}(T) & \text{for the thermal component.} \end{cases} \tag{2.93b}$$

The coefficients $\gamma_{1,2,3}$ are often expressed in terms of the diffusivity factor $D \equiv 1/\bar{\mu}$ instead of the mean zenith angle $\bar{\mu}$:

$$\gamma_1 = D\left[1 - a(1-b)\right], \qquad \gamma_2 = Dab, \qquad \gamma_3 = b(\mu_0). \tag{2.94}$$

Equation (2.92), or equivalently Eqs. (2.86) and (2.90), are the most common formulations of the two-stream equations in the literature (see e.g. Meador & Weaver 1980; Thomas & Stamnes 2002; Toon et al. 1989). For the thermal component, however, these equations should only be used if $D = 2$. To illustrate this we consider the thermal component in an isothermal atmosphere without scattering, i.e. $a = 0$. The two-stream equation becomes

$$\pm \frac{\mathrm{d}F_{\mathrm{d}}^{\pm}(\tau)}{\mathrm{d}\tau} = D F_{\mathrm{d}}^{\pm}(\tau) - 2\pi B_{\tilde{\nu}}(T), \tag{2.95}$$

which has the solution

$$F_{\mathrm{d}}^{\pm}(\tau) = A^{\pm} e^{\pm D\tau} + 2\pi B_{\tilde{\nu}}(T)/D, \tag{2.96}$$

where A is determined from the boundary conditions. For the up-welling component the exponential diverges as a function of τ, and we must have $A^{+} = 0$. At the top of the atmosphere $F_{\mathrm{d}}^{-}(\tau = 0) = 0$, and we consequently have $F_{\tilde{\nu}}(\tau = 0) = 2\pi B_{\tilde{\nu}}(T)/D$. A purely absorbing isothermal atmosphere is in fact a black-body, the emitted intensity of which should be $I_{\tilde{\nu}} = B_{\tilde{\nu}}(T)$. Using Eq. (2.3) to calculate the flux over the positive hemisphere we get $F_{\tilde{\nu}}(\tau = 0) = \pi B_{\tilde{\nu}}(T)$. This result could also have been obtained by solving the full radiative transfer equation, Eq. (2.77). For the two-stream approximation in the form of Eq. (2.92) to yield the correct black-body flux we must therefore require $D = 2$ for the thermal component.

It is possible, however, to derive an alternative version of the two-stream equations where the diffusivity D can be chosen freely for the thermal component as well as the stellar component. This will potentially increase the accuracy of the two-stream equations as the value of D can be chosen to reduce errors in fluxes and heating rates. In the next section we derive these

two-stream equations as it is this form that is used by the UM radiation scheme.

2.2.7 Two-stream equations from the differential intensity

For the thermal component the intensity may be close to the Planck function. Edwards (1996) introduced the differential intensity

$$I^{\pm}_{\mathrm{d,t}}{}'(\tau,\mu) = I^{\pm}_{\mathrm{d,t}}(\tau,\mu) - B_{\tilde{\nu}}(T), \qquad I^{\pm}_{\mathrm{d,t}}(\tau,\mu) = I^{\pm}_{\mathrm{d,t}}{}'(\tau,\mu) + B_{\tilde{\nu}}(T), \tag{2.97}$$

i.e. $I^{\pm}_{\mathrm{d,t}}{}'$ will contain the (small) corrections to the intensity from the Planck function. Inserting this into the radiative transfer equation, Eq. (2.77), yields

$$\pm \frac{\mathrm{d}}{\mathrm{d}\tau}\left[\mu I^{\pm}_{\mathrm{d,t}}{}'(\tau,\mu) + \mu B_{\tilde{\nu}}(T)\right] = I^{\pm}_{\mathrm{d,t}}{}'(\tau,\mu) + B_{\tilde{\nu}}(T) - \left[1 - a(\tilde{\nu})\right] B_{\tilde{\nu}}(T) - S^{\pm}_{\mathrm{d,t}}(\tau,\mu), \tag{2.98}$$

where the source function $S^{\pm}_{\mathrm{d},t}$ is

$$\begin{aligned} S^{\pm}_{\mathrm{d},t}(\tau,\mu) = {} & \frac{a(\tilde{\nu})}{2}\int_0^1 \mathrm{d}\mu' \left[I^{+}_{\mathrm{d,t}}{}'(\tau,\mu') + B_{\tilde{\nu}}(T)\right] p(\mu',\pm\mu) \\ & + \frac{a(\tilde{\nu})}{2}\int_0^1 \mathrm{d}\mu' \left[I^{-}_{\mathrm{d,t}}{}'(\tau,\mu') + B_{\tilde{\nu}}(T)\right] p(-\mu',\pm\mu). \end{aligned} \tag{2.99}$$

We wish to go directly to the two-stream approximated equations and consequently apply the operator $2\pi\int_0^1 \mathrm{d}\mu$ to both sides of Eq. (2.98). Introducing the azimuthally averaged differential intensity

$$I^{\pm}_{\mathrm{d,t}}{}'(\tau) = \int_0^1 \mathrm{d}\mu\, I^{\pm}_{\mathrm{d,t}}{}'(\tau,\mu), \quad \int_0^1 \mathrm{d}\mu\,\mu I^{\pm}_{\mathrm{d,t}}{}'(\tau,\mu) \approx \bar{\mu} I^{\pm}_{\mathrm{d,t}}{}'(\tau), \quad \bar{\mu} = \frac{\int_0^1 \mathrm{d}\mu\,\mu I^{\pm}_{\mathrm{d,t}}{}'(\tau,\mu)}{\int_0^1 \mathrm{d}\mu\, I^{\pm}_{\mathrm{d,t}}{}'(\tau,\mu)}, \tag{2.100}$$

with the two-stream average angle of the differential intensity $\bar{\mu} = 1/D$, and the differential flux

$$G^{\pm}_{\mathrm{d,t}}(\tau) = \pm 2\pi \int_0^1 \mathrm{d}\mu\,\mu I^{\pm}_{\mathrm{d,t}}{}'(\tau,\mu) \approx \pm 2\pi\bar{\mu} I^{\pm}_{\mathrm{d,t}}{}'(\tau), \tag{2.101}$$

we obtain

$$\pm \frac{\mathrm{d}G^{\pm}_{\mathrm{d,t}}(\tau)}{\mathrm{d}\tau} = -DG^{\pm}_{\mathrm{d,t}}(\tau) + S^{\pm}_{\mathrm{d,t}}{}'(\tau) \mp \frac{\mathrm{d}\pi B_{\tilde{\nu}}(T)}{\mathrm{d}\tau}, \tag{2.102}$$

with

$$S^{\pm}_{\mathrm{d,t}}{}'(\tau) = Da(\tilde{\nu})G^{\pm}_{\mathrm{d,t}}(\tau)\left[1-b\right] + Da(\tilde{\nu})G^{\mp}_{\mathrm{d,t}}(\tau)b, \tag{2.103}$$

where

$$b = \frac{\int_0^1 \mathrm{d}\mu'\, I^{\pm}_{\mathrm{d,t}}{}'(\tau,\mu')b(\mu')}{\int_0^1 \mathrm{d}\mu\, I^{\pm}_{\mathrm{d,t}}{}'(\tau,\mu)}. \tag{2.104}$$

Rewriting this in terms of the total flux $F^{\pm}_{\mathrm{d,t}}(\tau) = \pi B(T) + G^{\pm}_{\mathrm{d,t}}(\tau)$ we get

$$\frac{\mathrm{d}F^{+}}{\mathrm{d}\tau} = \gamma_1 F^{+} - \gamma_2 F^{-} - Q^{+}, \tag{2.105a}$$

$$\frac{\mathrm{d}F^{-}}{\mathrm{d}\tau} = \gamma_2 F^{+} - \gamma_1 F^{-} + Q^{-}, \tag{2.105b}$$

where the source function, $Q^{\pm}$, is given by

$$Q^{+} = \begin{cases} a(\tilde{\nu})\gamma_3 F^{\mathrm{s}} e^{-\tau/\mu_0} & \text{for the stellar component,} \\ D\pi\left[1-a\right] B_{\tilde{\nu}}(T) & \text{for the thermal component,} \end{cases} \tag{2.106a}$$

$$Q^{-} = \begin{cases} a(\tilde{\nu})\left[1-\gamma_3\right] F^{\mathrm{s}} e^{-\tau/\mu_0} & \text{for the stellar component,} \\ D\pi\left[1-a\right] B_{\tilde{\nu}}(T) & \text{for the thermal component,} \end{cases} \tag{2.106b}$$

and

$$\gamma_1 = D\left[1 - a(1-b)\right], \qquad \gamma_2 = Dab, \qquad \gamma_3 = b(\mu_0). \tag{2.107}$$

These are the two-stream equations solved by the UM radiation scheme, identical to the equations in Zdunkowski & Korb (1985), and to those in Zdunkowski et al. (1980) for $D = 2$ as noted by Edwards (1996). Compared to Eq. (2.92) this formulation is slightly different in that the thermal source function is $D\pi\left[1-a\right] B_{\tilde{\nu}}$ and not $2\pi\left[1-a\right] B_{\tilde{\nu}}$. This ensures the correct thermal source flux independent of the choice of D, and is consistent with the formulation used by Dobbs-Dixon & Agol (2013) and Rauscher & Menou (2012). To verify this let us revisit the example used in Section 2.2.6. The solution of the two-stream equations for the thermal component in an isothermal atmosphere without scattering becomes

$$F^{\pm}_{\mathrm{d}}(\tau) = A^{\pm} e^{\pm D\tau} + \pi B_{\tilde{\nu}}(T), \tag{2.108}$$

and comparing to Eq. (2.96) the factor $1/D$ has disappeared from the Planck term. Consequently, the correct flux is obtained at $\tau = 0$ independent of the choice of D.

2.2.8 Two-stream approximations

The above derivations of the two-stream equations may seem somewhat artificial. The same resulting equations are, however, obtained by assuming some (simple) form of $I(\tau, \mu)$ (or $I'(\tau, \mu)$) in Eqs. (2.76) and (2.77) and subsequently integrating over μ. Various assumptions on $I(\tau, \mu)$ lead to different values for $\bar{\mu}$ and b. Table 2.1 summarises a few different two-stream approximations. In this section we will briefly discuss a few of the different two-stream approximations, but will refer to the literature (Edwards 1996; Meador & Weaver 1980; Zdunkowski & Korb 1985; Zdunkowski et al. 1982, 1980) for the derivations.

Method	γ_1	γ_2	γ_3
Quadrature	$\sqrt{3}\left[2-a(1+g)\right]/2$	$\sqrt{3}a(1-g)/2$	$(1-\sqrt{3}g\mu_0)/2$
Hemispheric mean	$2-a(1+g)$	$a(1-g)$	$b(\mu_0)$
PIFM80	$2-a(5/4-3g/4)$	$3a(1-g)/4$	$1/2-(\mu_0 3(g-f))/(4(1-f))$
PIFM85	$D-a(D+3g/2)/2$	$a(D-3g/2)/2$	N/A

Table 2.1: Overview of the different two-stream approximations discussed in Section 2.2.8.

Quadrature

To derive the two-stream approximation for a two-point Gaussian quadrature it is necessary to go back to Eqs. (2.76) and (2.77), but written in terms of the whole-range intensity:

$$u\frac{\mathrm{d}I_{\mathrm{d,s}}(\tau,u)}{\mathrm{d}\tau} = I_{\mathrm{d,s}}(\tau,u) - S_{\mathrm{s}}(\tau,u) - S_{\mathrm{d,s}}(\tau,u), \tag{2.109}$$

$$u\frac{\mathrm{d}I_{\mathrm{d,t}}(\tau,u)}{\mathrm{d}\tau} = I_{\mathrm{d,t}}(\tau,u) - \left[1-a(\tilde{\nu})\right]B_{\tilde{\nu}}(T) - S_{\mathrm{d,t}}(\tau,u), \tag{2.110}$$

where the source functions $S_{\mathrm{s}}(\tau,u)$, $S_{\mathrm{d,s}}(\tau,u)$ and $S_{\mathrm{d,t}}(\tau,u)$ are given by Eqs. (2.74) and (2.78) with $\pm\mu$ replaced by u. The operator

$$2\pi\int_{-1}^{1}\mathrm{d}u \tag{2.111}$$

is applied to both sides, and Gaussian quadrature is used to approximate the integral of some function $f(u)$, e.g. the intensity, as

$$2\pi\int_{-1}^{1}\mathrm{d}u\, f(u) \approx w_1 f(u_1) + w_2 f(u_2), \tag{2.112}$$

where $w_1 = w_2 = 1$ and $u_1 = -1/\sqrt{3}$, $u_2 = 1/\sqrt{3}$. Using a phase function expanded to first order in Legendre polynomials, $l = 0, 1$ in Eq. (2.17), yields equations in the form of the two-stream approximation in Eq. (2.105) provided the quadrature is applied to the differential intensity for the thermal component with

$$\gamma_1 = \sqrt{3}\left[2-a(1+g)\right]/2, \qquad \gamma_2 = \sqrt{3}a(1-g)/2, \qquad \gamma_3 = (1-\sqrt{3}g\mu_0)/2. \tag{2.113}$$

In the absence of scattering $a = 0$ and we see that $D = \gamma_1 = \sqrt{3}$.

Hemispheric mean

Again starting with Eqs. (2.76) and (2.77), in the hemispheric mean approximation the intensity is assumed to be constant in the two hemispheres:

$$I_{\mathrm{d}}^{\pm}(\tau,\mu) = \bar{I}_{\mathrm{d}}^{\pm}(\tau), \tag{2.114}$$

and using this in Eq. (2.73) we again end up with equations in the form of the two-stream approximation in Eq. (2.105) with

$$\gamma_1 = 2 - a(1+g), \qquad \gamma_2 = a(1-g), \qquad \gamma_3 = b(\mu_0). \tag{2.115}$$

In the absence of scattering $a = 0$ and we see that $D = \gamma_1 = 2$.

Zdunkowski et al.'s Practical Improved Flux Method, 1980

The Practical Improved Flux Method from Zdunkowski et al. (1980) (PIFM80) was derived for use with the stellar component of the radiation. Scattering phase functions with strong scattering in the forward direction may require many terms in the Legendre expansion to be treated properly. The scaling approximation is often applied, which removes the scattering peak from the phase function and treats radiation within the peak as if it has not been scattered; see Thomas & Stamnes (2002) for more details.

The PIFM80 modifies the stellar source function to take this into account, giving

$$Q^+ = (1-f)ab(\mu_0)\frac{S}{\mu_0}, \tag{2.116}$$

$$Q^- = (1-f)a(1-b(\mu_0))\frac{S}{\mu_0}, \tag{2.117}$$

where f is the truncated fraction of the phase function and S is the direct stellar component of the radiation, and so

$$f = \frac{1}{4\pi}\int_{4\pi}\left[p(\cos\Theta) - p^{\mathrm{T}}(\cos\Theta)\right]\,\mathrm{d}\omega, \tag{2.118}$$

$$\frac{\mathrm{d}S}{\mathrm{d}\tau} = -(1-af)\frac{S}{\mu_0}, \tag{2.119}$$

were $p^{\mathrm{T}}(\cos\Theta)$ is the truncated phase function without the scattering peak. $p^{\mathrm{T}}(\cos\Theta)$ is expanded in terms of Legendre polynomials and truncated after the first order, as was done for the original phase function, which yields

$$b = \frac{3(1-g)}{8}, \qquad b(\mu_0) = \frac{1}{2} - \frac{\mu_0}{4}\frac{3(g-f)}{1-f}, \qquad D = 2, \tag{2.120}$$

where the choice $D = 2$ has been made and g is the original asymmetry factor. In terms of the coefficients γ_1 and γ_2, we obtain using Eq. (2.107)

$$\gamma_1 = 2 - a\left(\frac{5}{4} + \frac{3}{4}g\right), \qquad \gamma_2 = \frac{3a}{4}(1-g). \tag{2.121}$$

Zdunkowski et al.'s Practical Improved Flux Method, 1985

In the Practical Improved Flux Method from Zdunkowski & Korb (1985) (PIFM85) slightly different truncation choices are made for the backscattering coefficient, and a thermal source function is also included. We use this method for the thermal component only, where $b = 1/2 - 3g/(4D)$ (Edwards & Slingo 1996), and consequently

$$\gamma_1 = D - \frac{a}{2}\left(D + \frac{3}{2}g\right), \qquad \gamma_2 = \frac{a}{2}\left(D - \frac{3}{2}g\right). \tag{2.122}$$

Note that in this work we do not include scattering in the thermal component of the radiation, i.e. $a = 0$. Usually the diffusivity is taken to agree with Elasser's value $D = 1.66$ (Elasser 1942).

2.3 Inhomogeneous atmosphere

In this section we briefly go through how the two-stream equations are solved for an inhomogeneous atmosphere and refer to Thomas & Stamnes (2002) and the UM radiation code documentation (Edwards et al. 2012) for a more detailed discussion.

The atmosphere is divided into layers, as shown in Fig. 2.3, and each layer is assumed to be a homogeneous slab in which optical properties, i.e. the single-scattering albedo and backscattering coefficient, are constant. A closed-form solution to the two-stream equations, Eq. (2.105), can be obtained for each layer individually. These equations are a coupled set of two linear differential equations. The homogeneous solution (no source function) of this can be found by assuming a solution of the form $F_{\mathrm{h}}^{\pm}(\tau) = f^{\pm}e^{-\lambda\tau}$, $f^{\pm} = f(\pm\bar{\mu})$. The resulting equation can be written as a matrix equation, the result of which is an algebraic eigenvalue problem which can be diagonalised using standard linear algebra techniques. The solution is

$$F_{\mathrm{h}}^{\pm}(\tau) = Af^{\pm}e^{-k\tau} + Bf^{\pm}e^{+k\tau}, \tag{2.123}$$

where A and B are integration constants fixed by the boundary conditions, and

$$k = D\sqrt{(1-a)(1-a+2ab)}, \tag{2.124}$$

$$\frac{f^+}{f^-} = \frac{\sqrt{1-a+2ab} - \sqrt{1-a}}{\sqrt{1-a+2ab} + \sqrt{1-a}}. \tag{2.125}$$

It is straightforward to verify that $F_{\mathrm{p}}^{\pm}(\tau) = Z^{\pm}e^{-\tau/\mu_0}$ is a particular solution for the stellar component. The value of $Z^{\pm}$ can be obtained by substituting $F_{\mathrm{p}}^{\pm}(\tau)$ into Eq. (2.105). For the thermal component, the temperature dependence of the Planck function is approximated by a polynomial:

$$B[T(\tau)] = \sum_{l=0}^{K} b_l \tau^l. \tag{2.126}$$

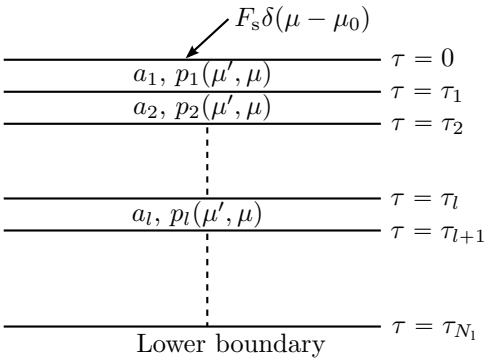

Figure 2.3: Schematic showing the discretisation of the atmosphere into layers. In each layer the atmosphere is approximated as being homogeneous.

By additionally assuming that the particular solution is a polynomial in τ,

$$F^{\pm}_{\mathrm{p}}(\tau) = \sum_{l=0}^{K} Y^{\pm}_{l} \tau^{l}, \tag{2.127}$$

and inserting Eqs. (2.126) and (2.127) into Eq. (2.105) an expression for the coefficients $Y^{\pm}_{l}$ can be obtained. It is normal to set $K = 1$, i.e. the Planck function is approximated as varying linearly as a function of τ across the layer. This has been observed to produce grid-scale waves in climate runs in the UM under the "old dynamics" dynamical core (Edwards et al. 2012). A quadratic polynomial ($K = 2$) was therefore introduced, and this is still used with the newer dynamical core "new dynamics" and the most recent dynamical core ENDGAME (Even Newer Dynamics for General Atmospheric Modelling of the Environment). We therefore also adopt a quadratic variation of the Planck function. In summary, in the two-stream approximation the flux in a homogeneous layer is given by

$$F^{\pm}_{l}(\tau) = A_l f^{\pm}_{l} e^{-k_l \tau} + B_l f^{\pm}_{l} e^{+k_l \tau} + U^{\pm}_{\mathrm{p},l}(\tau), \quad 1 \leqslant l \leqslant N_{\mathrm{l}}, \tag{2.128}$$

where $U^{\pm}_{\mathrm{p},l}(\tau)$ is the particular solution for the relevant component of the flux discussed above, N_{l} is the number of layers and we have added the subscript l to indicate that it is the flux in layer l.

Having obtained a closed-form solution to the two-stream equations in each layer, the solutions are coupled by using boundary conditions and assuming that the flux (or intensity) is continuous across interfaces. At the top of the atmosphere the down-going thermal flux is zero, while at the bottom it is given by Planckian emission from a surface with a given emissivity. The down-going stellar flux at the top of the atmosphere is given by the stellar spectrum, while the up-going stellar flux is zero at the bottom of the atmosphere. The down-going flux at the bottom of layer l must equal the down-going flux at the top of layer $l + 1$, and the up-going flux at the top of layer $l + 1$ must equal the up-going flux at the bottom of layer l. Together, these requirements lead to a set of $2N_{\mathrm{l}}$ equations determining the $2N_{\mathrm{l}}$ constants in Eq. (2.128).

This set of $2N_{\mathrm{l}}$ equations is usually written in the form of a matrix equation and solved using

a standard matrix solver. The resulting matrix is a sparse banded matrix, and for efficiency a Gaussian elimination algorithm is used that specifically takes into account where non-zero elements are located. We refer to Edwards et al. (2012) for more details about the implementation in the Edwards–Slingo radiation scheme. Having obtained fluxes at layer boundaries, heating rates are calculated using Eq. (2.37) in the UM or, for the stand-alone UM radiation scheme, Eq. (2.39).

Chapter 3

Calculation of opacities

In order to calculate fluxes and heating rates as described in Chapter 2, the absorption coefficient $\alpha(\tilde{\nu})$, scattering coefficient $\sigma(\tilde{\nu})$, and scattering phase function $p(\cos\Theta)$ are required. In this section we discuss the calculation of the absorption coefficient $\alpha(\tilde{\nu})$. Absorption coefficients, or opacities, must be calculated for all major absorbing species in the atmosphere, and combined with abundances provide the total absorption coefficient $\alpha(\tilde{\nu})$ for the atmosphere.

We discuss in Section 3.1 how the opacity is related to the transition probabilities between energy levels in atoms and molecules. These transition probabilities are provided as line lists, lists of spectral lines, and are available from external sources. We discuss our adopted line lists in Section 3.1.4. Line lists currently used by the ES radiation scheme cannot be used for hot Jupiter-like atmospheres as they are only valid up to about 400 K. The high temperature line lists required can be very large, causing the opacity calculation to require large amounts of computation time. We present in Section 3.3 a way to speed up the calculation of opacities from line lists significantly without loss of accuracy.

Absorption lines are broadened by temperature and pressure effects, and the pressure broadening parameters required to calculate opacities are highly uncertain. In Section 3.1.3 we discuss the various processes causing line broadening and compare van der Waals pressure broadening theory to pressure broadened widths obtained from experiments available in the literature in Section 3.2. We emphasise the large uncertainty in the broadening parameters for hot Jupiter-like conditions, as these are usually not explicitly mentioned in the literature.

The final tabulated molecular opacities have a complicated wavenumber dependence, causing the requirement for a high wavenumber resolution to obtain accurate total fluxes and heating rates. The correlated-k method is often adopted to reduce the required resolution and speed up radiation calculations, we discuss the specific implementation in the ES radiation scheme in Section 3.4. Finally, in Section 3.6, we briefly discuss the calculation of abundances adopted here.

Parts of the results in this chapter have been published in Amundsen et al. (2014).

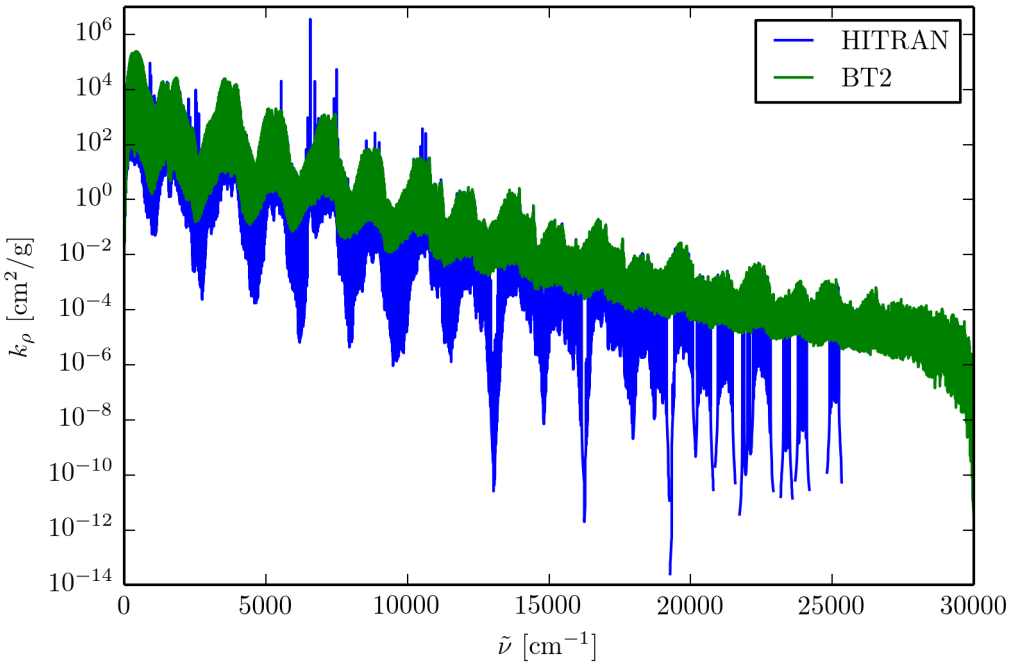

Figure 3.1: Absorption coefficient for $H_2^{16}O$ as a function of wavenumber calculated using both the HITRAN 2008 (Rothman et al. 2009) and BT2 (Barber et al. 2006) line lists at 1500 K and 1 bar. HITRAN underestimates the absorption coefficient by several orders of magnitude in certain spectral regions, making the use of high temperature line lists is essential.

3.1 Line lists and line broadening processes

A widely used line list database is the High Resolution TRANsmission (HITRAN) database (Rothman et al. 2013) currently used by the ES radiation scheme. These line lists are, however, Earth centric in that they are only valid for temperatures up to ~ 400 K. Temperatures in hot Jupiter atmospheres can reach > 1500 K, and the composition of the Earth's atmosphere (mainly N_2- and O_2-based) is very different from that of hot Jupiters (mainly H_2- and He-based). We must use high temperature line lists to calculate opacities for hot Jupiter atmospheres. For illustration we show in Fig. 3.1 the water absorption coefficient calculated at 1500 K using both HITRAN 2008 (Rothman et al. 2009) and our adopted high temperature line list BT2 (Barber et al. 2006). It is clear that the HITRAN line list underestimates the absorption by several orders of magnitude in certain spectral regions, clearly showing the need for high temperature line lists in hot Jupiter atmosphere models.

The high temperature line lists adopted here are mainly theoretical line lists. They are obtained from quantum mechanical calculations, but must be tuned to experimental line lists in order to achieve the desired accuracy (see e.g. Tennyson & Yurchenko 2012). High temperature line lists are often provided in many different formats, some tabulating Einstein coefficients, other oscillator strengths. In this section we describe how these quantities are related to the

absorption coefficient, including the various processes broadening the lines. The discussion here is based on that in Thomas & Stamnes (2002), Šimečková et al. (2006) and Rybicki & Lightman (2004), we provide some derivations in Appendix A.1.

3.1.1 Einstein coefficients

There are three ways in which a photon can interact with an atom or molecule where both the initial and final states are bound. Each is described by an Einstein coefficient:

1. Spontaneous emission occurs when an atom (or molecule) spontaneously decays from an upper level to a lower level. It is described by the coefficient A_{ul}, the probability per time that a molecule or atom in the upper energy state E_{u} spontaneously decays to the lower energy state E_{l}, emitting a photon.

2. Absorption, where a photon is absorbed by an atom (or molecule), exciting it from the lower energy level E_{l} to the upper energy level E_{u}. This process is described by the coefficient B_{lu}, the probability of a photon absorption event per unit time per unit energy density of the radiation field.

3. Stimulated emission occurs when an atom (or molecule) decays from an upper level to a lower level due to the influence of a radiation field, emitting a photon. This process is described by the coefficient B_{ul}, the probability of a stimulated emission event per unit time per unit energy density of the radiation field.

The Einstein coefficients are related to each other. We discuss the Einstein coefficients in more detail and derive the expressions relating them in Appendix A.1.1. The result is

$$A_{\mathrm{ul}} = 8\pi hc\tilde{\nu}^3 B_{\mathrm{ul}}, \tag{3.1a}$$

$$g_{\mathrm{l}} B_{\mathrm{lu}} = g_{\mathrm{u}} B_{\mathrm{ul}}, \tag{3.1b}$$

where h is Planck's constant, and g_{l} and g_{u} are the degeneracies of the lower and upper energy levels, respecitvely. B_{ul} and B_{lu} have here been defined using the energy density of the radiation field per wavenumber $\mathcal{U}_{\tilde{\nu}}$. Only one Einstein coefficient is needed in order to describe the probability of a transition as the remaining two can be calculated from Eq. (3.1). The coefficient chosen is usually A_{ul} due to the unambiguity of its definition.

Line lists are essentially lists of transitions with their corresponding A_{ul} coefficient and information on the upper and lower energy levels. We now proceed to discuss how the Einstein coefficients are related to the absorption coefficient.

3.1.2 Line intensity

We derive in Appendix A.1.2 the relationship between the Einstein coefficients and the absorption coefficient. The absorption cross section $\alpha_n(\tilde{\nu})$ (absorption coefficient per unit number density)

created by transition i can be expressed as

$$\alpha_n(\tilde{\nu}) = \mathcal{S}_i \Phi_i(\tilde{\nu}), \tag{3.2}$$

where we have introduced the line intensity $\mathcal{S}_i$ and line profile $\Phi_i(\tilde{\nu})$. Integrating over wavenumber the line profile is normalised to unity and the line intensity is therefore the integrated area under the absorption coefficient profile for transition i. We will discuss $\Phi_i(\tilde{\nu})$ in more detail in Section 3.1.3 as it is through $\Phi_i(\tilde{\nu})$ that line broadening processes are taken into account. The line intensity $\mathcal{S}_i$ is related to the Einstein $A_{\rm ul}$-coefficient by

$$\mathcal{S}_i = \mathcal{S}_i(T) = \frac{1}{8\pi c\tilde{\nu}_0^2} \frac{g_{\rm u} e^{-E_{\rm l}/k_{\rm B}T}}{Q(T)} \left(1 - e^{-hc\tilde{\nu}_0/k_{\rm B}T}\right) A_i, \tag{3.3}$$

where c is the speed of light, $E_{\rm l}$ is the energy of the lower level, $g_{\rm u}$ is the degeneracy of the upper level, $k_{\rm B}$ is Boltzmann's constant, T is the temperature, $Q(T)$ is the partition function at T for the atom or molecule, $\tilde{\nu}_0$ is the wavenumber of the transition and we have denoted the Einstein $A_{\rm ul}$-coefficient coefficient for transition i as A_i for convenience. Note that this formula has been derived including stimulated emission as negative absorption.

The line intensity is normally weighted by the fractional isotopic abundance I_a. In addition, in line lists on formats similar to that of HITRAN $\mathcal{S}_i$ is tabulated at the temperature $T_0 = 296\,\mathrm{K}$:

$$\mathcal{S}_i^{\rm H} = \mathcal{S}_i^{\rm H}(T_0) = \frac{I_a}{8\pi c\tilde{\nu}_0^2} \frac{g_{\rm u} e^{-E_{\rm l}/k_{\rm B}T_0}}{Q(T_0)} \left(1 - e^{-hc\tilde{\nu}_0/k_{\rm B}T_0}\right) A_i. \tag{3.4}$$

Note that from $\mathcal{S}_i^{\rm H}(T_0)$ it is possible to calculate $\mathcal{S}_i^{\rm H}(T)$ for any T using

$$\mathcal{S}_i^{\rm H}(T) = \mathcal{S}_i^{\rm H}(T_0) \frac{Q(T_0)}{Q(T)} \frac{e^{-E_{\rm l}/k_{\rm B}T}}{e^{-E_{\rm l}/k_{\rm B}T_0}} \frac{\left(1 - e^{-hc\tilde{\nu}_0/k_{\rm B}T}\right)}{\left(1 - e^{-hc\tilde{\nu}_0/k_{\rm B}T_0}\right)} \tag{3.5}$$

without loss of generality. A cut-off in intensity has been applied in HITRAN at room temperature, meaning that lines that are insignificant at $\sim 300\,\mathrm{K}$ are discarded from the database. According to Eq. (3.4), these lines can, and many of them do, become significant at higher temperatures. The reason is quite simple: high energy levels that are not populated at room temperature become populated at high temperatures, and the probability of transitions occurring to and from these levels therefore increases. This explains why HITRAN is unsuitable for hot Jupiter-like atmospheres.

To derive Eq. (3.3) local thermodynamic equilibrium (LTE) has been assumed. In this context LTE was assumed as the Boltzmann distribution was applied to calculate level populations, the fraction of particles in specific energy states. This greatly simplifies the line intensity calculation, which is important due to the large number of lines in our line lists. The use of the Boltzmann distribution requires the collisional excitation of molecules to dominate over other processes such as excitation by radiaiton. This assumption is likely to break down for small pressures where

the density is small, but consideration of non-LTE effects is beyond the scope of this work.

The (internal) partition function for a given molecule from Boltzmann statistics is

$$Q(T) = \sum_{i=0}^{\infty} g_i e^{-E_i/k_\mathrm{B}T}, \tag{3.6}$$

where the sum is over all energy levels i with energy E_i and degeneracy g_i. We need the partition function $Q(T)$ for all molecules we include in our opacity database. The partition function may be provided with the line list, or it may be necessary to use other sources. The HITRAN database (Rothman et al. 2009) provides the partition function for most species we include in tabulated form between 70 K and 3000 K, and serves as our fall-back partition function source when no other recent sources are available.

Occasionally oscillator strengths, or gf-values, are provided in line lists instead of Einstein coefficients. As the Einstein coefficients, gf-values describe transition probabilities and can be thought of as the correction factor to the transition probability of a classical harmonic oscillator. We discuss the oscillator strength in more detail in Appendix A.1.3, but a detailed quantum-mechanical discussion is beyond the scope of this work. The end result is that the oscillator strength is related to the Einstein A_ul-coefficient by

$$g_\mathrm{u} A_\mathrm{ul} = \frac{8\pi^2 e^2 \tilde{\nu}_0^2}{m_\mathrm{e} c} g_\mathrm{l} f_\mathrm{lu}, \tag{3.7}$$

where e is the electron charge in CGS-Gaussian units, and f_lu is the oscillator strength of the transition. The quantity $g_\mathrm{l} f_\mathrm{lu}$ is often referred to as the gf-value of the transition. Inserting Eq. (3.7) into Eq. (3.3), we get the line intensity in terms of the gf-value:

$$\mathcal{S}_i(T) = \frac{\pi e^2}{m_\mathrm{e} c^2} \frac{e^{-E_\mathrm{l}/k_\mathrm{B}T}}{Q(T)} \left(1 - e^{-hc\tilde{\nu}_0/k_\mathrm{B}T}\right) g_\mathrm{l} f_\mathrm{lu}. \tag{3.8}$$

3.1.3 Line broadening processes

For each transition i the line shape function $\Phi_i(\tilde{\nu})$ spreads the absorption coefficient over a wavenumber region. Various physical processes cause broadening of absorption lines. Here we discuss the natural, pressure and temperature broadening, the dominating broadening processes in hot Jupiter atmospheres, and the corresponding functional forms they take.

Natural broadening

From quantum-mechanics we have Heisenberg's energy-time uncertainty principle

$$\Delta E \Delta t \geqslant \frac{\hbar}{2}, \tag{3.9}$$

where ΔE is the uncertainty in the energy of a particular state and Δt is the lifetime of the state. This means that, unless the state has an infinite lifetime, there will be an intrinsic uncertainty in the energy of that state. Photons emitted by transitions between states with finite lifetimes will therefore not have one definite energy (or frequency/wavenumber), but rather a distribution of energies about some mean. This phenomenon is called natural broadening, and the resulting distribution is a Lorentzian with a width $\alpha_{\mathrm{L}}^{\mathrm{nat}}$. A typical lifetime of a state is $\Delta t \sim 10^{-8}\,\mathrm{s}$, which leads to $\alpha_{\mathrm{L}}^{\mathrm{nat}} \sim \frac{1}{4\pi c \Delta t} \sim 3 \times 10^{-4}\,\mathrm{cm}^{-1}$. This is much smaller than the width caused by pressure and Doppler broadening for hot Jupiter-like atmospheric conditions, and we consequently ignore natural broadening processes here.

Pressure broadening

Lines will be broadened by interactions with other molecules, this is called pressure broadening. Collisions between particles effectively reduce the lifetime of the upper and lower states of transitions, thereby causing a broadening of the line. The theory of pressure broadening is vast and complicated (Rutten 2003; Thomas & Stamnes 2002), and an in-depth discussion on this subject is beyond the scope of this work. Pressure broadening results in a Lorentzian line profile,

$$\Phi_{\mathrm{L}}(\tilde{\nu}) = \frac{1}{\pi} \frac{\alpha_{\mathrm{L}}}{(\tilde{\nu} - \tilde{\nu}_0)^2 + \alpha_{\mathrm{L}}^2}, \tag{3.10}$$

where α_{L} is the Lorentz width, with $2\alpha_{\mathrm{L}}$ the full width at half maximum (FWHM). The pressure broadened width α_{L}^p for the perturbing species p depends on both the pressure and temperature in a complex way, but the relationship is often approximated as (Sharp & Burrows 2007; Thomas & Stamnes 2002)

$$\alpha_{\mathrm{L}}^p(P_p, T) = \alpha_{\mathrm{L}}^p(P_0, T_0) \left(\frac{T_0}{T}\right)^{n_p} \frac{P_p}{P_0}, \tag{3.11}$$

where T_0 and P_0 is a reference temperature and pressure, respectively, P_p is the partial pressure, and n_p is the temperature exponent. The total pressure broadened width is the sum of the pressure broadened widths α_{L}^p for all perturbing species,

$$\alpha_{\mathrm{L}} = \sum_p \alpha_{\mathrm{L}}^p(P_p, T). \tag{3.12}$$

Both the reference Lorentz width $\alpha_{\mathrm{L}}^p(P_0, T_0)$ and the temperature exponent n_p are transition dependent.

Since Eq. (3.11) depends linearly on the partial pressure of each perturbing species P_p, the pressure broadened width will be dominated by collisions with the most abundant molecules. In HITRAN air- and self-broadening parameters are tabulated for each transition (Rothman et al. 2013). The atmospheres of hot Jupiters consist mainly of H_2 and He, and the broadening information provided in HITRAN is therefore not directly applicable. Information on pressure broadening by H_2 and He is extremely sparse (Freedman et al. 2008; Sharp & Burrows 2007),

and there is a large uncertainty in the values of $\alpha_{\rm L}^{p}(P_0, T_0)$ and n_p used in the literature. We discuss this issue in more detail in Section 3.2.

Doppler broadening

At low pressures and high temperatures Doppler broadening becomes important. As the name suggests, the physical effect responsible is the Doppler effect. While particles are absorbing and emitting photons they are in thermal motion. Particles will emit and absorb photons with wavenumber $\tilde{\nu}_0$ in their own frame of reference, causing a shift in the observed wavenumber of the photon. The thermal motion has no directional preference, and the accumulated effect is therefore a broadening of the line.

Again assuming LTE, the velocity distribution of molecules is given by the Maxwell-Boltzmann distribution for any direction, including the line of sight:

$$f_z(v_x)\mathrm{d}v_x = \sqrt{\frac{m_z}{2\pi k_{\rm B}T}} e^{-v_x^2/v_0^2}\,\mathrm{d}v_x, \qquad v_0 = \sqrt{\frac{2k_{\rm B}T}{m_z}}, \tag{3.13}$$

where v_x is the thermal velocity along the line of sight and m_z is the mean particle mass of species z. Imagine sending a photon with wavenumber $\tilde{\nu}$ towards the molecule. In the molecule's frame of reference, this photon will have a shifted frequency $\tilde{\nu}'$, which is to the lowest order in v_x (for non-relativistic velocities) given by

$$\tilde{\nu}' = \tilde{\nu} + v_x\tilde{\nu}/c \approx \tilde{\nu} + v_x\tilde{\nu}_0/c, \tag{3.14}$$

where in the last term $\tilde{\nu}$ has been replaced by the line centre frequency $\tilde{\nu}_0$, a valid approximation since $v_x/c \ll 1$. The absorption cross-section due to all possible velocities along the line of sight is therefore given by

$$\alpha_n(\tilde{\nu}) = \int_{-\infty}^{\infty} \mathrm{d}v_x\, f_z(v_x)\alpha_n'(\tilde{\nu} + v_x\tilde{\nu}_0/c) \tag{3.15}$$

$$= \sqrt{\frac{m_z}{2\pi k_{\rm B}T}} \int_{-\infty}^{\infty} \mathrm{d}v_x\, e^{-v_x^2/v_0^2}\alpha_n'(\tilde{\nu} + v_x\tilde{\nu}_0/c), \tag{3.16}$$

where α_n' is the absorption cross section without Doppler broadening. Ignoring both natural and pressure broadening, α_n' is a delta function, $\alpha_n'(\tilde{\nu} + v_x\tilde{\nu}_0/c) = \mathcal{S}_i\delta(\tilde{\nu} + v_x\tilde{\nu}_0/c - \nu_0)$, and we have

$$\alpha_n(\tilde{\nu}) = \mathcal{S}_i\sqrt{\frac{m_z}{2\pi k_{\rm B}T}} \int_{-\infty}^{\infty} \mathrm{d}v_x\, e^{-v_x^2/v_0^2}\delta(\tilde{\nu} + v_x\tilde{\nu}_0/c - \nu_0). \tag{3.17}$$

Changing the integration parameter to $x = \tilde{\nu} + v_x\tilde{\nu}_0/c - \nu_0$, which gives $v_x = -(\tilde{\nu} - \tilde{\nu}_0 - x)c/\tilde{\nu}_0$

and $\mathrm{d}v_x = (c/\tilde{\nu}_0)\mathrm{d}x$ yields

$$\alpha_n(\tilde{\nu}) = \mathcal{S}_i\sqrt{\frac{m_z}{2\pi k_\mathrm{B}T}}\frac{c}{\tilde{\nu}_0}\int_{-\infty}^{\infty}\mathrm{d}x\, e^{-((\tilde{\nu}-\tilde{\nu}_0-x)c/\tilde{\nu}_0)^2/v_0^2}\delta(x) \tag{3.18}$$

$$= \mathcal{S}_i\sqrt{\frac{m_z}{2\pi k_\mathrm{B}T}}\frac{c}{\tilde{\nu}_0}e^{-c^2(\tilde{\nu}-\tilde{\nu}_0)^2/(\tilde{\nu}_0 v_0)^2}. \tag{3.19}$$

The Doppler width is defined as $\alpha_\mathrm{D} = \tilde{\nu}_0 v_0/c$, which yields

$$\alpha_n(\tilde{\nu}) = \frac{\mathcal{S}_i}{\sqrt{\pi}\alpha_D}e^{-(\tilde{\nu}-\tilde{\nu}_0)^2/\alpha_\mathrm{D}^2} \equiv \mathcal{S}_i\Phi_\mathrm{D}(\tilde{\nu}), \tag{3.20}$$

where $\Phi_\mathrm{D}(\tilde{\nu})$ is the Doppler profile. The full width at half maximum (FWHM) is $2\ln(2)\alpha_\mathrm{D}$.

The Voigt profile

Including pressure broadening in Eq. (3.16) we get

$$\alpha_n(\tilde{\nu}) = \sqrt{\frac{m_z}{2\pi k_\mathrm{B}T}}\frac{1}{\pi}\int_{-\infty}^{\infty}\mathrm{d}v_x\,\frac{\alpha_\mathrm{L}e^{-v_x^2/v_0^2}}{(\tilde{\nu}+v_x\tilde{\nu}_0/c-\tilde{\nu}_0)^2+\alpha_\mathrm{L}^2}, \tag{3.21}$$

and again changing the integration variable yields

$$\alpha_n(\tilde{\nu}) = \mathcal{S}_i\frac{a}{\pi^{3/2}\alpha_\mathrm{D}}\int_{-\infty}^{\infty}\frac{\mathrm{d}y\, e^{-y^2}}{(v-y)^2+a^2} \equiv \mathcal{S}_i\Phi_\mathrm{V}(\tilde{\nu}), \tag{3.22}$$

where

$$v = (\tilde{\nu}-\tilde{\nu}_0)/\alpha_\mathrm{D}, \qquad a = \frac{\alpha_\mathrm{L}}{\alpha_\mathrm{D}}, \qquad \alpha_\mathrm{D} \equiv \frac{\tilde{\nu}_0}{c}\sqrt{\frac{2k_\mathrm{B}T}{m_z}}. \tag{3.23}$$

$\Phi_\mathrm{V}(\tilde{\nu})$ is the Voigt profile. For $a \to 0$, pure Doppler broadening is retrieved, while for $a \gg 1$ $\Phi_\mathrm{V}(\tilde{\nu})$ becomes a Lorentzian. The integral must be solved numerically, and many computational algorithms exist. We use the algorithm of Schreier (1992) based on the formulation of Humlícek (1982). The code was provided with the ES radiation scheme.

Unfortunately, real line profiles are not perfectly Voigtian (Thomas & Stamnes 2002). The Voigt profile is fairly accurate provided weak interactions between molecules, but for stronger interactions effects such as collisional narrowing and line shifts, where the line centre is shifted away from $\tilde{\nu}_0$, can occur. Line wings are particularly affected by this. We ignore these additional effects in our treatment of line profiles, which is the usual approach (Freedman et al. 2008; Sharp & Burrows 2007). To avoid overestimating absorption in the line wings, we apply a cut-off in the line profile at some distance from the line centre. We discuss this in more detail in Section 3.3.

Molecule	Isotope	Line list	Partition function
H_2O	$H_2{}^{16}O$	Barber et al. (2006)	Barber et al. (2006)
CH_4 (old)	$^{12}CH_4$ $^{13}CH_4$	Wenger & Champion (1998)	Wenger et al. (2008) Rothman et al. (2009)
CH_4	$^{12}CH_4$	Yurchenko & Tennyson (2014)	Yurchenko & Tennyson (2014)
CO_2	$^{12}C^{16}O$ $^{13}C^{16}O_2$ $^{12}C^{16}O^{18}O$ $^{12}C^{16}O^{17}O$	Tashkun & Perevalov (2011)	Rothman et al. (2009)
CO	$^{12}C^{16}O$ $^{13}C^{16}O$ $^{12}C^{18}O$ $^{12}C^{17}O$ $^{13}C^{18}O$ $^{13}C^{17}O$	Rothman et al. (2010)	Rothman et al. (2009)
NH_3	$^{14}NH_3$	Yurchenko et al. (2011)	Yurchenko et al. (2011)
TiO	$^{46}Ti^{16}O$ $^{47}Ti^{16}O$ $^{48}Ti^{16}O$ $^{49}Ti^{16}O$ $^{50}Ti^{16}O$	Plez (1998)	Sauval & Tatum (1984)
VO	$^{51}V^{16}O$	B. Plez (priv. comm.)	Sauval & Tatum (1984)
Na	^{23}Na	VALD3[1]	Sauval & Tatum (1984)
K	^{39}K	VALD3[1]	Sauval & Tatum (1984)

[1] Heiter et al. (2008) (`http://vald.astro.uu.se/~vald/php/vald.php`)

Table 3.1: Summary of which molecules we include in our opacity database, and our line list and partition function sources. We do not include CO_2 in the ES radiation scheme. The old STDS CH_4 line list by Wenger & Champion (1998) is used for the tests in Chapter 4, while for later chapters the new ExoMol YT10to10 line list (Yurchenko & Tennyson 2014) is used.

3.1.4 Opacity sources

The dominant absorbers in hot Jupiter atmospheres with solar metallicity are H_2O, CO, CH_4, NH_3, TiO, VO, H2–H2 and H2–He collision induced absorption (CIA), Na and K (Baraffe et al. 2010; Burrows & Sharp 1999). We also include details on CO_2 in this section, which we do not include in the ES radiation scheme, but do include in `ATMO`. In this section we briefly discuss the line lists we use to calculate the absorption coefficient for each opacity source. We use line lists and partition functions from several different sources, these are summarised in Table 3.1. We adopt isotopic abundances, I_a, from Asplund et al. (2009).

Water (H_2O)

For water ($H_2{}^{16}O$) we use the high temperature line list from the ExoMol[1] project (Barber et al. 2006), BT2, and use the partition function provided with the line list. BT2 is a theoretical line list for rotation-vibration transitions of water. Electronic transitions are ignored since the lowest

[1] `http://www.exomol.com`

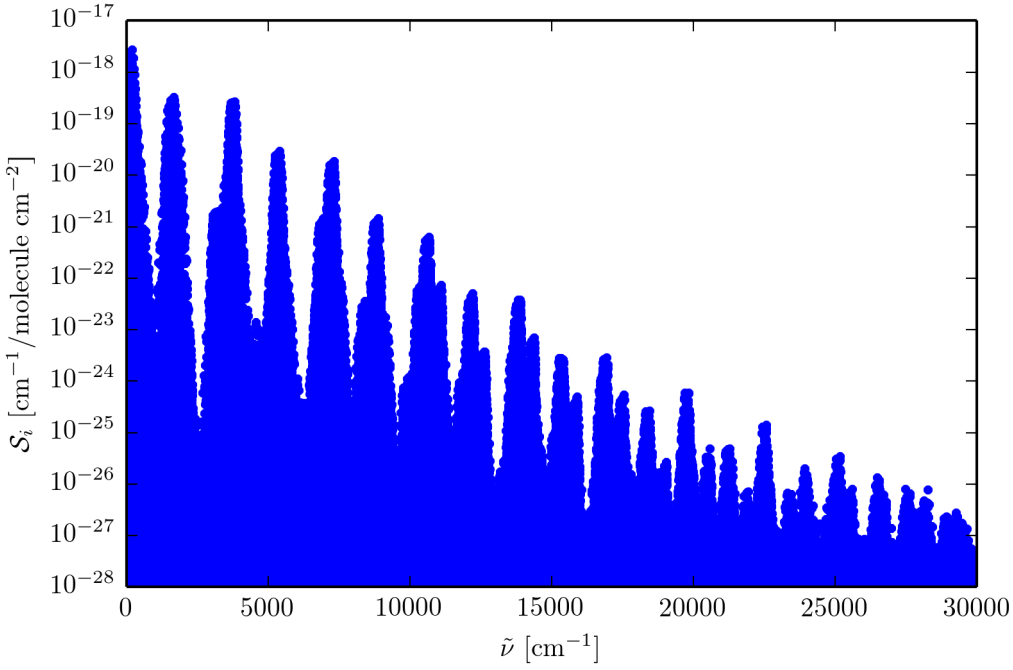

Figure 3.2: Line intensity for $H_2^{16}O$ calculated from the BT2 line list (Barber et al. 2006) using Eq. (3.3) at $T = 296\,\mathrm{K}$.

stable excited electronic state is above the dissociation energy for the molecule. ExoMol line lists come in to parts: (i) an energy levels file where each level is listed with its energy, quantum numbers, symmetry and a reference index, and (ii) a set of transition files listing the upper and lower energy levels' reference indices and the Einstein A_{ul} coefficient for each transition. The line list has 221 097 energy levels and 5.1×10^8 transitions. A plot of the line intensity calculated from the BT2 line list is shown in Fig. 3.2.

Ammonia (NH_3)

The BYTe high temperature line list for ammonia (Yurchenko et al. 2011) is a theoretical line list for rotation-vibration transitions of $^{14}NH_3$ from the ExoMol project. As for water we use the partition function provided with the line list. The authors consider it to be valid for temperatures up to 1500 K. We expect temperatures to exceed 1500 K in our models, and should therefore keep in mind that at higher temperatures the opacity due to ammonia is highly uncertain. The BYTe line list is, however, the best high temperature line list available, and at higher temperatures the ammonia abundance is expected to be small (Burrows & Sharp 1999). In total the line list contains 1 373 897 energy levels and 1.1×10^9 transitions. A plot of the line intensity calculated from the BYTe line list is given in Fig. 3.3.

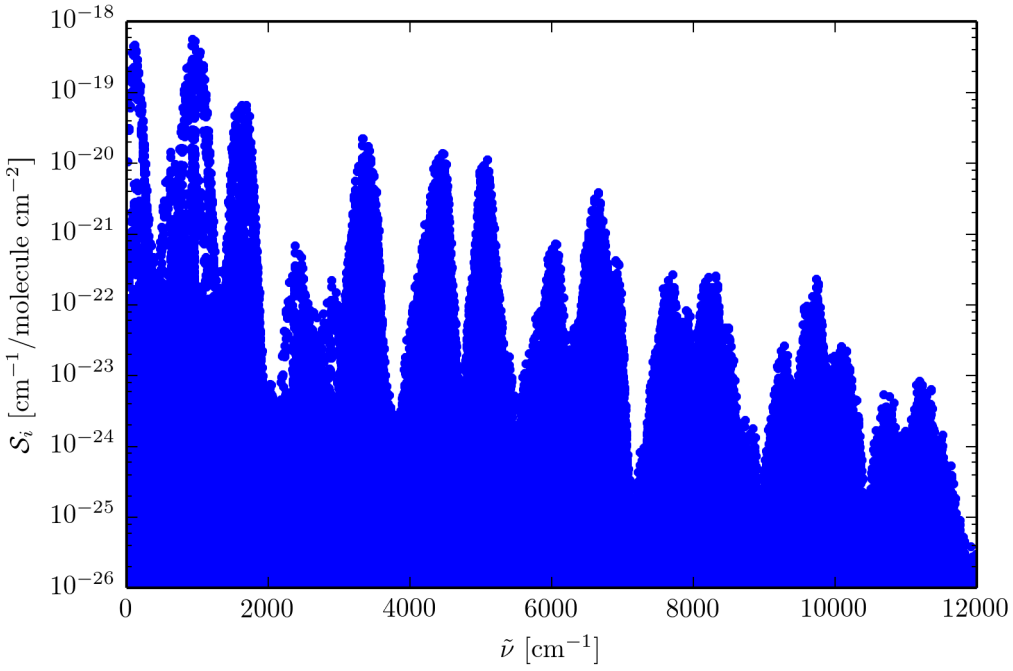

Figure 3.3: Line intensity for $^{14}NH_3$ calculated from the BYTe (Yurchenko et al. 2011) line list using Eq. (3.3) at $T = 296\,\mathrm{K}$.

Carbon dioxide (CO_2)

We do not include CO_2 in the ES radiation scheme, but its opacity has been calculated and included in `ATMO` from Chapter 5 on. We use the CDSD-4000 line list (Tashkun & Perevalov 2011) which contains 6.3×10^8 lines, is valid up to 4000 K and includes the major isotopes of CO_2: $^{12}C^{16}O$, $^{13}C^{16}O_2$, $^{12}C^{16}O^{18}O$ and $^{12}C^{16}O^{17}O$. Since a partition function is not included with the line list we use the HITRAN partition function, which is valid up to 3000 K. A plot of the line intensity is shown in Fig. 3.4.

Carbon monoxide (CO)

We use the CO line list from HITEMP (the HIgh TEMPerature molecular spectroscopic database, Rothman et al. 2010). It is based on the line list by Goorvitch (1994), and supplemented with lines from HITRAN (Rothman et al. 2009). Isotopes included in this line list are $^{12}C^{16}O$, $^{13}C^{16}O$, $^{12}C^{18}O$, $^{12}C^{17}O$, $^{13}C^{18}O$ and $^{13}C^{17}O$, and we adopt partition functions from HITRAN. A plot of the line intensity calculated from the HITEMP CO line list is given in Fig. 3.5.

Methane (CH_4)

Originally we used the STDS (Wenger & Champion 1998) line list for methane. A new and improved methane line list, YT10to10 (Yurchenko & Tennyson 2014), became available in late

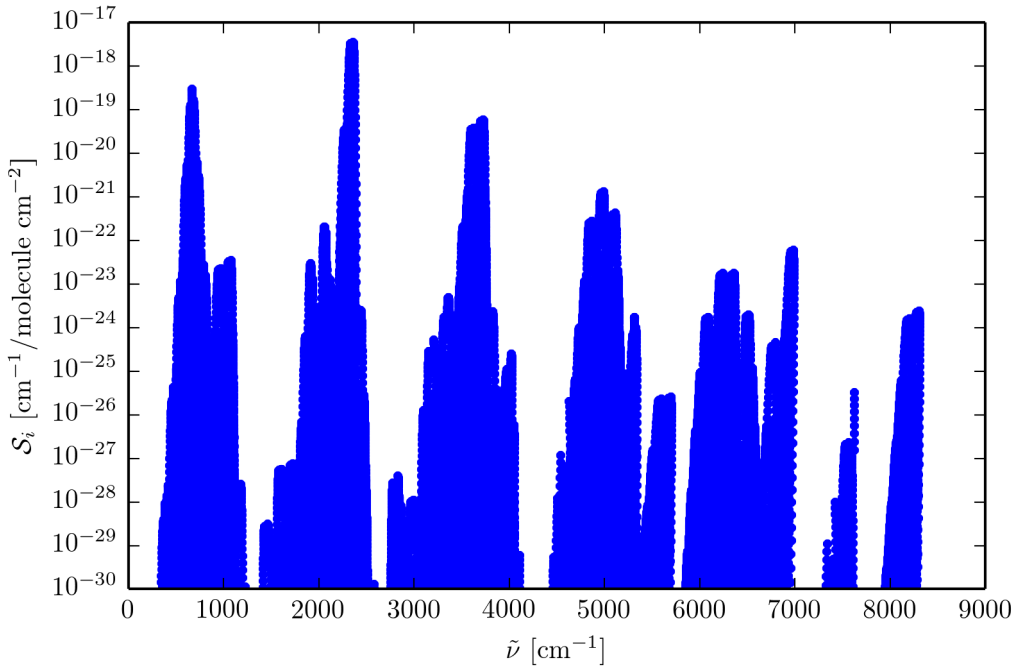

Figure 3.4: Line intensity for CO_2 calculated from the CDSD-4000 line list (Tashkun & Perevalov 2011) using Eq. (3.5) at $T = 296\,\mathrm{K}$.

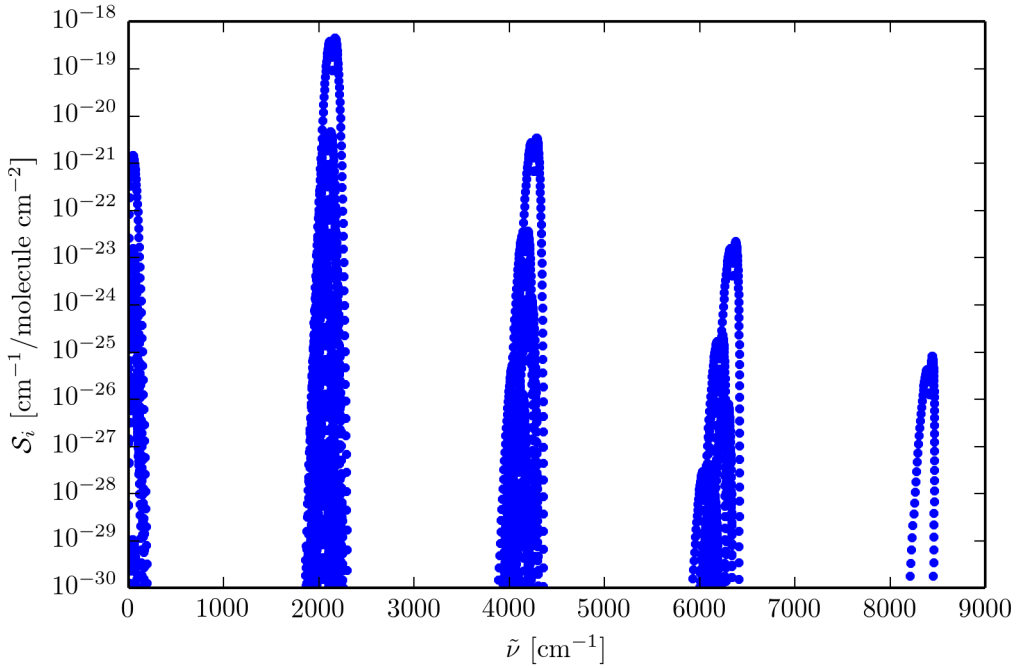

Figure 3.5: Line intensity for CO calculated from the HITEMP line list (Rothman et al. 2010) using Eq. (3.5) at $T = 296\,\mathrm{K}$.

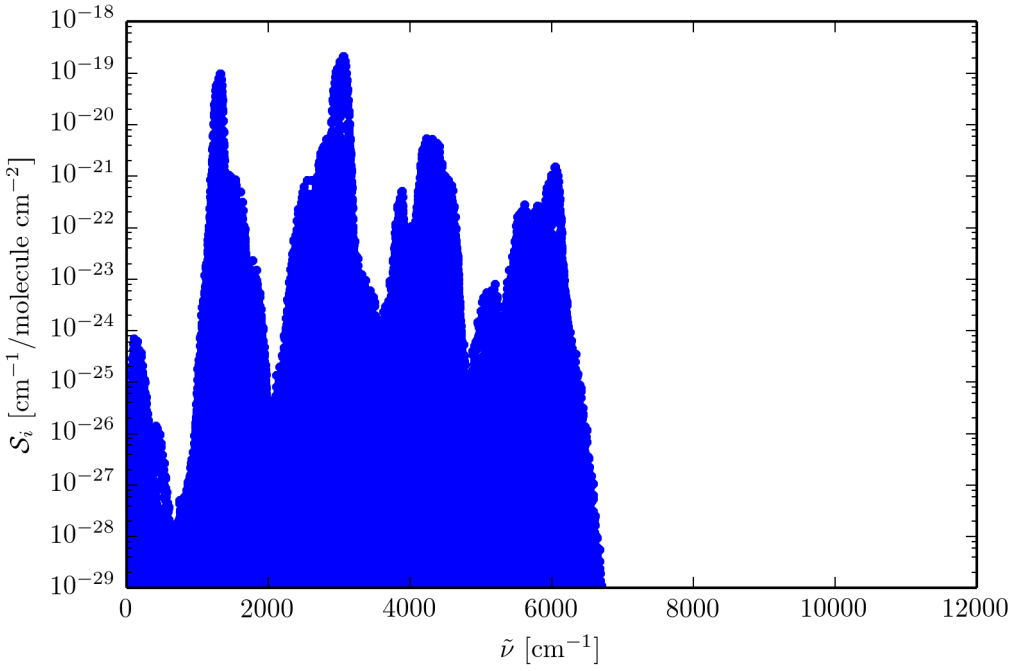

Figure 3.6: Line intensity for CH_4 calculated from STDS line list (Wenger & Champion 1998) using Eq. (3.5) at $T = 296\,\mathrm{K}$.

2013 and we therefore include details on both. The old STDS line list is used up to and including Chapter 4, and the new YT10to10 line list is used for all remaining chapters.

The Spherical Top Data System (STDS): Until the YT10to10 line list became available we used the Spherical Top Data System (STDS) (Wenger & Champion 1998) to calculate our high temperature methane line list. STDS supports both $^{12}CH_4$ and $^{13}CH_4$, and we used an angular momentum quantum number cut-off at $J_{\max} = 60$. A similar cut-off in $J_{\max}$ was used by Freedman et al. (2008), the reason for not increasing $J_{\max}$ further being time constraints: at $J_{\max} = 60$, it takes about a month to calculate the line list with an Intel Xeon CPU at 2.27 GHz. The parameter files used by STDS usually only have data for $J \lesssim 20$, and for higher J the data is extrapolated. Only a statistical description of the lines in a particular band can be expected. The wavenumber coverage is also rather small, as seen in Fig. 3.6 where the line intensity has been plotted as a function of wavenumber.

For $^{12}CH_4$ we use the partition function by Wenger et al. (2008), who found that HITRAN underestimates the $^{12}CH_4$ partition function by about 50 % at 3000 K. A interface is provided at `http://icb.u-bourgogne.fr/JSP/TIPS.jsp`, where the partition function can be calculated for temperatures up to 3000 K. We used this website to tabulate the partition function between 70 K and 3000 K in steps of 1 K. Due to lack of a better alternative we use the HITRAN partition function for $^{13}CH_4$.

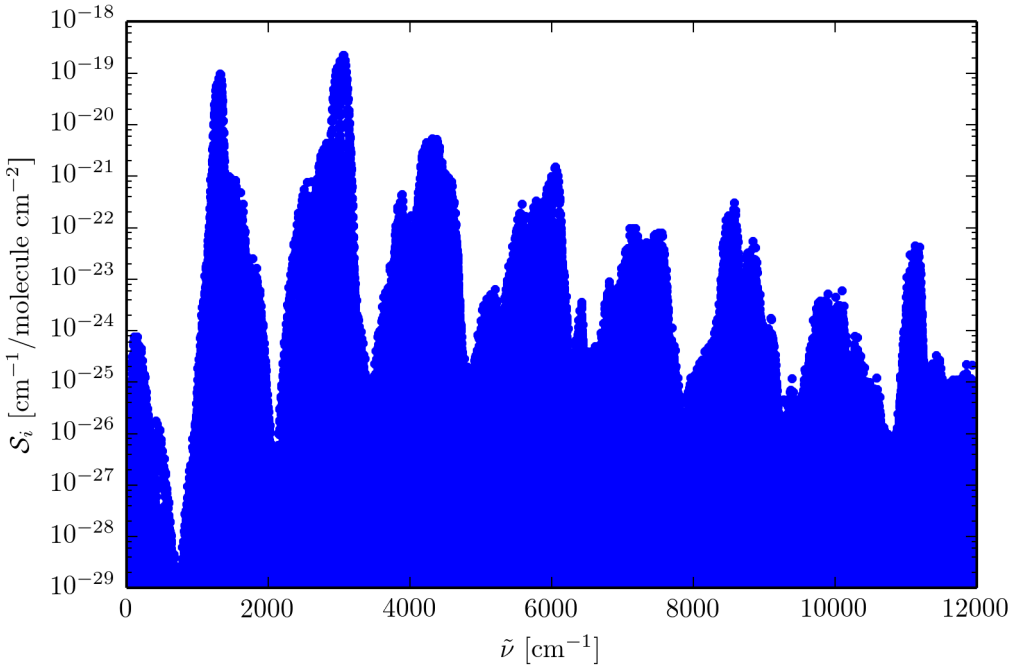

Figure 3.7: Line intensity for CH_4 calculated from YT10to10 line list (Yurchenko & Tennyson 2014) using Eq. (3.4) at $T = 296\,\mathrm{K}$. Can be compared with Fig. 3.6.

The YT10to10 methane line list: In December 2013 we were sent the new ExoMol $^{12}CH_4$ line list, YT10to10 (Yurchenko & Tennyson 2014). It has 9.8×10^9 transitions, i.e. about 10 times larger than BYTe. It is assumed to be valid up to about 1500 K and contains lines in the range $0\,\mathrm{cm}^{-1}$ to $12\,000\,\mathrm{cm}^{-1}$. We have plotted the line list in Fig. 3.7, which can be compared to Fig. 3.6. We use the partition function provided with it, and only include $^{12}CH_4$.

Titanium and vanadium oxide (TiO & VO)

For TiO we have chosen to use the line list by Plez (1998), updated in January 2012. This line list contains $\sim 4.2 \times 10^7$ lines for the isotopes $^{46}Ti^{16}O$, $^{47}Ti^{16}O$, $^{48}Ti^{16}O$, $^{49}Ti^{16}O$ and $^{50}Ti^{16}O$. The updated version provides the wavelength, gf-value and the lower energy level of the transition, we scale the gf-values with solar isotopic abundances from Asplund et al. (2009). A plot of the line intensity for TiO is shown in Fig. 3.8.

We prefer to use the Plez (1998) line list over the competing Schwenke (1998) line list for several reasons: the Schwenke (1998) line list contains $\sim 3.8 \times 10^7$ lines, i.e. less than the Plez (1998) line list, and the Plez (1998) line list has been regularly updated. In addition, Baraffe et al. (2015, in prep) compared these line lists using the atmosphere code PHOENIX and found the Plez line list to better predict M-dwarf photometry.

For VO we also use a line list provided by B. Plez (private communication), it contains $\sim 3.2 \times 10^6$ lines for the main isotope $^{51}V^{16}O$. The line list provides the wavenumber, gf-value

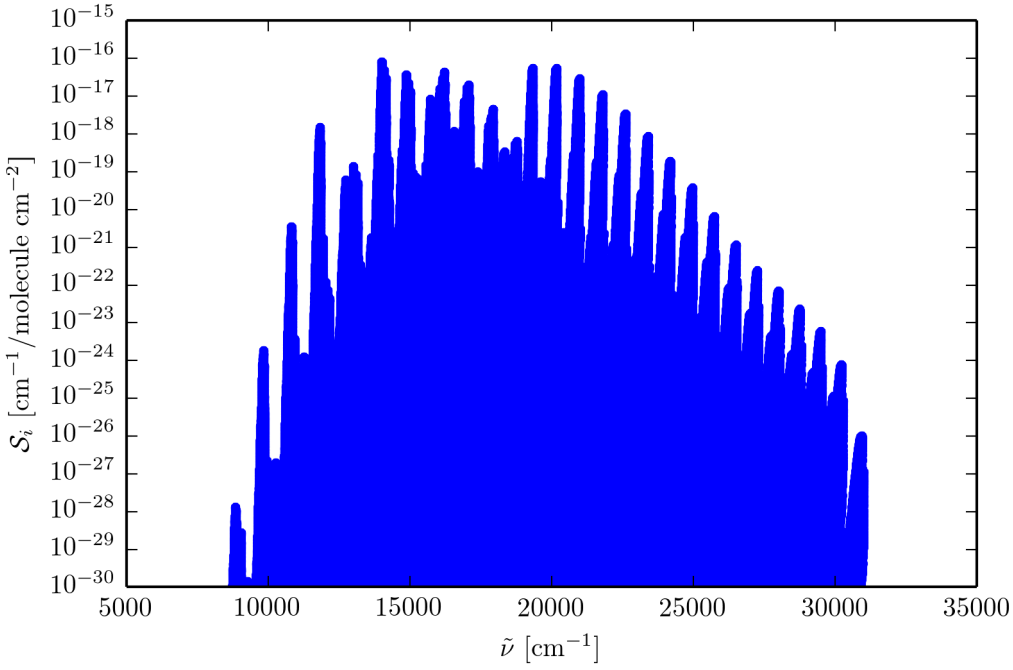

Figure 3.8: Line intensity for TiO calculated from the line list by Plez (1998) using Eq. (3.8) at $T = 296\,\mathrm{K}$.

and lower energy level of the transition, a plot of the line intensity for VO can be seen in Fig. 3.9.

Due to recommendation from B. Plez we use partition functions from Sauval & Tatum (1984) for TiO and VO. Sauval & Tatum (1984) provide polynomial fits for the partition functions obtained by using data from Huber & Herzberg (1979) for the temperature interval 1000 K to 9000 K. This is satisfactory for our purposes since the abundance of gaseous TiO and VO will be negligibly small for temperatures below 1000 K (Sharp & Burrows 2007).

Sodium and potassium (Na & K)

We include both the 0.589 µm sodium D and 0.77 µm potassium doublets, which are particularly strong. We use gf-values VALD3 (Vienna Atomic Line Database)[2], with sodium data from NIST (National Institute of Standards and Technology, Ralchenko et al. (2010)) and potassium data from Kurucz (2012). We adopt partition functions from Sauval & Tatum (1984).

Collision Induced Absorption (CIA)

Molecular hydrogen is the most abundant molecule in hot Jupiter atmospheres, but it is a symmetric molecule, which means that it does not have a permanent electric dipole moment. Both magnetic dipole and electric quadrupole moments will contribute to the absorption, but

[2] `http://vald.astro.uu.se/~vald/php/vald.php`

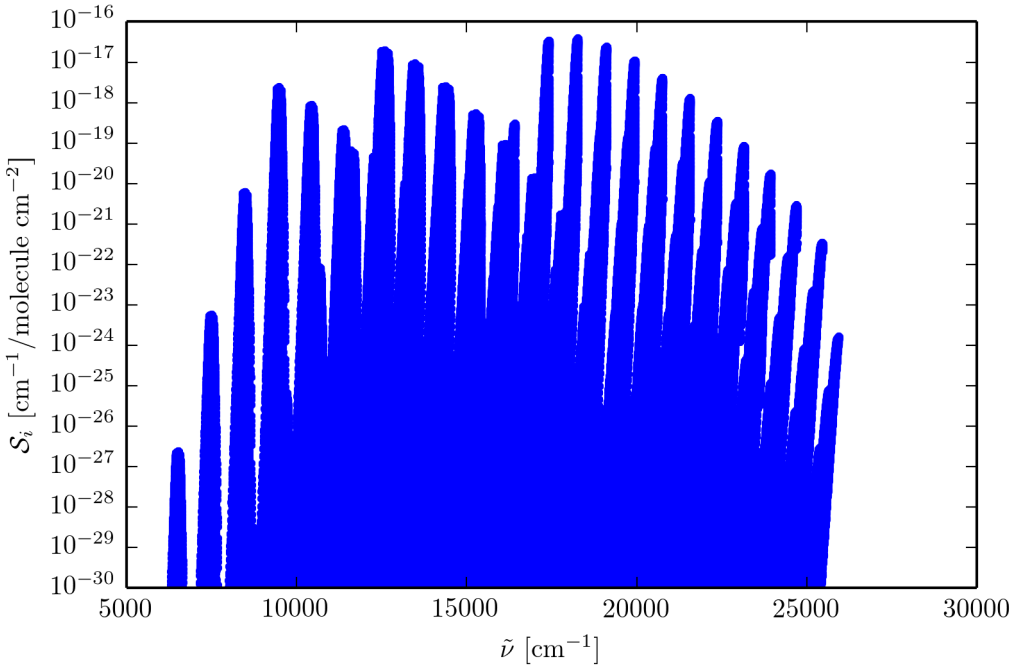

Figure 3.9: Line intensity for VO calculated from the line list by B. Plez (private communication) using Eq. (3.8) at $T = 296\,\mathrm{K}$.

their contributions are small, meaning that by itself H_2 is a very weak absorber. Collisions with other molecules can, however, induce a temporary dipole moment, which can contribute significantly to absorption. This is called collision induced absorption (CIA), and is proportional to both the density of H_2 and the perturbing species, H_2 or He. We use CIA coefficients from Richard et al. (2012), where it is tabulated as a function of both temperature and wavenumber.

3.2 Pressure-broadened line widths

Obtaining pressure-broadening parameters for all lines at all relevant temperatures and pressures is a challenging task. Pressure broadening originates in the interaction between the absorbing/emitting molecule and other molecules. In theory, all molecules contribute to the final pressure-broadened width, but, as seen in Eq. (3.11), the width is proportional to the partial pressure of the perturbing species. For this reason we only include broadening by H_2 and He for hot Jupiter atmospheres.

Due to the lack of data on broadening by molecular hydrogen and helium (Freedman et al. 2008; Sharp & Burrows 2007), we had originally opted to calculate pressure broadening parameters using van der Waals broadening theory. The results we obtained were unsatisfactory, however, which we discuss in more detail in Section 3.2.1. Currently we extrapolate predominately experimental data to obtain the necessary line widths; we detail this in Section 3.2.2. Note

that we denote the mass absorption coefficient by $k_\rho(\tilde{\nu})$ in this section for consistency with the literature.

3.2.1 Van der Waals broadening

Van der Waals broadening was originally developed for pressure-broadening of atomic lines by atomic hydrogen, and have mostly been applied to stellar atmospheres where the temperature is high enough to dissociate molecular hydrogen. It uses the impact approximation, where the perturber travels at high speeds causing brief interaction between the absorber and perturber. For a more detailed discussion see Unsöld (1955), Gray (2005) and Rutten (2003). It leads to a Lorentz FWHM given by

$$2\alpha_{\rm L}^{\rm vdW} = \gamma_{\rm vdW} = 17 C_6^{2/5} \langle v_{\rm rel} \rangle^{3/5} N_p, \tag{3.24}$$

where $\langle v_{\rm rel} \rangle$ is the average relative velocity between perturber and absorber and N_p is the number density of the perturber. The calculation of the interaction constant C_6 is based on Unsöld (1955), but modified to take into account different polarazibilities of each perturber as described in Schweitzer et al. (1996)[3]. The result is

$$C_6^0 = \frac{\alpha_{\rm p}}{\alpha_{\rm H}} \times 1.01 \times 10^{-32} (Z+1)^2 \left[\frac{E_{\rm H}^2}{(E-E_{\rm u})^2} - \frac{E_{\rm H}^2}{(E-E_{\rm l})^2} \right], \tag{3.25a}$$

$$C_6 = 10^{1.8} C_6^0, \tag{3.25b}$$

where $\alpha_{\rm p}$ is the polarisability of the perturber, Z is the charge of the absorber, $E_{\rm H}$ is the ionisation potential of hydrogen, E is the ionisation potential of the absorber, and $E_{\rm u}$ and $E_{\rm l}$ are the upper and lower energy levels of the absorber, respectively.

In Eq. (3.25b) a correction factor $10^{1.8}$ has been applied due to deviations between observed line widths for non-alkali-like elements and those predicted using Eq. (3.25a) for C_6. We take the value of this correction factor from Schweitzer et al. (1996), but it is not well determined.

The relative velocity $\langle v_{\rm rel} \rangle$ between the absorber and perturber, assuming that both follow the Maxwell-Boltzmann velocity distribution, is given by

$$\langle v_{\rm rel} \rangle = \sqrt{\frac{8 k_{\rm B} T}{\pi} \left(\frac{1}{m_z} + \frac{1}{m_p} \right)}, \tag{3.26}$$

where m_z and m_p are the molecular mass of the absorber and perturber, respectively. We provide the derivation in Appendix A.2. Values for the atomic and molecular constants needed when calculating $\gamma_{\rm vdW}$ using Eq. (3.24) are given in Table 3.2.

It is useful to calculate the temperature exponent of van der Waals Lorentz widths. We

[3]Note that in Schweitzer et al. (1996) there is a misprint: the order of the two terms inside the square brackets in Eq. (3.25a) should be switched.

Table 3.2: Polarizability ($\alpha_{\rm p}$) and ionisation potentials from Lide (1995) supplemented by data from NIST[a] (Ralchenko et al. 2010).

[a] `http://webbook.nist.gov/chemistry/`

Atom/molecule	$\alpha_{\rm p}$ [10^{-24} cm^3]	Ionisation potential [eV]
H	0.666793	13.59844
He	0.204956	-
H_2	0.8045	-
CO	-	14.0139
H_2O	-	12.612
CH_4	-	12.51
N_2	-	15.5808
NH_3	-	10.07
TiO	-	6.819
VO	-	7.2386

bring Eq. (3.24) on the form of Eq. (3.11) and get

$$\gamma_{\rm vdW} \propto T^{0.3} N_p \propto T^{-0.7} P_p, \tag{3.27}$$

where the ideal gas equation has been used. Comparing to Eq. (3.11) we see that the van der Waals broadening formula has the same form, where $\alpha_{\rm L}^p(P_p, T_0)$ varies between different transitions and perturbers, while n_p is always 0.7. The value of the temperature exponent when fitting and extrapolating experimental data is usually taken to be ~ 0.5 (Homeier 2005; Sharp & Burrows 2007), but can vary considerably. The value predicted by van der Waals broadening theory is therefore reasonable, if not accurate.

As the discussion above suggests, line widths for non-alkali metals are observed to deviate from those predicted by van der Waals broadening theory (Schweitzer et al. 1996). The correction factor tries to capture some of this, but the error varies significantly from line to line, and thus a constant correction factor cannot rectify this situation. As we begun calculating absorption coefficients using Eq. (3.24) for the Lorentz line width we found a significant deviation between our absorption coefficients and those shown in e.g. Sharp & Burrows (2007) and Freedman et al. (2008). Figures 3.10a and 3.10b show the water absorption coefficient calculated using the BT2 line list with both van der Waals theory and line widths gathered from the literature, as described in Section 3.2.2, at two temperatures and pressures. Figure 3.10a can be compared to Fig. 2 in (Sharp & Burrows 2007), while in Fig. 3.10b the line widths from the literature have not been extrapolated as a function of pressure and temperature and should therefore be reasonably accurate. Van der Waals broadening theory clearly overestimates the line widths causing visible differences in the absorption coefficients, and we have observed the same for other molecules. We have not included the correction factor in Eq. (3.25b) as suggested by Schweitzer et al. (1996) since this would further increase the van der Waals line widths. For this reason we choose to adopt line widths extrapolated from data collected from the literature as described in the next section.

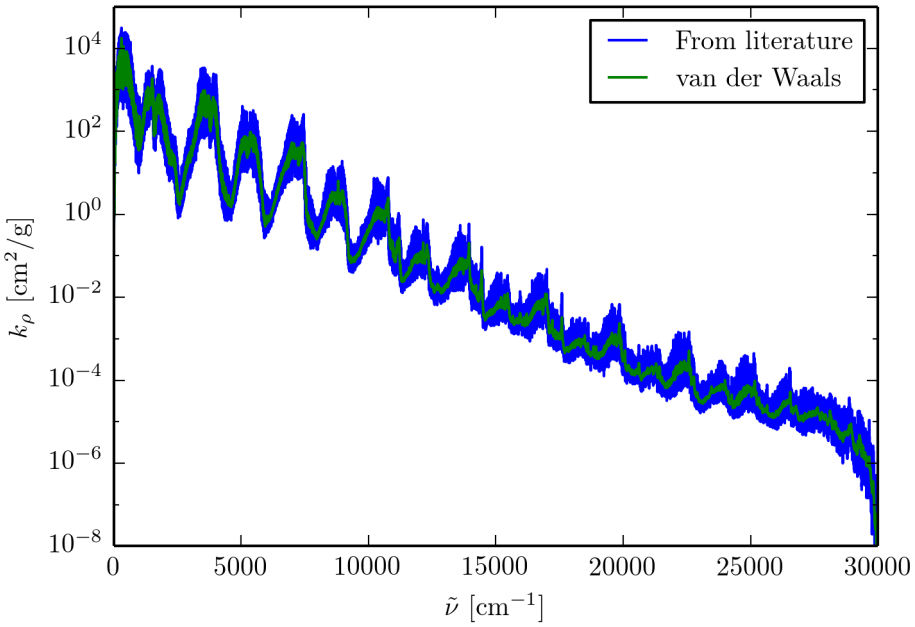

(a) Water absorption coefficient at $P_{\mathrm{tot}} = 10\,\mathrm{bar}$ and $T = 1600\,\mathrm{K}$ for easy comparison with Sharp & Burrows (2007).

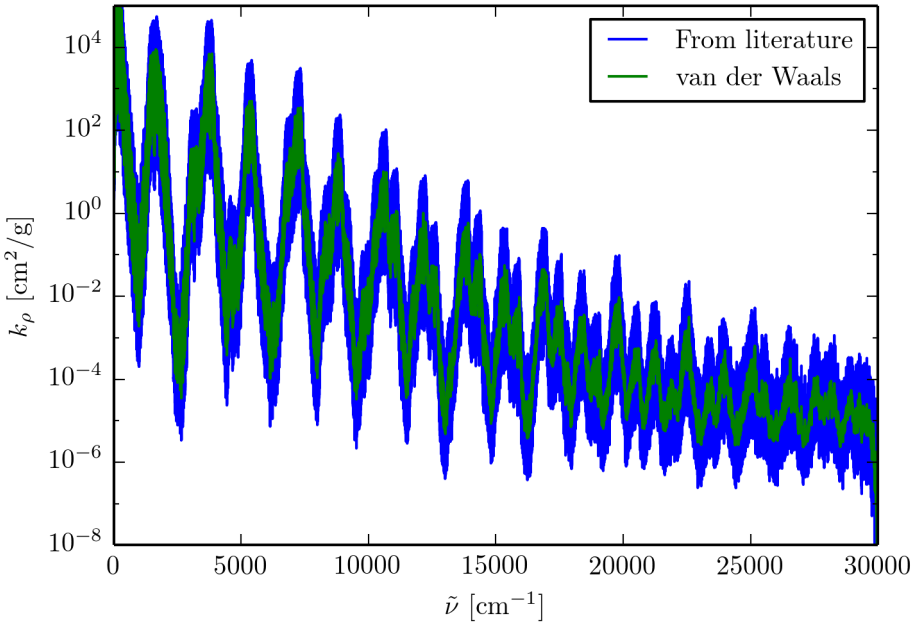

(b) Water absorption coefficient at $P_{\mathrm{tot}} = 1\,\mathrm{bar}$ and $T = 296\,\mathrm{K}$, i.e. line widths from the literature have not been extrapolated in temperature and pressure.

Figure 3.10: Absorption coefficients as a function of wavenumber for water calculated from the BT2 water line list using van der Waals theory (without correction factor) and line widths from the literature for two different temperatures and pressures. It is clear that van der Waals broadening theory overestimates line widths.

Molecule	Broadener	Line width reference
H_2O	H_2	Gamache et al. (1996)
	He	Solodov & Starikov (2009), Steyert et al. (2004)
CH_4	H_2	Pine (1992), Margolis (1993)
	He	Pine (1992)
CO_2	H_2	Padmanabhan et al. (2014)
	He	Thibault et al. (1992)
CO	H_2	Régalia-Jarlot et al. (2005)
	He	BelBruno et al. (1982), Mantz et al. (2005)
NH_3	H_2	Hadded et al. (2001); Pine et al. (1993)
	He	Hadded et al. (2001), Pine et al. (1993)
TiO	H_2	Burrows et al. (2007)
	He	Burrows et al. (2007)
VO	H_2	Burrows et al. (2007)
	He	Burrows et al. (2007)
Na	H_2	Allard et al. (2003, 1999, 2007)
	He	Allard et al. (2003, 1999, 2007)
K	H_2	Allard et al. (2003, 1999, 2007)
	He	Allard et al. (2003, 1999, 2007)

Table 3.3: Overview of our line width sources for broadening by hydrogen and helium.

3.2.2 Molecular line widths from the literature

We have gathered line widths for broadening of H_2O, NH3, CO, CO_2 and CH_4 lines by H_2 and He from the literature. Our sources are given in Table 3.3; they partly overlap with those used by Bailey & Kedziora-Chudczer (2012). The line width data is provided in tables with details on the individual transitions.

A transition is identified by several quantum numbers, which differ between different molecules. In the BT2 line list only the total rotational quantum number, J, and the symmetry are given for all levels, and these are therefore the only two parameters we can use to estimate the line widths for all lines. This is also the case for other molecules such as CH_4. In addition, line width data is only available for a very small fraction of all the lines in our line lists. We therefore adopt a very simple approach: we tabulate line widths found in the literature as a function of J for the lower level and use this as a basis for estimating line widths for all lines. This approach was chosen for its simplicity and applicability to all molecules, and similar approaches have previously been used to obtain air broadened line widths for transitions in the BT2 line list (Rothman et al. 2010; Voronin et al. 2010).

In Fig. 3.11 line widths are plotted as a function of the total angular momentum quantum number of the lower level, $J_{\rm low}$. The horizontal axes show the span of $J_{\rm low}$ required by our line lists. For all molecules there is an overall trend of a decreasing line width as a function of $J_{\rm low}$. We fit the line width as a function of $J_{\rm low}$ by a linear function using a least-squares regression. We have no constraints on which values this function should take for high $J_{\rm low}$, so we keep line widths constant for all $J_{\rm low}$ where data is unavailable to avoid introducing additional complexity. The constant value is the width of the line with the highest $J_{\rm low}$ where data is available as

Molecule	Broadener	n_p	Reference
H_2O	H_2	0.45	Gamache et al. (1996)
	He	0.44	Gamache et al. (1996)
CH_4	H_2	0.44	Margolis (1993)
	He	0.28	Varanasi & Chudamani (1990)
CO_2	H_2	0.60	Sharp & Burrows (2007)
	He	0.60	Thibault et al. (2000)
CO	H_2	0.60	Le Moal & Severin (1986)
	He	0.55	Mantz et al. (2005)
NH_3	H_2	0.68	Nouri et al. (2004)
	He	0.40	Sharp & Burrows (2007)
TiO	H_2	0.60	Sharp & Burrows (2007)
	He	0.40	Sharp & Burrows (2007)
VO	H_2	0.60	Sharp & Burrows (2007)
	He	0.40	Sharp & Burrows (2007)

Table 3.4: Table of the temperature exponents used in our absorption coefficient calculations. The sources are given in Table 3.3.

calculated using our linear fit.

The experiments measuring line widths are usually performed at room temperature and pressure. Equation (3.11) describes the expected temperature and pressure dependence of the Lorentz line width: it is a linear function of partial pressure and a power law in temperature. We also use temperature exponents n_p from the literature, again mostly experimental data, with sources given in Table 3.4. Temperature exponents are obtained by measuring line widths at a few temperatures, usually at room temperature and below, and fitting the result to Eq. (3.11). n_p is also transition dependent, but available data is even sparser than for the line widths themselves, and we therefore use a fixed value for a given molecule and perturber. This constant value may be an average value for several transitions, or the value for one transition that is believed to be representative. Table 3.4 lists the values of n_p we use in our calculations.

To estimate when pressure broadening becomes important we can calculate the pressure at which the Doppler and Lorentz widths are equal. For H_2O broadened by H_2 the Lorentz width is approximately $0.1\,\mathrm{cm}^{-1}$ at room temperature and pressure from Fig. 3.11a. For the pressure broadened width to equal the Lorentz width, we must have from Eqs. (3.11) and (3.23)

$$\alpha_{\mathrm{L}}^{p}(P_0, T_0) \left(\frac{T_0}{T}\right)^{n_p} \frac{P_p}{P_0} = \frac{\tilde{\nu}_0}{c}\sqrt{\frac{2k_{\mathrm{B}}T}{m_z}}, \tag{3.28}$$

where P_p is the partial pressure of the perturbing gas. This yields

$$P_p = \frac{\tilde{\nu}_0}{c}\sqrt{\frac{2k_{\mathrm{B}}T}{m_z}} \left(\frac{T_0}{T}\right)^{-n_p} \frac{1}{\alpha_{\mathrm{L}}^{p}(P_0, T_0)} P_{p,0}, \tag{3.29}$$

which for H_2O, with $\tilde{\nu}_0 = 5000\,\mathrm{cm}^{-1}$, $T = 1500\,\mathrm{K}$ yields $P_p \approx 0.4\,\mathrm{bar}$. This pressure is expected to be in the region where the atmosphere transitions from being optically thin to optically

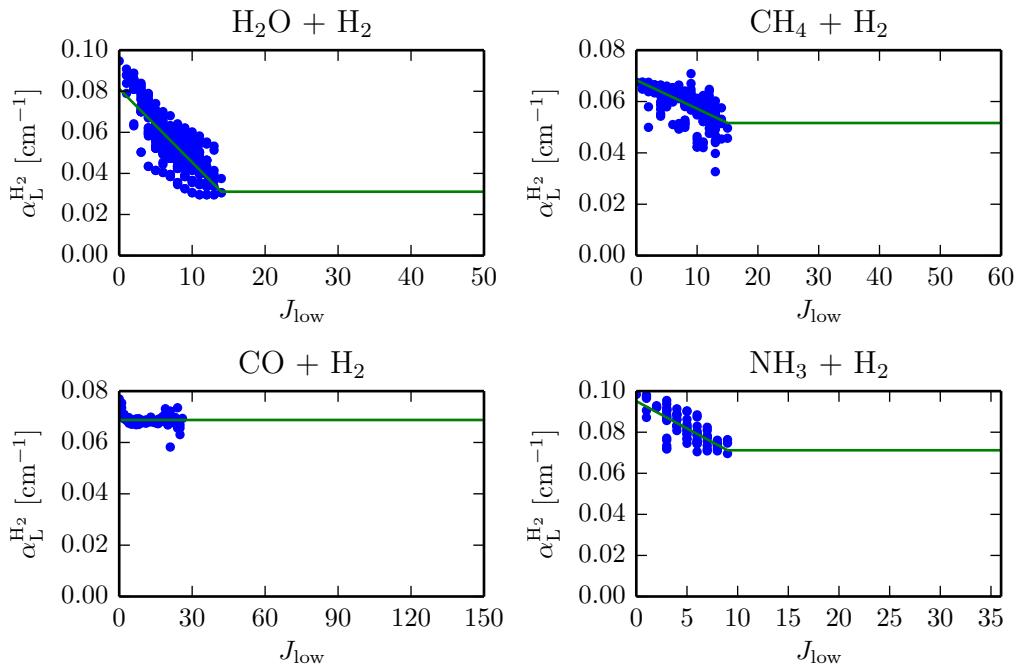

(a) Line widths as a function of J_{low} for broadening by H_2.

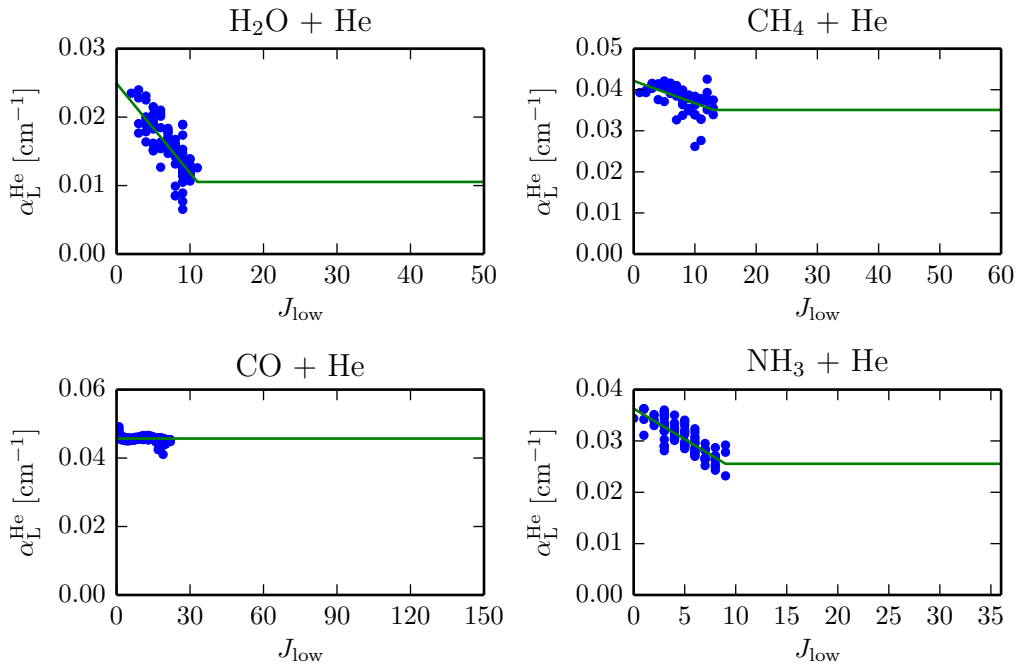

(b) Line widths as a function of J_{low} for broadening by He.

Figure 3.11: Line widths at $T = 296\,\text{K}$ and $P_{H_2} = P_{He} = 1\,\text{bar}$ from the literature. The blue dots are the data collected from the sources in Table 3.3, the green solid line is our interpolated and extrapolated line widths as used in our absorption coefficient calculations.

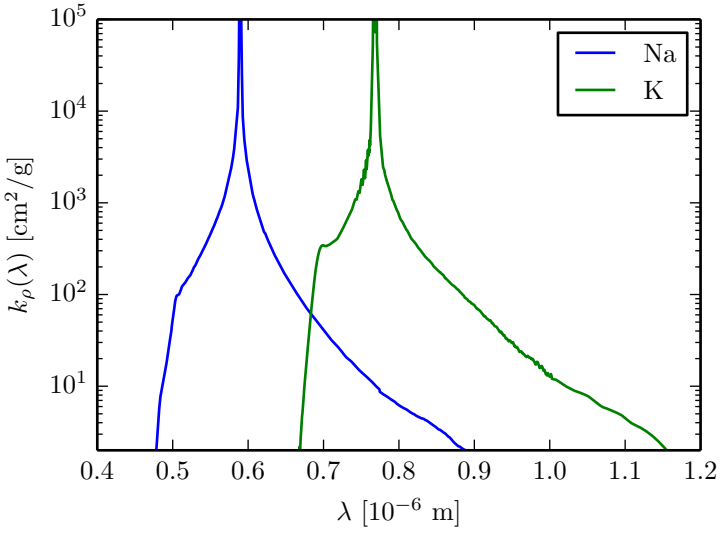

Figure 3.12: Sodium and potassium opacities calculated with the PHOENIX routines sent us by Derek Homeier at 1657 K, 0.92 bar.

thick (see Chapter 4) and pressure broadening is therefore an important issue that needs to be considered.

A more robust treatment of line broadening parameters is, of course, desirable. We extrapolate the temperature dependence by an order of magnitude, the widths as a function of $J_{\rm low}$ by a factor of four or more, and the scatter of the data points about the linear fit in Fig. 3.11 can be quite large. We are currently setting up a collaboration with the ExoMol group at University College London (UCL) and V.E. Zuev Institute of Atmospheric Optics in Tomsk, Russia to improve these line widths and investigate the effect on model atmospheres and spectra.

3.2.3 Sodium and potassium line profiles

Both the 0.589 µm sodium D and the 0.77 µm potassium doublets are particularly strong, and their line wings are important at large distances from the line centres (Allard et al. 2003; Burrows et al. 2000). For the far-wings the classical approximations used to derive the pressure broadened Lorentz profiles break down. It is therefore necessary to use a more detailed line broadening theory in order to treat the line wing absorption accurately.

Several studies use quantum mechanical calculations to derive more accurate line profiles for these lines (Allard et al. 2003, 1999; Burrows & Volobuyev 2003; Zhu et al. 2006). We adopt the line profiles used in the PHOENIX atmosphere code (Allard et al. (2003, 1999, 2007), Derek Homeier, private communication). A plot of the calculated opacity using these line profiles for both sodium and potassium are shown in Fig. 3.12.

3.3 Numerical considerations

We now discuss some of the numerical details of computing absorption coefficients. We discuss the treatment of line wings, parallelisation using OpenMP and MPI, and our opacity table, which is used as a basis for calculating the k-coefficients discussed in Section 3.4.

3.3.1 Treatment of line wings

The use of high-temperature line lists raises computational issues due to their size. In the HITRAN 2012 database (Rothman et al. 2013), the NH_3 line list has about 4.6×10^4 lines, while the ExoMol NH_3 line list, BYTe (Yurchenko et al. 2011), has about 1.1×10^9 lines. Consequently, calculating absorption coefficients from high-temperature line lists is significantly more computationally expensive than using smaller line lists such as HITRAN. In the literature this problem is often overcome by ignoring all lines with line intensities smaller than some value, sometimes evaluated at a fixed temperature (Sharp & Burrows 2007). The line intensity is, however, a strong function of temperature, and knowing where to apply the cut-off may be difficult.

A second cut-off has to be made, both for physical and computational reasons. According to Eq. (3.22) lines are infinite in extent and follow a Voigt profile. Unfortunately, real line profiles are not perfectly Voigtian (Thomas & Stamnes 2002). The Voigt profile is fairly accurate provided interactions between molecules are weak, but for stronger interactions effects such as collisional narrowing may occur. Line wings are most affected, and to avoid overestimating the line wing absorption, it is common practice to apply a cut-off at some distance d from the line centre (Freedman et al. 2008; Sharp & Burrows 2007). This distance may be fixed or be a function of pressure and/or temperature. In addition, evaluation of the Voigt profile is computationally expensive, and computing the line profiles to distances where it can be neglected adds an unnecessary computational cost.

To cope with these problems we have developed a scheme to combine the line wing cut-off with an elimination of unimportant weak lines to decrease computation time. The cut-off distance d is calculated "on-the-fly" by estimating when the line mass absorption coefficient has reached some value, k_ρ^{cut}. This is done by approximating the line profile as Lorentzian with a width equal to the sum of the Doppler and pressure broadened widths to facilitate analytical treatment and ensure that the profile width is not underestimated. This yields the following formula for d:

$$d = \sqrt{\tilde{\alpha} \max\left(\frac{\mathcal{S}_i}{\pi k_\rho^{\mathrm{cut}}} - \tilde{\alpha}, 0\right)}, \qquad \tilde{\alpha} = \alpha_{\mathrm{L}} + \alpha_{\mathrm{D}}, \tag{3.30}$$

For very weak lines, $\mathcal{S}_i/\pi k_\rho^{\mathrm{cut}} - \tilde{\alpha} < 0$, i.e. the value of the line mass absorption coefficient at the line centre is smaller than k_ρ^{cut}, and consequently the line can be ignored completely.

Lines are added one-by-one to the total mass absorption coefficient spectrum. The value of k_ρ^{cut} is chosen to be some fraction f_{AK} of the latest value of the total mass absorption coefficient

at the line centre of the current line as line profiles are summed up: $k_\rho^{\rm cut} = f_{\rm AK} k_\rho^{\rm latest}(\tilde{\nu}_0)$. We use the abbreviation AK (adaptive $k_\rho^{\rm cut}$) to denote this cut-off method. Some lines can become unrealistically broad, however, so we include an upper limit on d of $100\,{\rm cm}^{-1}$. Note that this cut-off scheme cannot be used if the water continuum is included since it requires a cut-off at a fixed distance from the line centre (Clough et al. 1989). The water continuum is, however, only suitable for use in models of Earth-like atmospheres.

The main motivation for using this scheme is computational efficiency and not physical considerations, and the final absorption coefficient will depend slightly on the order in which lines have been added up. The advantages are, however, that weak lines can be discarded on-the-fly taking into account the line intensity at the current temperature, making a simple cut-off in line intensity unnecessary. It also ensures that strong lines are computed to larger distances from the line centres than weaker lines. The current lack of robust line broadening schemes for conditions characteristic of hot Jupiters forces us to use such artificial schemes.

We have, however, tried to limit the impact of our treatments by testing other schemes used in the literature. We compare our line profile cut-off scheme to two other schemes: (i) A cut-off at a fixed distance $d_{\rm FW}$ from the line centre (fixed width, FW) and (ii) a cut-off at a distance from the line centre given by the sum of the Doppler and pressure broadened widths multiplied by some factor $f_{\rm FF}$ (fixed factor, FF). The former scheme is similar to that used when including the water continuum from Clough et al. (1989), where all lines have to be cut-off $25\,{\rm cm}^{-1}$ from the line centre, while the latter is similar to that used by Sharp & Burrows (2007). Note that when using FF, we still apply the upper limit of $100\,{\rm cm}^{-1}$ on d.

In Fig. 3.13, we show both the average absorption coefficient between $1000\,{\rm cm}^{-1}$ and $1001\,{\rm cm}^{-1}$ at $10^5\,{\rm Pa}$, $1500\,{\rm K}$ and the computation time required for the three schemes as a function of the cut-off parameters. The three cut-off methods reach approximately the same average absorption coefficient for the largest values of the cut-off distances (see Fig. 3.13). Comparing the levels in the left-hand panels to the computation times in the right-hand panel, however, clearly shows the advantage of the AK method. At $f_{\rm AK} = 10^{-6}$, this method reaches approximately the same level as FW at $d_{\rm FW} = 10^2\,{\rm cm}^{-1}$ and FF at $f_{\rm FF} = 10^3$. The computation time is, however, more than two orders of magnitude smaller. Due to the uncertainties in line widths and the significant decrease in computation time, we have decided to adopt this scheme for all our molecules using $f_{\rm AK} = 10^{-6}$ except for CO.

CO lines are divided into several clearly separate, narrow bands. Consequently, the absorption coefficient will vary by many orders of magnitude on the scale of the bands. The AK scheme is unsuited to such situations since it will tend to produce large cut-off distances at the beginning of the cross-section calculation. These line wings will normally be hidden by stronger lines, but for CO they become non-negligible due to the lack of strong lines in certain wavelength regions. For CO we therefore use the FF method with $f_{\rm FF} = 10^2$ without discarding any lines.

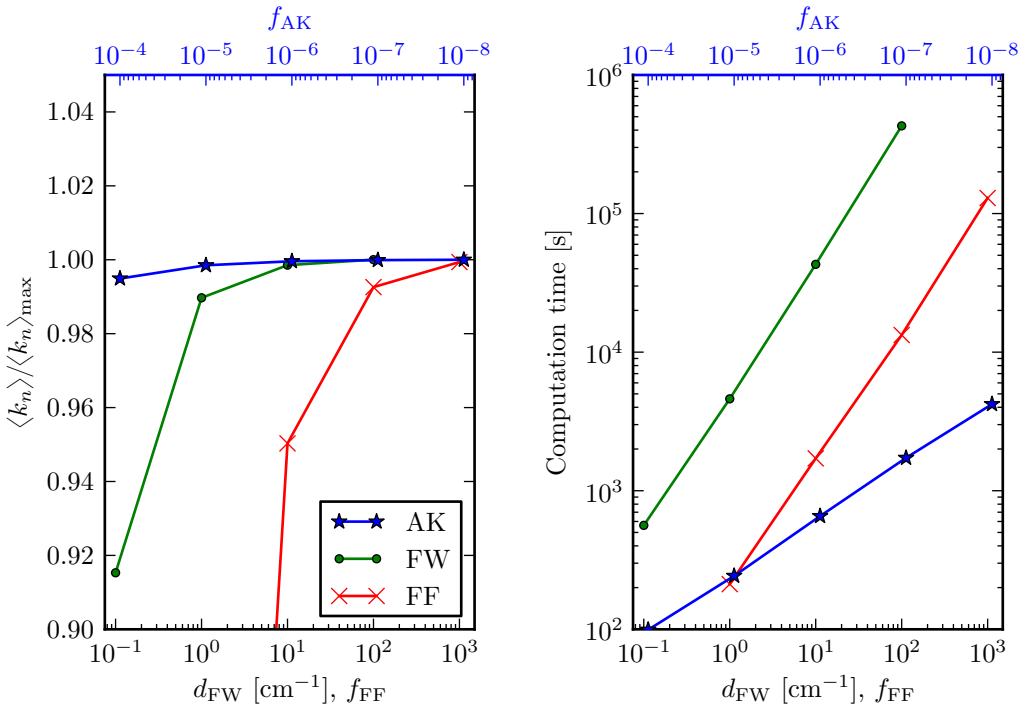

Figure 3.13: Left-hand panel: Arithmetic mean of the H_2O absorption coefficient between 1000 cm^{-1} and 1001 cm^{-1} calculated using the adaptive (AK), fixed width (FW), fixed factor (FF) cut-off schemes as a function of the cut-off parameters (f_{AK}, d_{FW} and f_{FF}, respectively) at 10^5 Pa, 1500 K. The mean absorption coefficients have been normalised by the value obtained using AK with $f_{\mathrm{AK}} = 10^{-8}$. Right-hand panel: Computation time required using 12 cores at 2.8 GHz as a function of the cut-off parameter. We see that our adaptive cut-off scheme is about two orders of magnitude faster than the two other methods for a given average absorption coefficient.

3.3.2 Parallelisation using OpenMP and MPI

Initially our absorption coefficient calculation code was parallelised using only OpenMP[4] (Open Multi-Processing), which enables shared memory multiprocessing in Fortran. The code reads in a section of the line list and the loop over lines is split over many cores using OpenMP. Once completed a new section of the line list is read and the calculation continues. Both the line list section read and the tabulated absorption coefficient are stored in memory shared by all processors. For NH_3, having the largest of our adopted line lists with more than 1.1×10^9 lines, computation of absorption coefficients take about 11 days using our adaptive cut-off scheme on a computer with an Intel Xeon X5660 processor with 12 cores at 2.8 GHz.

Later the code was parallelised using MPI[5] (Message Passing Interface), which enables multiprocessing in Fortran on systems with distributed memory, in addition to OpenMP. Consequently the code can be run on several computing nodes not sharing the same memory. In our current implementation each computing node has one MPI thread. Each MPI thread reads

[4] `http://openmp.org/`
[5] `http://mpi-forum.org/`

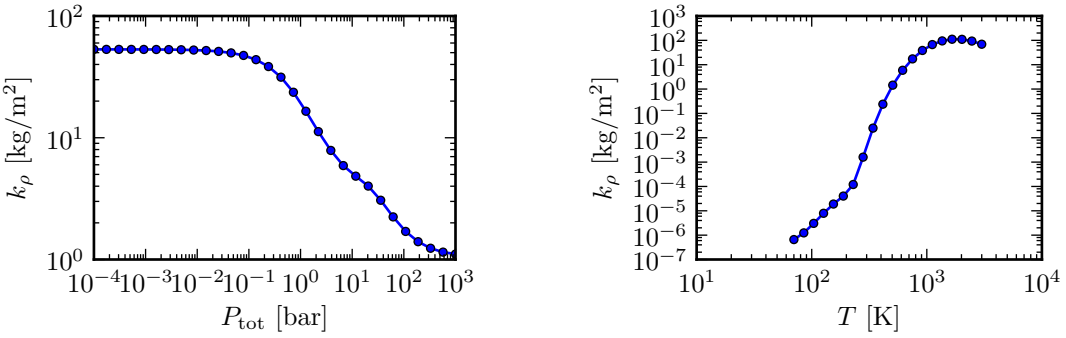

(a) Mass absorption coefficient as a function of total pressure at $T = 916\,\mathrm{K}$.

(b) Mass absorption coefficient as a function of temperature at $P = 0.24\,\mathrm{bar}$.

Figure 3.14: Mass absorption coefficients as a function of both pressure and temperature at $\tilde{\nu} = 5000\,\mathrm{cm}^{-1}$ for $H_2{}^{16}O$ calculated using BT2. Our resolution is sufficient to capture the temperature and pressure dependence of the opacities.

a section of the line list and calculates the absorption coefficient for this section as described above. Once completed new sections of the line list are read and the calculation continues. We found the speed-up to be almost linear with the number of MPI threads.

3.3.3 Opacity tables

We tabulate the absorption coefficients on a fixed wavenumber grid for a range of temperatures and pressures. We use a wavenumber resolution of $1 \times 10^{-3}\,\mathrm{cm}^{-1}$ in order to properly resolve lines at both small temperatures and pressures. This resolution is technically not high enough to resolve all lines at very small wavenumbers, temperatures and pressures, where both Doppler and Lorentz widths are small. We have found, however, that for hot Jupiter-like conditions it is sufficient for the solution to have converged by successively increasing the resolution with our line-by-line code detailed in Section 4.1.2.

A logarithmic grid in both temperature and pressure is used, where $70\,\mathrm{K} \leqslant T \leqslant 3000\,\mathrm{K}$ with 20 grid points and $10^{-3}\,\mathrm{Pa} \leqslant P_{\rm tot} \leqslant 10^{8}\,\mathrm{Pa}$ with 40 grid points, i.e. a total of $20 \times 40 = 800$ temperature-pressure points. Figure 3.14 shows the dependence of the mass absorption coefficient for water as a function of both total pressure and temperature for a particular wavenumber. Both functions are fairly smooth, and our chosen resolution seems to be sufficient to resolve the temperature and pressure dependence.

3.4 The correlated-k method

The radiative transfer equation must be solved independently for each wavenumber, yielding the spectral flux $F_{\tilde{\nu}}$ and heating rate $\mathcal{H}_{\tilde{\nu}}$, respectively. The total flux and heating rate are obtained

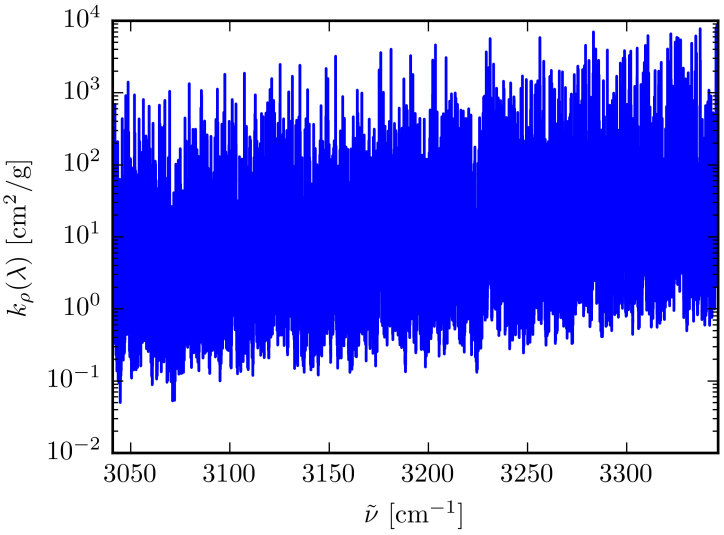

Figure 3.15: Water opacity, k_ρ, as a function of wavenumber, $\tilde{\nu}$, for band 9 in Table 4.2 at $P = 9.2 \times 10^4$ Pa, $T = 1.1 \times 10^3$ K. It illustrates the complicated wavenumber dependence of the opacity, causing a large resolution in wavenumber to be required when calculating e.g. the transmission given by Eq. (3.31).

by integrating these quantities over all wavenumbers. This is called a line-by-line (LbL) approach. Our wavenumber resolution $\Delta\tilde{\nu} = 1 \times 10^{-3}\,\mathrm{cm}^{-1}$ yields on the order of 10^7 wavenumber points. It becomes unfeasible to use a LbL approach in the UM due to the computational expense of performing about 10^7 monochromatic calculations. The ES radiation scheme uses the correlated-k method to tackle this issue. This method was originally introduced by Lacis & Oinas (1991) and has since been widely applied to treat opacities in both planetary and brown dwarf atmospheres.

The absorption coefficient will take similar values at several wavenumbers. Combining the calculation of fluxes for these wavenumbers can potentially lead to a significant decrease in the number of monochromatic calculations needed, the correlated-k method provides a way of doing this. Note that in this section we denote mass absorption coefficients by $k_\rho(\tilde{\nu})$ to be in agreement with the literature on the correlated-k method.

Currently the ES radiation scheme uses a combination of the exponential sum fitting of transmissions (ESFT) technique (Wiscombe & Evans 1977) and the correlated-k method (Goody et al. 1989; Lacis & Oinas 1991). In the following, the species index i will be dropped for ease of notation. Consider the transmission through a homogeneous slab between the wavenumbers $\tilde{\nu}_1$ and $\tilde{\nu}_2$:

$$\mathcal{T}(u) = \frac{1}{\tilde{\nu}_2 - \tilde{\nu}_1} \int_{\tilde{\nu}_1}^{\tilde{\nu}_2} \mathrm{d}\tilde{\nu}\, e^{-k_\rho(\tilde{\nu})u}, \tag{3.31}$$

where u is the mass column density. In the following we drop the subscript ρ on the absorption coefficient for simplicity. Due to the complexity of $k(\tilde{\nu})$, as shown in Fig. 3.15, a very high wavenumber resolution may be required to calculate the transmission integral accurately. This can be avoided by considering the probability distribution of the absorption coefficient. The absorption coefficient will take similar values for several wavenumbers in Eq. (3.31), and these can be combined into a single exponential multiplied by the probability of this absorption

coefficient occurring between $\tilde{\nu}_1$ and $\tilde{\nu}_2$. We introduce $f(k)$, where $f(k)\,\mathrm{d}k$ is the probability of the absorption coefficient taking a value between k and $k + \mathrm{d}k$. $f(k)$ is found by dividing the spectral interval $[\tilde{\nu}_1, \tilde{\nu}_2]$ into subintervals $\Delta\tilde{\nu}_j = \tilde{\nu}_{j+1/2} - \tilde{\nu}_{j-1/2}$, where $\tilde{\nu}_{j\pm1/2}$ are the wavenumber points at which the absorption coefficient has been calculated, and the absorption coefficient range $[k_{\min}, k_{\max}]$ into subintervals (or bins) Δk_l, where $\Delta k_l = k_{l+1} - k_l$. Wavenumber intervals $\Delta\tilde{\nu}_j$ which have absorption coefficients between k_l and $k_l + \Delta k_l$ are then summed to obtain

$$f(k_l) = \frac{1}{\tilde{\nu}_2 - \tilde{\nu}_1} \sum_j \left| \frac{\Delta\tilde{\nu}_j}{\Delta k_l} \right| W(k_l, k_l + \Delta k_l), \tag{3.32}$$

where $W(k_l, k_l + \Delta k_l)$ is a "window" function that is zero everywhere except between k_l and $k_l + \Delta k_l$ where it is unity. The transmission, Eq. (3.31), can then be written as

$$\mathcal{T}(u) = \int_{k_{\min}}^{k_{\max}} \mathrm{d}k\, f(k) e^{-ku}, \tag{3.33}$$

and we introduce the cumulative probability g, where $\mathrm{d}g = f(k)\,\mathrm{d}k$ and

$$g(k) = \int_0^k \mathrm{d}k'\, f(k'). \tag{3.34}$$

The probability of the absorption coefficient being smaller than k is given by $g(k)$, and $g \in [0, 1]$ and is a monotonically increasing as a function of k. Thus it can be inverted, and we can write the absorption coefficient as a function of the cumulative probability variable: $k(g)$. g therefore functions as a pseudo wavenumber variable, and we can write the transmission integral as

$$\mathcal{T}(u) = \int_0^1 \mathrm{d}g\, e^{-k(g)u} \approx \sum_{l=1}^{n_k} w_l e^{k_l u}, \tag{3.35}$$

where n_k is the number of quadrature points used to evaluate the integral numerically. $k(g)$ is a smooth function, see Fig. 3.16, and the transmission integral on the form of Eq. (3.35) can be evaluated numerically using only a few quadrature points. If a fixed wavenumber spacing $\Delta\tilde{\nu}_j$ is used, $g(k)$ can be obtained by simply sorting the absorption coefficients in terms of increasing strength. We discuss below how the ES scheme obtains the k-coefficients k_l and weights w_l.

Until now no approximations have been made, Eq. (3.35) is exact for a homogeneous slab, and this approach is called the k-distribution method. Planetary atmospheres are not homogeneous, however, and to extend the k-distribution method to inhomogeneous atmospheres the correlated-k method is used: $k(g)$ is calculated for all layers in the atmosphere and n_k pseudo-monochromatic calculations are performed with the corresponding k_l for each layer. This corresponds to keeping g constant throughout the atmosphere instead of the wavenumber $\tilde{\nu}$, and assumes that absorption coefficients in different layers map onto the same value of g in all layers, i.e. it is assumed that absorption coefficients in different layers are correlated. The correlated-k method will not

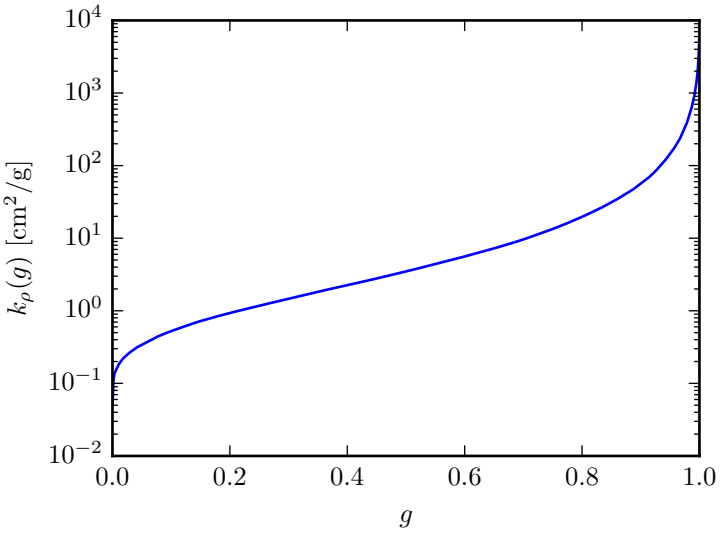

Figure 3.16: Water opacity, k_ρ, as a function of the cumulative probability variable, g, for band 9 in Table 4.2 at $P = 9.2 \times 10^4$ Pa, $T = 1.1 \times 10^3$ K. Compared to $k_\rho(\tilde{\nu})$, $k_\rho(g)$ is a slowly varying function that can be integrated using only a few integration points, see Eq. (3.35).

completely converge to the LbL solution even with many k-coefficients: $g(k)$ is calculated at each P–T independently. If the absorption coefficient decreases with height at one wavenumber and increases with height at a different wavenumber within the same band, the two wavenumbers will no longer correspond to the same value of g. A pseudo-monochromatic calculation where g is kept constant is therefore not equivalent to a proper monochromatic calculation except in a few special cases, see e.g. Goody et al. (1989) for more details.

The transmission integral in Eq. (3.31) assumes the flux to be constant between ν_1 and ν_2. This assumption can be relaxed by introducing the weighting function $w(\tilde{\nu})$,

$$w(\tilde{\nu}) = \frac{F_{\tilde{\nu}}}{\int_{\tilde{\nu}_1}^{\tilde{\nu}_2} \mathrm{d}\tilde{\nu}\, F_{\tilde{\nu}}}, \tag{3.36}$$

which is normalised to 1. The transmission integral becomes

$$\mathcal{T}(u) = \int_{\tilde{\nu}_1}^{\tilde{\nu}_2} \mathrm{d}\tilde{\nu}\, w(\tilde{\nu}) e^{-k_\rho(\tilde{\nu})u}, \tag{3.37}$$

and the weight is included in the probability distribution $f(k)$:

$$f_w(k_l) = \sum_j \left| \frac{\Delta\tilde{\nu}_j}{\Delta k_l} \right| w(\tilde{\nu}_{j+1/2}) W(k_l, k_l + \Delta k_l). \tag{3.38}$$

The transmission can be calculated using Eq. (3.35), where $k(g_w)$ is the inverse of $g_w(k)$ given by Eq. (3.34), with $f(k)$ given by Eq. (3.38).

As the flux $F_{\tilde{\nu}}$ is not known when k-coefficients are calculated, the flux in Eq. (3.36) is normally chosen to be the Planck function at the local temperature for the thermal component and the stellar flux at the top of the atmosphere for the stellar component of the radiation.

Alternatively it can also be assumed constant, i.e. $w(\tilde{\nu}) = 1/(\tilde{\nu}_2 - \tilde{\nu}_1)$. We test these three different weighting schemes in Chapter 4.

The discussion above only considers the transmission, but the correlated-k method is equally applicable when calculating other quantities that depend on wavenumber only through the absorption coefficient such as fluxes and heating rates.

3.4.1 Obtaining k-coefficients

The spectrum is divided into bands, $[\tilde{\nu}_b, \tilde{\nu}_{b+1}]$, and in each band and at each pressure and temperature the absorption coefficients from the line-by-line wavenumber grid are reordered according to strength in increasing order and divided into n_k subintervals with limits k_l and k_{l+1} with $l \in [1, n_k + 1]$, see Fig. 3.17. The k-coefficient for subinterval l is found by fitting transmissions for this subinterval to a single exponential $e^{k_\rho^{\mathrm{opt},l} u_j}$ over a set of n_u column densities, u_j, i.e.

$$\frac{1}{w_l} \int_{g_l}^{g_{l+1}} \mathrm{d}g_w \, e^{k_\rho(g_w) u_j} \approx e^{k_\rho^{\mathrm{opt},l} u_j}, \qquad w_l = \int_{g_l}^{g_{l+1}} \mathrm{d}g_w \tag{3.39}$$

where $k_\rho^{\mathrm{opt},l}$ is the optimal k-coefficient in subinterval l and g_l is the g-coordinate corresponding to the beginning of the subinterval for k-term l and g_{n_k+1} is the g-coordinate for the end of k-term n_k, see Fig. 3.17. In practice the integrals on the left-hand side of Eq. (3.39) are calculated by integrating over all wavenumbers contributing to the absorption in subinterval l line-by-line:

$$\int_{g_l}^{g_{l+1}} \mathrm{d}g_w \, e^{k_\rho(g_w) u_j} = \sum_i \Delta\tilde{\nu}_i w(\tilde{\nu}_{i+1/2}) e^{k_\rho(\tilde{\nu}_{i+1/2}) u_j}, \tag{3.40}$$

$$\int_{g_l}^{g_{l+1}} \mathrm{d}g_w = \sum_i \Delta\tilde{\nu}_i w(\tilde{\nu}_{i+1/2}), \tag{3.41}$$

where the sums are over all i satisfying $k(\tilde{\nu}_i) \in [k_l, k_{l+1}]$.

The spacing of the subintervals l, and consequently the number of k-coefficients in a band, must be the same for all P–T and would ideally be spaced logarithmically in k. Rather than using logarithmic k-intervals defined at a particular P–T point, an average absorption coefficient $k_{\rho,i}^{\mathrm{avg}}(\tilde{\nu})$ for species i is calculated from the top of the atmosphere down to an optical depth of one:

$$k_{\rho,i}^{\mathrm{avg}}(\tilde{\nu}) u_{\tau=1}^i = \int_{z_{\tau=1}}^{\infty} \mathrm{d}z' \, \zeta_i(z') \rho(z') k_{\rho,i}(\tilde{\nu}, z') \tag{3.42}$$

$$= \frac{1}{g} \int_0^{P_{\tau=1}} \mathrm{d}P' \, \zeta_i(P') k_{\rho,i}(\tilde{\nu}, P') \equiv 1, \tag{3.43}$$

where $\zeta_i(z)$ is the mass mixing ratio of species i, $u_{\tau=1,i}$ is the column density of species i down to $\tau = 1$ and hydrostatic equilibrium has been assumed. This is similar to the approach of

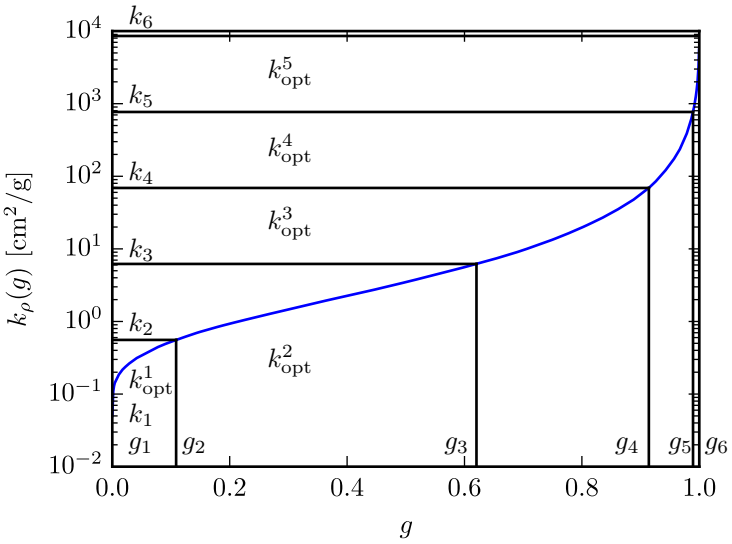

Figure 3.17: Same as Fig. 3.16. Lines illustrating the subdivision into $n_k = 5$ subintervals is shown. A k-coefficient is found for each subintervall using exponential sum fitting of transmissions (ESFT), Eq. (3.39).

Hogan (2010) and provides an optimal subdivision for the part of the spectrum that is most important in each layer: k-terms are subdivided at the P–T where the optical depth reaches one for each k-term, i.e. at large pressures for weak k-terms and small pressures for strong k-terms. We use an isothermal P–T profile at 1116 K, one of the temperatures in our P–T grid, for this calculation as a compromise between day- and night-side P–T profiles of hot Jupiters.

The number of k-coefficients in each band is determined by setting a tolerance on the total error in Eq. (3.39) for all column densities j and k-coefficients l using the average absorption coefficient $k_{\rho,\mathrm{avg}}(\tilde{\nu})$. The error for k-term l is defined as the root mean square (RMS) of the difference between the fitted exponential and exact LbL transmission for all column densities:

$$\epsilon_l = \sqrt{\frac{1}{n_u}\sum_{j=1}^{n_u}\left(\frac{1}{w_l}\int_{g_l}^{g_{l+1}} \mathrm{d}g_w\, e^{k_\rho(g_w)u_j} - e^{k_\rho^{\mathrm{opt},l}u_j}\right)^2}. \tag{3.44}$$

The total error in a band, ϵ, is defined as

$$\epsilon = \sqrt{\sum_{l=1}^{n_k} w_l \epsilon_l^2}, \tag{3.45}$$

A tolerance is set on the total error in a band, $\epsilon_{\max}$. The number of k-terms in a band is chosen to be the smallest satisfying the criterion $\epsilon < \epsilon_{\max}$ using the average absorption coefficients $k^i_{\rho,\mathrm{avg}}(\tilde{\nu})$ defined in Eq. (3.43). Having determined the number and placement of these subintervals, the fitting of optimal k-coefficients is repeated for each P–T. In the tests presented in Chapter 4 we use two values for $\epsilon_{\max}$: 5×10^{-3} and 1×10^{-4}, where $\epsilon_{\max} = 1 \times 10^{-4}$ is expected to reduce the error from the correlated-k method significantly.

The maximum column density over which k-coefficients are to be fitted must be determined.

The column density of species i is given by

$$u_i = \int_z^\infty \mathrm{d}z'\, \zeta_i(z')\rho(z') = \frac{1}{g}\int_0^P \mathrm{d}P'\, \zeta_i(P') = \frac{\zeta_i P}{g}, \tag{3.46}$$

where we have assumed a constant mass mixing ratio. We set the maximum column density using Eq. (3.46) with the maximum pressure and mixing ratio in our P–T table. In the ES radiation scheme, the mass mixing ratio used in Eq. (3.43) is calculated from the maximum column density using Eq. (3.46).

To obtain the total flux in band b, n_k pseudo-monochromatic calculations are performed, each yielding a flux F_l. The band-integrated flux is then given by

$$F_b = \sum_{l=1}^{n_k} w_l^* F_l. \tag{3.47}$$

The weight w_l^* for the thermal component should ideally be given by the Planck function evaluated at the local temperature. For simplicity, however, the weights w_l at the temperature where $\tau = 1$ in the calculation of k-coefficients are adopted, i.e. 1116 K in our case. For the stellar component, w_l^* is the stellar spectrum at the top of the atmosphere. We later compare these weighting schemes to a uniform weighting scheme and show that, using the bands adopted here, the exact weighting scheme does not affect fluxes and heating rates to a significant degree.

3.4.2 Mixture of gases with overlapping absorption

In order to include more than one absorbing species in the radiative transfer calculations, k-coefficients for gas mixtures must be calculated. Here, we consider three different methods for obtaining the absorption properties of gas mixtures: pre-mixing of gases, the random overlap method and equivalent extinction.

Pre-mixing of gases

An "effective" absorption coefficient is calculated by summing absorption coefficients for all absorbing species weighted by their relative abundance:

$$k_\rho^{\mathrm{eff}}(\tilde{\nu}, P, T) = \sum_{i=1}^{N_\mathrm{s}} k_{\rho,i}(\tilde{\nu}, P, T)\zeta_i(P, T), \tag{3.48}$$

where the sum is over all N_s species, and $k_{\rho,i}(\tilde{\nu}, P, T)$ and $\zeta_i(P, T)$ are the mass absorption coefficient and (equilibrium) mass mixing ratio of gas i at (P, T), respectively. The total absorption coefficient at a given (P, T) is then given by $k_\rho^{\mathrm{eff}}\rho$, where ρ is the total mass density. This approach has several advantages: it is fast, requiring only one set of k-coefficients for each temperature and pressure, and it is simple to implement. This technique is currently used by

Showman et al. (2009). It is not particularly flexible, however, as local abundances $\zeta_i(P,T)$ must be determined before the calculation of k-coefficients. In cases where the abundance of a particular species changes rapidly with either pressure or temperature, it also leads to increased errors since the product of absorption coefficients and mass mixing ratios are tabulated and then interpolated to the local pressure and temperature. We discuss this in more detail in Chapter 4.

Random overlap

The second method is the random overlap method, described in (Lacis & Oinas 1991). Assuming that the mass absorption coefficient of one gas a, $k_a(\tilde{\nu})$ is uncorrelated to that of a second gas b, $k_b(\tilde{\nu})$, the total transmission of the gas mixture over some column density (u_a, u_b) is given by a simple scalar product,

$$\mathcal{T}(u_a, u_b) = \mathcal{T}(u_a) \times \mathcal{T}(u_b). \tag{3.49}$$

The assumption of uncorrelation between the absorption coefficients of different gases is generally considered to be good, but may depend on the bands adopted and should be checked. Equation (3.49) can be derived by looking at the transmission integral:

$$\mathcal{T}(u_a, u_b) = \int_{\tilde{\nu}_1}^{\tilde{\nu}_2} \mathrm{d}\tilde{\nu}\, w(\tilde{\nu}) e^{-k_a(\tilde{\nu})u_a - k_b(\tilde{\nu})u_b} = \int_{\tilde{\nu}_1}^{\tilde{\nu}_2} \mathrm{d}\tilde{\nu}\, w(\tilde{\nu}) e^{-k_a(\tilde{\nu})u_a} e^{-k_b(\tilde{\nu})u_b}, \tag{3.50}$$

where we have for simplicity assumed that the medium is homogeneous. Let the operator E denote

$$E[f(\tilde{\nu})] = \int_{\tilde{\nu}_1}^{\tilde{\nu}_2} \mathrm{d}\tilde{\nu}\, w(\tilde{\nu}) f(\tilde{\nu}), \tag{3.51}$$

and $X_i = e^{k_i(\tilde{\nu})u_i}$, we then have

$$\mathcal{T}(u_a, u_b) = E[X_a X_b]. \tag{3.52}$$

If $k_a(\nu)$ and $k_b(\nu)$ are uncorrelated, X_a and X_b are too. The correlation coefficient is zero, and consequently the covariance $\sigma(X_a, X_b)$, defined by

$$\sigma(X_a, X_b) \equiv E[(X_a - E[X_a])(X_b - E[X_b])] = E[X_a X_b] - E[X_a]E[X_b], \tag{3.53}$$

is zero. Consequently $E[X_a X_b] = E[X_a]E[X_b]$.

The transmission through one layer is, using Eq. (3.49),

$$\mathcal{T}(u_a, u_b) = \int_{\tilde{\nu}_1}^{\tilde{\nu}_2} \mathrm{d}\tilde{\nu}\, w(\tilde{\nu}) e^{-k_a(\tilde{\nu})u_a} \times \int_{\tilde{\nu}_1}^{\tilde{\nu}_2} \mathrm{d}\tilde{\nu}'\, w(\tilde{\nu}) e^{-k_b(\tilde{\nu}')u_b} \tag{3.54}$$

$$\approx \sum_{l=1}^{n_{k,a}} \sum_{m=1}^{n_{k,b}} w_{a,l} w_{b,m} e^{-k_a^{\mathrm{opt},l} u_a - k_b^{\mathrm{opt},m} u_b} \tag{3.55}$$

Defining $u_{ab} = u_a + u_b$, we can write the above transmission as

$$\mathcal{T}(u_a, u_b) = \sum_{l=1}^{n_{k,a}} \sum_{m=1}^{n_{k,b}} w_{ab,lm} e^{-k_{ab}^{\mathrm{opt},lm} u_{ab}}, \tag{3.56}$$

where

$$k_{ab}^{\mathrm{opt},lm} = \frac{k_a^{\mathrm{opt},l} u_a + k_b^{\mathrm{opt},m} u_b}{u_a + u_b} = \frac{k_a^{\mathrm{opt},l} \zeta_a u + k_b^{\mathrm{opt},m} \zeta_b u}{\zeta_a u + \zeta_b u} = \frac{k_a^{\mathrm{opt},l} \zeta_a + k_b^{\mathrm{opt},m} \zeta_b}{\zeta_a + \zeta_b}, \tag{3.57}$$

and

$$w_{ab,lm} = w_{a,l} w_{b,m}. \tag{3.58}$$

Running $n_{k,a} n_{k,b}$ pseudo-monochromatic calculations using these k-coefficients, the flux can be calculated as normal using Eq. (3.47).

Note that the computation time increases by a factor of n_k for each added gas, which makes this method computationally expensive. Lacis & Oinas (1991) circumvent this by reordering the $k_{ab}^{\mathrm{opt},lm}$-coefficients and resampling them to obtain the original $n_{k,a}$ k-coefficients. This approach is much more flexible than the pre-mixing of gases as gas abundances can be manipulated on-the-fly. In the ES scheme the random overlap method is implemented without reordering and resampling.

Equivalent extinction

The ES scheme uses equivalent extinction to treat gaseous overlap (Edwards 1996). It utilizes the fact that in most bands there is a primary absorber, and additional minor absorbers are included as grey processes in bands. The theoretical foundation of equivalent extinction is discussed in Appendix A.3, here we describe the results.

In each layer an equivalent absorption or extinction $\bar{K}$ is calculated for each minor gas, which for the thermal component is given by

$$\bar{K} = \frac{\sum_{l=1}^{n_k} w_l K_l F_{\mathrm{v},l}}{\sum_{l=1}^{n_k} w_l F_{\mathrm{v},l}}, \tag{3.59}$$

where K_l are the k-coefficients of the minor gas in the layer with corresponding weights w_l, and $F_{\mathrm{v},l}$ is the thermal flux in the layer including only absorption by k-term K_l. Pseudo-monochromatic calculations are performed for all n_k k-coefficients of the major gas in a band with all other minor absorbers included by using the equivalent grey absorption $\bar{K}$. This effectively reduces the number of pseudo-monochromatic calculations to one per k-coefficient per gas.

The direct component of the stellar flux is readily included by calculating the transmission for each gas separately and then taking the product since, assuming random overlap, direct transmissions are multiplicative. For the diffuse stellar beam, which will be non-zero if Rayleigh-

scattering is included, the equivalent extinction is calculated using

$$\bar{K} \approx \frac{\sum_{l=1}^{n_k} w_l K_l F_{\mathrm{s}*,l}}{\sum_{l=1}^{n_k} w_l F_{\mathrm{s}*,l}}, \tag{3.60}$$

$F_{\mathrm{s}*,l}$ is the direct flux at the lower boundary including only k-term l. The use of $F_{\mathrm{s}*,l}$ is not ideal for hot Jupiter atmospheres as the direct stellar flux at the bottom boundary may be zero. In this case the ES scheme uses the smallest k-coefficient for the minor gas, though this is expected to be less accurate than to use the full expression in Eq. (3.60). In this work the main stellar radiation is contained in the direct beam, however, and Eq. (3.60) should be sufficient for the results presented here. This issue will have to be revisited when significant scattering is introduced for the stellar component of the radiation.

Equivalent extinction is currently used by default in the ES radiation scheme, and we test it for hot Jupiter atmospheres in Chapter 4 and adopt in our GCM simulations presented in Chapters 5 and 6. Equivalent extinction has not been compared to the random overlap method including reordering and resampling. It is therefore unclear which is better in terms of speed and accuracy.

3.5 Band-averaged absorption coefficients

Band-averaged absorption coefficients have been applied in exoplanet GCMs (Dobbs-Dixon & Agol 2013) and stellar/substellar atmosphere radiation hydrodynamical models (see e.g Freytag et al. 2010). In Dobbs-Dixon & Agol (2013), an average absorption coefficient is calculated in each band as

$$\bar{k}_b = \frac{\int_{\tilde{\nu}_b}^{\tilde{\nu}_{b+1}} \mathrm{d}\tilde{\nu}\, w(\tilde{\nu}) k_\rho(\tilde{\nu})}{\int_{\tilde{\nu}_b}^{\tilde{\nu}_{b+1}} \mathrm{d}\tilde{\nu}\, w(\tilde{\nu})}, \tag{3.61}$$

where $\tilde{\nu}_b$ is the lower bound of bin b. The upper bound of the last band is defined as $\tilde{\nu}_{n_\mathrm{b}+1}$, where n_b is the number of bands. The fluxes F_b are obtained by performing n_b pseudo-monochromatic calculations, the total flux being the sum of the individual fluxes in each band. In Dobbs-Dixon & Agol (2013), the weighting function $w(\tilde{\nu})$ is a black-body spectrum evaluated at the local temperature for the thermal component, i.e. $\bar{k}_b$ is the Planck mean in each band, known to be applicable in the optically thin limit. The stellar spectrum at the top of the atmosphere is used as the weight for the stellar component. The bands were selected as in Showman et al. (2009), see Table 4.2.

Improved schemes utilising mean absorption coefficients exist, but we limit our discussion to the approach used by Dobbs-Dixon & Agol (2013) and compare its accuracy to a full correlated-k treatment. For this purpose, we show in Chapter 4 results obtained with band-averaged absorption coefficients designed to replicate the treatment used in Dobbs-Dixon & Agol (2013).

Element (i)	$\log N_X/N_H + 12$
C	8.50
N	7.86
O	8.76
Na	6.24
K	5.11
Si	7.51
Ti	4.95
V	3.93

Table 3.5: Our adopted solar-like elemental abundances (Asplund et al. 2009). N_i is the number density of element i and N_H is the number density of hydrogen.

3.6 Abundances

Here we discuss the chemical equilibrium abundance calculations we adopt in the UM. We use solar-like elemental abundances from Asplund et al. (2009), see Table 3.5.

3.6.1 H_2 and He

We assume the gas to be ideal. H_2 and He partial pressures are calculated by assuming the atmosphere to be pure hydrogen and helium with atomic hydrogen and helium number fractions of $A_H = 0.91183$ and $A_{He} = 1 - A_H$, respectively. This is a reasonable assumption as the abundances of higher mass elements are much smaller than that of hydrogen (see Table 3.5). Assuming all hydrogen atoms are bound in molecular hydrogen, H_2, we have

$$N_{H_2} = \frac{A_H/2}{A_H/2 + A_{He}} N_{tot}, \tag{3.62}$$

$$N_{He} = \frac{A_{He}}{A_H/2 + A_{He}} N_{tot}, \tag{3.63}$$

where N_i is the number density of element i and N_{tot} is the total number density of particles. The mean molecular weight is then given by:

$$\bar{m} = \frac{A_H/2}{A_H/2 + A_{He}} m_{H_2} + \frac{A_{He}}{A_H/2 + A_{He}} m_{He} \approx 2.3376\,\mathrm{g/mol}, \tag{3.64}$$

where m_z is the mean weight of species z.

3.6.2 CO, CH_4, H_2O, N_2 and NH_3

Abundances of CO, CH_4, H_2O, N_2 and NH_3 are calculated using the analytical formulas given in the appendix of Burrows & Sharp (1999). They are derived by making the following assumptions: (i) temperatures are below about 2500 K, (ii) dissociation of H_2 can be neglected and (iii) the composition ratios are approximately solar with $N_O > N_C + N_{Si}$.

Table 3.6: Constants used in Eq. (3.71) to calculate equilibrium abundances of CO, CH_4, H_2O, N_2 and NH_3.

	$i = 1$	$i = 2$
a_i	$1.106\,131 \times 10^6$	$8.164\,13 \times 10^5$
b_i	-5.6895×10^4	-2.9109×10^4
c_i	62.565	58.5878
d_i	$-5.813\,96 \times 10^{-4}$	-7.8284×10^{-4}
e_i	$2.346\,515 \times 10^{-8}$	$4.729\,048 \times 10^{-8}$

Defining

$$A'_i = \frac{N_i}{N_{\rm H}}, \qquad\qquad B_z = \frac{P_z}{P_{\rm H_2}}, \tag{3.65}$$

where P_z is the partial pressure of molecule z, the partial pressures as a function of temperature T are given by

$$B_{\rm CO} = A'_{\rm C} + A'_{\rm O} + \frac{P^2_{\rm H_2}}{2K_1(T)} - \sqrt{\left[A'_{\rm C} + A'_{\rm O} + \frac{P^2_{\rm H_2}}{2K_1(T)}\right]^2 - 4A'_{\rm C}A'_{\rm O}}, \tag{3.66}$$

$$B_{\rm CH_4} = 2A'_{\rm C} - B_{\rm CO}, \tag{3.67}$$

$$B_{\rm H_2O} = 2A'_{\rm O} - B_{\rm CO}, \tag{3.68}$$

and

$$B_{\rm N_2} = A'_{\rm N} + \frac{P^2_{\rm H_2}}{8K_2(T)} - \sqrt{\left[A'_{\rm N} + \frac{P^2_{\rm H_2}}{8K_2(T)}\right]^2 - 4A'^2_{\rm N}}, \tag{3.69}$$

$$B_{\rm NH_3} = 2\left(A'_{\rm N} - B_{\rm N_2}\right). \tag{3.70}$$

The equilibrium constants are given by

$$K_i(T) = \exp\left[\left(a_i/T + b_i + c_iT + d_iT^2 + e_iT^3\right)/RT\right], \tag{3.71}$$

where the constants $a_i, b_i, \ldots, e_i$ are given in Table 3.6 and R is the ideal gas constant in units of cal/(K mol).

The effective number of available oxygen atoms $N'_{\rm O}$ is slightly reduced because of the removal of oxygen by condensates, mainly those of silicon and magnesium, at low temperatures. For $T < 1500\,{\rm K}$ the abundance of available oxygen atoms is approximated as

$$N'_{\rm O} = N_{\rm O} - x_{\rm Si}N_{\rm Si}, \tag{3.72}$$

where $x_{\rm Si}$ is the number of oxygen atoms removed per silicon atom. According to Burrows & Sharp (1999) $x_{\rm Si} = 3.28$, and $N_{\rm O}$ is consequently replaced by $N'_{\rm O}$ in Eq. (3.65).

The partial pressure of H_2 is calculated using Eq. (3.62):

$$P_{H_2} = \frac{N_{H_2}}{N_{tot}} P = \frac{A_H/2}{A_H/2 + A_{He}} P, \tag{3.73}$$

where P is the total pressure of the gas.

3.6.3 TiO, VO, Na, K: Parametrisation

For TiO and VO we use a simple parametrisation scheme to prescribe their abundances. Ti and V are thought to sequester deeper than 10^6 Pa to 10^7 Pa, while at low temperatures Ti and V will be bound to condensates (Fortney et al. 2006b; Showman et al. 2009). We therefore parametrise the abundance of TiO and VO by assuming no absorbing TiO and VO to be present in the atmosphere for temperatures below T_{crit} or pressures above P_{crit}. For temperatures above T_{crit} and pressures below P_{crit}, however, we assume TiO and VO to be present, with partial pressures estimated by assuming all Ti bound in TiO and similarly all V bound in VO. This is a reasonable assumption since the abundances of both Ti and V are much smaller than that of oxygen, see Table 3.5. TiO and VO will therefore have a negligible effect on the availability of oxygen in the atmosphere.

We use $T_{crit} = 1500\,\mathrm{K}$, $P_{crit} = 10^7\,\mathrm{Pa}$ for the tests in Chapter 4. Later in Chapter 6 we modified these values to be in better agreement with the condensation curves shown in Burrows & Sharp (1999), and use $T_{crit}^{TiO} = 1800\,\mathrm{K}$, $T_{crit}^{VO} = 1600\,\mathrm{K}$ while leaving $P_{crit}^{TiO} = P_{crit}^{VO} = 10^7\,\mathrm{Pa}$.

For sodium and potassium, which we include in Chapters 5 and 6, we use a similar parametrisation, but do not include a critical pressure. We choose $T_{crit}^{Na} = 1000\,\mathrm{K}$ and $T_{crit}^{K} = 1100\,\mathrm{K}$, in agreement with the chemical transformation curves in Burrows & Sharp (1999) and abundance profiles in Sharp & Burrows (2007).

3.7 Summary and conclusions

In this chapter we have discussed the calculation of absorption coefficients from high temperature molecular line lists suitable for H_2 and He dominated atmospheres. Our main results are:

- High temperature line lists are crucial in order to correctly capture absorption in hot Jupiter atmospheres.
- H_2 and He pressure broadening parameters obtained using van der Waals broadening theory significantly overestimates line widths.
- We adopt pressure broadening parameters from the literature, which are obtained mainly from experiments at room temperature and pressure. Significant extrapolation is necessary in order to apply these line widths to hot Jupiter-like conditions, and the validity of these extrapolations are highly uncertain. We are currently setting up a collaboration

with the ExoMol group at University College London (UCL) and V.E. Zuev Institute of Atmospheric Optics in Tomsk, Russia to improve the pressure broadened line widths.

- High temperature line lists are extremely large, and this can cause absorption coefficient calculations to become very computationally expensive. We presented a line profile cut-off scheme that decreases the computation time required to calculate absorption coefficients by a factor of ~ 100 compared to other methods used in the literature, while still giving accurate results.

A method for reducing the wavenumber resolution of absorption coefficients is needed to apply the tabulated opacities in GCMs. The correlated-k method is widely used for this, and we presented the implementation of the correlated-k method in the ES radiation scheme. We also briefly discussed the chemical equilibrium abundances adopted in this work.

Chapter 4

Accuracy tests of radiation schemes used in hot Jupiter global circulation models

In this chapter we investigate the accuracy of the ES radiation scheme by applying it to several different scenarios designed to test a range of physical conditions representative of hot Jupiters. In addition to testing the two-stream approximation and correlated-k method as implemented in the ES scheme, we perform calculations using band-averaged opacities, which has recently been used in a GCM applied to the hot Jupiter HD 189733b (Dobbs-Dixon & Agol 2013).

Due to the large uncertainties related to the sources of scattering in hot Jupiter atmospheres and the complexity it adds to radiation transport, we limit the discussions here to purely absorbing atmospheres and postpone the inclusion of scattering to future work. The exception is the very last test where we include Rayleigh scattering by H_2 and He. A gravitational acceleration of $9.42\,\mathrm{m/s^2}$ is used, suitable for HD 209458b. Unless otherwise stated, k-coefficients were calculated using $\epsilon_{\mathrm{max}} = 5 \times 10^{-3}$, a Planckian weighting scheme for the thermal component and a solar spectrum for the stellar component are used unless stated otherwise, see Section 3.4.

The atmospheric domain extends from $10^{-1}\,\mathrm{Pa}$ to $10^{8}\,\mathrm{Pa}$, and we use 100 pressure points on a logarithmic scale. We have tested the convergence of the solution as a function of the number of pressure levels and found that only 50 layers is sufficient for the solution to have converged. To ease comparison between the different two-stream approximations (Section 2.2.8) and opacity treatments (Sections 3.4 and 4.3.3) we introduce the L^1 norm,

$$
\begin{aligned}
L^1 &= \int_{\log_{10} P_{\mathrm{min}}}^{\log_{10} P_{\mathrm{max}}} (\mathrm{d}\log_{10} P) \left[\frac{|\mathcal{H}_{\mathtt{ATMO}}|}{\int_{\log_{10} P_{\mathrm{min}}}^{\log_{10} P_{\mathrm{max}}} (\mathrm{d}\log_{10} P)\ |\mathcal{H}_{\mathtt{ATMO}}|} \times \frac{|\mathcal{H}_{\mathrm{ES}} - \mathcal{H}_{\mathtt{ATMO}}|}{|\mathcal{H}_{\mathtt{ATMO}}|} \right] \\
&= \frac{\int_{\log_{10} P_{\mathrm{min}}}^{\log_{10} P_{\mathrm{max}}} (\mathrm{d}\log_{10} P)\ |\mathcal{H}_{\mathrm{ES}} - \mathcal{H}_{\mathtt{ATMO}}|}{\int_{\log_{10} P_{\mathrm{min}}}^{\log_{10} P_{\mathrm{max}}} (\mathrm{d}\log_{10} P)\ |\mathcal{H}_{\mathtt{ATMO}}|},
\end{aligned}
\tag{4.1}
$$

given here for the heating rate, where $\mathcal{H}_{\mathrm{ES}}$ and $\mathcal{H}_{\texttt{ATMO}}$ are the heating rates from the ES radiation scheme and `ATMO`, respectively. P_{min} and P_{max} are the minimum and maximum pressures in our calculations, respectively. This is a convenient measure to use when comparing errors between different two-stream approximations and opacity treatments, and represents the relative error of some quantity, in this case the heating rate, weighted by the current value of that quantity integrated over all pressures.

We begin by briefly summarising changes we have made to the ES radiation scheme and describing the line-by-line (LbL) discrete ordinate (DO) code `ATMO` we use for comparison. In Section 4.2 we present some simple initial tests of both the ES scheme and `ATMO` for an isothermal atmosphere without irradiation and gradually increase the complexity of the absorption.

In Section 4.3.1 we study the accuracy of the radiation scheme when applied to a typical hot Jupiter night side and include absorption by CO, CH_4, H_2O, NH_3, H_2–H_2 and H_2–He CIA. Different methods for computing k-coefficients for gas mixtures, as discussed in Section 3.4.2, are compared. Next, in Section 4.3.2 we use a P–T profile typical for a hot Jupiter day side and also include irradiation and absorption by TiO and VO in the upper atmosphere. In the final test in this section we include Rayleigh scattering by H_2 and He. We finish by discussing the average opacity scheme used by Dobbs-Dixon & Agol (2013) in more detail in Section 4.3.3.

The results presented here are an expansion of the work published in Amundsen et al. (2014).

4.1 Radiation codes

In this section we briefly discuss the radiation codes used in this chapter. We discuss the changes made to the ES radiation scheme and introduce our benchmark line-by-line discrete ordinate code `ATMO` used for comparison.

4.1.1 The Edwards–Slingo (ES) radiation scheme

The ES radiation scheme solves the two-stream equations (Edwards 1996; Zdunkowski & Korb 1985; Zdunkowski et al. 1982, 1980) to obtain fluxes and heating rates as described in Sections 2.2.7 and 2.3. For the opacities the ES radiation scheme uses a combination of the exponential sum fitting of transmissions (ESFT) technique (Wiscombe & Evans 1977) and the correlated-k method (Goody et al. 1989; Lacis & Oinas 1991) to obtain k-coefficients, which we have described in Section 3.4. Maximum column densities used when fitting k-coefficients, calculated as described in Section 3.4 using Eq. (3.46), are provided in Table 4.1. k-coefficients are tabulated in spectral files, one for the thermal and one for the stellar component, which are used as input to the flux and heating rate calculations. For use with equivalent extinction described in Section 3.4.2 absorbers are sorted in each band according to importance using the column densities in Table 4.1. Note that we do not include Na and K absorption in these tests, but we do not expect the results to change significantly when including additional absorbers.

Molecule	$u_{\max}$ [kg/m^2]
H_2O	6.7×10^4
CO	5.8×10^4
CH_4	3.3×10^4
NH_3	8.8×10^3
Na	3.1×10^2
K	3.9×10^1
TiO	44
VO	4.4
H_2	7.7×10^6
He	3.0×10^6

Table 4.1: Maximum column densities used when fitting k-coefficients. To calculate these the maximum possible abundance for each absorber was used throughout the atmosphere as described in Section 3.4.

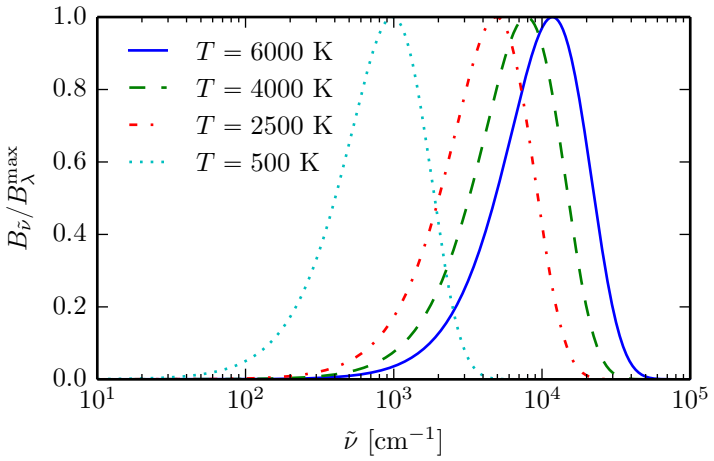

Figure 4.1: Planck functions for objects with different temperatures normalised by their maximum value. The overlap between planet and star temperatures is significant, consequently we include all bands in both the thermal and stellar components of the radiation.

Our opacity bands are very similar to those used by Showman et al. (2009), and we list them in Table 4.2. Three small modifications have been made compared to the bands listed in Showman et al. (2009): (i) The upper limit of band 30 has been reduced from 38 314 cm^{-1} to 28 000 cm^{-1} to reduce the memory usage of our correlated-k code, (ii) Band 31 has been added to capture absorption up to the small wavelength limit of our line lists, and (iii) Band 32 has been added to capture most of the stellar flux at small wavelengths.

Planet temperatures are usually between about 500 K to 2500 K (Showman et al. 2009), with star temperatures between about 4000 K to 6000 K[1]. We have in Fig. 4.1 plotted the Planck functions for objects with effective temperatures of 500 K, 2500 K, 4000 K and 6000 K. The overlap is significant, and we therefore choose to include all bands in both the thermal and stellar components.

We describe the main changes made to the ES radiation scheme below.

[1] `http://exoplanets.org/`

Band	$\tilde{\nu}_{\rm min}$ [cm^{-1}]	$\tilde{\nu}_{\rm max}$ [cm^{-1}]	Available absorber data
1	31	217	H_2O, NH_3, CH_4, CO, TiO, H_2-H_2, H_2-He
2	217	500	H_2O, NH_3, CH_4, CO, TiO, H_2-H_2, H_2-He
3	500	962	H_2O, NH_3, CH_4, TiO, H_2-H_2, H_2-He
4	962	1550	H_2O, NH_3, CH_4, CO, TiO, H_2-H_2, H_2-He
5	1550	1916	H_2O, NH_3, CH_4, CO, TiO, H_2-H_2, H_2-He
6	1916	2273	H_2O, NH_3, CH_4, CO, TiO, H_2-H_2, H_2-He
7	2273	2632	H_2O, NH_3, CH_4, CO, TiO, H_2-H_2, H_2-He
8	2632	3041	H_2O, NH_3, CH_4, CO, TiO, H_2-H_2, H_2-He
9	3041	3346	H_2O, NH_3, CH_4, CO, TiO, H_2-H_2, H_2-He
10	3346	3992	H_2O, NH_3, CH_4, CO, TiO, VO, H_2-H_2, H_2-He
11	3992	4608	H_2O, NH_3, CH_4, CO, K, TiO, VO, H_2-H_2, H_2-He
12	4608	4950	H_2O, NH_3, CH_4, CO, K, TiO, VO, H_2-H_2, H_2-He
13	4950	5627	H_2O, NH_3, CH_4, CO, Na, K, TiO, VO, H_2-H_2, H_2-He
14	5627	6277	H_2O, NH_3, CH_4, CO, Na, K, TiO, VO, H_2-H_2, H_2-He
15	6277	6680	H_2O, NH_3, CH_4, CO, Na, K, TiO, VO, H_2-H_2, H_2-He
16	6680	7519	H_2O, NH_3, CH_4, Na, K, TiO, VO, H_2-H_2, H_2-He
17	7519	8354	H_2O, NH_3, CH_4, CO, Na, K, TiO, VO, H_2-H_2, H_2-He
18	8354	9091	H_2O, NH_3, CH_4*, CO, Na, K, TiO, VO, H_2-H_2, H_2-He
19	9091	9950	H_2O, NH_3, CH_4*, Na, K, TiO, VO, H_2-H_2, H_2-He
20	9950	10 417	H_2O, NH_3, CH_4*, Na, K, TiO, VO, H_2-H_2, H_2-He
21	10 417	10 989	H_2O, NH_3, CH_4*, Na, K, TiO, VO, H_2-He
22	10 989	11 628	H_2O, NH_3, CH_4*, Na, K, TiO, VO, H_2-He
23	11 628	12 739	H_2O, NH_3, CH_4*, Na, K, TiO, VO, H_2-He
24	12 739	13 423	H_2O, Na, K, TiO, VO, H_2-He
25	13 423	14 815	H_2O, Na, K, TiO, VO, H_2-He
26	14 815	16 340	H_2O, Na, K, TiO, VO, H_2-He
27	16 340	17 483	H_2O, Na, K, TiO, VO, H_2-He
28	17 483	20 202	H_2O, Na, K, TiO, VO, H_2-He
29	20 202	25 000	H_2O, Na, K, TiO, VO
30	25 000	28 000	H_2O, Na, K, TiO, VO
31	28 000	31 761	H_2O, Na, K, TiO
32	31 761	50 000	Na, K

Table 4.2: Bands used for the correlated-k method. They are almost identical to the bands in Showman et al. (2009), the differences are explained in the text. Sodium and potassium are not included in the tests presented in this chapter. *The STDS line list (Wenger & Champion 1998) is used in this chapter and does not include CH_4 absorption in these bands. The ExoMol YT10to10 line list (Yurchenko & Tennyson 2014) is adopted in Chapters 5 and 6 and does include absorption by CH_4 in these bands.

Format of LbL opacity files: We do not use the ES radiation scheme to calculate line-by-line (LbL) opacities from line lists, but tabulate LbL opacities using our own code optimised for high temperature line lists and using pressure broadening by H_2 and He as described in Chapter 3. Previously the format of the LbL opacity files in the ES radiation scheme included a division of both wavenumber and absorption coefficients into the bands used when calculating k-coefficients. This is not desirable as we would like to have the possibility of adjusting band limits without changing the LbL opacity files. We modified the format of the LbL opacity files to not include any information about bands to make it compatible with the opacity files we calculate from high temperature line lists.

Read LbL opacities in band-by-band: Previously all absorption coefficients for all P, T and $\tilde{\nu}$ were kept in memory throughout the calculation of k-coefficients in the ES radiation scheme. Due to our large $(P, T, \tilde{\nu})$ grid this would require an unreasonable amount of computer memory. We modified the correlated-k code to read the LbL opacity files band-by-band, drastically reducing the required computer memory.

Look-up table for band-integrated Planck functions: The band-integrated Planck function evaluated at the local temperature is required for the thermal component of the radiation scheme. In the original version of the ES scheme a polynomial was fitted to the band-integrated Planck function as a function of temperature, this was then used when solving the radiative transfer equation. For the Earth the required temperature range is quite small and a polynomial fit is reasonably accurate. Our absorption coefficients are tabulated from 70 K to 3000 K, and we would like the polynomial fit to be valid on a similar range. At low temperatures the Planck function will generally be much smaller than at high temperatures, which may cause the polynomial fit to oscillate between positive and negative values at low temperatures. For this reason we have implemented the option to use a look-up table of band-integrated Planck functions to circumvent this problem.

The Planck function is given by Eq. (2.4):

$$B_{\tilde{\nu}}(T)\,\mathrm{d}\tilde{\nu} = \frac{2hc^2\tilde{\nu}^3}{e^{hc\tilde{\nu}/k_\mathrm{B}T} - 1}\,\mathrm{d}\tilde{\nu}, \tag{4.2}$$

which we integrate numerically over each band. Depending on the temperature, the required wavenumber resolution needed to integrate $B_{\tilde{\nu}}(T)$ accurately may vary. For purposes of numerical integration it is therefore convenient to introduce a dimensionless integration variable. We introduce

$$x = \frac{hc}{k_\mathrm{B}T}\tilde{\nu} \qquad \Rightarrow \qquad \tilde{\nu} = \frac{k_\mathrm{B}T}{hc}x, \qquad \mathrm{d}\tilde{\nu} = \frac{k_\mathrm{B}T}{hc}\mathrm{d}x, \tag{4.3}$$

which yields

$$B_x(T)\,\mathrm{d}x = \frac{2k_\mathrm{B}^4T^4}{h^3c^2}\frac{x^4}{e^x-1}\,\mathrm{d}x. \tag{4.4}$$

The band-integrated Planck function is therefore given by

$$\int_{x_b}^{x_{b+1}} B_x(T)\,\mathrm{d}x = \frac{2k_\mathrm{B}^4T^4}{h^3c^2}\int_{x_b}^{x_{b+1}}\frac{x^4}{e^x-1}\,\mathrm{d}x, \tag{4.5}$$

i.e. the integral is independent of T and can easily be integrated numerically for varying T with a fixed resolution in x. Note that the integral limits x_b and x_{b+1} do have a temperature dependence. The numerical integration is performed using Simpsons rule, we use $\Delta x = 1\times10^{-4}$. The tabulated band-integrated Planck-function is included in the spectral file for the thermal component.

Rayleigh scattering by H_2 and He: Rayleigh scattering by a H_2- and He-dominated atmosphere has been added to the ES radiation scheme. The Rayleigh scattering coefficient is given by Eq. (2.27). The index of refraction less unity, $m_r - 1$, is proportional to the mass density as long as the composition does not change. We can therefore write Eq. (2.27) as

$$\sigma_\rho^\mathrm{RAY} = \frac{8\pi^3(m_\mathrm{r,STP}^2-1)^2\rho^2/\rho_\mathrm{STP}^2}{3\lambda^4}\frac{\bar{m}}{N_\mathrm{A}\rho^2}f(\rho_n) = \frac{8\pi^3(m_\mathrm{r,STP}^2-1)^2}{3\lambda^4}\frac{\bar{m}}{N_\mathrm{A}\rho_\mathrm{STP}^2}f(\rho_n), \tag{4.6}$$

where $m_\mathrm{r,STP}$ and ρ_STP are the refractive index and mass density at standard temperature and pressure (STP). σ_ρ^RAY is therefore independent of density, and the band-integrated scattering coefficient weighted by the stellar spectrum is tabulated in the stellar spectral file.

The correction factor $f(\rho_n)$ applied to take into account the anisotropy of the scattering particles is given by Eq. (2.24). For air $\rho_n \approx 0.035$, which yields $f(\rho_n) \approx 1.06$. For H_2 and He, ρ_n has been measured to 0.0221 and 0.025, respectively (Penndorf 1957). We adopt $\rho_n = 0.02$ for simplicity, which yields $f(\rho_n) \approx 1.03$.

We use refractive indices for H_2 from Leonard (1974) and He from Mansfield & Peck (1969)[2]. The H_2 data is provided in tabular form, we use linear interpolation to obtain the index of refraction for an arbitrary wavelength, and use the value at the extreme values for wavelengths outside the tabulated range. The He refractive index is approximated by a simple formula,

$$n_\mathrm{He}(\lambda) = 1 + \frac{0.01470091}{423.98-\lambda^{-2}}, \qquad [\lambda] = \mu\mathrm{m}. \tag{4.7}$$

There are several formulas for calculating the index of refraction of a mixture, we use one of the most widely applicable, the Lorentz–Lorentz relation (Heller 1965):

$$\frac{n_{12}^2-1}{n_{12}^2+2} = \phi_1\frac{n_1^2-1}{n_1^2+2} + \phi_2\frac{n_2^2-1}{n_2^2+2}, \tag{4.8}$$

[2]Data downloaded from `http://refractiveindex.info/`.

where n_1, n_2 and n_{12} are the refractive indices of gas 1, 2 and the mixture, respectively, and ϕ_i is the volume fraction of gas i in the mixture. Since we have assumed that the gas is ideal, ϕ_i is equal to the number fraction of species i, see Section 3.6.1. Note that Eq. (4.8) reduces to the simpler and more intuitive form

$$n_{12} = \phi_1 n_1 + \phi_2 n_2 \tag{4.9}$$

assuming volume additivity and using $n_{12} \to n_1$ and $n_2 \to n_1$ (Heller 1965). Rayleigh scattering is not included in the below tests unless stated otherwise, but we do include it in Chapters 5 and 6.

4.1.2 `ATMO`

`ATMO` is a 1D radiative convective equilibrium code written by Pascal Tremblin and Wolfgang Hayek. It can be used both to calculate fluxes and heating rates for a given P–T profile and to derive radiative and convective equilibrium P–T profiles for a given effective temperature, gravity and irradiation. It follows the method of the MARCS code (for a description, see Gustafsson et al. 2008), with some modifications.

The 1D plane-parallel radiative transfer equation is solved using the discrete ordinates method (see e.g. Thomas & Stamnes 2002), i.e. solving the radiative transfer equation for discrete ray directions μ_i, which are selected according to Gauss-Legendre quadrature. The angular dependence of the intensity is therefore properly resolved in contrast to the two-stream approximation where only two directions are used. We use 16 rays, and we have checked the convergence by using up to 32 rays.

To treat opacities it can both use line-by-line or the correlated-k method. In this chapter we use its line-by-line mode in order to investigate the accuracy of the correlated-k method as implemented in the Edwards–Slingo radiation scheme. The code has been parallelised to facilitate a high wavenumber resolution. By successively increasing the resolution, we found that a resolution of about $\sim 10^{-3}\,\mathrm{cm}^{-1}$ was necessary for the solution to have converged, i.e. about 5×10^7 wavenumber points. In contrast we use a few hundred pseudo-monochromatic calculations in the ES scheme, illustrating the large gain in computational efficiency achieved by using the correlated-k method.

For further discussion of `ATMO`, see Tremblin et al. (2015).

4.2 Isothermal atmosphere

Here we perform tests with an isothermal atmosphere at a temperature $T_\mathrm{c} = 1500\,\mathrm{K}$. In Section 4.2.1 we describe a test where analytical solutions to both the two-stream approximated and the full radiative transfer equations exist. A grey opacity is used to eliminate errors from the correlated-k method, and we use this scenario to test both the accuracy of the numerical solvers and the two-stream approximation in isolation. Next we gradually add complexity

in the opacity by considering only H_2–H_2 collision induced (continuum) absorption (CIA) in Section 4.2.2, minimising the error caused by the correlated-k method, and only water absorption in Section 4.2.3.

4.2.1 With grey opacity

This test is based on a grey atmosphere without scattering and irradiation at the top of the atmosphere, and a lower boundary that emits as a perfect black body at a temperature T_c. To facilitate analytical treatment, we make an additional assumption: the lower boundary is located at a constant optical depth $\tau = \tau^*$. This is done in both the ES radiation scheme and `ATMO` by explicitly keeping the total mass absorption coefficient, k_ρ, constant as a function of pressure and placing the lower boundary at a constant pressure.

Analytical solutions

Analytical solutions to the two-stream approximated and full radiative transfer equations are available and provided below. The analytical solutions are compared to the numerical solutions obtained by the ES radiation scheme and to the discrete ordinate solution from `ATMO`.

The two-stream approximation: The two-stream approximated radiative transfer equation for the thermal component, ignoring scattering, is given by Eq. (2.105) with $a = 0$. Integrating Eq. (2.105) with respect to wavenumber yields

$$\pm \frac{1}{D}\frac{\mathrm{d}F^{\pm}(\tau)}{\mathrm{d}\tau} = F^{\pm}(\tau) - \sigma T_c^4, \tag{4.10}$$

where Stefan-Boltzmann's law has been used. The above equation is a simple inhomogeneous linear first order differential equation in optical depth, τ, and can be solved using traditional techniques. The homogeneous solution, i.e. ignoring the Planck emission, is given by

$$F_h^{\pm}(\tau) = A_{\pm} e^{\pm D\tau}, \tag{4.11}$$

where $A_\pm$ is determined by boundary conditions, while the particular solution in this case is given by

$$F_p^{\pm}(\tau) = \sigma T_c^4, \tag{4.12}$$

which yields the complete solution

$$F^{\pm}(\tau) = F_h^{\pm}(\tau) + F_p^{\pm}(\tau) = A_{\pm} e^{\pm D\tau} + \sigma T_c^4. \tag{4.13}$$

At the upper boundary, i.e. $\tau = 0$, we have

$$F^{-}(\tau = 0) = A_{-} + \sigma T_c^4 = 0 \quad \Rightarrow \quad A_{-} = -\sigma T_c^4. \tag{4.14}$$

At the lower boundary, which we place at an optical depth of $\tau = \tau^*$, we have

$$F^+(\tau = \tau^*) = A_+ e^{D\tau^*} + \sigma T_c^4 = \sigma T_c^4 \quad \Rightarrow \quad A_+ = 0. \tag{4.15}$$

The upwelling, downwelling and total fluxes are therefore

$$F^+(\tau) = \sigma T_c^4, \tag{4.16}$$
$$F^-(\tau) = \sigma T_c^4 \left[1 - e^{-D\tau}\right], \tag{4.17}$$
$$F(\tau) = F^+(\tau) - F^-(\tau) = \sigma T_c^4 e^{-D\tau}. \tag{4.18}$$

Using Eq. (2.47) and assuming hydrostatic equilibrium, the optical depth can be related to the pressure by

$$\tau(\tilde{\nu}, P) = \frac{1}{g}\int_0^P \mathrm{d}P'\, k_\rho(\tilde{\nu}, P') = \frac{k_\rho}{g} P, \tag{4.19}$$

since $k_\rho(\tilde{\nu}, P) = k_\rho$ is assumed to be independent of both wavenumber $\tilde{\nu}$ and pressure P. The heating rate is given by Eq. (2.39), and using Eq. (4.19) we get

$$\begin{aligned}\mathcal{H} &= -\frac{\mathrm{d}F}{\mathrm{d}z} = k_\rho \rho \frac{\mathrm{d}F}{\mathrm{d}\tau} = \frac{k_\rho P \bar{m}}{RT}\frac{\mathrm{d}F}{\mathrm{d}\tau} = -\frac{k_\rho P \bar{m} D}{RT}\sigma T_c^4 e^{-D\tau} \\ &= -\frac{k_\rho P \bar{m} D}{RT}\sigma T_c^4 e^{-Dk_\rho P/g}.\end{aligned} \tag{4.20}$$

The angular dependent radiative transfer equation: The full angular dependent (but still azimuthally averaged) radiative transfer equation without scattering and irradiation is given by Eq. (2.48) with $a = 0$,

$$u\frac{\mathrm{d}I_{\tilde{\nu}}(\tau, u)}{\mathrm{d}\tau} = I_{\tilde{\nu}}(\tau, u) - B_{\tilde{\nu}}(T_c), \tag{4.21}$$

where $u = \cos\theta$. From above, the general solution is given by

$$I_{\tilde{\nu}}(\tau, u) = A_{\tilde{\nu}}(u) e^{\tau/u} + B_{\tilde{\nu}}(T_c). \tag{4.22}$$

Note that a discrete ordinate method gives the same equation and solution, except u is replaced by the quadrature points u_i. No downward radiation at the upper boundary implies $I_{\tilde{\nu}}(\tau = 0, u < 0) = 0$, which yields

$$I_{\tilde{\nu}}(\tau, u < 0) = B_{\tilde{\nu}}(T_c)\left[1 - e^{\tau/u}\right]. \tag{4.23}$$

Perfect black-body radiation in the upward direction at the lower boundary implies $I_{\tilde{\nu}}(\tau = \tau^*, u > 0) = B_{\tilde{\nu}}(T_c)$, which yields

$$I_{\tilde{\nu}}(\tau, u > 0) = B_{\tilde{\nu}}(T_c). \tag{4.24}$$

Note that $I_{\tilde{\nu}}(\tau, u)$ is anisotropic in the downward direction except in the limit of high optical depths, $\tau \to \infty$. The intensity at a given optical depth in the downward direction, $u < 0$, is dictated by the amount of atmosphere above it emitting thermally in the direction of the radiation. The "effective optical depth" or optical path in the direction of the radiation is higher for smaller values of $\bar{\mu}$, and the intensity consequently cannot be isotropic. The exception is at high optical depths, where the atmosphere becomes optically thick in all directions.

The upward flux is

$$F^+_{\tilde{\nu}}(\tau) = 2\pi \int_0^1 \mathrm{d}\mu\, \mu I_{\tilde{\nu}}(\tau, \mu) = 2\pi B_{\tilde{\nu}}(T_\mathrm{c}) \int_0^1 \mathrm{d}\mu\, \mu = \pi B_{\tilde{\nu}}(T_\mathrm{c}), \tag{4.25}$$

while the downward flux is

$$F^-_{\tilde{\nu}}(\tau) = 2\pi \int_0^1 \mathrm{d}\mu\, \mu I_{\tilde{\nu}}(\tau, -\mu) = 2\pi B_{\tilde{\nu}}(T_\mathrm{c}) \int_0^1 \mathrm{d}\mu\, \mu \left[1 - e^{-\tau/\mu}\right] \tag{4.26}$$

$$= \pi B_{\tilde{\nu}}(T_\mathrm{c}) - 2\pi B(T_\mathrm{c}) \int_0^1 \mathrm{d}\mu\, \mu e^{-\tau/\mu}. \tag{4.27}$$

This integral does not have a simple closed-form solution, but can be found numerically. Integrating over all wavenumbers and using Stefan-Boltzmann's law, the total flux is given by

$$F(\tau) = F^+(\tau) - F^-(\tau) = 2\sigma T_\mathrm{c}^4 \int_0^1 \mathrm{d}\mu\, \mu e^{-\tau/\mu}, \tag{4.28}$$

i.e. dictated by this integral and clearly not equivalent to Eq. (4.18). Note that the two-stream approximation effectively evaluates the integral in Eq. (4.28) using a single quaderature point $\bar{\mu} = 1/D$ which can be chosen using e.g. Gauss–Legendre quadrature or an empirical fit. The heating rate, Eq. (2.37), is similarly given by

$$\mathcal{H} = \frac{k_\rho P \bar{m}}{RT} \frac{\mathrm{d}F}{\mathrm{d}\tau} = \frac{2k_\rho P \bar{m}}{RT} \sigma T_\mathrm{c}^4 \int_0^1 \mathrm{d}\mu\, \mu \frac{\mathrm{d}}{\mathrm{d}\tau} \left[e^{-\tau/\mu}\right] \tag{4.29}$$

$$= -\frac{2k_\rho P \bar{m}}{RT} \sigma T_\mathrm{c}^4 \int_0^1 \mathrm{d}\mu\, e^{-\tau/\mu}. \tag{4.30}$$

Accuracy of the two-stream approximation

Fluxes and heating rates with errors are plotted in Figs. 4.2 and 4.3 using the solutions in Eqs. (4.18), (4.20), (4.28) and (4.30). At small optical depths, the flux is equal to the black-body flux while at large optical depths, the flux is zero, as expected. The heating rate is zero at both low and high optical depths, while at intermediate optical depths the atmosphere is cooled (the heating rate is negative). Interestingly, the relative error in both flux and heating rate approaches unity at large optical depths, a consequence of the two-stream solutions approaching zero faster than the full solution. We do not consider this as a problem, however, as it has a negligible impact on the atmospheric heat budget.

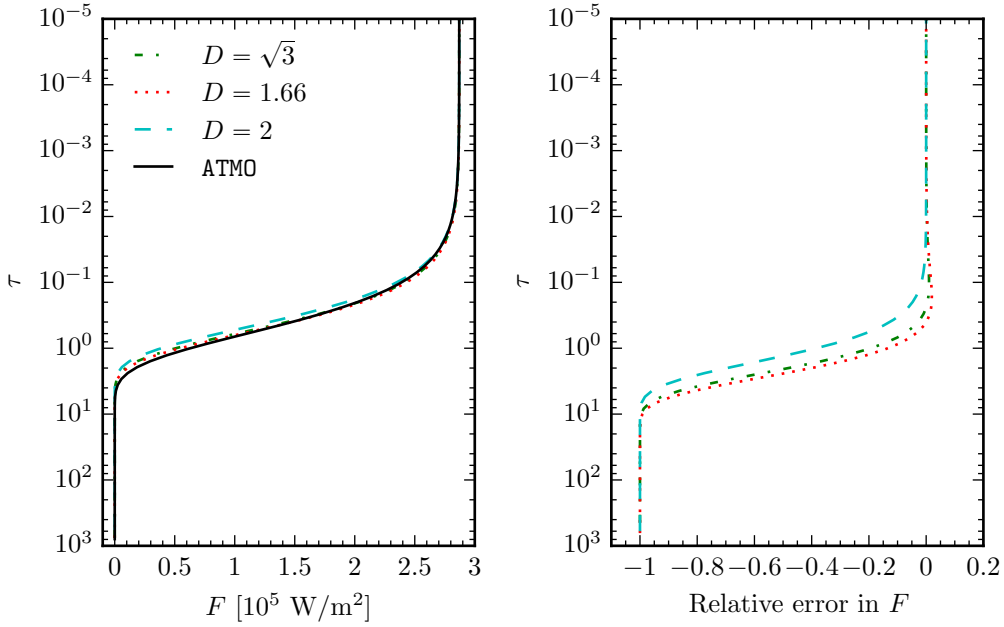

Figure 4.2: The left-hand panel shows the fluxes obtained using the two-stream flux in Eq. (4.18) and exact flux in Eq. (4.28) obtained with $D = \sqrt{3}$ (dotted, red), $D = 1.66$ (dashed-dotted, green), $D = 2$ (dashed, cyan) and solving the fully angular dependent radiative transfer equation (solid, black). The right-hand panel shows the calculated relative errors in the two-stream fluxes. Relative errors become unreasonably large only where the flux is very small.

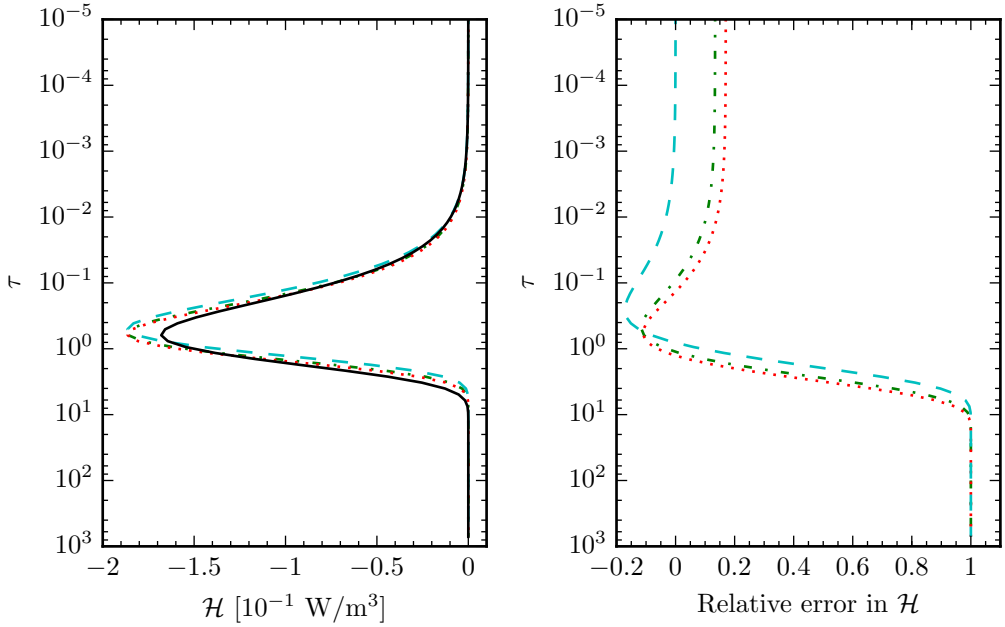

Figure 4.3: Same as Fig. 4.2 for heating rates. Relative errors become unreasonably large only where the heating rate is very small.

Table 4.3: Computed flux (F) and heating rate ($\mathcal{H}$) L^1 norms using the analytical solutions in Section 4.2.1 shown in Figs. 4.2 and 4.3 thereby eliminating the errors from the numerical solution schemes. The smallest errors are obtained with $D = 1.66$.

	L^1, F	L^1, $\mathcal{H}$
$D = \sqrt{3}$	0.007	0.103
$D = 1.66$	0.006	0.094
$D = 2$	0.015	0.174

Table 4.4: Computed flux (F) and heating rate ($\mathcal{H}$) L^1 norms from Fig. 4.4 comparing the numerical and analytical solutions to check the accuracy of the numerical schemes.

	L^1, F	L^1, $\mathcal{H}$
ES radiation scheme	3.88×10^{-5}	3.55×10^{-3}
`ATMO`	6.20×10^{-4}	1.22×10^{-3}

In Table 4.3 we show the calculated L^1 norms using the analytical solutions derived above. The smallest errors are achieved with $D = 1.66$, but using $D = \sqrt{3}$ only yields slightly larger errors. This is verified by looking at the relative error in Figs. 4.2 and 4.3.

It is worth noting that the different values for D yield different convergence towards zero heating rate at low optical depths, evident in the right-hand panel of Fig. 4.3, caused by the factor D in Eq. (4.20). Comparing Eqs. (4.20) and (4.30), it is clear that only $D = 2$ will yield the correct behaviour of the heating rate at low optical depths. The effect on the heating rate itself is small, however, and $D = 1.66$ yields the most correct heating rate overall.

Accuracy of the numerical scheme

We use the analytical expressions in Eqs. (4.18), (4.20), (4.28) and (4.30) to estimate the errors in the numerical solution schemes in both the ES radiation scheme and `ATMO`. We show the numerical error in Fig. 4.4 as a function of optical depth, and the L^1 errors are provided in Table 4.4. The errors are small for small optical depths, while at large optical depths the errors increase significantly. The error in the flux and heating rate reach 10 % at about $\tau = 10$ and $\tau = 4$, respectively, for the ES radiation scheme, while `ATMO` is accurate to a somewhat larger optical depth. The L^1 errors reflects this, keeping in mind that the error in `ATMO` is also caused by a finite number of rays in the Gaussian quadrature, which may become important at the accuracy level of the numerical solver. Both numerical schemes are seen to yield errors significantly smaller than errors caused by the two-stream approximation. This confirms that both numerical solvers yield satisfactory accuracy.

4.2.2 Only H_2–H_2 CIA

We proceed by introducing a frequency dependent absorption coefficient. Since the frequency dependence of molecular absorption is quite complicated we start by including only H_2–H_2 CIA, which has a slowly varying absorption coefficient with frequency. This will help minimise errors caused by the correlated-k method. We compare the numerical solutions obtained with the ES

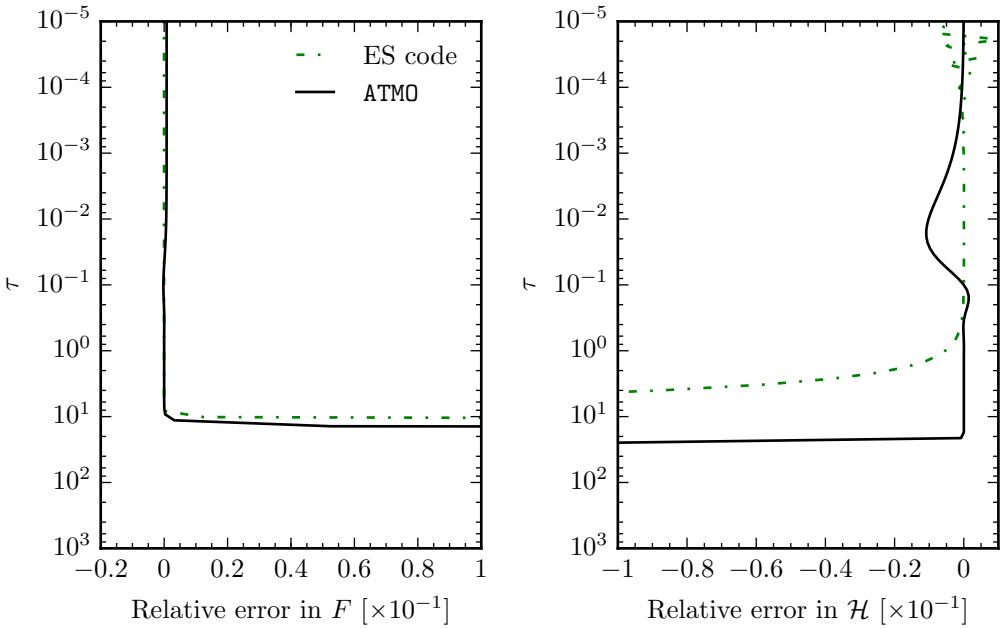

Figure 4.4: Relative error in the numerical solutions from the ES radiation scheme (dashed-dotted, green) and `ATMO` (solid, black) calculated using the analytical solution in Eqs. (4.18), (4.20), (4.28) and (4.30). Relative numerical errors become large at large optical depths, caused by both fluxes and heating rates approaching zero.

radiation scheme and `ATMO`, and errors are calculated assuming the line-by-line discrete ordinate solution from `ATMO` is correct.

Fluxes and heating rates obtained with $\epsilon_{\max} = 5 \times 10^{-3}$ (default), $\epsilon_{\max} = 1 \times 10^{-4}$ and with band-averaged absorption coefficients are shown in the left-hand panels of Figs. 4.5 and 4.6, all with $D = 1.66$. As in Section 4.2.1 with a grey opacity the flux approaches the black-body flux at small optical depths, but it does not approach 0 in the optically thick limit. The reason for this is that H_2-H_2 CIA data is only available between $20\,\mathrm{cm}^{-1}$ and $10\,000\,\mathrm{cm}^{-1}$, i.e. only emission and absorption from this spectral region will be included from the atmosphere. Consequently the downward flux at large optical depths will be a black-body flux inside this spectral range and zero otherwise. The lower surface emits as a black-body at 1500 K, causing the upward flux to be the black-body flux for all wavenumbers. The downward flux at large optical depths is consequently slightly smaller than the upward flux, causing the total flux to become non-zero.

The right-hand panels of Figs. 4.5 and 4.6 show the relative error in fluxes and heating rates, respectively. Both fluxes and heating rates agree fairly well irrespective of the choice of opacity precision, relative errors stay below about 20 %. Some numerical noise is evident in the relative error of the heating rate at small pressures, but looking at the absolute values of $\mathcal{H}$ the noise does not become unreasonably large. As in Section 4.2.1 with a grey opacity the heating rate approaches 0 at high optical depths causing the relative error to become large. We do not consider this as a problem, however, as it has a negligible impact on the atmospheric

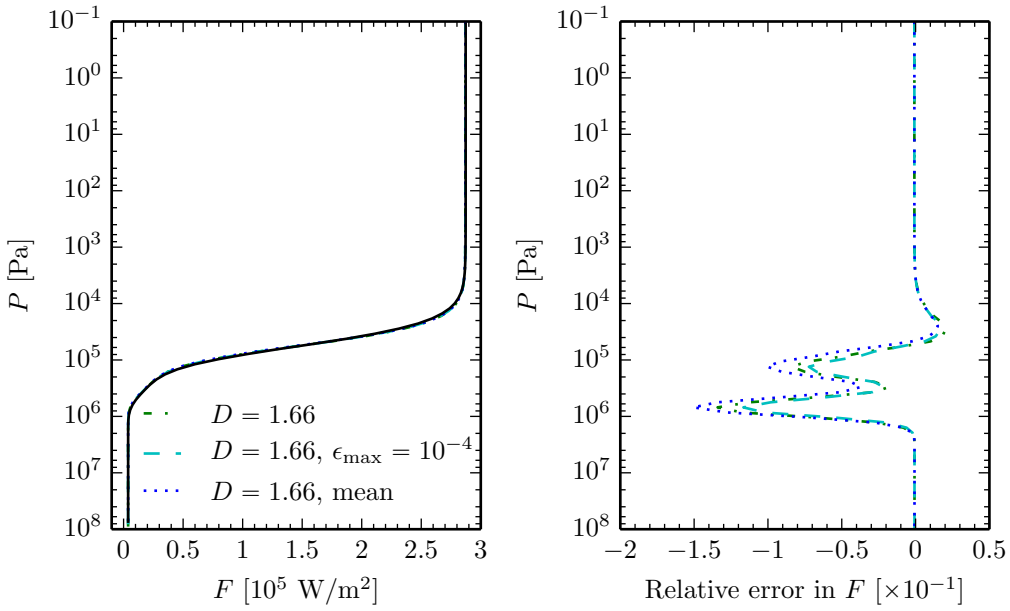

Figure 4.5: The left-hand panel shows the fluxes obtained with ES radiation scheme using $D = 1.66$ and $\epsilon_{\max} = 5 \times 10^{-3}$ (dashed-dotted, green), $\epsilon_{\max} = 10^{-4}$ (dashed, cyan), and mean absorption coefficients (dotted, blue), for an isothermal atmosphere with only H_2–H_2 CIA. The `ATMO` LbL DO result is also shown in this panel (solid, black) and is used to calculate the relative errors shown in the right-hand panel. Relative errors stay below 15 % throughout the atmosphere irrespective of the choice of k-coefficients.

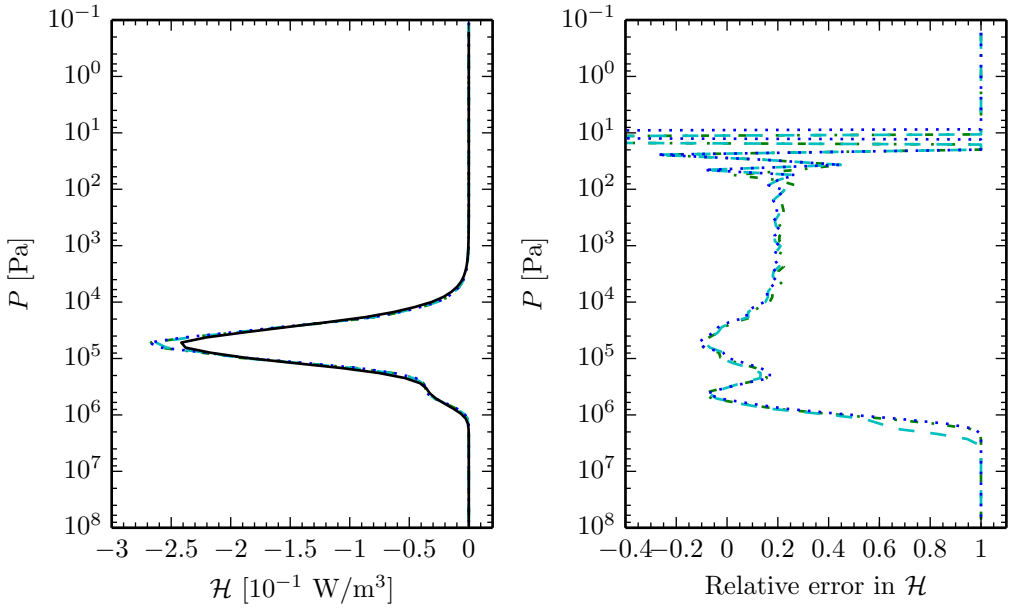

Figure 4.6: Same as Fig. 4.5, but for heating rates. Relative errors stay below about 20 % throughout the atmosphere.

	Flux	Heating rate
$D = \sqrt{3}$	0.004	0.076
$D = 1.66$	0.004	0.074
$D = 2$	0.007	0.118
$D = 1.66$, $\epsilon_{\max} = 10^{-4}$	0.003	0.061
$D = 1.66$, UW	0.004	0.073
$D = 1.66$, mean	0.004	0.075

Table 4.5: Computed L^1 norms for an isothermal atmosphere including only H_2–H_2 CIA (Section 4.2.2), the last two rows correspond to a uniform weighting scheme (UW) and band-averaged (mean) absorption coefficients, respectively. The smallest errors are obtained with $D = 1.66$. Only minor differences are seen for the various k-coefficients used due to the slowly varying H_2–H_2 CIA with wavenumber. Consequently errors are mainly caused by the two-stream approximation.

heat budget as mentioned above and reflected by the L^1 norms in Table 4.5.

Table 4.5 also includes results for diffusivities $D = \sqrt{3}$ and 2, and a uniform weighting (UW) scheme. The smallest errors are obtained with $D = 1.66$ or $\sqrt{3}$, while the weighting scheme used does not affect the error significantly. Decreasing the tolerance from $\epsilon_{\max} = 5 \times 10^{-3}$ to $\epsilon_{\max} = 1 \times 10^{-4}$ does not have a large effect on the error. This is caused by the smooth wavenumber dependence of H_2–H_2 CIA. $\epsilon_{\max} = 5 \times 10^{-3}$ yields approximately $n_k = 1$ k-coefficient in each band, while for $\epsilon_{\max} = 1 \times 10^{-4}$ $n_k \sim 10$. The remaining error is consequently mostly due to the two-stream approximation. This is also the reason why the band-averaged (mean) opacity yields similarly small errors.

4.2.3 Only water absorption

This test includes only absorption by H_2O, otherwise it is identical to the tests in Sections 4.2.1 and 4.2.2. A constant mass mixing ratio of 3.3477×10^{-3} is adopted, which corresponds to the smallest mass mixing ratio predicted by Eq. (3.68). Adopting $\epsilon_{\max} = 5 \times 10^{-3}$ and $\epsilon_{\max} = 10^{-4}$ yield ~ 10 and ~ 100 k-coefficients in each band, respectively. Note, however, that the number of k-coefficients can vary significantly between different bands.

Figures 4.7 and 4.8 show the fluxes and heating rates, respectively, with corresponding relative errors. Since the atmosphere is isothermal, the upward flux is again the Planck flux throughout the atmosphere. At the upper boundary the downward flux is 0, while at the lower boundary it is the Planck flux due to the high optical depth. Since the H_2O line list extends to 30 000 cm, much larger wavenumbers than H_2–H_2 CIA in Section 4.2.2, the total flux is approximately zero at large optical depths, while at small optical depths the planet radiates as a black body, as expected. The heating rate peaks at a pressure of $\sim 10^4$ Pa. Errors in fluxes and heating rates generally stay below about 10 % at pressures where the heating is significant, while using $\epsilon_{\max} = 10^{-4}$ yields considerably more accurate results. Table 4.6 shows L^1 errors, indicating that $D = 1.66$ and $\sqrt{3}$ yield the most accurate results. There is no significant difference between a Planckian and a uniform weighting (UW) scheme.

Using mean absorption coefficients yield very inaccurate fluxes and heating rates (see Figs. 4.7 and 4.8, and Table 4.6). The flux is underestimated at all pressures, while the heating rate peak occurs at pressures about two orders of magnitude smaller than the peak of the LbL DO result.

Table 4.6: Computed flux (F) and heating rate ($\mathcal{H}$) L^1 norms for an isothermal atmosphere including only water absorption (Section 4.2.3). The most accurate fluxes and heating rates are obtained with $D = 1.66$ and $\sqrt{3}$. Decreasing $\epsilon_{\max}$ from 5×10^{-3} to 1×10^{-4} is seen to improve the accuracy significantly.

	L^1, F	L^1, $\mathcal{H}$
$D = \sqrt{3}$	0.007	0.044
$D = 1.66$	0.007	0.046
$D = 2$	0.013	0.063
$D = 1.66$, $\epsilon_{\max} = 10^{-4}$	0.004	0.021
$D = 1.66$, UW	0.007	0.044
$D = 1.66$, mean	0.227	0.837

The fact that one k-coefficient per band is not sufficient to resolve the opacity is reflected by the need for ~ 10 k-coefficients in each band to achieve a tolerance of $\epsilon_{\max} = 5 \times 10^{-3}$ for H_2O. The failure of this method is discussed in more detail in Section 4.3.3.

4.3 Hot Jupiter-like atmospheres

We next consider conditions representative of a real hot Jupiter atmosphere. We use the polynomial fits to the night and day side P–T profiles of HD 209458b from Heng et al. (2011), which are based on a P–T profile from Iro et al. (2005), with the smoothing described in Mayne et al. (2014a). These profiles are in agreement with P–T profiles found in the literature (Baraffe et al. 2008; Showman et al. 2009). The lower boundary emits as a black body with $T_{\rm lb} = T(P_{\rm lb})$, where $T_{\rm lb}$ and $P_{\rm lb}$ are the temperature and pressure at the lower boundary, respectively.

As discussed in Section 3.4.2, k-coefficients for a gas mixture may be obtained by calculating k-coefficients from an effective absorption coefficient for the gas mixture (pre-mixing), the random overlap method or equivalent extinction. Up until now there has been no difference between these three schemes as we have only included one absorber and the mass mixing ratio has been kept constant. Here we we investigate the difference between these three schemes, but will for the main tests of the two-stream approximation and correlated-k method use pre-mixed k-coefficients as this was the approach used by Showman et al. (2009).

4.3.1 Night side of HD 209458b

We show the night side P–T profile from Mayne et al. (2014a) in Fig. 4.9. The temperature varies from about 400 K in the upper atmosphere to above 1600 K at 10^8 Pa, consistent with the literature (see e.g. Fig. 6 in Showman et al. (2009) and Fig. 7 in Baraffe et al. (2008)). Irradiation at the upper boundary is not included as this is a night side profile. We first include only water absorption, and then extend to a mixture of gases using all schemes for treating gaseous overlap described in Section 3.4.2.

Only water absorption

We begin by including only absorption by water, but the abundance is allowed to vary according to Eq. (3.68). For brevity we consider only $D = 1.66$ and $\epsilon_{\max} = 5 \times 10^{-3}$ in this section.

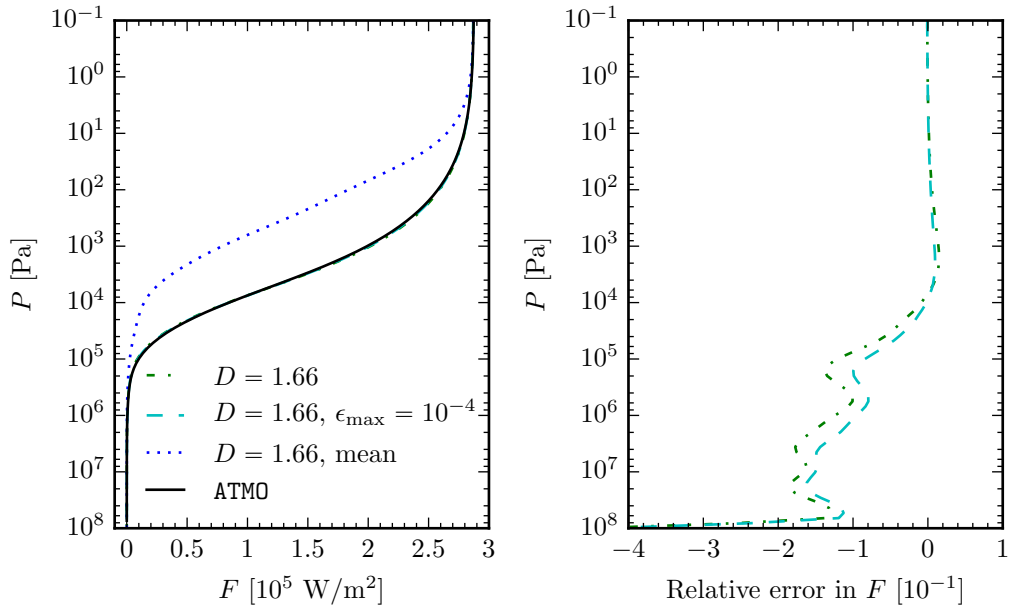

Figure 4.7: The left-hand panel shows the fluxes obtained with ES radiation scheme using $D = 1.66$ and $\epsilon_{\max} = 5 \times 10^{-3}$ (dashed-dotted, green), $\epsilon_{\max} = 10^{-4}$ (dashed, cyan), and mean absorption coefficients (dotted, blue), for an isothermal atmosphere with pure H_2O absorption. The ATMO LbL DO result is also shown in this panel (solid, black) and is used to calculate the relative errors shown in the right-hand panel (except for the mean absorption coefficient case since errors are too large). Relative errors stay below 30 % throughout the atmosphere.

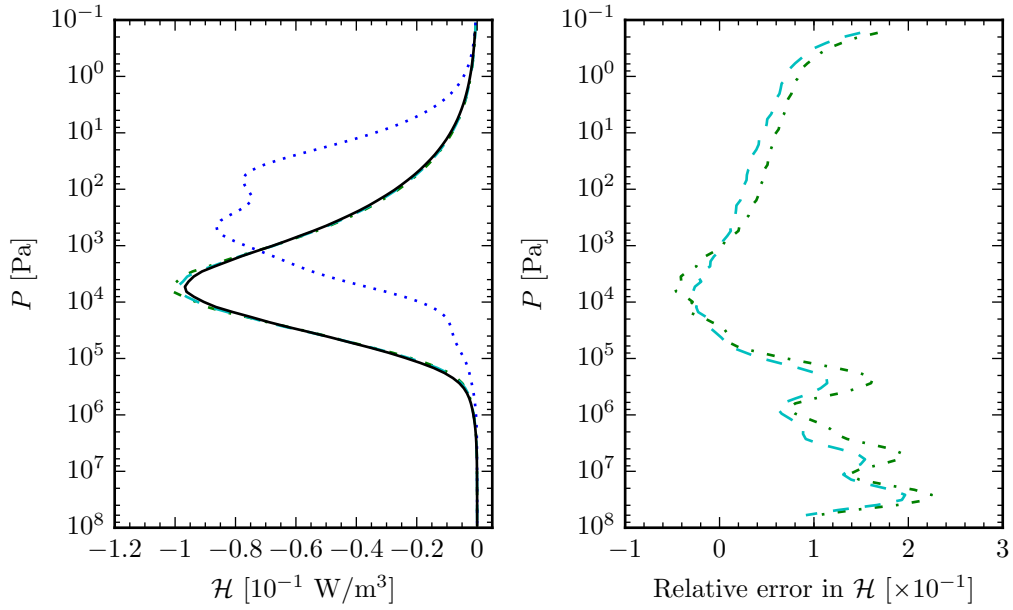

Figure 4.8: Same as Fig. 4.7, but for heating rates. Relative errors stay below 30 % throughout the atmosphere. Note that in the region where the heating rate (magnitude) is large, the error remains small.

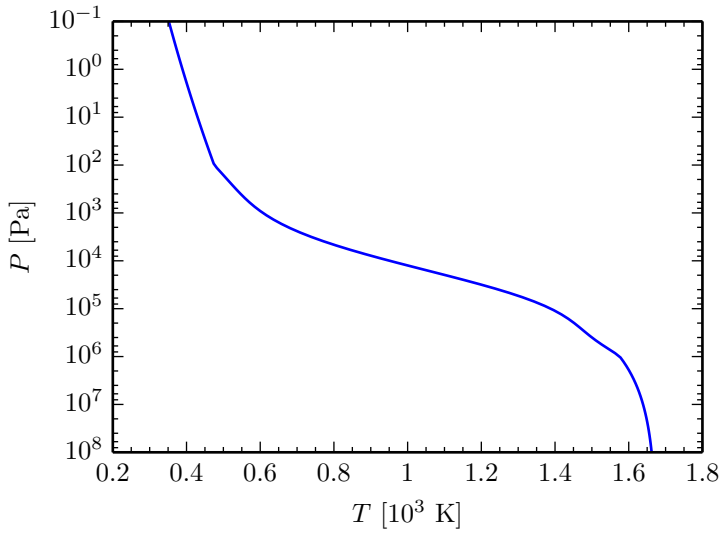

Figure 4.9: The P–T profile used in Section 4.3.1. From the polynomial fit (Heng et al. 2011) to the night side profile of HD 209458b from Iro et al. (2005) with the smoothing described in Mayne et al. (2014a).

Fluxes and heating rates calculated by the ES radiation scheme are shown in Fig. 4.10 both for pre-mixed k-coefficients and those obtained using the random overlap (RO) method. The difference between the two schemes is small, but non-zero, and to explain this we plot the temperature dependence of $B_{\mathrm{H_2O}}$ in Fig. 4.11 at 1 bar using Eq. (3.68) at the same resolution as in our opacity files. The sharp transition in water abundance may not be well represented in the pre-mixed case as the product of the opacity and mass mixing ratio is interpolated. In the random overlap case only the opacity is interpolated, while the mass mixing ratio is calculated using Eq. (3.68) at the local pressure and temperature, causing the rapid transition to be represented more accurately.

To verify that this is indeed the problem we replace the water abundance curve in Fig. 4.11 with a linearly decreasing function in temperature from the maximum to the minimum abundance over the whole temperature interval, and show the result in Fig. 4.12. The resulting difference between the two is vanishingly small, clearly showing that the discrepancies seen in Fig. 4.10 are caused by the rapid transition in the mass mixing ratio in temperature. We will revisit this issue when including absorption by many gases.

Precomputed mixture

Next we include absorption by CO, CH_4, H_2O, NH_3, H_2–H_2 and H_2–He CIA, with abundances as described in Section 3.6. Fluxes and heating rates are calculated from effective pre-mixed k-coefficients in the ES radiation scheme and compared to equivalent LbL DO results from `ATMO` obtained with an effective LbL pre-mixed opacity table. We plot fluxes and heating rates with relative errors in Figs. 4.13 and 4.14, with L^1 errors given in Table 4.7, from which it is clear that $D = 1.66$ yields the most accurate fluxes and heating rates overall. The results are similar to those obtained in Section 4.2.3. Note that calculations with mean absorption coefficients in

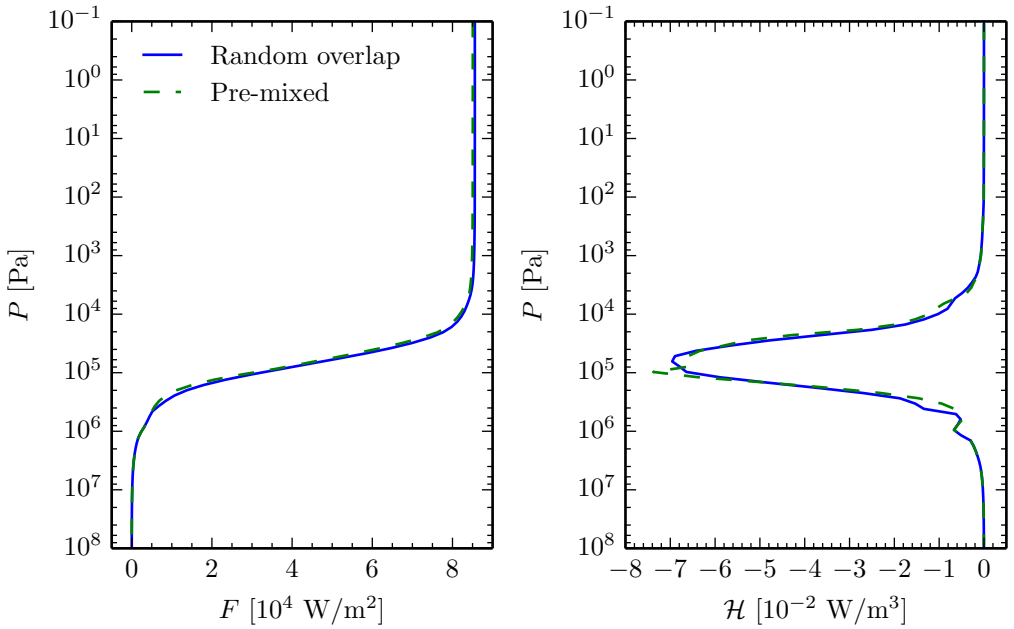

Figure 4.10: Fluxes (left) and heating rates (right) obtained using the ES radiation scheme including only water absorption for both pre-mixed k-coefficients (interpolation of product of opacity and mixing ratio) and using the random overlap method (interpolation of opacity only).

	L^1, F	L^1, $\mathcal{H}$
$D = \sqrt{3}$	0.065	0.096
$D = 1.66$	0.043	0.080
$D = 2$	0.133	0.173
$D = 1.66$, $\epsilon_{\max} = 10^{-4}$	0.012	0.070
$D = 1.66$, UW	0.031	0.081
$D = 1.66$, mean	0.700	0.926

Table 4.7: Computed flux (F) and heating rate ($\mathcal{H}$) L^1 norms for the night side of HD 209458b in Section 4.3.1 (Figs. 4.13 and 4.14), showing that the most accurate fluxes and heating rates are obtained with $D = 1.66$.

each band significantly underestimates the flux and result in heating rate peaks with the wrong amplitude.

Random overlap method and equivalent extinction

We now compare the results obtained with pre-mixed opacities to using the random overlap (RO) method and equivalent extinction (EE) to calculate k-coefficients for the mixture. We restrict the discussion to $D = 1.66$, $\epsilon_{\max} = 5 \times 10^{-3}$ for brevity, results will be representable for other choices as well. Fluxes and heating rates, with corresponding relative errors calculated assuming the RO result is exact, are shown in Figs. 4.15 and 4.16, respectively. There are significant differences between the three schemes, the discrepancies between RO and pre-mixed k-coefficients being mainly caused by rapid abundance transitions not captured properly by the temperature resolution of our opacity tables.

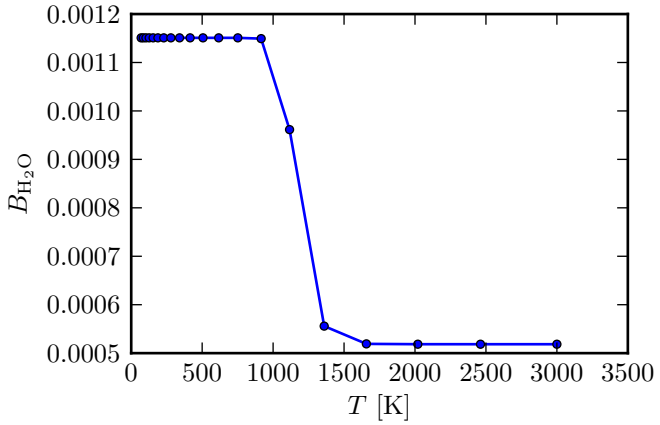

Figure 4.11: Temperature dependence of the water abundance B_{H_2O} using Eq. (3.68) at 1 bar. The transition between the two plateaus is sharp and not well resolved with only 20 temperature points as we have in our effective opacity table.

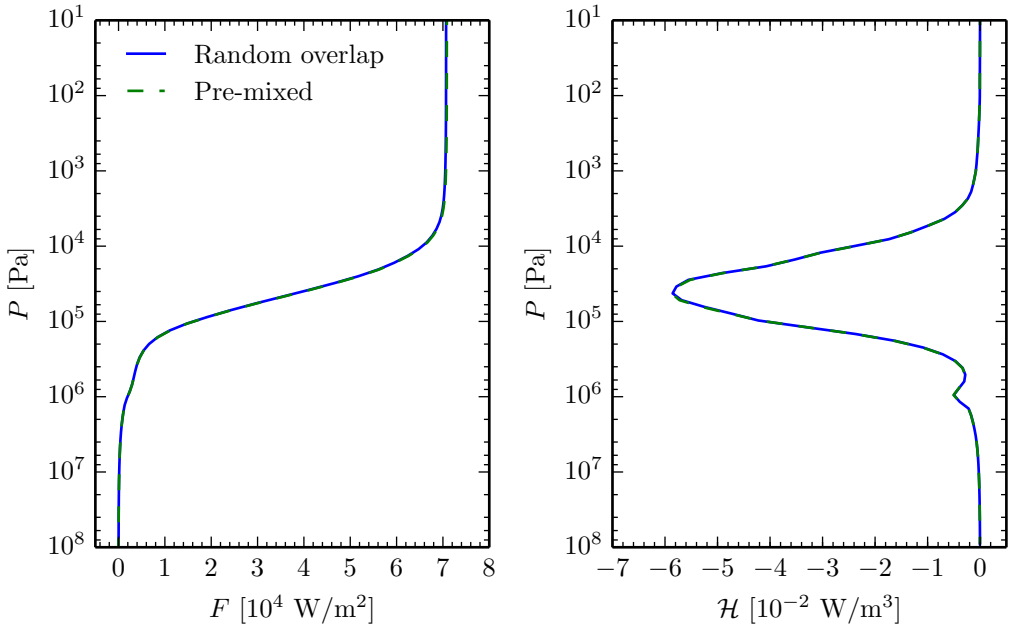

Figure 4.12: Fluxes (left) and heating rates (right) obtained using the ES radiation scheme including only water absorption for both pre-mixed k-coefficients (interpolation of product of opacity and mixing ratio) and using the random overlap method (interpolation of opacity only). The water abundance has been forced to decrease linearly with increasing temperature, removing the difference between the mixing schemes seen in Fig. 4.10.

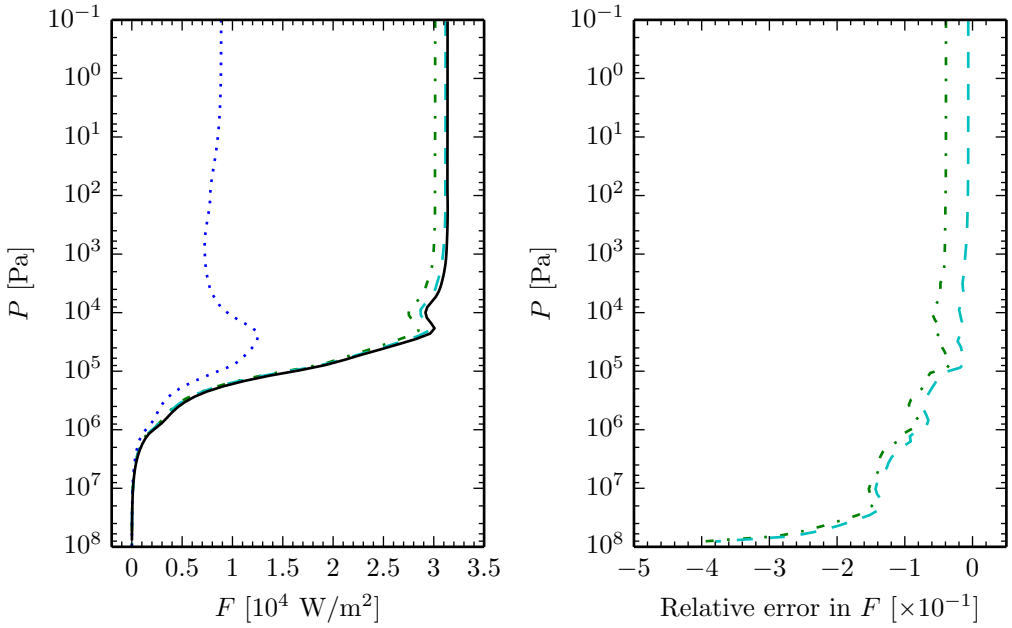

Figure 4.13: The left-hand panel shows the fluxes obtained for the night side of HD 209458b in Section 4.3.1 with the ES radiation scheme and `ATMO` using the P–T profile in Fig. 4.9. Absorption by CO, CH_4, H_2O, NH_3, H_2–H_2 and H_2–He CIA are included. The `ATMO` LbL DO result is also shown in this panel and is used to calculate the relative errors shown in the right-hand panel. Lines are as in Fig. 4.7.

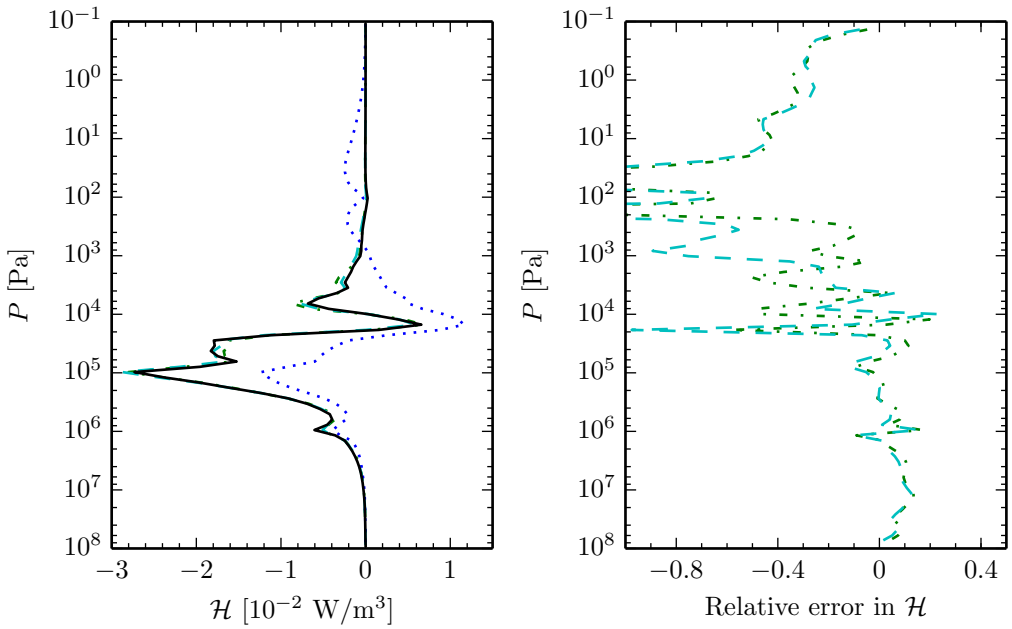

Figure 4.14: Same as Fig. 4.13 for the heating rates. Note that when the heating rate is very small relative errors may become large. The effect on the heating budget will be small, however, so we do not consider this a problem.

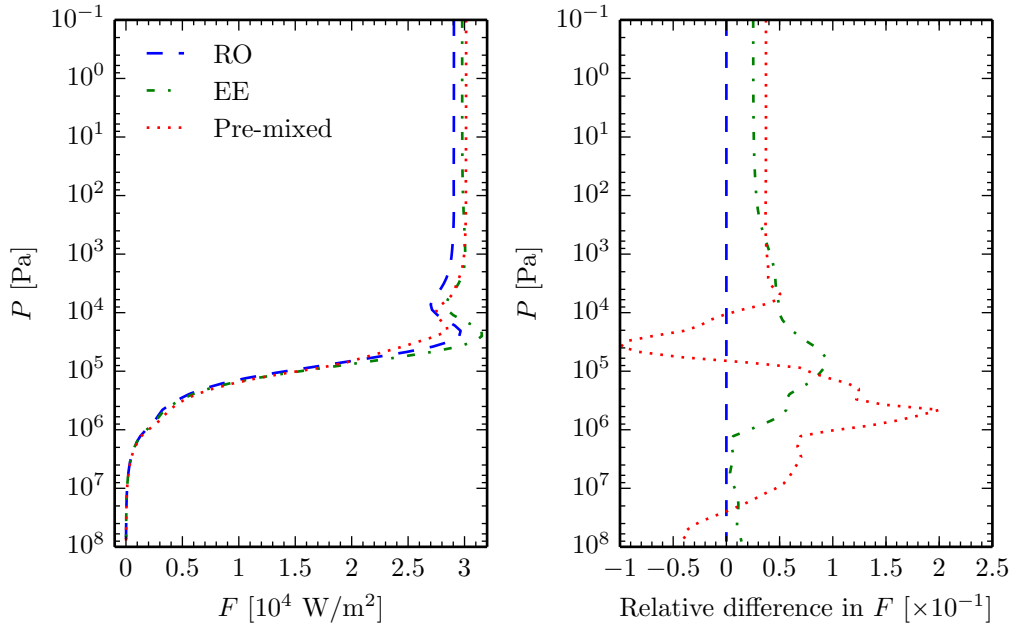

Figure 4.15: The left-hand panel shows the fluxes obtained for the night side of HD 209458b in Section 4.3.1 with the ES radiation scheme using the pre-mixed k-coefficients, the random overlap method and equivalent extinction. Absorption by CO, CH_4, H_2O, NH_3, H_2–H_2 and H_2–He CIA is included. The random overlap result is used to calculate relative errors caused by using equivalent extinction and pre-mixed k-coefficients shown in the right-hand panel.

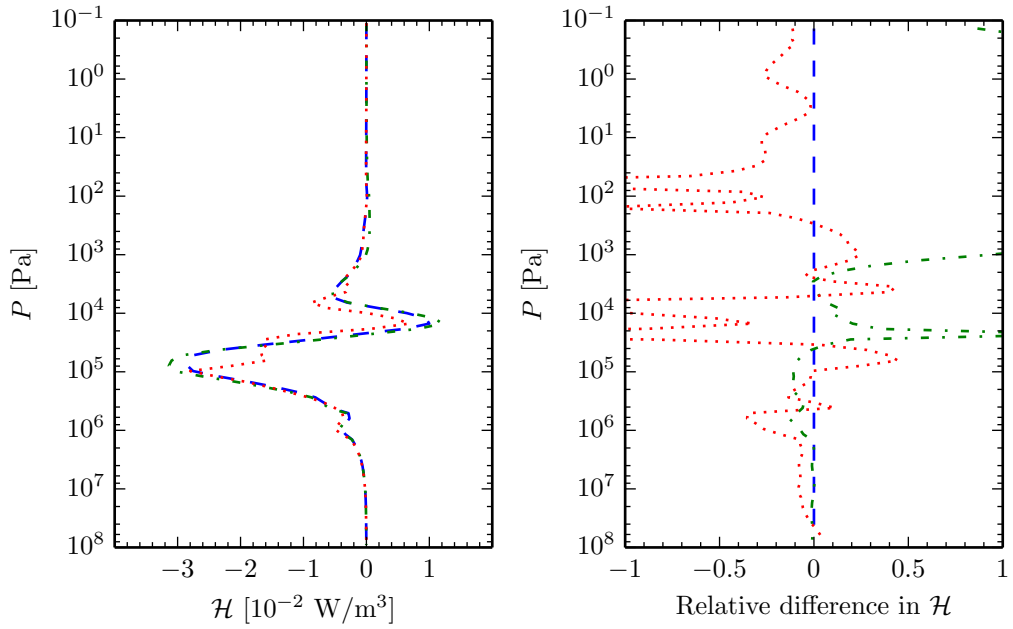

Figure 4.16: Same as Fig. 4.15 but for heating rates. Note that when the heating rate is very small relative errors may become large. The effect on the heating budget will be small, however, so we do not consider this a problem.

	Computation time [s]	Flux	Heating rate
RO	22.6939	-	-
EE	0.0178	0.038	0.132
Pre-mixed	0.0072	0.042	0.307

Table 4.8: Computed flux (F) and heating rate ($\mathcal{H}$) L^1 norms for the night side of HD 209458b from comparing the random overlap (RO) method to equivalent extinction (EE) and pre-mixed k-coefficients.

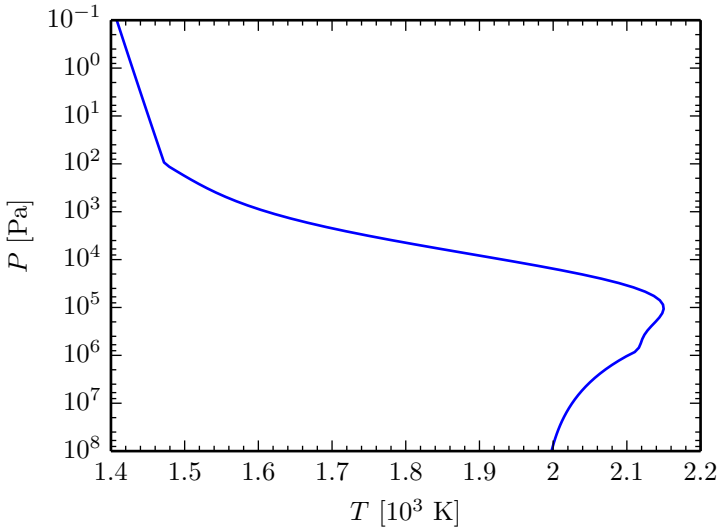

Figure 4.17: The P–T profile used in Section 4.3.2. From the polynomial fit (Heng et al. 2011) to the day side profile of HD 209458b from Iro et al. (2005) with the smoothing described in Mayne et al. (2014a).

Errors caused by using EE are on the order of the errors caused by the two-stream approximation and correlated-k method, and smaller than those caused by using pre-mixed opacities, as confirmed by the L^1 norms in Table 4.8. In this table we also provide the computation times for fluxes and heating rates, where EE is only slightly slower than using pre-mixed opacities. The excessive computation time required by RO is due to the lack of resorting and resampling to reduce the number of k-coefficients as discussed in Section 3.4.2.

4.3.2 Day side of HD 209458b

Our last tests adopt conditions suitable to the day side of hot Jupiters. We show the adopted day side P–T profile from Mayne et al. (2014a) in Fig. 4.17. The thermal and stellar components of the flux are calculated separately and then summed to obtain the total flux and heating rate. For the thermal component the lower boundary again emits as a black body at $T_{\rm lb} = T(P_{\rm lb})$, i.e. 1998 K using the P–T profile in Fig. 4.17. Note that, due to the separation of the intensity into direct and diffuse components, the stellar component of the intensity will only be subject to errors caused by the correlated-k method when scattering is ignored. Absorption by CO, CH_4, H_2O, NH_3, TiO, VO, H_2–H_2 and H_2–He CIA is included, with abundances as described in Section 3.6. As in Section 4.3.1 we compare all schemes for treating gaseous overlap described in Section 3.4.2. Rayleigh scattering by H_2 and He is included in our final test.

We assume an orbital distance $a_{\rm orbit} = 0.047$ au and a parent star effective temperature

	L^1, F	L^1, $\mathcal{H}$
$D = \sqrt{3}$	0.026	0.100
$D = 1.66$	0.015	0.098
$D = 2$	0.064	0.128
$D = 1.66$, $\epsilon_{\max} = 10^{-4}$	0.014	0.033
$D = 1.66$, UW	0.012	0.097
$D = 1.66$, mean	0.425	0.711

Table 4.9: Computed flux (F) and heating rate ($\mathcal{H}$) L^1 norms for the thermal component of the day side of HD 209458b in Section 4.3.2 (Figs. 4.18 and 4.19). The smallest errors are again obtained with $D = 1.66$.

$T_{\text{eff}}^{\text{star}} = T_{\text{eff}}^{\text{Sun}} = 5785\,\text{K}$ and radius $R_{\text{star}} = R_{\text{Sun}}$. Using Stefan-Boltzmann's law, the stellar irradiation at the top of the planet's atmosphere is given by

$$F_{\text{TOA}}^{\text{star}} = \sigma \left(T_{\text{eff}}^{\text{star}}\right)^4 \left(\frac{R_{\text{star}}}{a_{\text{orbit}}}\right)^2 = 6.092 \times 10^5\,\text{W/m}^2. \tag{4.31}$$

We adopt a zero solar zenith angle and use a solar spectrum from Kurucz[3]. At smaller wavelengths than available, we set the stellar flux to zero, while at larger wavelengths we extrapolate using a black-body spectrum with the effective temperature of the Sun ($T = 5785\,\text{K}$).

Precomputed mixture

Fluxes and heating rates for the mixture are calculated from effective k-coefficients in the ES radiation scheme and compared to equivalent LbL DO results from `ATMO` obtained with an effective LbL opacity table. Figures 4.18 and 4.19 show the thermal flux and heating rate with relative errors. The flux error is small in regions with non-negligible flux. The heating rate error also remains small in regions with significant cooling. This is confirmed by the computed L^1 norms listed in Table 4.9. A diffusitivy of $D = 1.66$ yields the smallest error, and it is approximately halved by decreasing $\epsilon_{\max}$ from 5×10^{-3} to 10^{-4}. Whether a black-body or uniform weighting scheme is used does not affect the accuracy significantly, but using a mean absorption coefficient does result in large errors.

Figures 4.20 and 4.21 show the stellar flux and heating rate with relative errors. At the top of the atmosphere, the flux is $-6.092 \times 10^5\,\text{W/m}^2$, as prescribed, and is subsequently absorbed. The heating rate is positive, i.e. the atmosphere is heated due to the absorption of stellar radiation, as expected. The accuracy is acceptable, the error in the flux stays below 10 %, while the heating rate error also stays below 10 % in the regions with strong heating. This is reflected in the L^1 errors listed in Table 4.10. Using $\epsilon_{\max} = 10^{-4}$ significantly reduces the error from the correlated-k method, and changing the weighting scheme does not alter the results significantly. The use of an average absorption coefficient, however, is seen to still result in significant errors. See Section 4.3.3 for discussion and more details.

[3]See `http://kurucz.harvard.edu/`.

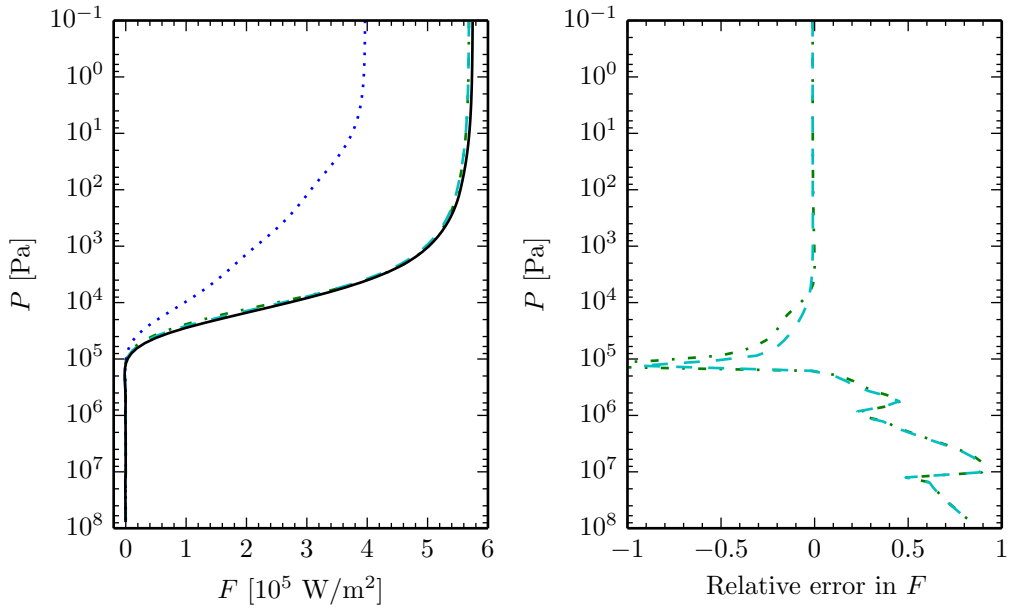

Figure 4.18: The left-hand panel shows the thermal component of the flux as a function of total pressure for the day side of HD 209458b in Section 4.3.2 with the ES radiation scheme and `ATMO` using the P–T profile in Fig. 4.17. Absorption by CO, CH_4, H_2O, NH_3, TiO, VO, H_2–H_2 and H_2–He CIA is included. The `ATMO` LbL DO result is also shown in this panel and is used to calculate the relative errors shown in the right-hand panel. Lines are as in Fig. 4.7. At high pressures the relative error becomes large, similar to that seen in Fig. 4.14 for the heating rate. As the flux itself is small, however, this is not a problem.

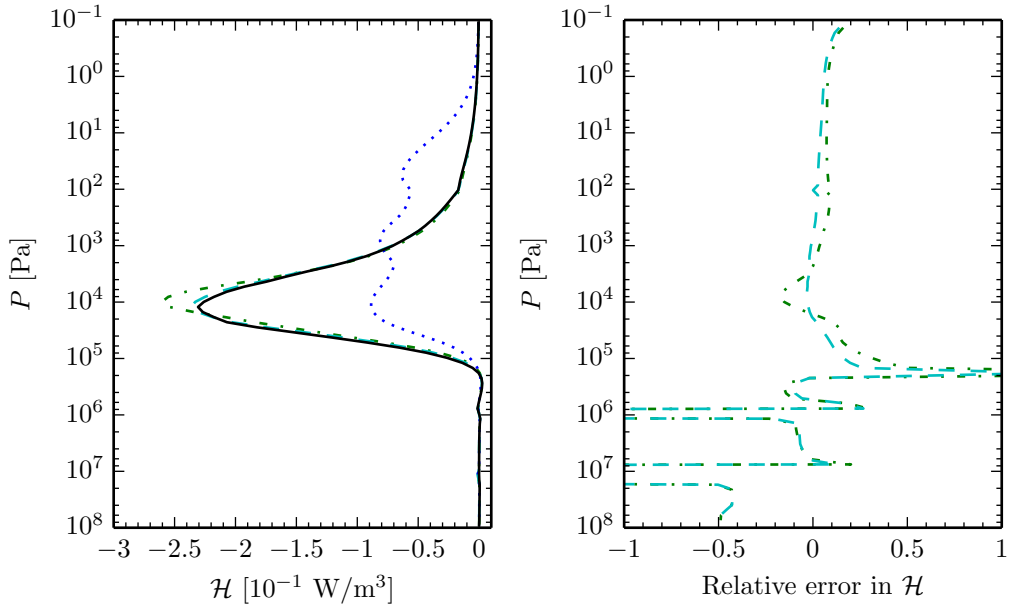

Figure 4.19: Same as Fig. 4.18 for the thermal component of the heating rate. Relative errors become unreasonably large only where the heating rate is very small.

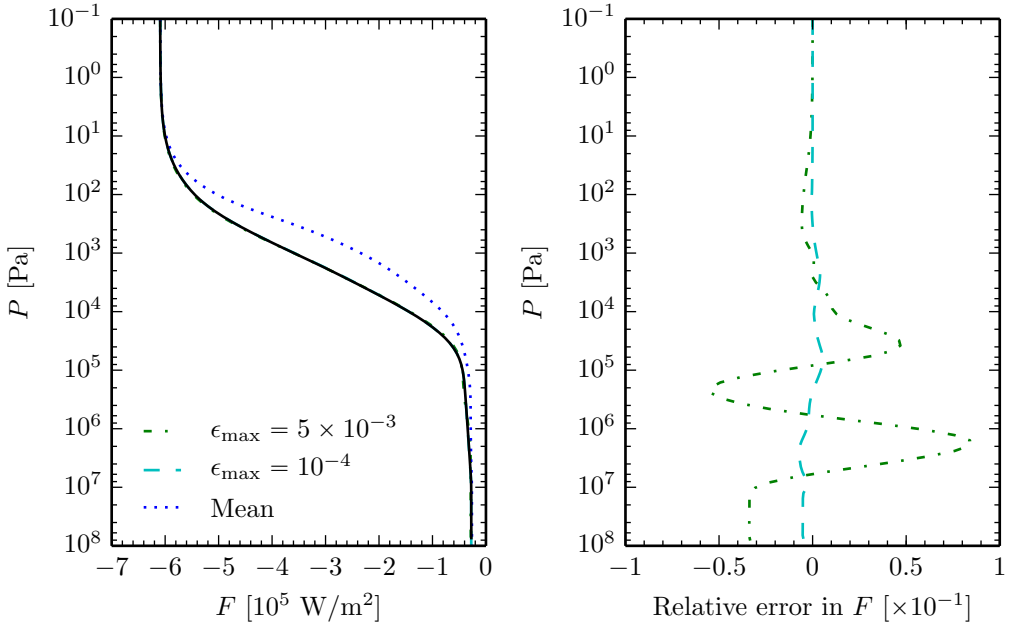

Figure 4.20: The left-hand panel shows the stellar component of the flux as a function of total pressure for the day side of HD 209458b in Section 4.3.2 with the ES radiation scheme using $\epsilon_{\rm max} = 5 \times 10^{-3}$ (dashed-dotted, green) and $\epsilon_{\rm max} = 10^{-4}$ (dashed, cyan) and `ATMO` (solid, black) using the P–T profile in Fig. 4.17. Absorption by CO, CH_4, H_2O, NH_3, TiO, VO, H_2–H_2 and H_2–He CIA is included. The `ATMO` LbL DO result is used to calculate the relative errors shown in the right-hand panel. Errors are small, and using $\epsilon_{\rm max} = 10^{-4}$ almost completely eliminates errors in the ES radiation scheme.

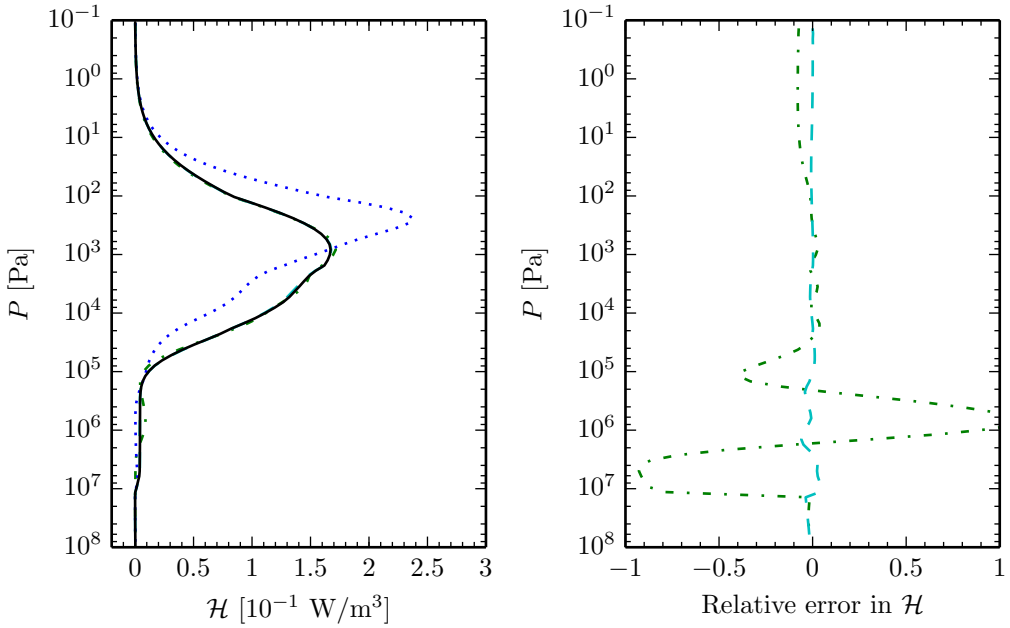

Figure 4.21: Same as Fig. 4.20 for the stellar component of the heating rate.

	L^1, F	L^1, $\mathcal{H}$
$\epsilon_{\max} = 5 \times 10^{-3}$	0.004	0.035
$\epsilon_{\max} = 10^{-4}$	0.001	0.005
$\epsilon_{\max} = 5 \times 10^{-3}$, UW	0.006	0.045
Mean	0.094	0.432

Table 4.10: Computed flux (F) and heating rate ($\mathcal{H}$) L^1 norms for the stellar component of the day side of HD 209458b in Section 4.3.2 (Figs. 4.18 and 4.19). The correlated-k method is seen to introduce errors of about 4 %.

	L^1, F	L^1, $\mathcal{H}$
$D = \sqrt{3}$	0.164	0.132
$D = 1.66$	0.097	0.124
$D = 2$	0.387	0.169
$D = 1.66$, $\epsilon_{\max} = 10^{-4}$	0.081	0.043
$D = 1.66$, UW	0.090	0.116
$D = 1.66$, mean	2.034	0.624

Table 4.11: Computed flux (F) and heating rate ($\mathcal{H}$) L^1 norms for the total flux and heating rate using the day side of HD 209458b in Section 4.3.2 (Figs. 4.22 and 4.23). Again $D = 1.66$ yields the smallest errors.

The total flux and heating rate, obtained by summing up the stellar and thermal components of the flux and heating rate, are shown in Figs. 4.22 and 4.23, respectively. The main region of heating and cooling, seen separately in Figs. 4.19 and 4.21, respectively, are still clearly distinguishable in Fig. 4.23. The atmosphere is heated at low pressures and cooled slightly at higher pressures. Note that errors remain small using the correlated-k method, as also shown in Table 4.11. The error introduced by using mean absorption coefficients is significant.

Random overlap method and equivalent extinction

We now compare the results obtained with pre-mixed opacities above to using the random overlap (RO) method and equivalent extinction (EE) to calculate k-coefficients for the mixture. We restrict the discussion to $D = 1.66$, $\epsilon_{\max} = 5 \times 10^{-3}$ for brevity. Fluxes and heating rates, with corresponding relative errors calculated assuming the RO result is exact, are shown in Figs. 4.24 and 4.25, respectively.

There are significant differences between the three schemes. There is a discontinuity in the derivative of the flux at about 10^2 Pa, which causes the discontinuity and spike in the heating rate, as seen in the RO and EE results. Comparing to Fig. 4.17 this discontinuity occurs as the temperature exceeds 1500 K, which is where TiO and VO abundances become non-zero in this test. Both molecules are strong absorbers in the visible, and the presence of these molecules leads to a strong absorption of the stellar component of the radiation. The transition is sudden due to the rapid increase in TiO and VO abundance, but it is smoothed out when using a pre-mixed opacity table due to the interpolation of the product of the opacity and mixing ratio instead of the opacity only. Consequently, the use of pre-mixed opacities can lead to large errors in both fluxes and heating rates if abundance transitions are not properly resolved.

We show the L^1 norms in Table 4.12, which confirms that using pre-mixed opacities can lead to significant errors if abundance transitions are not properly resolved. Condensation can therefore not be expected to be treated accurately with pre-mixed opacities without a very

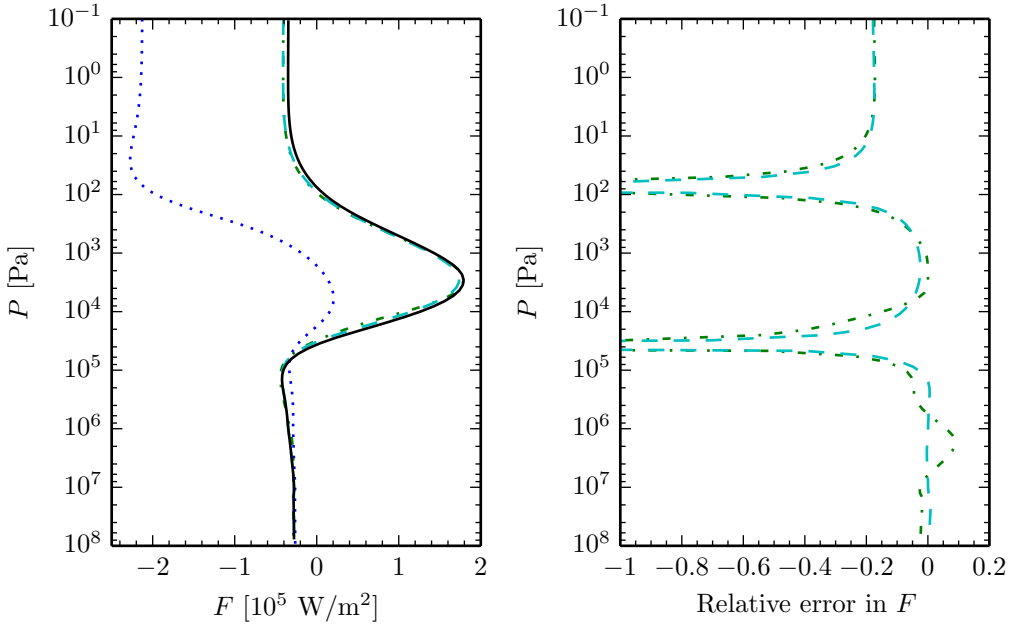

Figure 4.22: The left-hand panel shows the total flux as a function of total pressure for the day side of HD 209458b in Section 4.3.2 with the ES radiation scheme obtained by combining the thermal and stellar components in Figs. 4.18 to 4.21. The `ATMO` LbL DO result is also shown in this panel and is used to calculate the relative errors shown in the right-hand panel. Lines are as in Fig. 4.7. Again, relative errors become unreasonably large only where the flux is very small.

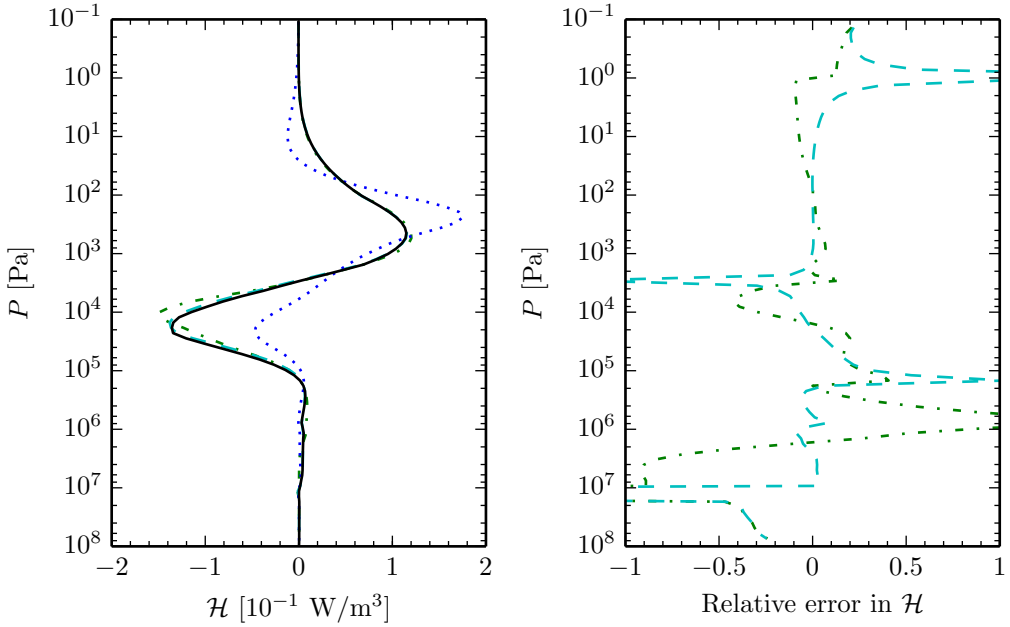

Figure 4.23: Same as Fig. 4.22 for the total heating rate. Relative errors become unreasonably large only where the heating rate is very small, with a negligible effect on the heating budget.

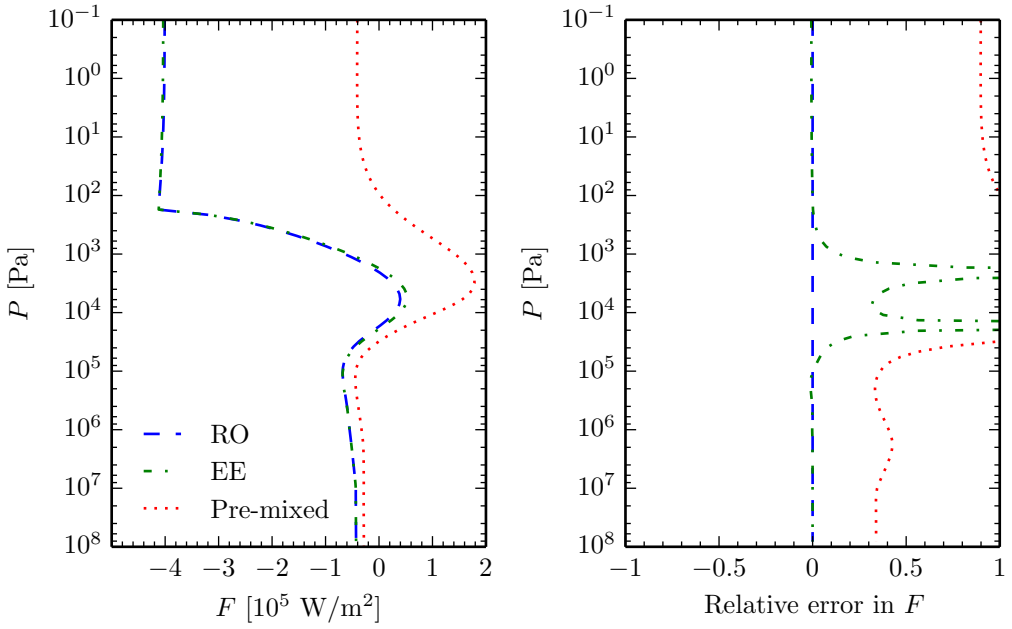

Figure 4.24: The left-hand panel shows the total fluxes obtained for the day side of HD 209458b in Section 4.3.2 with the ES radiation scheme using the pre-mixed k-coefficients, the random overlap method and equivalent extinction. Absorption by CO, CH_4, H_2O, NH_3, H_2–H_2 and H_2–He CIA is included. The random overlap result is used to calculate relative errors caused by using equivalent extinction and pre-mixed k-coefficients shown in the right-hand panel.

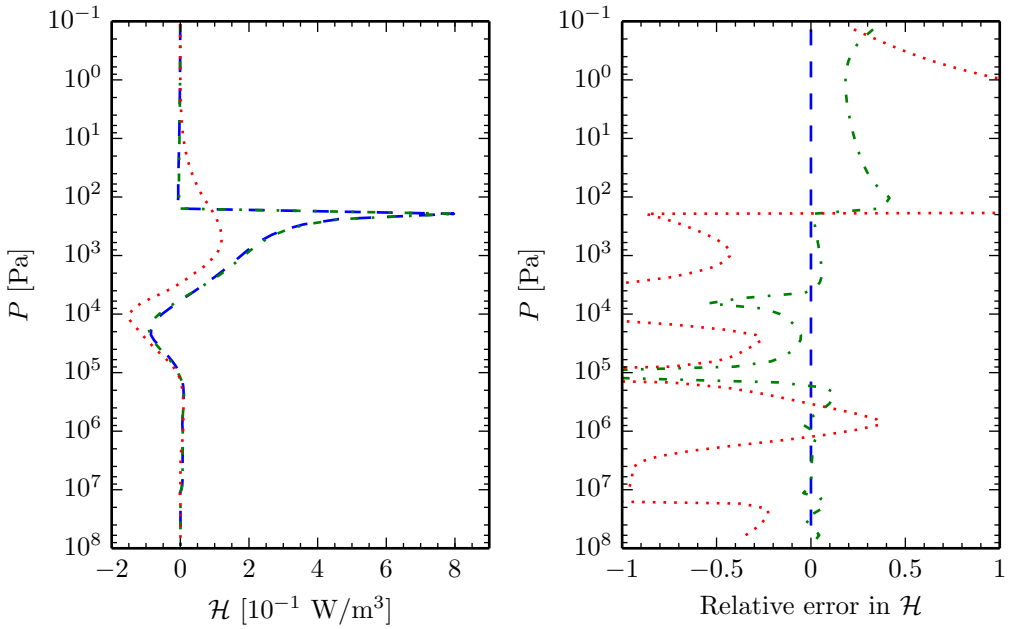

Figure 4.25: Same as Fig. 4.24 but for heating rates.

	Computation time [s]	Flux	Heating rate
RO	$22.32 + 24.715 = 47.04$	-	-
EE	$0.0182 + 0.0166 = 0.035$	0.016	0.050
Pre-mixed	$0.0073 + 0.0065 = 0.014$	0.992	0.863

Table 4.12: Computed flux (F) and heating rate ($\mathcal{H}$) L^1 norms for the day side of HD 209458b from comparing the random overlap (RO) method to equivalent extinction (EE) and pre-mixed k-coefficients. The first computation time is the thermal component, the second the stellar component.

Table 4.13: Computed flux (F) and heating rate ($\mathcal{H}$) L^1 norms for the day side of HD 209458b with Rayleigh scattering from comparing various two-stream approximations for the stellar component to PIFM80. Differences in fluxes and heating rates are negligibly small. Comparing to the non-scattering case there is a significant difference in the flux while heating rates are similar. See Figs. 4.26 and 4.27.

	Flux	Heating rate
PIFM80	0.000	0.000
DO	0.002	0.001
PIFM85, $D = 1.66$	0.003	0.001
HM	0.001	0.001
PIFM80, EE	0.020	0.051
No scattering	0.368	0.022

high resolution temperature and pressure grid for the opacity. Equivalent extinction, on the other hand, follows the DO result closely. As discussed in Section 3.4.2 there are no differences between RO and EE in the direct stellar component, i.e. the errors originate from the thermal component since we do not include scattering. From Table 4.12 equivalent extinction is much quicker than the random overlap method, and errors are again on the order of the errors due to the two-stream and correlated-k method.

Rayleigh scattering

So far we have not included any form of scattering, but even though we do not include clouds we do include Rayleigh scattering by H_2 and He in Chapters 5 and 6 as described in Sections 2.1.5 and 4.1.1. We try several different two-stream approximations to investigate the difference between them. As a basis we use the Practical Improved Flux Method from Zdunkowski et al. (1980) (PIFM1980), as described in Section 2.2.8, as this is the two-stream approximation recommended for use by the Met Office for the stellar component.

In Figs. 4.26 and 4.27 we show the fluxes and heating rates, respectively, computed with the ES scheme for several different two-stream approximations for the stellar component. The corresponding L^1 norms, computed by comparing to PIFM80, are provided in Table 4.13. For all cases we use $D = 1.66$ for the thermal component and random overlap to combine k-coefficients for different gases except for one case where equivalent extinction is used. Differences between two-stream approximations are very small, and errors caused by equivalent extinction are again on the order of errors caused by the two-stream approximation and correlated-k method. We consequently adopt PIFM80 as our default two-stream scheme for the stellar component as it is used by the Met Office, and combine k-coefficients using equivalent extinction.

Comparing to the no Rayleigh scattering case there is a significant difference in the flux

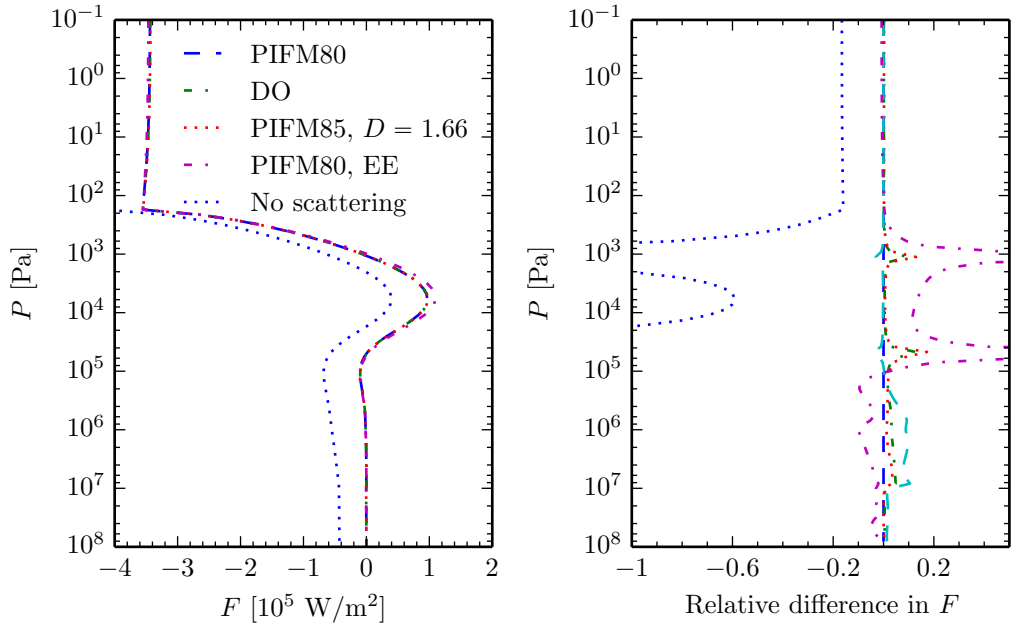

Figure 4.26: The left-hand panel shows the total fluxes obtained with the ES radiation scheme using various two-stream schemes for the stellar component (see Section 2.2.8): practical improved flux methods (PIFM80, PIFM85 with $D = 1.66$), discrete ordinate (DO) and hemispheric mean (HM). The relative difference on the right is calculated relative to PIFM80. The setup is otherwise identical to that in Fig. 4.24 with random overlap (RO) except for the case marked EE (equivalent extinction).

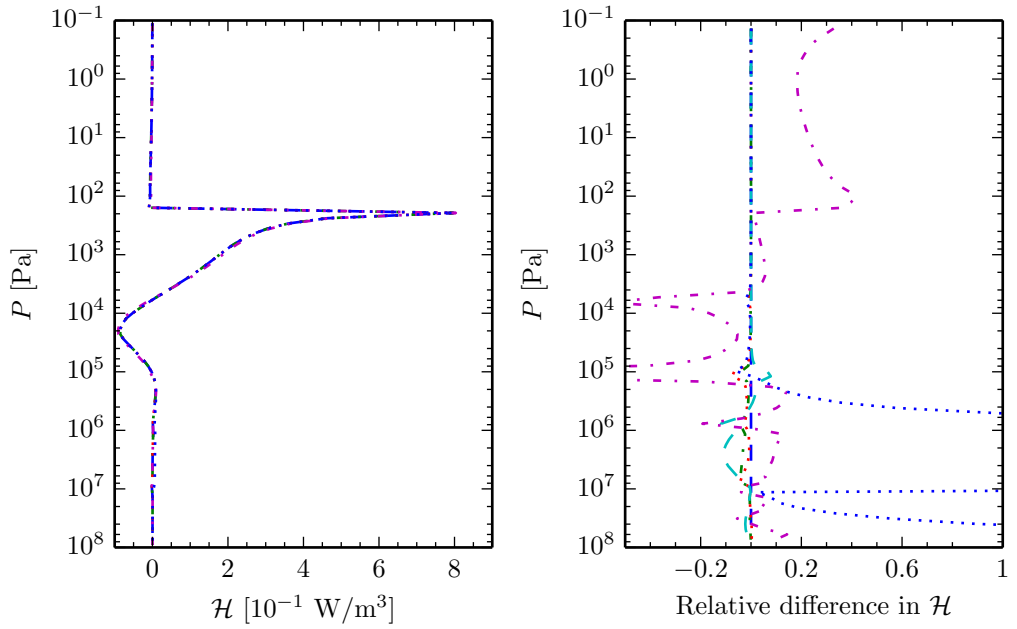

Figure 4.27: Same as Fig. 4.26 but for heating rates. Almost no difference in the heating rate is seen between various two-stream approximations for the stellar component and between cases with and without Rayleigh scattering.

due to the non-zero albedo as some of the short-wave stellar radiation is reflected back out of the atmosphere. In the heating rate, on the other hand, only minor differences are seen. The explanation for this is the $1/\lambda^4$ form of the Rayleigh-scattering coefficient. Rayleigh scattering will redistribute and lower the radiative energy in the atmosphere mainly at very short wavelengths where absorption is relatively weak even with TiO and VO. Consequently Rayleigh scattering only has a minor effect on the heating rate.

4.3.3 Discussion of the failure of mean absorption coefficients

Inspection of Figs. 4.7, 4.8, 4.13, 4.14 and 4.18 to 4.23 suggests systematic deviations of results based on the band-averaged absorption coefficients. For a given pressure, the thermal and stellar fluxes are underestimated, often resulting in heating rate peaks occurring at lower pressures and having the wrong magnitude. In an attempt to explain this behaviour, we first consider the direct stellar component.

The band-integrated direct stellar component of the flux is given by

$$F^-_{\mathrm{s},b}(u_\rho) = \frac{1}{\mu_0}\int_{\tilde{\nu}_b}^{\tilde{\nu}_{b+1}} \mathrm{d}\tilde{\nu}\, F_\mathrm{s} e^{-k_\rho(\tilde{\nu})u_\rho/\mu_0}, \tag{4.32}$$

where the atmospheric slab has been assumed to be homogeneous where u_ρ is the mass column density down to some height z. Using a mean absorption coefficient instead, the corresponding flux is

$$F^-_{\mathrm{s},b}(u_\rho) = \frac{e^{-\bar{k}_b u_\rho/\mu_0}}{\mu_0}\int_{\tilde{\nu}_b}^{\tilde{\nu}_{b+1}} \mathrm{d}\tilde{\nu}\, F_\mathrm{s}. \tag{4.33}$$

For simplicity we assume the incoming stellar radiation at the top of the atmosphere is wavenumber independent within a given band. Using a mean absorption coefficient then implies

$$\int_{\tilde{\nu}_b}^{\tilde{\nu}_{b+1}} \mathrm{d}\tilde{\nu}\, e^{-k_\rho(\tilde{\nu})u_\rho/\mu_0} \approx (\tilde{\nu}_{b+1}-\tilde{\nu}_b)e^{-\bar{k}_b u_\rho/\mu_0}. \tag{4.34}$$

Within a band the absorption coefficient $k_\rho(\tilde{\nu})$ will vary by orders of magnitude, causing some regions in the band to have a small transmission and others to have a large transmission. The mean in Eq. (3.61) is an arithmetic mean, i.e. the largest values of $k_\rho(\tilde{\nu})$ will dominate $\bar{k}_b$. Regions with high transmission due to small $k_\rho(\tilde{\nu})$ will be overshadowed by this large mean, causing the overall transmission to be underestimated. This explains the deviation in the flux seen in Fig. 4.20.

A similar argument can be used in the thermal region, but upward and downward radiation need to be considered separately. The radiative transfer equation is

$$\frac{\mathrm{d}I_{\tilde{\nu}}}{\mathrm{d}s} = k(\tilde{\nu},s)\left[B_{\tilde{\nu}}(s) - I_{\tilde{\nu}}(s)\right], \tag{4.35}$$

where s is the path over which radiation travels. We first consider the isothermal case, where the

upward radiation is constant and equal to the black-body flux throughout the atmosphere. At the top of the atmosphere, the downward flux is zero, i.e. the change in intensity will, according to Eq. (4.35), be dominated by thermal emission ($B_{\tilde{\nu}}(s) > I_{\tilde{\nu}}(s)$). Using a band-mean absorption coefficient effectively increases $k(\tilde{\nu}, s)$, which in Eq. (4.35) yields a larger intensity at a given s or pressure. The downward radiation contributes negatively to the total flux, i.e. the total flux will be smaller for a given pressure, as seen in Fig. 4.7.

If the atmosphere has non-zero temperature gradients, the upward flux will also depend on pressure. In both P–T profiles used here, the temperature decreases with height overall. At the lower boundary the upward intensity is simply the Planck intensity, i.e. the right-hand side of Eq. (4.35) is zero. As the temperature decreases, $B_{\tilde{\nu}}(s)$ will generally decrease, causing $B_{\tilde{\nu}}(s) < I_{\tilde{\nu}}(s)$. The upward flux is therefore dominated by absorption, and effectively increasing $k_\rho(\tilde{\nu})$ will cause the upward flux to become smaller for a given s or pressure. This explains why the total flux at the top of the atmosphere is underestimated when using a band-mean absorption coefficient, as seen in Figs. 4.7, 4.13 and 4.22.

These results show that large errors in both fluxes and heating rates may occur when the mean opacity scheme described in Dobbs-Dixon & Agol (2013) is applied in radiation schemes hot Jupiter GCMs. Improved mean opacity schemes have been developed by the stellar atmosphere community (see e.g. Nordlund 1982; Skartlien 2000), which may be applicable to hot Jupiter atmospheres. Further developments of these improved schemes may be needed, however, as they rely on correlations induced by strong vertical stratification, and longitude–latitude-dependent stellar heating has not been considered.

4.4 Summary and conclusions

The accuracy of radiation schemes used in GCMs has been studied extensively for Earth-like conditions, but detailed analysis for hot Jupiter-like conditions are lacking. In this chapter we have analysed the accuracy and uncertainties in state-of-the-art radiation schemes used in several GCMs applied to hot Jupiters. Both the two-stream approximation and correlated-k method's applicability to hot Jupiter atmospheres have been analysed by comparing the Edwards–Slingo radiation scheme to discrete ordinate line-by-line calculations. Our main results are:

- The ES radiation scheme's performance in these tests shows that we have successfully adapted it to hot Jupiter-like atmospheres. We found that a diffusivity factor of $D = 1.66$ for the thermal component, already widely used in both Earth and hot Jupiter GCMs, yields the smallest errors from the two-stream approximation, although $D = \sqrt{3} \approx 1.73$ is only slightly less accurate.

- About 10 k-coefficients in each band for molecular line absorption yield satisfactory accuracy. Using ~ 100 k-coefficients per band does improve the overall accuracy, but errors decrease by less than 50 %, while the radiative transfer computation time increases by a

factor of 10. We therefore choose to adopt the former as a balance between accuracy and computational cost.

- Using a mean absorption coefficient in each band, as in Dobbs-Dixon & Agol (2013), yields inaccurate fluxes and heating rates for molecular absorption. Heating rate errors can reach 100 % or more, even in regions with significant heating. Band-averaged absorption coefficients should thus be used with caution.

- The use of pre-mixed opacities can incur significant errors if abundances change rapidly, such as when an absorber is condensing. An unreasonably high resolution in pressure and temperature would be required in the pre-mixed opacity table to capture such behaviour, but random overlap as implemented in the ES radiation scheme is too slow for use in a GCM. Equivalent extinction is a much quicker way of combining k-coefficients for different absorbers. We show that errors caused by using equivalent extinction are on the order of the errors caused by the two-stream approximation and correlated-k method for hot Jupiters, and we consequently adopt this scheme in the GCM.

Both the two-stream approximation and the correlated-k method contribute non-negligibly to the total error, with overall heating rate errors of $\lesssim 10\,\%$ in regions with non-zero heating rates. Flux errors are similar or smaller. Whether a black-body spectrum, solar spectrum or uniform (in wavenumber) weighting scheme is used has little effect on the overall accuracy given the bands used here (see Tables 4.5 to 4.7 and 4.9 to 4.11). We therefore choose to adopt a uniform weighting scheme, enabling the use of the same k-coefficients in both the thermal and stellar spectral regions and for different irradiation spectra.

Rayleigh scattering has been shown to be relatively unimportant for the heating budget, mainly caused by the $1/\lambda^4$-dependence of the Rayleigh scattering coefficient. We note that the current implementation of equivalent extinction will need to be modified if significant scattering is introduced in the stellar component of the radiation as mentioned in Section 3.4.2.

Any radiation scheme applied to hot Jupiters should be checked against the tests we have presented here. These tests, and the detailed descriptions of our methods and approximations, will be useful for future adaptation of radiation schemes in other GCMs. Current observational constraints on exoplanets do not require the level of accuracy we have applied in this work. The field develops at an amazing pace, however, and modellers should now develop the best theoretical and numerical tools to tackle the challenges posed by the increasing accuracy expected from future large observational projects.

Chapter 5

Coupling to the UM dynamical core ENDGAME

In the previous chapters we have discussed the adaptation of the ES radiation scheme to hot Jupiters, and in Chapter 4 we confirmed that the adapted radiation scheme performs well, with errors $\lesssim 10\,\%$ in fluxes and heating rates, for hot Jupiter-like conditions. The UM dynamical core ENDGAME has been tested independently for hot Jupiter-like conditions using a temperature-forcing scheme as discussed in Chapter 1, and the results have been presented in Mayne et al. (2014a,b). Mayne et al. found that ENDGAME accurately reproduces hot Jupiter benchmark results in the literature and concluded that this dynamical core can indeed be applied to hot Jupiters. In this chapter we discuss the coupling of the adapted ES radiation scheme to the dynamical core and modifications we have made to the UM.

In Section 5.1 we briefly discuss the equations of fluid dynamics and how they are coupled to the heating rate (Section 2.1.7) from the radiation scheme through the thermodynamic equation. Then, in Section 5.2, we describe the model set-up and the changes we have made to the UM. This includes the initial condition, uniform radiation mode that enables us to compare the UM to 1D equilibrium models, and boundary conditions. We perform a comparison between our 1D radiative-convective equilibrium code `ATMO` and the UM in Section 5.3 and detail modifications we have made to abundances to improve numerical stability in Section 5.4. At the end of this chapter, in Section 5.5, we discuss how synthetic observations are calculated from UM output. This includes phase curves, transmission and emission spectra.

5.1 Fluid dynamics and the UM dynamical core

Here we introduce the fluid dynamics equations and the UM dynamical core. We leave out a thorough discussion as the focus of this work is on the radiation scheme, but refer to Vallis (2006) for more details on fluid dynamics in general and Mayne et al. (2014a,b) and references therein for a much more thorough discussion of the UM dynamical core and its applicability to

hot Jupiter-like atmospheres.

5.1.1 The material derivative

In fluid dynamics the evolution of fluid properties can be specified from two different viewpoints. The first is called the Lagrangian view, and involves looking at individual fluid parcels and following their properties (e.g. position, velocity and temperature) with time. This is similar to standard solid-body mechanics: Newton's laws and the laws of thermodynamics can be applied to each parcel. The second is called the Eularian view, where fluid properties are described by fields, e.g. a temperature field $T(\boldsymbol{x}, t)$ where $\boldsymbol{x}$ is the position vector and t is time, specifying some property of the material at a given position and time. The material derivative relates these two viewpoints.

Consider a fluid described by a velocity field $\boldsymbol{v}(\boldsymbol{x}, t)$ and a fluid parcel property described by ϕ. Using the chain rule, the change in ϕ is given by

$$\delta\phi = \frac{\partial\phi}{\partial t}\delta t + \frac{\partial\phi}{\partial x}\delta x + \frac{\partial\phi}{\partial t}\delta y + \frac{\partial\phi}{\partial z}\delta z = \frac{\partial\phi}{\partial t}\delta t + (\delta\boldsymbol{x}\cdot\nabla)\,\phi. \tag{5.1}$$

The total time derivative of the field is then, letting $\delta t, \delta x, \delta y, \delta z \to 0$,

$$\frac{\mathrm{d}\phi}{\mathrm{d}t} = \frac{\partial\phi}{\partial t} + \left(\frac{\mathrm{d}\boldsymbol{x}}{\mathrm{d}t}\cdot\nabla\right)\phi = \frac{\partial\phi}{\partial t} + (\boldsymbol{v}\cdot\nabla)\,\phi, \tag{5.2}$$

where we have replaced $\mathrm{d}\boldsymbol{x}/\mathrm{d}t$ with the velocity field $\boldsymbol{v}$. The material derivative is usually denoted by the operator $\mathrm{D}/\mathrm{D}t$ to separate it from other derivatives, and we have

$$\frac{\mathrm{D}}{\mathrm{D}t} = \frac{\partial}{\partial t} + (\boldsymbol{v}\cdot\nabla)\,. \tag{5.3}$$

The first term on the right-hand side describes the local rate of change of ϕ, while the second term arises due to the spatial variation of ϕ experienced only if a particle moves. This operator applies equally well to scalar and vector fields and describes the rate of change in a fluid parcel property.

5.1.2 The thermodynamic equation

The thermodynamic equation relates the heat added or lost by radiation and other processes to the change in temperature in the atmosphere. It is common to use the potential temperature θ defined as the temperature a fluid parcel would have if moved adiabatically, i.e. without any heat exchange, to a reference pressure P_0. We derive the relation between the temperature and potential temperature in Appendix A.4.2, the result is:

$$\theta = T\left(\frac{P_0}{P}\right)^{\mathcal{R}/c_P}, \tag{5.4}$$

where $\mathcal{R} = R/\bar{m}$ is the specific gas constant, c_P is the specific heat capacity at constant pressure and R is the ideal gas constant. Another useful quantity is the Exner pressure (or function) defined as

$$\Pi = \left(\frac{P}{P_0}\right)^{\mathcal{R}/c_P} = \frac{T}{\theta}, \tag{5.5}$$

which means that $T = \theta\Pi$. Consequently Exner pressure Π and potential temperature θ can be used in place of pressure P and temperature T, respectively.

We derive the thermodynamic equation in Appendix A.4, the result is an equation for the time evolution of the potential temperature:

$$\frac{\mathrm{D}\theta}{\mathrm{D}t} = \frac{\theta}{T}\frac{\dot{Q}}{c_P}, \tag{5.6}$$

where c_P is the heat capacity at constant pressure and $\dot{Q}$ is the heating rate per unit mass. The unit of the heating rate $\mathcal{H}$ in Eq. (2.37) is per unit volume. These two quantities are therefore related by the density ρ, and we have $\dot{Q} = \mathcal{H}/\rho$. Note that $\dot{Q}$ can also include other heating sources, e.g. viscous heating, not considered here.

5.1.3 The equations of fluid dynamics

Here we introduce the equations of fluid dynamics, and the formulation used by the UM dynamical core ENDGAME.

The Euler and Navier-Stokes equations

The equations of motion for a fluid are essentially conservation equations, which are closed by an equation of state:

$$\frac{\mathrm{D}\rho}{\mathrm{D}t} = -\rho\nabla\cdot\boldsymbol{v} \qquad \text{mass continuity equation,} \tag{5.7a}$$

$$\frac{\mathrm{D}\boldsymbol{v}}{\mathrm{D}t} = -\frac{\nabla P}{\rho} + \nu\nabla^2\boldsymbol{v} + \boldsymbol{F} \qquad \text{momentum equation,} \tag{5.7b}$$

$$\frac{\mathrm{D}\theta}{\mathrm{D}t} = \frac{\theta}{T}\frac{\dot{Q}}{c_P} \qquad \text{thermodynamic equation,} \tag{5.7c}$$

$$P = f(\theta,\rho) \qquad \text{equation of state,} \tag{5.7d}$$

where ν is the viscosity and $\boldsymbol{F}$ represents any external body forces such as gravity. These equations are called the Navier-Stokes equations, while if the viscosity term is omitted ($\nu = 0$) they are called the Euler equations. This leaves us with six scalar equations with six unknowns; ρ, P, θ and $\boldsymbol{v}$.

Effects of rotation: It is common practice, and indeed convenient, to describe flows relative to a planet's surface (or lower boundary). Most planets are rotating, which means that velocities

measured relative to the planet surface and in an inertial frame will not be the equal. The momentum equation is therefore often rewritten in a rotating frame of reference where velocities $\boldsymbol{v}$ are measured relative to the planet surface. It can be shown that (see Appendix A.5)

$$\left(\frac{\mathrm{d}\boldsymbol{v}_\mathrm{R}}{\mathrm{d}t}\right)_\mathrm{R} = \left(\frac{\mathrm{d}\boldsymbol{v}_\mathrm{I}}{\mathrm{d}t}\right)_\mathrm{I} - 2\boldsymbol{\Omega}\times\boldsymbol{v}_\mathrm{R} - \boldsymbol{\Omega}\times(\boldsymbol{\Omega}\times\boldsymbol{r}), \tag{5.8}$$

where the subscript 'I' and 'R' denotes that the quantities are measured in the inertial and rotating reference frames, respectively, $\boldsymbol{\Omega}$ is the angular velocity and $\boldsymbol{r}$ is the position vector. The second and third terms on the right-hand side (including the minus signs) are the Coriolis and centrifugal forces, respectively. Note that these are fictitious forces since they are an artefact of measuring quantities in a rotating reference frame.

Combining Eqs. (5.7b) and (5.8) yields the momentum equation in a rotating frame

$$\frac{\mathrm{D}\boldsymbol{v}}{\mathrm{D}t} = -\frac{\nabla P}{\rho} + \nu\nabla^2\boldsymbol{v} - 2\boldsymbol{\Omega}\times\boldsymbol{v} - \boldsymbol{\Omega}\times(\boldsymbol{\Omega}\times\boldsymbol{r}) + \boldsymbol{F} \qquad \text{momentum equation,} \tag{5.9}$$

where $\boldsymbol{v}$ is the velocity in the rotating frame.

Equations solved by the UM dynamical core

The UM dynamical core ENDGAME solves the Euler equations, Eq. (5.7) with $\nu = 0$, for a rotating spherical shell using Exner pressure and potential temperature:

$$\frac{\mathrm{D}u}{\mathrm{D}t} = \frac{uv\tan\phi}{r} - \frac{uw}{r} + fv - f'w - \frac{c_\mathrm{P}\theta}{r\cos\phi}\frac{\partial\Pi}{\partial\lambda} + D(u), \tag{5.10a}$$

$$\frac{\mathrm{D}v}{\mathrm{D}t} = -\frac{u^2\tan\phi}{r} - \frac{vw}{r} - uf - \frac{c_\mathrm{P}\theta}{r}\frac{\partial\Pi}{\partial\phi} + D(v), \tag{5.10b}$$

$$\frac{\mathrm{D}w}{\mathrm{D}t} = \frac{u^2+v^2}{r} + uf' - g(r) - c_P\theta\frac{\partial\Pi}{\partial r}, \tag{5.10c}$$

$$\frac{\mathrm{D}\rho}{\mathrm{D}t} = -\rho\left[\frac{1}{r\cos\phi}\frac{\partial u}{\partial\lambda} + \frac{1}{r\cos\phi}\frac{\partial(v\cos\phi)}{\partial\phi} + \frac{1}{r^2}\frac{\partial(r^2w)}{\partial r}\right], \tag{5.10d}$$

$$\frac{\mathrm{D}\theta}{\mathrm{D}t} = \frac{1}{\Pi}\frac{\dot{Q}}{c_P} + D(\theta), \tag{5.10e}$$

$$\Pi^{\frac{1-\kappa}{\kappa}} = \frac{\mathcal{R}\rho\theta}{P_0}, \tag{5.10f}$$

where λ, ϕ, r, and t are the longitude, latitude (from equator to poles), radial distance from the centre of the planet and time, respectively. u, v and w are the zonal (longitudinal direction), meridional (latitudinal direction) and vertical velocity components, respectively, $\kappa \equiv \mathcal{R}/c_P$, P_0 is a chosen reference pressure as in Eqs. (5.4) and (5.5) and $g(r)$ is the acceleration due to gravity given by

$$g(r) = g_\mathrm{p}\left(\frac{R_\mathrm{p}}{r}\right)^2, \tag{5.11}$$

where g_p and R_p are the gravitational acceleration at and radial position of the inner boundary, respectively. The self-gravity of the atmosphere is ignored. f and f' are the Coriolis parameters defined as

$$f = 2\Omega \sin\phi \qquad\qquad f' = 2\Omega \cos\phi. \tag{5.12}$$

D is the diffusion operator, given by Eq. (19) and (20) in Mayne et al. (2014a). In physical flows eddies and turbulence can cause cascades of energy down to very small scales where it is eventually converted to thermal energy. GCMs do not have the resolution to resolve these energy cascades and artificial viscosities or diffusion operators are usually added to remove kinetic energy from the system. We refer to Mayne et al. (2014a) for a discussion of diffusion schemes and artificial viscosities. In this work the diffusion operator is applied to the horizontal velocity components only, and the removed kinetic energy is not added back into the energy equation.

Note that the centrifugal force $-\boldsymbol{\Omega} \times (\boldsymbol{\Omega} \times \boldsymbol{r})$ is not included in Eq. (5.10). Over time the Earth has developed an equatorial bulge to compensate for and neutralise the centrifugal force. Instead of explicitly including this oblateness in GCMs the centrifugal force is omitted to approximately take it into account.

The UM dynamical core ENDGAME solves Eq. (5.10) on a latitude-longitude-height grid using a finite difference method, see Mayne et al. (2014a), Wood et al. (2014) and references therein for more details.

5.2 Coupling the adapted radiation scheme to the dynamical core ENDGAME

As a starting point we used the idealised temperature-forced HD 209458b test case described in Mayne et al. (2014a); see Sections 1.4.1 and 6.2.1. In this model only the dynamical core of the UM is used, combined with a temperature-forcing scheme. We turn the temperature-forcing scheme off and the radiation scheme on. The radiation scheme itself has been updated with the latest changes described in Section 4.1.1 in order to use a look-up table for the band-integrated Planck function and gases added such as TiO and VO. Components specific to the Earth in the radiation scheme, such as boundary conditions determined by continents, sea and ice caps, and clouds were turned off.

A new namelist, a Fortran construct allowing for format free input of variables, was created containing planetary constants such as orbital period, orbital distance, rotation period and the stellar flux at the top of the atmosphere. We have implemented the simple analytical chemical equilibrium abundance formulas described in Section 3.6 for all the gases we include. These mixing ratios are calculated on-the-fly, and equivalent extinction is used to combine k-coefficients for different gases, as discussed in Section 3.4.2 and Chapter 4. All gases except water can be turned on or off as desired in namelists. Rayleigh scattering by H_2 and He, as described in

Parameter	Value
Radius, R_p	$9.0 \times 10^7\,\mathrm{m} = 1.259 R_\mathrm{Jup}$
Mass, M_p	$1.31 \times 10^{27}\,\mathrm{kg} = 0.690 M_\mathrm{Jup}$
Specific heat capacity c_P	$1.3 \times 10^4\,\mathrm{J/(kg\,K)}$
Specific gas constant, $\mathcal{R} = R/\bar{m}$	$3556.8\,\mathrm{J/(kg\,K)}$
Lower boundary pressure, P_bottom	200 bar
Rotation rate, Ω	$2.06 \times 10^{-5}\,\mathrm{s}^{-1}$
Intrinsic temperature, T_int	100 K
Vertical damping coefficient	0.15
Height of upper boundary	9×10^6 m (no TiO/VO), 1.1×10^7 m (with TiO/VO)
Horizontal resolution	144 (longitude), 90 (latitude)
Vertical resolution	66
Dynamical time step	30 s (no TiO/VO), 15 s (with TiO/VO)
Radiative time step	150 s (no TiO/VO), 75 s (with TiO/VO)

Table 5.1: Default parameter set for HD 209458b. Parameters are similar to those in Mayne et al. (2014a) with a few differences explained in the text.

Sections 2.1.5 and 4.1.1, is also included. We have changed both the upper and lower boundary conditions, and we detail these changes in Sections 5.2.4 and 5.2.5.

5.2.1 Model setup

We have made a few modifications to the set-up of the HD 209458b benchmark in Mayne et al. (2014a). We have listed our default set of parameters for HD 209458b in Table 5.1. Compared to Mayne et al. (2014a) the radius of the inner boundary R_p has been lowered slightly to take into account the vertical extent of the atmosphere in the model. This radius and mass M_p are used to calculate the gravity at the lower boundary. The specific heat capacity c_P has been changed slightly to agree with the value used by Showman et al. (2009). The specific gas constant $\mathcal{R} = R/\bar{m}$ has been reduced to be consistent with the mean molecular weight used by the radiation scheme, $\bar{m} = 2.34\,\mathrm{g/mol}$. The pressure at the lower boundary has been reduced from 220 bar to 200 bar, again to be consistent with Showman et al. (2009). We discuss the height of the upper boundary and time steps in more detail below.

The mean molecular weight used in the HD 209458b benchmark in Heng et al. (2011), and subsequently in Mayne et al. (2014a), can be derived from the specific gas constant given in Table 1 of Heng et al. (2011), $\mathcal{R} = 4593\,\mathrm{J/(kg\,K)}$. Using $R = 8.3145\,\mathrm{J/(mol\,K)}$ for the ideal gas constant, we get

$$\bar{m} = R/\mathcal{R} = 1.81\,\mathrm{g/mol}, \tag{5.13}$$

which is very small compared to the 2.34 g/mol derived in Section 3.6.1. In order to achieve such a low mean molecular weight the atmosphere needs to contain a significant fraction of dissociated H_2, which should not be the case since all temperatures in these simulations are $< 2000\,\mathrm{K}$.

In our coupled models we have found that, both for numerical stability and accuracy, we

needed to use a dynamical time step of 30 s without TiO and VO, and 15 s with TiO and VO. This is much smaller than the time step used in Mayne et al. (2014a), but it is in agreement with time steps used by Showman et al. (2009).

It is common practice in GCMs to call the radiation scheme, i.e. update fluxes and heating rates, less frequently than every dynamical time step. This is done mainly for computational efficiency, and is possible as changes in fluxes and heating rates may be small between dynamical time steps. We have tried several different radiative time steps, from calling the radiation scheme every dynamical time step to calling it every 10 dynamical time steps, and have found that calling it every five dynamical time steps is a good compromise between numerical accuracy and computational cost. This leads to radiative time steps of 150 s and 75 s without and with TiO and VO, respectively. The smaller time step needed when including TiO and VO is due to the need to resolve the short radiative time scale in the upper atmosphere where TiO and VO absorption dominates.

5.2.2 Initial condition

Initialising hot Jupiter GCMs is a difficult issue, mainly due to the absence of spatially resolved observations of the atmospheres of these planets. It is common to initialise these models with the same P–T profile across the whole globe with no winds (Heng et al. 2011; Mayne et al. 2014a; Showman et al. 2009). Temperature-forced models are usually initialised with an equilibrium forcing profile, while the model of Showman et al. (2009) was initialised with a globally averaged profile from a 1D radiative-convective equilibrium code.

We initialise with equilibrium P–T profiles calculated with the 1D radiative-convective equilibrium code `ATMO`; details are provided for the specific model runs. Throughout we use a stellar zenith angle $\mu_0 = 0.5$ in `ATMO`, which corresponds to the average day side zenith angle:

$$\bar{\mu}_0 = \frac{\int_0^{2\pi}\int_0^{\pi/2} \cos\theta_0 \, \sin\theta_0 \, \mathrm{d}\theta_0 \mathrm{d}\phi}{\int_0^{2\pi}\int_0^{\pi/2} \mathrm{d}\sin\theta_0 \mathrm{d}\phi} = 0.5. \tag{5.14}$$

A redistribution parameter f is introduced to take into account redistribution of heat from the day side to the night side, as discussed in Section 1.3.1. We use $f = 0.5$ (full redistribution) and $f = 1$ (day side redistribution) only. Abundances are calculated using the formulas in Section 3.6.

We have implemented the possibility to read in an initial P–T profile from file in the UM. The input P–T profile is interpolated onto the vertical height grid in the UM. A hydrostatic profile is built by assuming that temperature and gravity are constant across each layer, and then brought onto numerical hydrostatic equilibrium for the ENDGAME dynamical core through the call to a Newton–Rhapson (NR) solver. This final profile is then used as the initial profile.

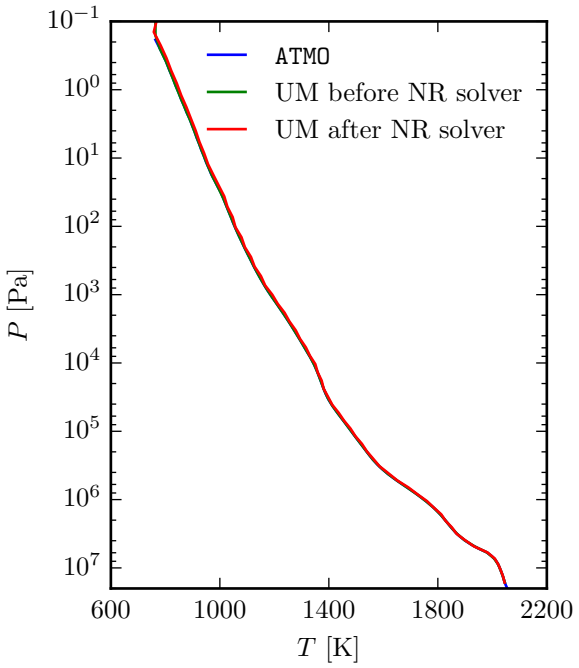

Figure 5.1: One of the radiative-convective equilibrium profiles from `ATMO` we use to initialise the UM. All profiles, the original from `ATMO`, the profile interpolated onto the UM grid, and the profile after the hydrostatic equilibrium NR solver agree well.

Verification

To verify our implementation of the initial conditions we show in Fig. 5.1 one of the radiative-convective equilibrium P–T profiles from `ATMO` we use to initialise the UM. This profile was computed without TiO and VO and with $f = 0.5$. We plot the original P–T profile from `ATMO`, and the profile interpolated onto the UM vertical grid both before and after the Newton–Raphson solver, all of which agree.

We also started a UM run initialised with this profile while turning all forcing (both temperature-forcing schemes and radiation) and rotation off. This resulted in maximum wind velocities of $\ll 1\,\mathrm{m/s}$, which shows that the atmosphere is indeed stable and in hydrostatic equilibrium, as desired.

5.2.3 Uniform irradiation

To ease boundary condition tests and comparison to 1D radiative-convective models such as `ATMO`, we have implemented uniform irradiation in the UM. We do this by enforcing the same irradiation everywhere with a fixed value of μ_0, and setting the planetary rotation rate to zero. This enables us to effectively use the UM as a radiative and hydrostatic equilibrium solver, where the stellar heating equals the thermal cooling. The horizontal winds will be small, while the vertical winds will become smaller as the profile converges towards equilibrium.

5.2.4 Lower boundary condition

The lower boundary condition normally used in hot Jupiter GCMs is a surface radiating as a black-body with a fixed temperature $T_{\rm surf}$ (Showman et al. 2009). This is an input parameter, does not evolve with the model, and consequently must be chosen carefully. We have implemented a new lower boundary condition for the radiation that is more consistent with gas giants as they do not have a solid surface with a fixed temperature. When planets form they contract gravitationally, which in turn releases heat. The atmospheres of non-irradiated sub-stellar objects are usually classified by two numbers, the gravity and the effective temperature $T_{\rm eff}$, where $T_{\rm eff}$ describes the heat-flux from the interior of the planet. The flux at the top of the atmosphere is then given by Stefan-Boltzmann's law, $F^{\rm TOA} = \sigma T_{\rm eff}^4$, and assuming a stable plane-parallel atmosphere the net flux must be given by $\sigma T_{\rm eff}^4$ throughout the atmosphere due to energy conservation. For more details, see Baraffe et al. (2010) and references therein.

The atmosphere of a hot Jupiter cannot be expected to be in radiative convective equilibrium due to atmospheric circulation, but there will still be a heat flux from the interior of the planet. This can be described by $\sigma T_{\rm int}^4$, where $T_{\rm int}$ is the intrinsic temperature of the planet. This is not a real temperature, but can be thought of as the effective temperature the object would have had without irradiation.

At the lower boundary essentially all stellar irradiation has been absorbed. The total flux at the lower boundary is then given by the intrinsic flux of the planet, and we would like to be able to specify this. The ES radiation scheme requires a temperature, albedo and emissivity for the lower boundary in order to calculate the upward flux at the lower boundary, $F_{\rm surf}^+$. We set the albedo to zero, emissivity to one, and need to derive an expression for the temperature of the lower boundary given the intrinsic flux $\sigma T_{\rm int}^4$.

The intrinsic flux at the top of the atmosphere is, per definition, given by

$$F_{\rm int} = \sigma T_{\rm int}^4, \tag{5.15}$$

which yields a total energy output of

$$L_{\rm int} = 4\pi (R_{\rm p} + h)^2 \sigma T_{\rm int}^4, \tag{5.16}$$

where $R_{\rm p}$ is the radius of the planet at the bottom of our modelling domain and h is the height of the modelled atmosphere. The net energy transport through the surface is given by

$$L_{\rm surf} = 4\pi R_{\rm p}^2 F_{\rm surf} = 4\pi R_{\rm p}^2 (F_{\rm surf}^+ - F_{\rm surf}^-). \tag{5.17}$$

For a planet in equilibrium the atmosphere is not warming up or cooling down with time globally.

Consequently, if radiation is the only mechanism for net vertical energy transport[1], we must have $L_{\rm int} = L_{\rm surf}$, i.e.

$$4\pi(R_{\rm p}+h)^2\sigma T_{\rm int}^4 = 4\pi R_{\rm p}^2(F_{\rm surf}^+ - F_{\rm surf}^-). \tag{5.18}$$

We solve this with respect to $F_{\rm surf}^+$ and get

$$F_{\rm surf}^+ = \frac{(R_{\rm p}+h)^2}{R_{\rm p}^2}\sigma T_{\rm int}^4 + F_{\rm surf}^-. \tag{5.19}$$

It is convenient to convert $F_{\rm surf}^+$ to an equivalent black-body temperature, i.e. $F_{\rm surf}^+ \equiv \sigma T_{\rm surf}^4$, which yields

$$T_{\rm surf} = \left(\frac{(R_{\rm p}+h)^2}{R_{\rm p}^2}T_{\rm int}^4 + \frac{F_{\rm surf}^-}{\sigma}\right)^{1/4}. \tag{5.20}$$

To implement this consistently in the ES radiation scheme, Eq. (5.19) would need to be added to the equation set solved. If temporal changes in fluxes at the lower boundary are small compared to the radiative time step, however, it is possible to approximate $F_{\rm surf}^+$ in Eq. (5.19) by the value obtained at the previous radiation time step.

In the UM we have added $T_{\rm int}$ as an input parameter, and Eq. (5.20) is used to calculate the surface temperature using the value of $F_{\rm surf}^-$ at the previous radiation time step. Consequently, the value of $T_{\rm surf}$, and therefore the upward surface flux $F_{\rm surf}^+$ used in the lower boundary condition, will lag one radiative time step behind the radiative transfer calculation. If the temporal temperature variations are small at the lower boundary compared to the radiative time step this is a good approximation.

Verification

Commonly used values of the intrinsic temperature applicable to e.g. HD 209458b at its current evolutionary stage are $T_{\rm int} = 100\,{\rm K}$ to $300\,{\rm K}$. To verify the implementation of the lower boundary condition we run models of HD 209458b with parameters as in Table 5.1 except for $P_{\rm bottom} = 220\,{\rm bar}$, $R_{\rm p} = 9.44\times10^7\,{\rm m}$ and $c_P = 14\,308.4\,{\rm J/(kg\,K)}$ in this particular test. The top panel of Fig. 5.2 shows the temperature at some surface point as a function of time with $T_{\rm int} = 300\,{\rm K}$. The first few time steps are dominated by small oscillations in the surface temperature as it equilibrates. The surface temperature increases slowly with time. The dashed line, the surface temperature that would have been calculated at any given time step with $T_{\rm int} = 0\,{\rm K}$, shows that the increment in surface temperature due to the intrinsic temperature is relatively small. Also, the increment in surface temperature between radiative time steps is $\ll 1\,\%$, confirming the validity of using the downward flux at the previous time step in Eq. (5.20).

[1]This assumption is acceptable as long as the lower boundary is in the radiative regime of the atmosphere (i.e. energy transport is dominated by radiation). This is a good assumption for all models studied here. With a very deep lower boundary or high intrinsic temperature, however, a significant fraction of the vertical energy transport is due to convection and it will be necessary to revisit the lower boundary condition.

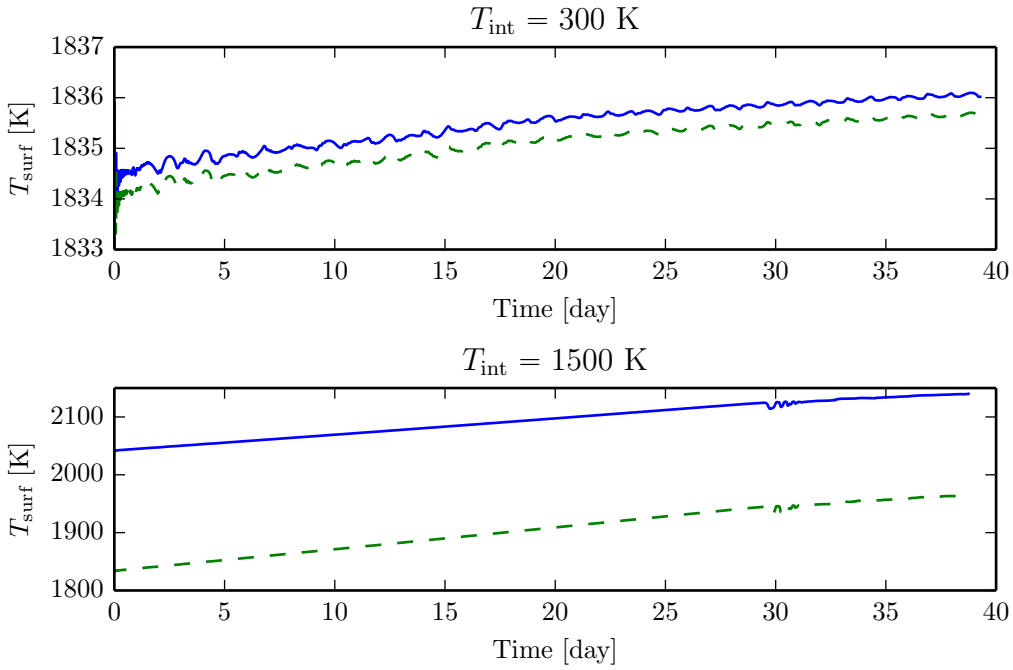

Figure 5.2: Temperature at some surface point as a function of time for two different intrinsic temperatures $T_{\rm int} = 300\,\mathrm{K}$ and $T_{\rm int} = 1500\,\mathrm{K}$. The solid line is the actual surface temperature, the dashed lines are the surface temperatures that would have been calculated at at any given time step with $T_{\rm int} = 0\,\mathrm{K}$ in Eq. (5.20), i.e. zero net flux at the lower boundary.

Also note that the surface temperature is much larger than the intrinsic temperature, $T_{\rm surf} \gg T_{\rm int}$.

The bottom panel of Fig. 5.2 shows the same as the top panel, but for an intrinsic temperature of $T_{\rm int} = 1500\,\mathrm{K}$. The increment in the surface temperature due to the intrinsic flux is significant, and this is seen to significantly affect the evolution of the surface temperature. In the first 40 days, the surface temperature increases by approximately 2 K for $T_{\rm int} = 300\,\mathrm{K}$, while for $T_{\rm int} = 1500\,\mathrm{K}$ the surface temperature increases by about 100 K. This shows that inner boundary condition indeed heats the deeper layers of the atmosphere, as expected.

5.2.5 Upper boundary condition

Ideally we would like to place the upper boundary high enough so that any absorption above it will be negligible. This may, however, be difficult to achieve as the upper boundary in the UM is located at a constant height. The day side of a hot Jupiter can reach more than 2000 K, while on the night side temperatures are much lower. Consequently, the pressure scale height will vary significantly between the day and night side, causing the upper boundary at the day side to be placed at a much higher pressure than the night side for a given model atmosphere height. This large horizontal pressure gradient has been observed to cause numerical instabilities with the ENDGAME dynamical core (Mayne et al. 2014a).

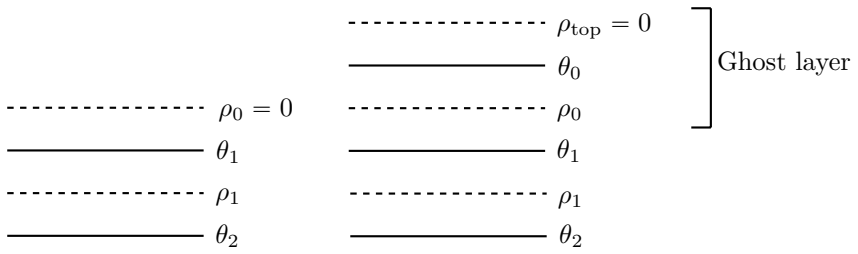

Figure 5.3: The vertical grids used by the UM dynamical core and ES radiation scheme without a ghost layer (left) and with a ghost layer (right).

We therefore need to place the upper boundary at such a height that the model can run stably while at the same time taking into account any absorption above the upper boundary on the day side. For this reason we add an extra layer, a "ghost layer", in the radiation scheme that is not included in the dynamical domain. The ES radiation scheme already included an option for this; we have adapted it to hot Jupiter-like atmospheres.

Ghost layer implementation

The vertical discretisation used by the ENDGAME dynamical core and ES radiation scheme are slightly different; we show a schematic of the vertical grids in Fig. 5.3. In the dynamical core, θ_1 is the top of the model, where θ is potential temperature. The radiation scheme uses the ρ-levels, where $\rho = \Pi$ is Exner pressure, as layer boundaries and therefore requires an additional ρ-level placed above θ_1. We label this level ρ_0, as seen in the left part of Fig. 5.3. By default $\rho_0 = 0$ and the temperature at is set to the temperature at θ_1.

With a ghost layer the situation changes slightly. Again an extra ρ_0 level not included in the dynamical core is added in the radiation scheme, but an additional θ and ρ level are also added. We label these θ_0 and ρ_{top}, as seen in the right-hand part of Fig. 5.3. The top ρ-level is placed at zero pressure, i.e. $\rho_{\text{top}} = 0$. We calculate the pressure at ρ_0 by

$$\log P_{\rho_0} = \log P_{\theta_1} - (\log P_{\rho_1} - \log P_{\theta_1}) \,, \tag{5.21}$$

while we set $\log P_{\theta_0} = (\log P_{\rho_0})/2$ and extrapolate the temperature linearly in $\log P$ to both ρ_0 and θ_0. The temperature at ρ_0 is set to zero, which effectively means the Planck function will be evaluated at the lowest temperature in our P–T grid, i.e. 70 K.

Verification

In order to verify the implementation of the ghost layer we set up the model with uniform irradiation and no rotation as discussed in Section 5.2.3. We vary the height of the upper boundary to verify that the radiative equilibrium P–T profile obtained has converged as a function of the height of the upper boundary. Parameters are as in Table 5.1 except $P_{\text{bottom}} = 220$ bar,

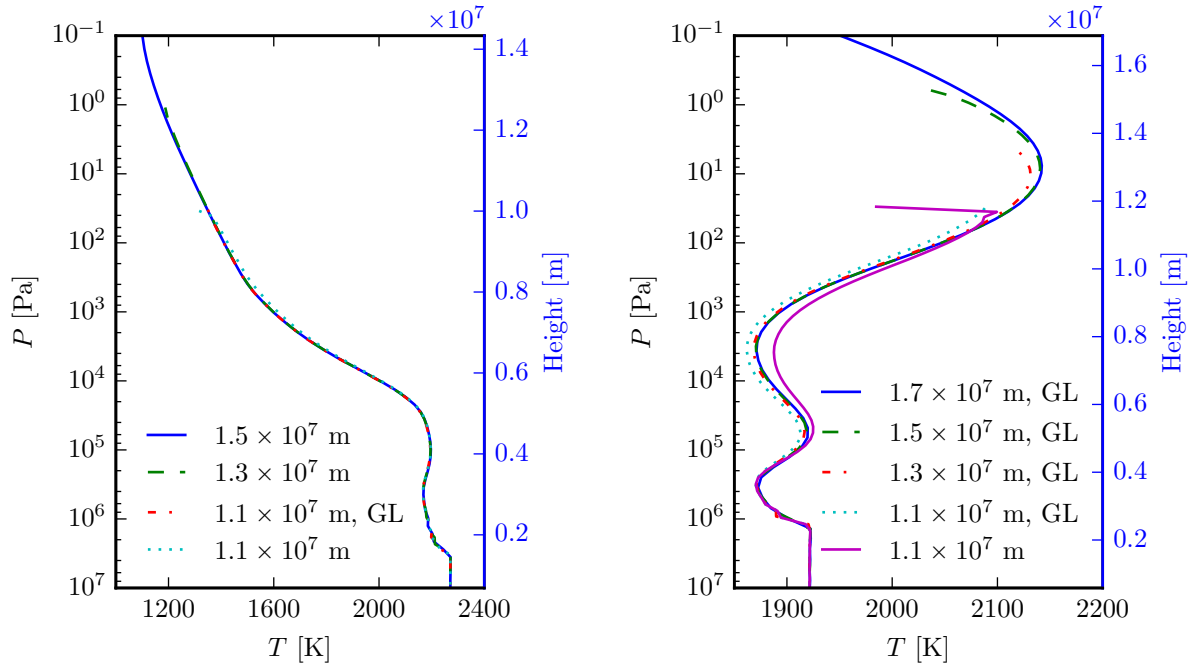

(a) Without TiO and VO. **(b)** With TiO and VO everywhere.

Figure 5.4: Equilibrium P–T profiles obtained with the UM for varying values of the height of the upper boundary. Without TiO and VO placing the upper boundary at about 40 Pa while including the ghost layer (GL) is sufficient to match the profile with a higher upper boundary, while with TiO and VO (everywhere) the upper boundary must be placed at a lower pressure, about 4 Pa, also including the ghost layer. The height axis has been included for the set-ups with the highest upper boundary.

$R_\mathrm{p} = 9.44 \times 10^7$ m and $c_P = 14\,308.4$ J/(kg K). We set $\mu_0 = 1$ and initialise the model with equilibrium profiles from `ATMO`. We find that the UM has converged to an equilibrium profile for pressures < 1 bar after a few days. In Fig. 5.4 we show the obtained UM P–T profiles for various heights of the upper boundary both with and without TiO and VO. The legend numbers give the height of the upper boundary, while the abbreviation GL indicates that a ghost layer was included.

Without TiO and VO the differences between the equilibrium profiles are small. The profile with the upper boundary at 1.1×10^7 m including the ghost layer is better than that obtained without the ghost layer, as can be seen by comparing to profiles with a larger vertical domain. The small numerical discrepancy at the top of the profile with an atmosphere height of 1.1×10^7 m without the ghost layer indicates that the radiation is not properly resolved. This feature is seen to disappear when including the ghost layer.

With TiO and VO present throughout the atmosphere temperatures become significantly higher, causing an inflation of the atmosphere, and the upper boundary must be placed at a larger height. This is also needed due to the very strong absorption by TiO and VO even at small pressures. Placing the upper boundary at about 4 Pa when including a ghost layer is seen to cause only minor deviations, $\lesssim 10$ K, comparing to a profile with a higher upper boundary.

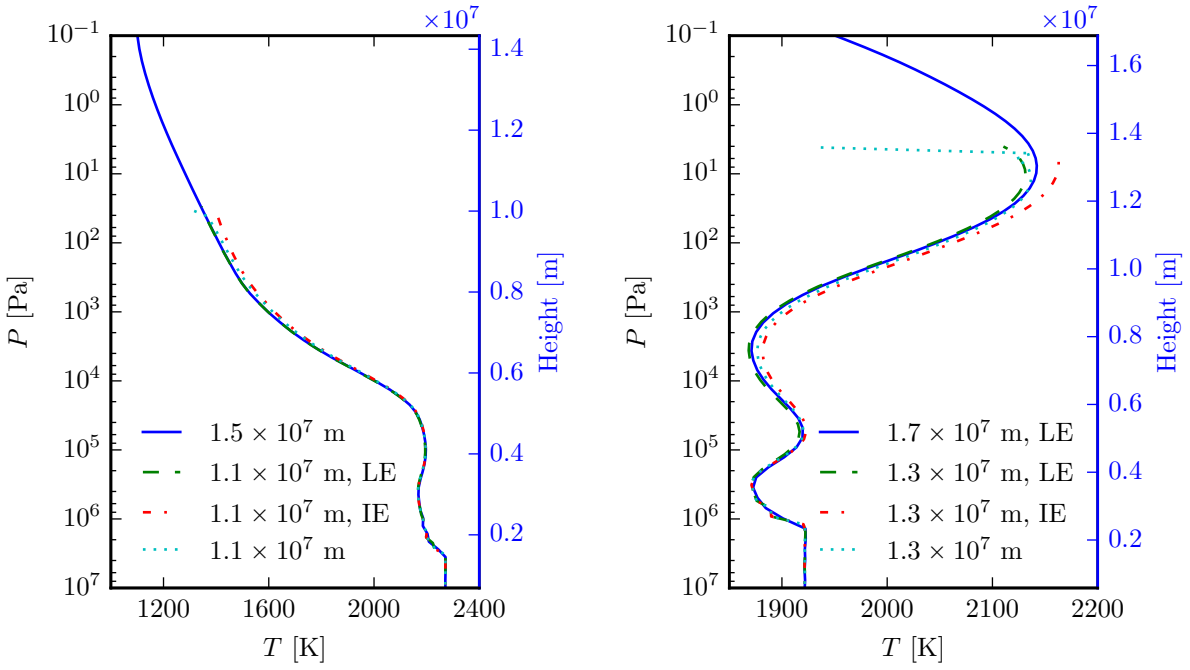

(a) Without TiO and VO. **(b)** With TiO and VO everywhere.

Figure 5.5: Equilibrium P–T profiles obtained with the UM using the linear extrapolation (LE) and isothermal extrapolation (IE) schemes for the ghost layer temperatures. Profiles without extrapolation label were obtained without the ghost layer. The height axis has been included for the set-ups with the highest upper boundary.

Again the profile with the upper boundary placed too low (1.1×10^7 m) without a ghost layer is seen to exhibit an unphysical numerical feature at the top due to the unresolved absorption.

Previously the Met Office used an isothermal extrapolation scheme, keeping the temperature constant above the highest θ-level. In Fig. 5.5 we compare our linear extrapolation (LE) scheme for the ghost layer to the isothermal extrapolation (IE) scheme. We see that our new extrapolation scheme is indeed an improvement, both with and without TiO and VO.

5.3 Comparison between the UM and `ATMO`

In this section we compare radiative equilibrium profiles obtained with the UM and `ATMO`. We use the uniform irradiation option described in Section 5.2.3 and no rotation in the UM. Model set-ups are as similar as possible, see Table 5.1, with the same gravity at the lower boundary, intrinsic temperature and chemistry. `ATMO` has difficulties converging profiles where abundances of molecules change rapidly. In place of the abundances of Na, K, TiO and VO described in Section 3.6 we therefore enforce in both `ATMO` and the UM constant abundances equal to the maximum possible abundance for Na, K, TiO and VO.

As discussed in Section 5.2.2 a redistribution factor f may be included in the model to

take into account redistribution of heat from the day side to the night side. The effective area receiving irradiation is $\pi R_{\rm p}^2$, while the total area of the planet is $4\pi R_{\rm p}^2$, i.e. a ratio of 1/4 between irradiated area and planet area. Our use of $\mu_0 = 0.5$ already reduces the flux at the top of the atmosphere by a factor of 1/2. Consequently we further reduce the top-of-atmosphere flux by a factor $f = 0.5$ for redistribution over the entire planet and $f = 1$ for day side redistribution only.

We initialise the UM using the equilibrium P–T profiles obtained with `ATMO` and find that at pressures $\lesssim 10^5$ Pa the profile has converged after about 1 d (one Earth day). In Fig. 5.6 we show the P–T profiles obtained with both `ATMO` and the UM after 10 d of simulation time for $\mu_0 = 0.5$ and $f = 0.5$ and 1. Without TiO and VO the agreement is very good, only small differences are seen for both $f = 0.5$ and 1. With TiO and VO present everywhere differences are larger, but still $\lesssim 6\,\%$. It is difficult to determine exactly what these differences are caused by, but even though we have tried to make the model set-ups in the UM and `ATMO` as similar as possible there are differences in the approximations made. For example the mean molecular weight is computed consistently in `ATMO` while held constant in the UM, `ATMO` combines k-coefficients for gases using the random overlap method with reordering and resampling as described in Section 3.4.2, slightly different Rayleigh scattering cross sections are used, but the biggest difference is most likely caused by the angular resolution in the radiative transfer equation and treatment of overlapping absorption. Unfortunately this is difficult to test since lowering the angular resolution in `ATMO` will yield incorrect fluxes as the intensity cannot be integrated properly with 2 quadrature points. In addition the random overlap method with reordering and resampling is not implemented in the ES scheme, and equivalent extinction is not implemented in `ATMO`. We consider the differences observed, which are $\lesssim 6\,\%$ for both cases, acceptable.

5.4 Numerical problems with discontinuous abundances

Models of HD 209458b proved difficult to run when including TiO and VO. We found that the stability of the models was improved by introducing a smoother abundance change compared to simply setting a particular abundance to zero below the condensation temperature. We choose a Fermi-Dirac distribution in temperature, yielding an abundance profile

$$\phi(T) = \frac{1}{e^{-(T-T_{\rm crit})/\Delta T_{\rm char}} + 1}, \tag{5.22}$$

where $T_{\rm crit}$ is the critical temperature for condensation and $\Delta T_{\rm char}$ is the characteristic scale over which the abundance changes. In Fig. 5.7 we have plotted the relative abundance profile as a function of temperature for $T_{\rm crit} = 1000\,{\rm K}$ and $\Delta T_{\rm char} = 10\,{\rm K}$. The temperature range over which the transition occurs is very small, and thus should not affect our final results significantly. Also, a smoothing can be justified by the fact that temperature fluctuations within a layer can cause absorbers to not be completely condensed out if the temperature is close to the condensation temperature, even in equilibrium. In our hot Jupiter GCM runs presented in

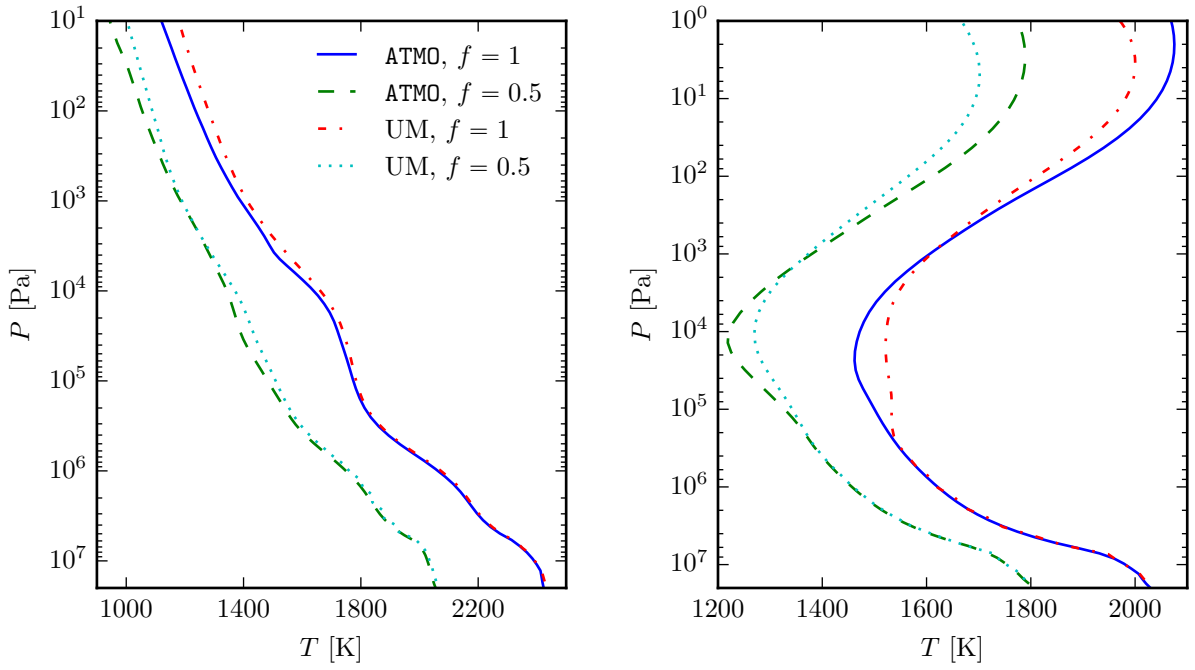

(a) Without TiO and VO.

(b) With TiO and VO everywhere.

Figure 5.6: Equilibrium P–T profiles obtained with `ATMO` and the UM (after 10 d, where 1 d is an Earth day). Differences are small without TiO and VO, $\lesssim 4\,\%$, while including TiO and VO everywhere differences are larger, $\lesssim 6\,\%$, but still acceptable.

Chapter 6 we use Eq. (5.22) for Na, K, TiO, VO and O with $\Delta T_{\text{char}} = 10\,\text{K}$ and with T_{crit} set to the condensation or chemical transformation temperature for each absorber as described in Section 3.6.

5.5 Synthetic observations

As discussed in Section 1.2 observations of hot Jupiters are mainly on the form of phase curves, emission and transmission spectra. In this section we describe how we calculate synthetic observations from both 1D P–T profiles and from 3D UM output. We use the framework of the discrete ordinate line-by-line code `ATMO`, described in Section 4.1.2, to calculate synthetic observations. In Section 5.5.1 we describe the calculation of transmission spectra[2], Section 5.5.2 explains how emission spectra are calculated, and finally in Section 5.5.3 calculation of phase curves is discussed.

[2]Pierre Mourier (a summer student) developed a preliminary version of the code to calculate transmission spectra from 1D P–T profiles. I have rewritten it and developed the capability of calculating synthetic transmission spectra from UM output.

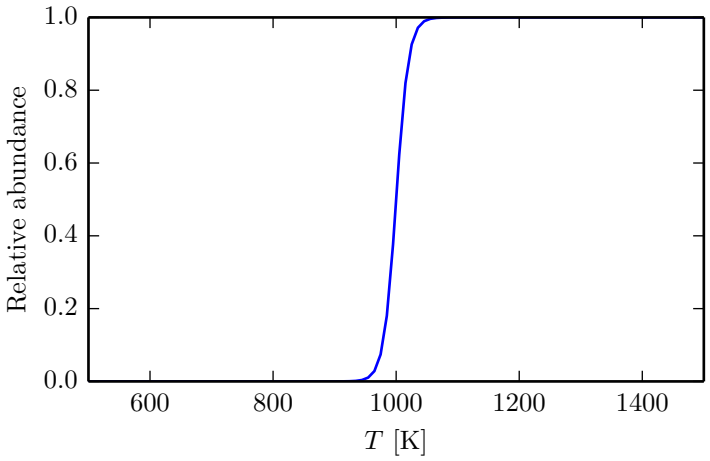

Figure 5.7: The relative abundance profile used for species with parametrised abundances, i.e. Na, K, TiO, VO and O (see Section 3.6). This is used to improve the stability of the model compared to using a step function.

5.5.1 Transmission spectroscopy

The ratio of the area of a completely opaque planetary disk and the stellar disk is given by the ratio between the absorbed stellar flux and the total stellar flux observed at Earth,

$$\frac{R_{\mathrm{p,eff}}(\tilde{\nu})^2}{R_*^2} = \frac{F_*^{\mathrm{abs}}}{F_*}, \tag{5.23}$$

where $R_{\mathrm{p,eff}}(\tilde{\nu})$ is the effective radius of the planet as a function of wavenumber, R_* is the stellar radius, F_*^{abs} is the stellar flux absorbed by the planetary atmosphere and F_* is the stellar flux, both as observed at Earth.

A small correction applies to the previous expression to take into account the thermal emission from the the planet night side,

$$\frac{R_{\mathrm{p,eff}}^{\mathrm{obs}}(\tilde{\nu})^2}{R_*^2} = \frac{F_*^{\mathrm{abs}}}{F_{\mathrm{p}} + F_*}, \tag{5.24}$$

where F_{p} is the flux emitted by the planet. We can express $R_{\mathrm{p,eff}}^{\mathrm{obs}}(\tilde{\nu})$ in terms of $R_{\mathrm{p,eff}}(\tilde{\nu})$ with a correction factor:

$$\frac{R_{\mathrm{p,eff}}^{\mathrm{obs}}(\tilde{\nu})^2}{R_*^2} = \frac{F_*^{\mathrm{abs}}}{F_{\mathrm{p}} + F_*} = \frac{F_*^{\mathrm{abs}}/F_*}{F_{\mathrm{p}}/F_* + 1} = \frac{R_{\mathrm{p,eff}}(\tilde{\nu})^2/R_*^2}{F_{\mathrm{p}}/F_* + 1}, \tag{5.25}$$

which means we have

$$R_{\mathrm{p,eff}}^{\mathrm{obs}}(\tilde{\nu})^2 = \frac{R_{\mathrm{p,eff}}(\tilde{\nu})^2}{1 + F_{\mathrm{p}}/F_*}. \tag{5.26}$$

Thermal emission from the planet is not included in the synthetic observations presented here as $F_{\mathrm{p}}/F_* \ll 0.001$ for wavelengths where observations are available, see Figs. 6.22 and 6.25.

We show the geometry in Fig. 5.8, where the stellar rays going towards the observer are

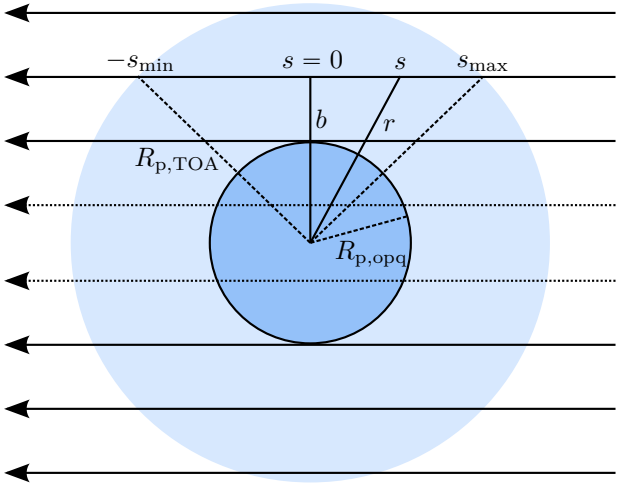

Figure 5.8: Schematic showing the geometry of the transmission spectrum. Rays going from the star to the observer through the planet atmosphere are shown as arrows. The planet is assumed to be optically thick below the atmosphere at a radius $r = R_{\mathrm{p,opq}}$. The impact parameter b is the radial distance between the centre of the planet and the rays, while s is the path coordinate following the direction of the rays from the top of the atmosphere on one side, $s_{\max}$, to the other side, $-s_{\min}$. The optical depth of the atmosphere $\tilde{\tau}$ is calculated along these rays.

shown as arrows. The stellar flux observed at Earth is

$$F_* = F_*^{\mathrm{surf}} \frac{R_*^2}{D_{\mathrm{o}}^2}, \tag{5.27}$$

where F_*^{surf} is the surface flux of the star and D_{o} is the distance between the star and the observer.

The stellar flux absorbed by the planet is similarly given by

$$F_*^{\mathrm{abs}} = \frac{1}{\pi D_{\mathrm{o}}^2} \int_0^{2\pi} \mathrm{d}\phi \int_0^{\infty} b \,\mathrm{d}b \, F_*^{\mathrm{surf}}(b,\phi) \left(1 - e^{-\tilde{\tau}(b,\phi)}\right) \tag{5.28}$$

$$= \frac{F_*^{\mathrm{surf}}}{\pi D_{\mathrm{o}}^2} \int_0^{2\pi} \mathrm{d}\phi \int_0^{R_{\mathrm{p,TOA}}} b \,\mathrm{d}b \, \left(1 - e^{-\tilde{\tau}(b,\phi)}\right), \tag{5.29}$$

where $\tilde{\tau}(b,\phi)$ is the optical depth of the atmosphere, $R_{\mathrm{p,TOA}}$ is the radius at the top of the atmosphere and $F_*^{\mathrm{surf}}(b,\phi)$ is the surface flux of the star in the direction of the observer. We assumed that the stellar surface flux is constant when the integrand is non-zero, i.e. over the planet disk. The planet is assumed completely opaque below a certain impact parameter

$b = R_{\mathrm{p,opq}}$, typically the bottom of a model atmosphere, and Eq. (5.29) becomes, using Eq. (5.27),

$$F_*^{\mathrm{abs}} = \frac{F_*}{\pi D_{\mathrm{o}}^2}\left[\int_0^{2\pi}\mathrm{d}\phi\int_0^{R_{\mathrm{p,opq}}} b\,\mathrm{d}b + \int_0^{2\pi}\mathrm{d}\phi\int_{R_{\mathrm{p,opq}}}^{R_{\mathrm{p,TOA}}} b\,\mathrm{d}b\,\left(1-e^{-\tilde{\tau}(b,\phi)}\right)\right] \tag{5.30}$$

$$= \frac{F_*}{\pi D_{\mathrm{o}}^2}\left[\pi R_{\mathrm{p,opq}}^2 + \int_0^{2\pi}\mathrm{d}\phi\int_{R_{\mathrm{p,opq}}}^{R_{\mathrm{p,TOA}}} b\,\mathrm{d}b\,\left(1-e^{-\tilde{\tau}(b,\phi)}\right)\right] \tag{5.31}$$

With a one-dimensional pressure–temperature profile

For one-dimensional P–T profiles the planet atmosphere is assumed to be spherically symmetric. In Eq. (5.31) this means that $\tilde{\tau}(b,\phi)$ is independent of ϕ, and we get

$$F_*^{\mathrm{abs}} = \frac{F_*}{\pi D_{\mathrm{o}}^2}\left[\pi R_{\mathrm{p,opq}}^2 + 2\pi\int_{R_{\mathrm{p,opq}}}^{R_{\mathrm{p,TOA}}} b\,\mathrm{d}b\,\left(1-e^{-\tilde{\tau}(b)}\right)\right]. \tag{5.32}$$

Inserting Eqs. (5.27) and (5.32) into Eq. (5.23), we get

$$\frac{R_{\mathrm{p,eff}}(\tilde{\nu})^2}{R_*^2} = \frac{R_{\mathrm{p,opq}}^2 + 2\int_{R_{\mathrm{p,opq}}}^{R_{\mathrm{p,TOA}}} b\,\mathrm{d}b\,\left(1-e^{-\tilde{\tau}(b)}\right)}{R_*^2}, \tag{5.33}$$

which yields

$$R_{\mathrm{p,eff}}(\tilde{\nu})^2 = R_{\mathrm{p,opq}}^2 + 2\int_{R_{\mathrm{p,opq}}}^{R_{\mathrm{p,TOA}}} b\,\mathrm{d}b\,\left(1-e^{-\tilde{\tau}(b)}\right). \tag{5.34}$$

Using Fig. 5.8, the optical depth for a given impact parameter is given by

$$\tilde{\tau}(b) = \int_{-s_{\min}}^{s_{\max}} \mathrm{d}s\, k_\rho(\tilde{\nu},s)\rho(s) = 2\int_0^{s_{\max}} \mathrm{d}s\, k_\rho(\tilde{\nu},s)\rho(s), \tag{5.35}$$

where the path s is given by

$$s = \sqrt{r^2-b^2}, \qquad r = \sqrt{s^2+b^2}, \tag{5.36}$$

and $s_{\max} = \sqrt{R_{\mathrm{p,TOA}}^2 - b^2}$.

With three-dimensional output from the UM

With the full output from the UM the atmosphere can no longer be assumed to be spherically symmetric, and we cannot make the simplifications made previously. The integral in Eq. (5.31) needs to be calculated explicitly. Using Eqs. (5.23), (5.27) and (5.31) we get

$$\frac{R_{\mathrm{p,eff}}(\tilde{\nu})^2}{R_*^2} = \frac{\pi R_{\mathrm{p,opq}}^2 + \int_0^{2\pi}\mathrm{d}\phi\int_{R_{\mathrm{p,opq}}}^{R_{\mathrm{p,TOA}}} b\,\mathrm{d}b\,\left(1-e^{-\tilde{\tau}(b,\phi)}\right)}{\pi R_*^2}. \tag{5.37}$$

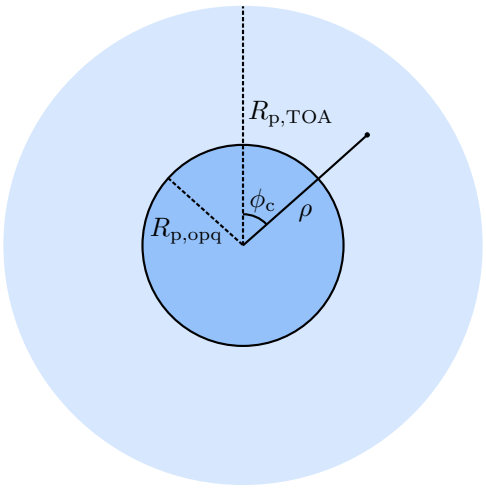

Figure 5.9: Schematic of the cylindrical grid constructed to integrate over the planet hemisphere when calculating transmission spectra from UM output. The optical depth $\tilde{\tau}$ is calculated for each radial distance ρ and azimuth angle ϕ_{c}.

The optical depth integral also need to be calculated explicitly:

$$\tilde{\tau}(b, \phi_{\mathrm{c}}) = \int_{-s_{\mathrm{min}}}^{s_{\mathrm{max}}} \mathrm{d}s \, k_{\rho}(\tilde{\nu}, b, \phi_{\mathrm{c}}, s) \rho(b, \phi_{\mathrm{c}}, s), \tag{5.38}$$

where s_{min} and s_{max} is the top of the atmosphere for a given value of the impact parameter b.

The geometry is shown in Fig. 5.9 where the observer is located into the page, directly opposite the star. The optical depth $\tilde{\tau}$ needs to be integrated for all values of the cylindrical coordinates ρ and ϕ_{c}.

5.5.2 Emission spectrum

Given a P–T profile `ATMO` can calculate the intensity at the top of the atmosphere, $I_{\mathrm{TOA}}(\theta, \phi, \vartheta, \varphi)$, where (θ, ϕ) are the latitude and longitude, and (ϑ, φ) is the direction of the radiation in the same coordinate system. To derive an expression for the measured planet flux we need to be a bit more careful than in the derivation of the transmission radius to take into account planetary limb darkening. We follow the derivation in Seager (2010), but retain the full angular notation of the intensity for clarity.

The geometry is shown in Fig. 5.10. To ease notation we assume the z axis to point towards the observer. To obtain the measured flux, we need to integrate over the planetary disk as seen from the observer. The intensity in the direction of the observer at (θ, ϕ) is given by $I_{\mathrm{s}}(\theta, \phi, \vartheta_{\mathrm{o}}, \varphi_{\mathrm{o}})$. Due to the orientation of the z axis towards the observer, the angle ϕ will be the same at both the planet and the observer. The observed flux at Earth is then given by

$$F_{\mathrm{o}} = \int_0^{2\pi} \int_0^{R_{\mathrm{p,TOA}}/D_{\mathrm{o}}} I_{\mathrm{s}}(\theta, \phi, \vartheta_{\mathrm{o}}, \varphi_{\mathrm{o}}) \sin\omega \, \mathrm{d}\omega \mathrm{d}\phi, \tag{5.39}$$

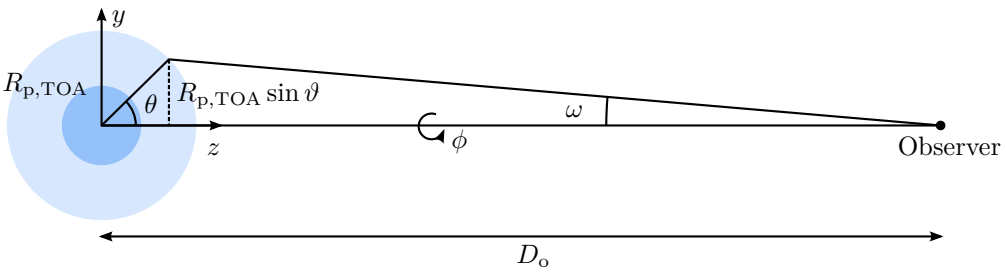

Figure 5.10: Schematic of the geometry of the emission of a planet as observed at Earth. The azimuth angle ϕ is the same at both the planet and observer. The observer azimuth angle ω can be replaced by the planet azimuth angle θ by the relation $\omega = (R_{\mathrm{p,TOA}}/D_{\mathrm{o}}) \sin\theta$ since the planet radius at the top of the atmosphere, $R_{\mathrm{p,TOA}}$, is much smaller than the distance between the planet and the observer, D_{o}.

where $(\vartheta_{\mathrm{o}}, \varphi_{\mathrm{o}})$ is the direction of the observer, $R_{\mathrm{p,TOA}}$ is the radius of the planet at the top of the (model) atmosphere, ω is the angle between the line between the observer and the position on the disk and the line between the planet and the observer (z-axis), and D_{o} is the distance between the planet and the observer. From Fig. 5.10 we see that ω is related to θ by

$$\omega = \frac{R_{\mathrm{p,TOA}}}{D_{\mathrm{o}}} \sin\theta, \qquad \mathrm{d}\omega = \frac{R_{\mathrm{p,TOA}}}{D_{\mathrm{o}}} \cos\theta \, \mathrm{d}\theta \tag{5.40}$$

Using $R_{\mathrm{p,TOA}} \ll D_{\mathrm{o}}$ we have $\omega \ll 1$ and can approximate $\cos\omega \approx 1$ and $\sin\omega \approx \omega$. This yields

$$F_{\mathrm{o}} = \left(\frac{R_{\mathrm{p,TOA}}}{D_{\mathrm{o}}}\right)^2 \int_0^{2\pi} \int_0^{\pi/2} I_{\mathrm{s}}(\theta, \phi, \vartheta_{\mathrm{o}}, \varphi_{\mathrm{o}}) \cos\theta \sin\theta \, \mathrm{d}\theta \mathrm{d}\phi. \tag{5.41}$$

From `ATMO`, we get $I'_{\mathrm{s}}(\theta, \phi, \vartheta', \varphi')$ for each column, where (ϑ', φ') is the direction of the radiation in a coordinate system where z is normal to the planet surface. Since the radiation calculation is 1D and plane parallel, the intensity is independent of φ', and we drop the φ' notation from now on. The surface normal at (θ, ϕ) is, by necessity, (θ, ϕ). Since the observer is located in the direction of the z axis, the angle between the direction of the observer and the surface normal is θ, i.e. $\vartheta'_{\mathrm{o}} = \theta$ and the intensity in the direction of the observer becomes

$$I_{\mathrm{s}}(\theta, \phi, \vartheta_{\mathrm{o}}, \varphi_{\mathrm{o}}) = I'_{\mathrm{s}}(\theta, \phi, \vartheta'_{\mathrm{o}} = \theta), \tag{5.42}$$

where I'_{s} is the intensity as calculated by `ATMO`. This gives us a way of relating the intensity as calculated by `ATMO` to the intensity in Eq. (5.41).

5.5.3 Phase curve

The phase curve is essentially the emission from the planet, as viewed from Earth, as a function of time or phase angle, as shown in Fig. 5.11. The integrated emission as a function of time, or orbital phase, is given by Eq. (5.41) for different observer directions $(\vartheta_{\mathrm{o}}, \varphi_{\mathrm{o}})$. The direction of the observer in the coordinate system of the planet, ϕ_{o}, is given by the phase angle $\alpha \in [0, 2\pi)$,

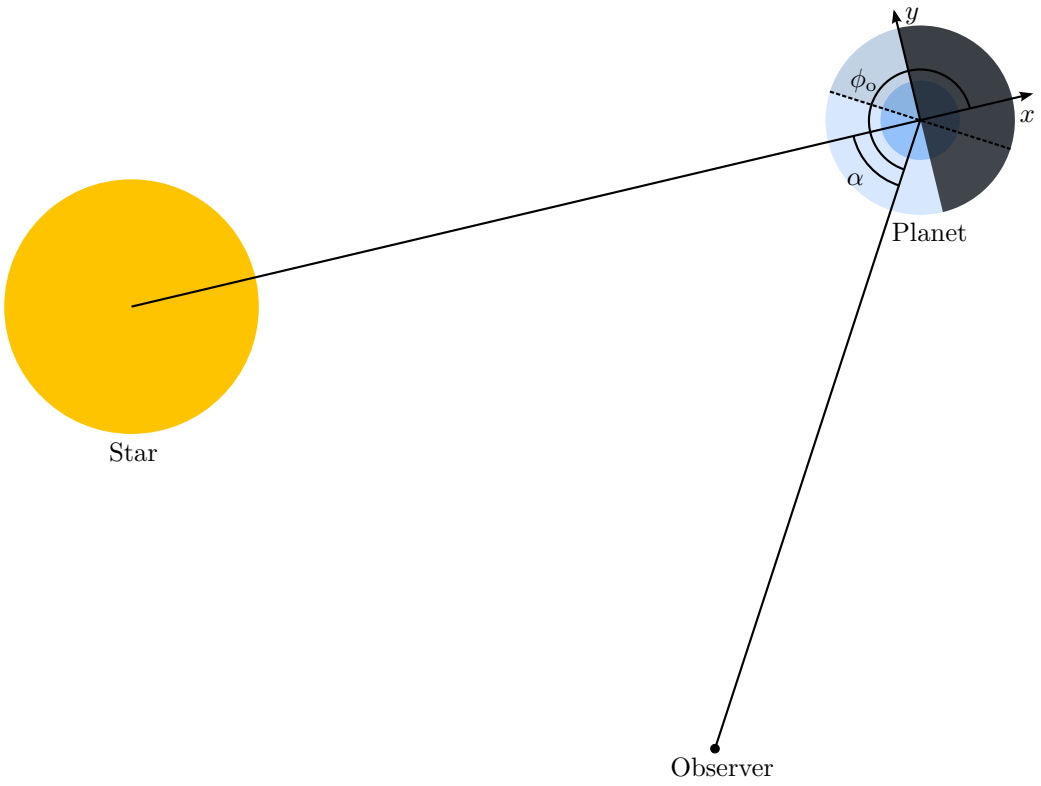

Figure 5.11: Schematic showing the phase curve geometry. The direction of the observer in the coordinate system of the planet where the z axis points towards the north pole is given by $\phi_o = \pi + \alpha$ where α is the phase angle. The dark region of the planet is the night side of the planet, while the dotted line indicates the hemisphere viewed from Earth.

$\phi_o = \pi + \alpha$ from Fig. 5.11. Assuming the planet is tidally locked and in a steady-state the intensity at the top of the atmosphere for a given latitude and longitude will be constant as a function of time. This simplification enables us to calculate intensities at the top of the atmosphere only once for the entire phase curve, greatly decreasing the computation time. As Fortney et al. (2006a) we ignore the small inclination of the orbit.

5.6 Summary and conclusions

In this chapter we have briefly presented the UM dynamical core ENDGAME and discussed how it is coupled to the radiation scheme through the thermodynamic equation. We have also presented our default HD 209458b model set-up and detailed changes made to the boundary conditions. A uniform irradiation mode was implemented, essentially turning the UM into a 1D radiative equilibrium solver, and resulting P–T profiles were compared to the 1D radiative equilibrium code `ATMO`. Good agreement was found with temperature differences $\lesssim 6\,\%$. We have also discussed how synthetic transmission spectra, emission spectra and phase curves can be calculated from UM output.

In the next chapter we apply our coupled hot Jupiter UM for the first time to a hot Jupiter, HD 209458b.

Chapter 6

The coupled UM applied to HD 209458b

In Chapter 5 we described the coupling of the ES radiation scheme adapted to hot Jupiters to the UM dynamical core ENDGAME and subsequent testing. In this chapter we apply this model to the well-studied hot Jupiter HD 209458b. It was the first transiting exoplanet discovered, and transmission and emission spectra, in addition to one phase curve, are now available. HD 209458b has also been a frequent target of modelling work as discussed in Sections 1.3 and 1.4. This makes it an ideal target for the first application of the hot Jupiter UM.

Before discussing our model results we discuss existing observations for this planet in Section 6.1 (for a discussion of models see Sections 1.3 and 1.4). Next, in Section 6.2 we discuss our GCM results. The temperature-forced model of HD 209458b from Mayne et al. (2014a) is briefly reproduced in Section 6.2.1 before discussing the coupled model in Sections 6.2.2 and 6.2.3. Since the presence of TiO and VO in hot Jupiter atmospheres is highly debated we have run models both where we do not and do allow TiO and VO to form (Sections 6.2.2 and 6.2.3, respectively). We compare our models to observations, producing synthetic phase curves, emission and transmission spectra in Section 6.3.

6.1 Available observations of HD 209458b

HD 209458b is one of the most well-observed exoplanets to date, and was the first planet observed to transit its parent star (Charbonneau et al. 2000; Henry et al. 2000). Together with radial velocity measurements of the parent star (Butler et al. 2006; Mazeh et al. 2000) this has provided constraints on the mass, radius and bulk density of the planet. It was found to be much less dense than Jupiter, the latest measurements giving a mass of $0.690 M_{\rm Jup} \pm 0.024 M_{\rm Jup}$ (Butler et al. 2006) and a radius of $1.359 R_{\rm Jup} \pm 0.015 R_{\rm Jup}$ (Torres et al. 2008)[1].

[1] `http://exoplanets.org/detail/HD_209458_b`

Charbonneau et al. (2002) detected sodium absorption by the atmosphere of HD 209458b using transit spectroscopy, and this has since initiated extensive research aiming to detect other atoms and molecules, and to constrain temperatures in the atmosphere. Thermal emission from the planet was detected by Deming et al. (2005) using Spitzer 24 µm secondary eclipse measurements, with emission at shorter IR wavelengths later observed by Swain et al. (2008) and Knutson et al. (2008), also using Spitzer. Swain et al. (2008), with data from 7.46 µm to 15.25 µm, found that 1D models accounting for significant heat redistribution between the day and night side of the planet best fit the observations. On the other hand, Knutson et al. (2008), using data between 3.6 µm to 8.0 µm, found that standard atmosphere models did not fit the data particularly well and suggested the presence of a thermal inversion layer to explain this. Using the NICMOS instrument on the Hubble Space Telescope (HST) to observe HD 209458b during secondary transit, Swain et al. (2009) claimed detection of water, methane and CO_2 features in the day side emission spectrum.

The thermal inversion invoked to explain observations in Knutson et al. (2008) is, however, debated. A reanalysis of all available Spitzer secondary-eclipse data performed by Diamond-Lowe et al. (2014) found that it was unnecessary to introduce a temperature inversion in order to fit the day side emission data to models, and concluded that there is no evidence for a temperature inversion in the atmosphere of HD 209458b after all.

Zellem et al. (2014) measured the 4.5 µm full-orbit phase curve using the IRAC instrument on Spitzer, and found the brightness temperature for the day side and night side to be (1499 ± 15) K and (972 ± 44) K, respectively. Small deviations from GCM predictions from Showman et al. (2009) were found, and were taken as an indication of disequilibrium chemistry or deficiencies in the CH_4 line list. The new measurement of the day side 4.5 µm flux in Zellem et al. (2014) is much closer to the reanalysis of the data from Knutson et al. (2008) by Diamond-Lowe et al. (2014) than the original analysis in Knutson et al. (2008).

Sing et al. (2008) used STIS on HST to obtain the transmission spectrum at visible wavelengths and confirmed sodium absorption as detected by Charbonneau et al. (2002). Deming et al. (2013), using the WFC-3 instrument on HST, detected a muted water feature in the near-IR transmission spectrum.

By measuring the Doppler signature of the planet itself using ground-based transmission spectroscopy, Snellen et al. (2010) was able to detect a Doppler shift of (2 ± 1) km/s of CO spectral lines in the transmission spectrum. This is, as of yet, the only constraint on wind velocities on an exoplanet. Using similar techniques Hoeijmakers et al. (2014) attempted to detect TiO in the optical transmission spectrum, but failed due to inaccuracies in the high temperature line list for TiO. Schwarz et al. (2015) looked for CO in the high resolution day side emission spectrum at 2.3 µm, but failed to detect a signal. As CO has been detected in the transmission spectrum (Snellen et al. 2010), this indicates that the atmosphere is close to isothermal at the pressures probed by these measurements.

In conclusion there are many observations available of HD 209458b, with detections of

water, sodium, and CO, and inferred detections of methane and CO_2. Measured brightness temperatures indicate that the redistribution of heat between the day and night side is significant, but there does not seem to be conclusive evidence for a temperature inversion. In order to better understand these observations 3D atmosphere models are needed.

6.2 General circulation models of HD 209458b

In this section we present results from our GCM simulations of the atmosphere of HD 209458b. We briefly present the temperature-forced model from Mayne et al. (2014a) in Section 6.2.1, and discuss the coupled models where we do not and do allow TiO and VO to form in Sections 6.2.2 and 6.2.3, respectively. In Section 6.3 we use these results to calculate synthetic observations and compare these to available observations of HD 209458b.

6.2.1 The temperature-forced model from Mayne et al. (2014a)

The results from the temperature-forced model are discussed in detail in Mayne et al. (2014a). In this section we include results from this model sampled at the same times as the coupled model run presented in Section 6.2.2 for convenience.

As discussed in Section 1.4.1, temperature-forcing schemes force the temperature towards assumed equilibrium P–T-profiles on some timescale, $\tau_{\rm rad}$. The heating rate $\dot{Q}$ as stated in Eq. (5.10) is given by

$$\dot{Q} = \dot{Q}_{\rm TF} = -\mathit{\Pi}\left(\frac{\theta - \theta_{\rm eq}}{\tau_{\rm rad}}\right) c_P, \tag{6.1}$$

where $\theta_{\rm eq}$ is the equilibrium potential temperature. $T_{\rm eq} = \theta_{\rm eq}(P/P_0)^{\mathcal{R}/c_P}$, the equilibrium temperature, is modified as a function of longitude and latitude to take into account the varying stellar zenith angle on the day side:

$$T_{\rm eq} = \begin{cases} \left[T_{\rm night}^4 + \left(T_{\rm day}^4 - T_{\rm night}^4\right)\cos(\lambda - 180°)\cos\phi\right]^{\frac{1}{4}}, & 90° \leqslant \lambda \leqslant 270°, \\ T_{\rm night}, & \text{otherwise}, \end{cases} \tag{6.2}$$

where $T_{\rm night}$ and $T_{\rm day}$ are the equilibrium night and day side P–T profiles, respectively, which we show in Fig. 6.1a. The sub-stellar point is consequently located at longitude $\lambda = 180°$, latitude $\phi = 0°$. The equlibrium temperature profiles and radiative timescales, shown in Fig. 6.1b are from Iro et al. (2005), as described in Heng et al. (2011) and Mayne et al. (2014a).

In order to gain a better understanding of $\tau_{\rm rad}$ it is instructive to derive a simple estimate from analytical arguments. Consider an atmospheric layer with mass M and cross-sectional area A. In radiative equilibrium it will emit as much energy as it absorbes, i.e.

$$F_{\rm eq}^{\rm em} = \sigma T_{\rm eq}^4 = F_{\rm eq}^{\rm abs}, \tag{6.3}$$

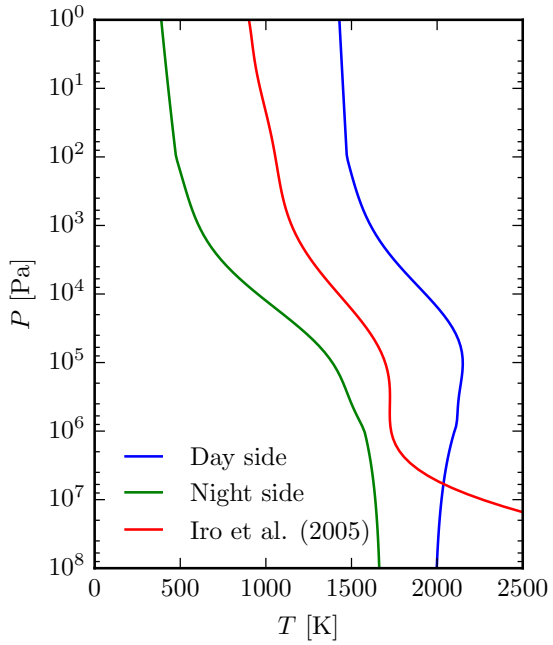

(a) Equilibrium forcing profiles from Iro et al. (2005) as adopted by Heng et al. (2011) and modified by Mayne et al. (2014a) (day and night side profiles).

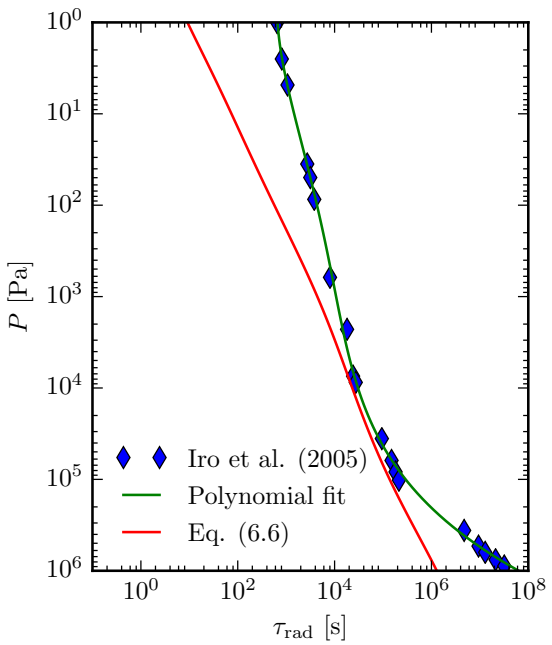

(b) Radiative timescales from Iro et al. (2005) as adopted by Heng et al. (2011) (polynomial fit). Also shown is the prediction using Eq. (6.6) with the P–T profile from Iro et al. (2005) shown in Fig. 6.1a.

Figure 6.1: Equilibrium P–T profiles and radiative time scales used in the temperature-forced model of HD 209458b.

where σ is Boltzmann's constant. If the temperature is perturbed slightly, $T = T_{\rm eq} + \Delta T$, the thermal emission will change but the absorption will be approximately the same. The change in emitted flux is approximately

$$\Delta F_{\rm em} = 4\sigma T^3 \Delta T, \tag{6.4}$$

And the time required to bring the layer back to the equilibrium temperature is given by

$$\tau_{\rm rad} \approx \frac{c_P M \Delta T}{\Delta F_{\rm em} A} = \frac{c_P M}{4\sigma T^3 A}. \tag{6.5}$$

In hydrostatic equilibrium the weight of the layer must be balanced by the pressure, $Mg = A\Delta P$. Assuming the layer to have a fixed height as a function of pressure we have $\Delta P \approx P$, and consequently

$$\tau_{\rm rad} \approx \frac{c_P P}{4g\sigma T^3} = \frac{c_P \rho R}{4g\sigma T^2 \bar{m}}, \tag{6.6}$$

where we have used the ideal gas equation. The temperature T normally varies by a factor of 2 to 3, while the density and pressure vary by many orders of magnitude. The main reason for the increase in the radiative timescale with atmospheric depth, as seen in Fig. 6.1b, is the increase in density causing a set amount of heating to yield a smaller ΔT at larger pressures compared to

smaller pressures. We have plotted the radiative timescale as given by Eq. (6.6) in Fig. 6.1b for comparison to the more accurate timescales from Iro et al. (2005). The agreement is reasonably good between 10^4 Pa and 10^5 Pa, but differences increase significantly both with decreasing and increasing pressure.

Going back to the temperature-forced model, we initialise it using the mean between the day and night side equilibrium forcing profiles with zero winds. The first 200 d are normally discarded to let initial transients disappear. In the literature temporal averages are calculated from 200 d for temperature-forced models, but we only look at model results using output at a given time after the initialisation of the model due to the lack of long simulation times for our coupled models. In Figs. 6.2 to 6.5 we show the temperature as colours and contours and wind velocities as arrows as a function of longitude and latitude after 600 d at 100 Pa, 3×10^3 Pa, 3×10^4 Pa and 1×10^5 Pa.

At low pressures winds diverge from the hotspot located at substellar point (180° longitude, 0° latitude). Temperatures reach about 1400 K on the day side, while the night side is a much colder, about 400 K. It is worth noting that, due to the very small radiative timescale at 100 Pa, the temperature is almost identical to the equilibrium temperature $T_{\rm eq}$. For increasing pressures, dynamical processes start redistributing the heat away from the substellar point. An equatorial jet is seen to develop spanning all longitudes. Temperatures increase with increasing pressure, as expected from the radiative equilibrium forcing profiles, and the temperature difference between the day and night side decreases. Note the symmetry about the equator as the obliquity is zero.

We show in Fig. 6.6 the zonal mean of the zonal wind as a function of pressure and latitude. The zonal jet in the eastward direction mentioned previously is clearly seen, and it reaches its maximum strength at about 10^3 Pa with a velocity of about 7 km/s. At higher latitudes the mean flow is in the opposite (westward) direction, and much weaker in amplitude, with a maximum of about 1.2 km/s.

In Fig. 6.7 we plot P–T profiles for several different latitudes and longitudes. The temperature varies significantly across the globe, with night side temperatures down to ~ 500 K and day side temperatures of ~ 1500 K at 10^3 Pa. A temperature inversion is even seen on the day side of the planet, which is caused by strong heating at the top of the atmosphere due to the short radiative timescale and the equatorial jet bringing cold material from the night side to the day side cooling the atmosphere down at higher pressures.

Before discussing results from the coupled model we briefly mention the disadvantages of using temperature-forcing schemes, as in e.g. Cooper & Showman (2005), Heng et al. (2011), Mayne et al. (2014a), Menou & Rauscher (2009), Rauscher & Menou (2010), Showman & Guillot (2002) and Showman et al. (2008), to treat the radiation:

1. The equilibrium P–T profiles used in the forcing may have a limited accuracy, it is difficult to calculate equilibrium P–T profiles for a 3D object with a 1D model.

2. Radiative timescales may have a limited accuracy and will vary in a non-trivial way as a

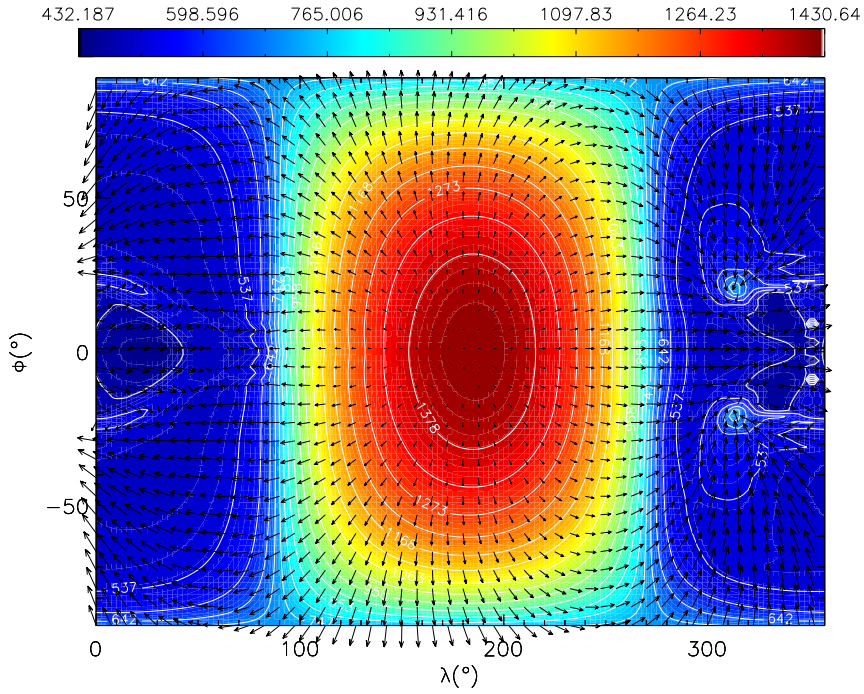

Figure 6.2: The horizontal wind velocity as arrows and temperature [K] as colours and contours at 100 Pa after 600 d for the temperature-forced model of HD 209458b discussed in Section 6.2.1.

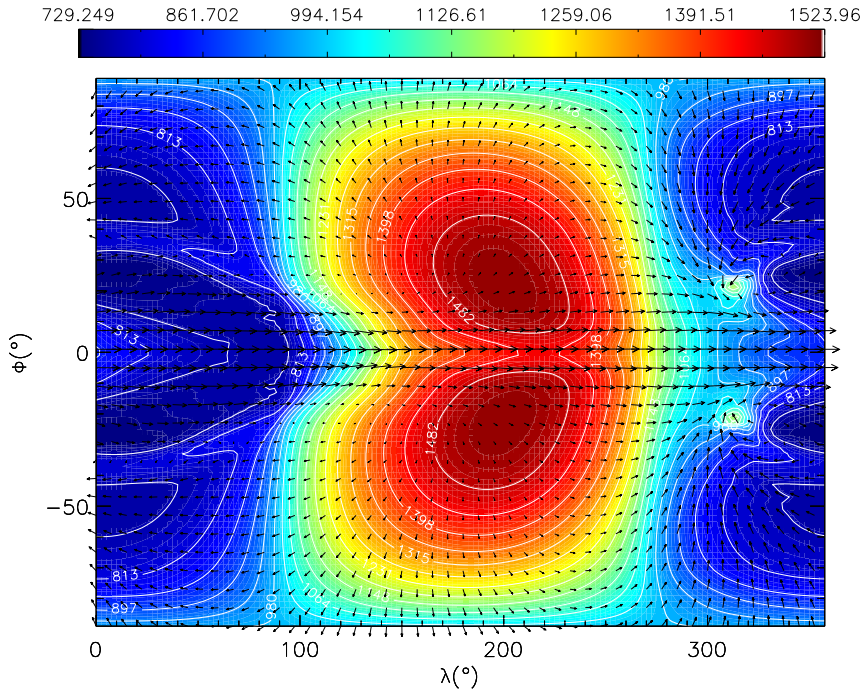

Figure 6.3: The same as Fig. 6.2 but at 3×10^3 Pa.

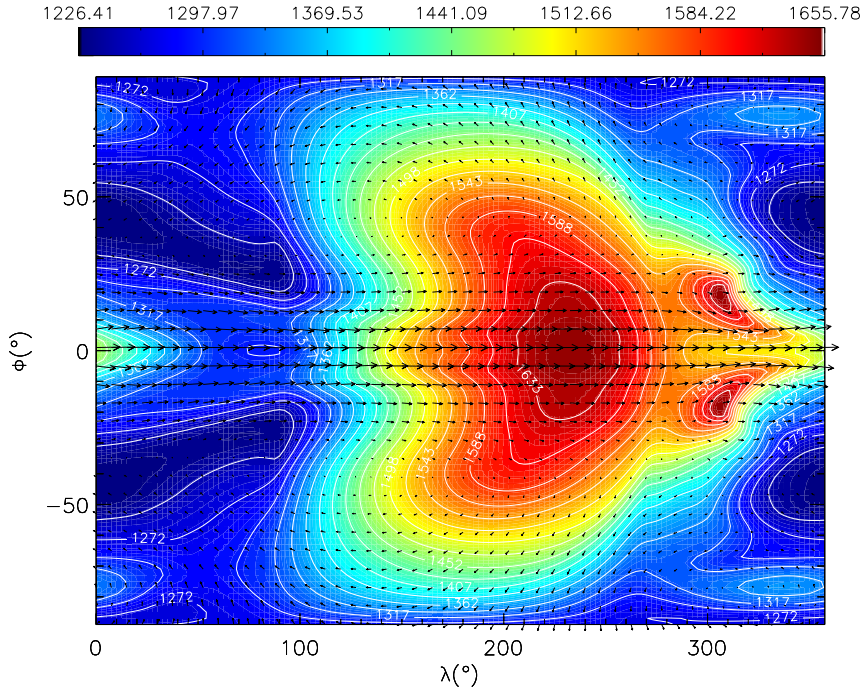

Figure 6.4: The same as Fig. 6.2 but at 3×10^4 Pa.

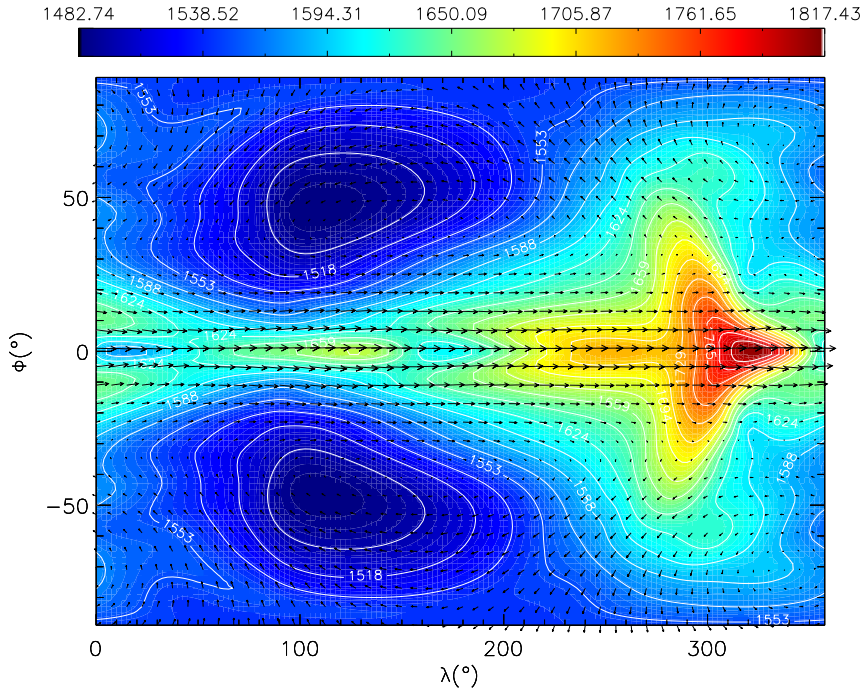

Figure 6.5: The same as Fig. 6.2 but at 1×10^5 Pa.

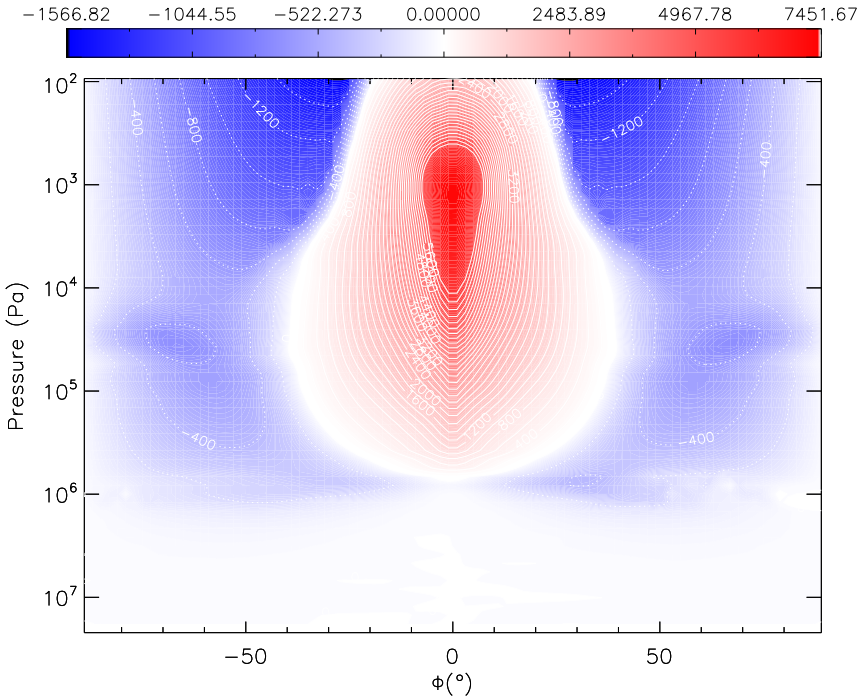

Figure 6.6: The zonal mean of the zonal wind velocity [m/s] after 600 d for the temperature-forced model of HD 209458b discussed in Section 6.2.1. Red indicates a prograde wind, blue indicates a retrograde wind.

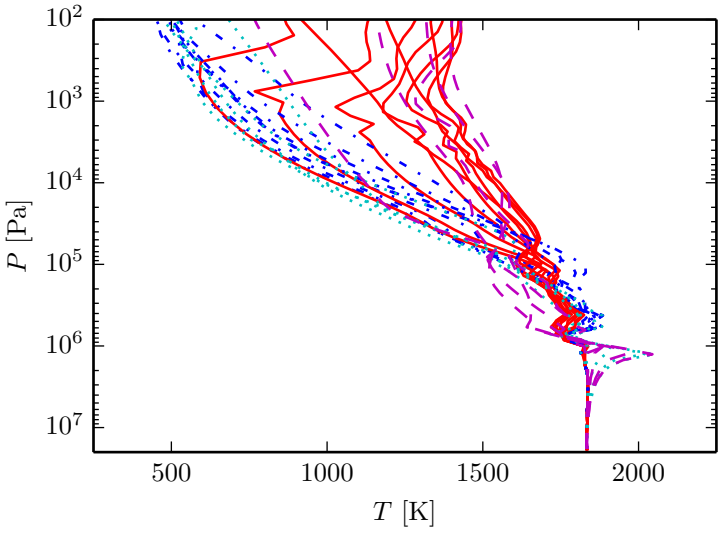

Figure 6.7: *P*–*T* profiles around the globe after 600 d for the temperature-forced model of HD 209458b discussed in Section 6.2.1. Red solid lines and blue dashed-dotted lines are day and night side profiles, respectively, at 0° latitude. Magenta dashed lines and cyan dotted lines are profiles between 0° and 90° latitude for longitudes 180° and 0°, respectively.

function of latitude, longitude and height. They will also depend on the local temperature, which is ignored in the forcing scheme used here.

3. As a result of the two above points, the forcing parametrisation itself may not be physically realistic.

4. The model flexibility is poor since for each new planet modelled, the forcing must be changed. New equilibrium P–T-profiles and radiative time scales must be derived using e.g. 1D models.

Global circulation models including a proper treatment of radiative heating and cooling is therefore essential in order to both improve model flexibility and, as discussed in Section 1.4 and we will show in Section 6.3, improve agreement with observations.

6.2.2 Without TiO and VO

Here we present our first results obtained with the coupled model applied to HD 209458b. We do not allow TiO and VO to form, an assumption we relax in Section 6.2.3. This enables us to investigate the effect TiO and VO has on the atmosphere, and compare the coupled model to the temperature-forced model as the 1D equilibrium profiles were derived without TiO and VO. We initialise the model using the globally averaged P–T profile seen in Fig. 5.6a with zero winds. Horizontal wind velocities and temperatures are plotted in Figs. 6.8 to 6.11 after 600 d at several different pressures, and can be compared to Figs. 6.2 to 6.5 obtained with the temperature-forced model.

General features are similar to those found with the temperature-forced model. At low pressures, Fig. 6.8, the flow is again diverging from the substellar point, but the equatorial jet is more prominent in the coupled model than in the temperature-forced model, consistent with results in Showman et al. (2009). The hotspot is also slightly more shifted from the substellar point, which indicates that dynamical effects have a larger impact on the general circulation at low pressures in the coupled model than the temperature-forced model. This may be due to an underestimate of the radiative timescale used in the temperature-forced model.

A noticeable increase in the night side temperature is evident compared to the temperature-forced model. This is most likely due to the cold night side forcing profile seen in Fig. 6.1, as it was estimated from the globally averaged profile from Iro et al. (2005). Day side temperatures are generally lower in the coupled model than the temperature-forced model. Combined this yields a smaller day-night temperature contrast in the coupled model compared to the temperature-forced model.

In Fig. 6.12 we show the zonal mean zonal wind velocity after 600 d as a function of pressure and latitude. Again the eastward equatorial jet is clearly seen, and the overall zonal wind structure is in agreement with the temperature-forced model in Fig. 6.6. The most noticeable

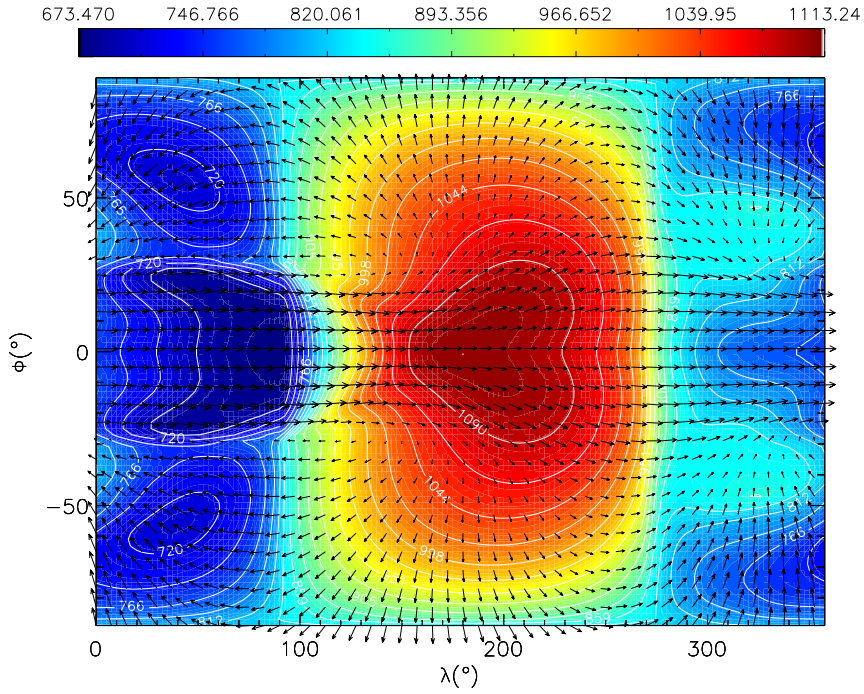

Figure 6.8: The horizontal wind velocity as arrows and temperature [K] as colours and contours at 2 Pa after 600 d for the coupled model of HD 209458b without TiO and VO discussed in Section 6.2.2.

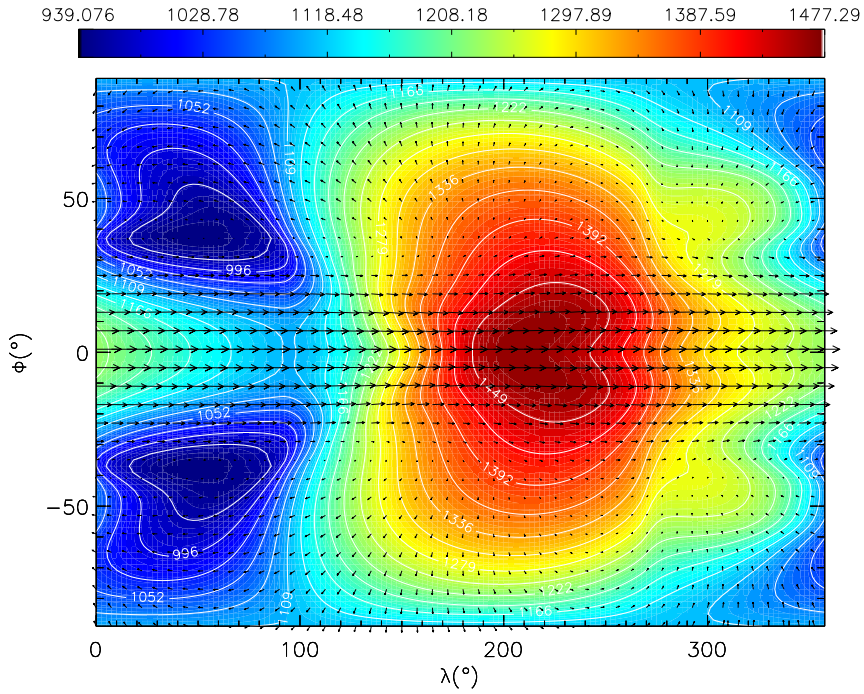

Figure 6.9: Same as Fig. 6.8 but at 3×10^3 Pa.

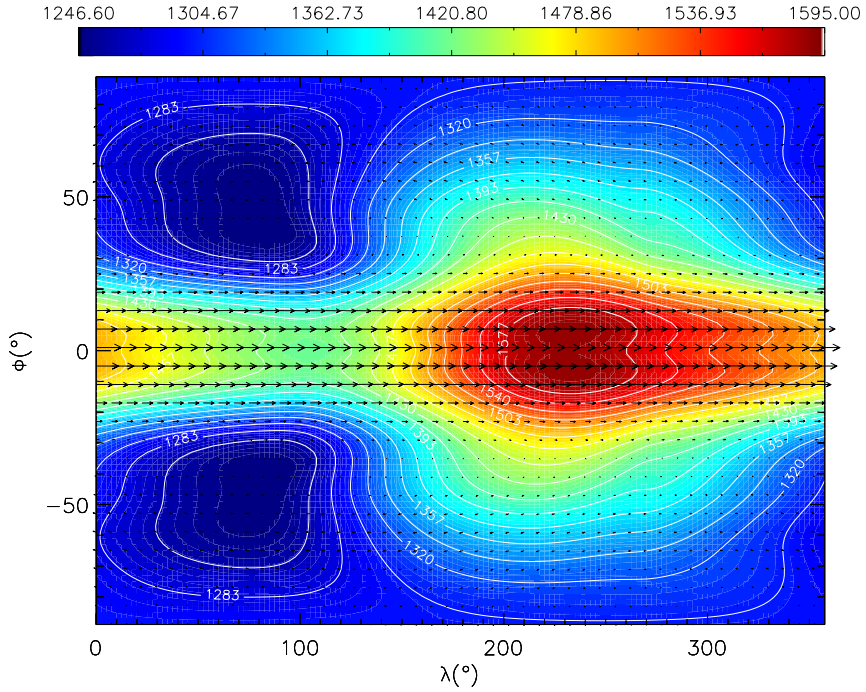

Figure 6.10: Same as Fig. 6.8 but at 3×10^4 Pa.

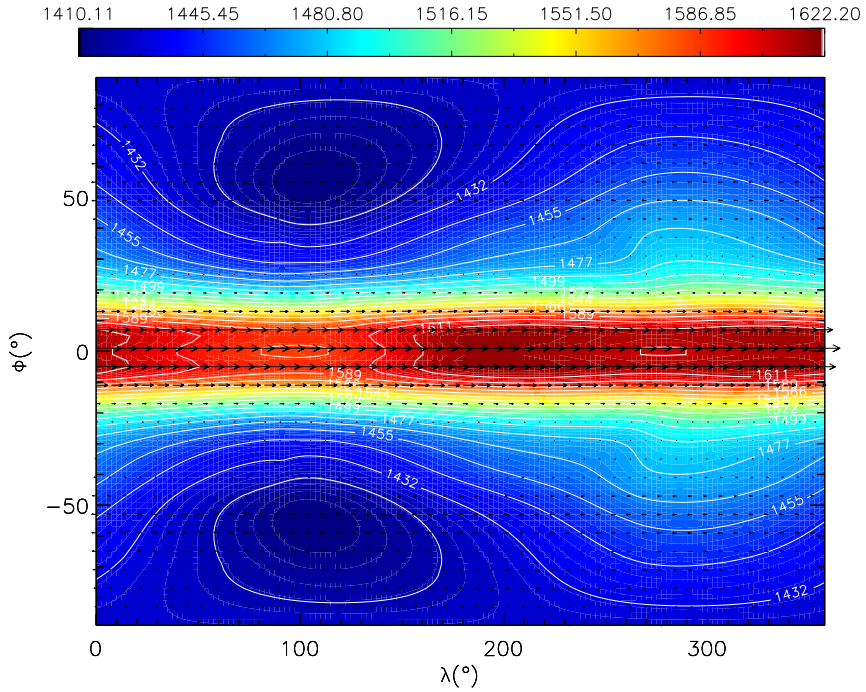

Figure 6.11: Same as Fig. 6.8 but at 1×10^5 Pa.

difference is the slightly broader jet at low pressures in the coupled model caused by the equatorial jet being more prominent at lower pressures as previously discussed.

In Fig. 6.13 we show the variation in P–T profiles across the globe. A large variation is evident, and some night side profiles have higher temperatures than some day side profiles. This is due to the advection eastward of the sub-stellar point causing the terminator at 270° longitude to be much warmer than that at 90° longitude as seen in e.g. Fig. 6.9.

For pressures $\gg 1 \times 10^5$ Pa profiles at 0° latitude are dominated by the equatorial jet, causing very small temperature variations as a function of longitude. At other latitudes, however, temperature variations are larger. By looking at temporal changes of temperatures and winds we find that the atmosphere has reached an approximate steady state for pressures $\lesssim 1 \times 10^5$ Pa, while much longer simulation times will be needed to study the evolution of the deep atmosphere where pressures are $> 1 \times 10^6$ Pa.

6.2.3 With TiO and VO

Now we allow TiO and VO to form in the atmosphere if the temperature is above the critical temperatures as described in Sections 3.6.3 and 5.4. For stability reasons we initialise the model with the day side average profile in Fig. 5.6a, where the upper atmosphere is too cool for TiO and VO to exist, and again we initialise with zero winds. TiO and VO will then form naturally in the model if the temperature increases above the critical temperatures. In Fig. 6.14 we show the horizontal wind velocity as vectors and temperature as colours and contours at 5 Pa after 100 d. A patch has formed around the substellar point where it is hot enough for TiO and VO to form. Due to the extremely steep temperature gradient the wind diverges from the substellar point. The material flowing eastward forms the eastward equatorial jet seen in Sections 6.2.1 and 6.2.2 for the temperature-forced model and coupled model without TiO and VO. Material flowing westward eventually meets the equatorial jet, and is pushed to higher latitudes.

In Figs. 6.15 to 6.18 we show winds and temperatures after 500 d at 5 Pa, 3×10^3 Pa, 3×10^4 Pa and 1×10^5 Pa. At 5 Pa after 500 d cool material from the west, as part of the equatorial jet, has cooled down a part of the patch around the substellar point containing TiO and VO to below the condensation temperature. At higher pressures the winds and temperatures are similar, if somewhat faster and higher, respectively, compared to the case where we did not allow TiO and VO to form, Figs. 6.9 to 6.11.

The zonal jet can be seen more clearly in Fig. 6.19 where we have plotted the zonal mean of the zonal wind velocity as a function of pressure and latitude. Wind velocities are similar to the case without TiO and VO in Fig. 6.12, but with slightly stronger wind velocities around the equator and slightly weaker at higher latitudes.

We show P–T profiles after 500 d at different latitudes and longitudes around the globe in Fig. 6.20. A temperature inversion, caused by the strong absorption of the stellar irradiation by TiO and VO, can clearly be seen for some of the day side P–T profiles at low pressures.

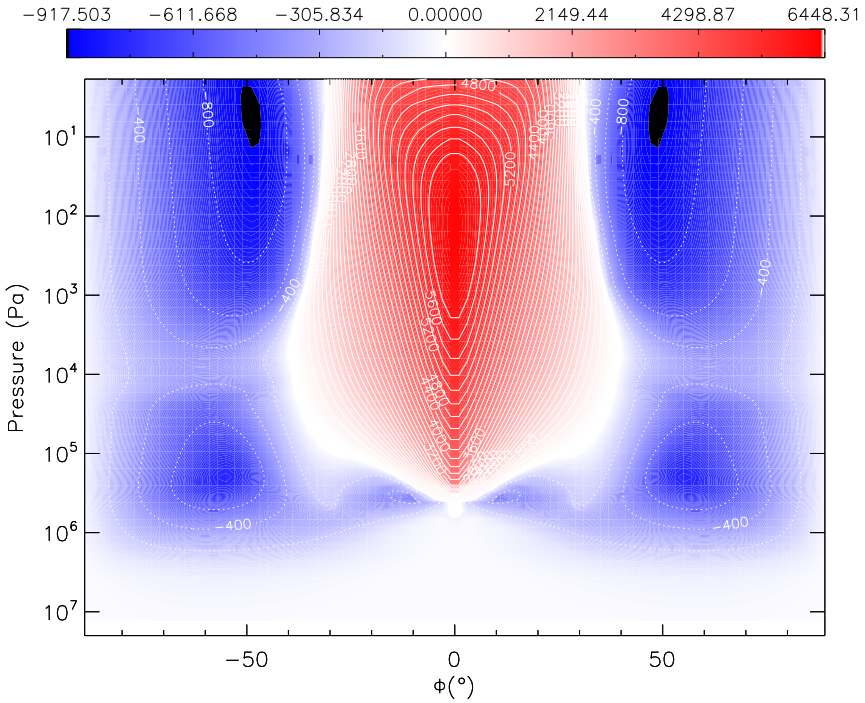

Figure 6.12: The zonal mean of the zonal wind velocity [m/s] after 600 d for the coupled model of HD 209458b without TiO and VO discussed in Section 6.2.2.

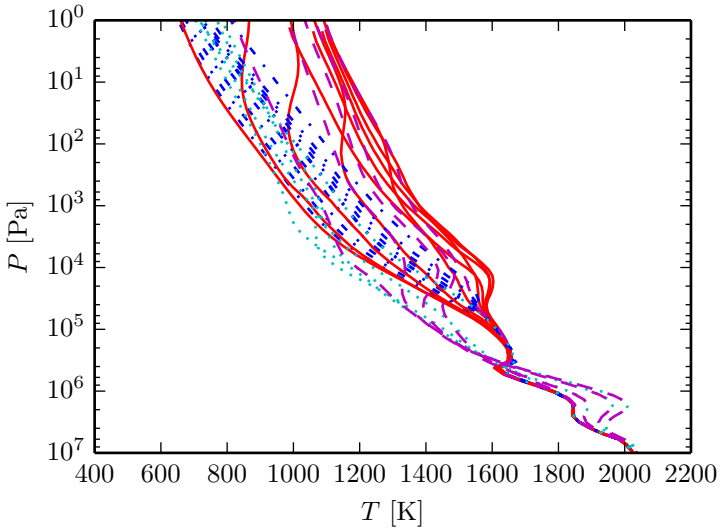

Figure 6.13: P–T profiles around the globe after 600 d for the coupled model of HD 209458b discussed in Section 6.2.2 without TiO and VO. Red solid lines and blue dashed-dotted lines are day and night side profiles, respectively, at 0° latitude. Magenta dashed lines and cyan dotted lines are profiles between 0° and 90° latitude for longitudes 180° and 0°, respectively.

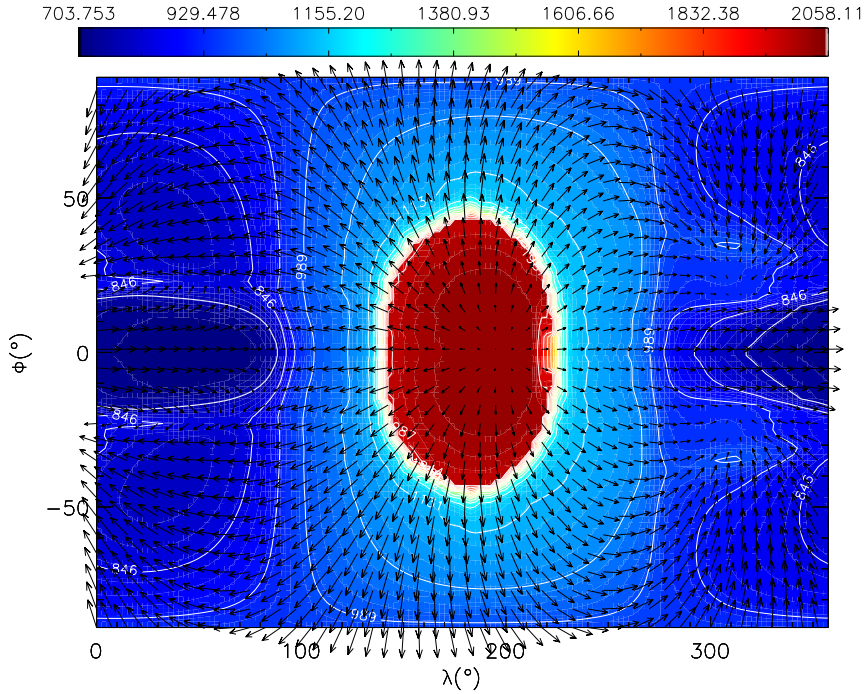

Figure 6.14: The horizontal wind velocity as arrows and temperature as colours and contours at 5 Pa after 100 d for the coupled model of HD 209458b. TiO and VO are allowed to form.

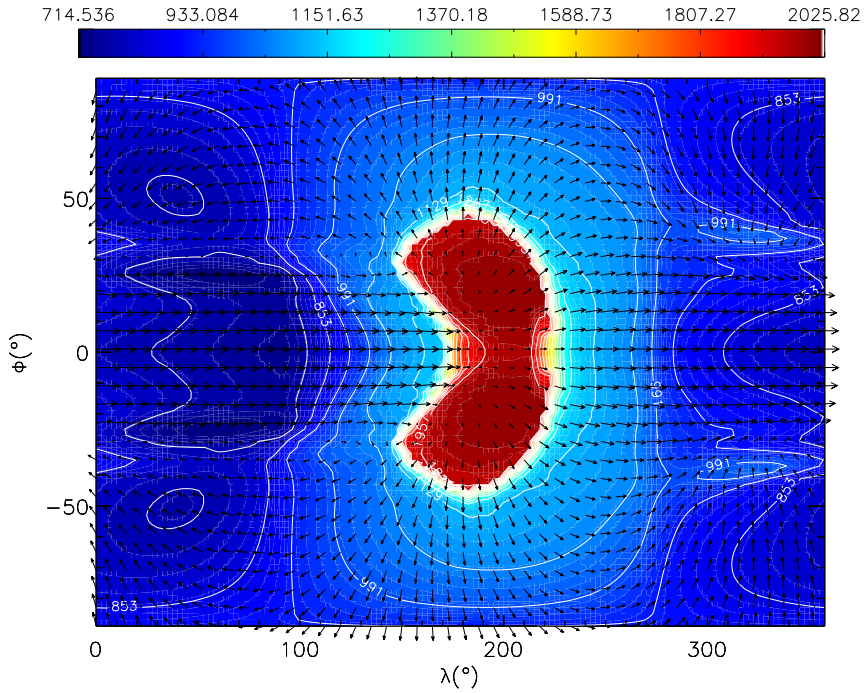

Figure 6.15: The horizontal wind velocity as arrows and temperature [K] as colours and contours at 5 Pa after 500 d for the coupled model of HD 209458b discussed in Section 6.2.3 where TiO and VO are allowed to form.

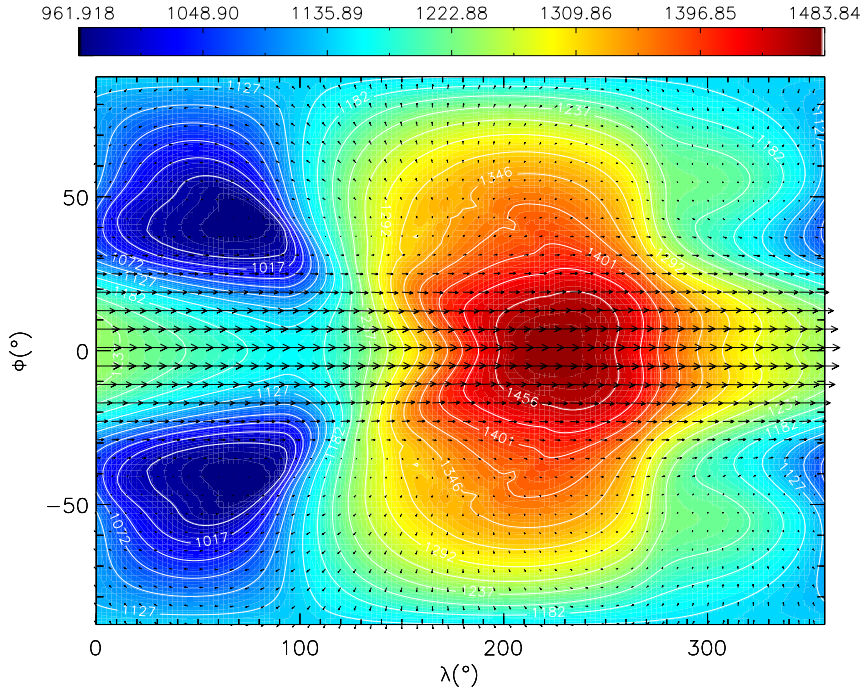

Figure 6.16: Same as Fig. 6.15 but at 3×10^3 Pa.

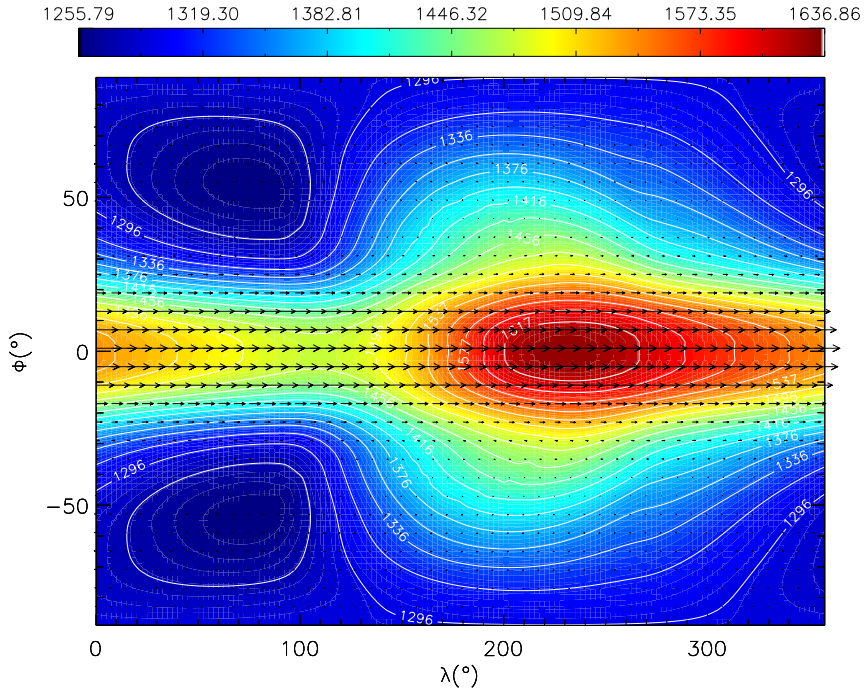

Figure 6.17: Same as Fig. 6.15 but at 3×10^4 Pa.

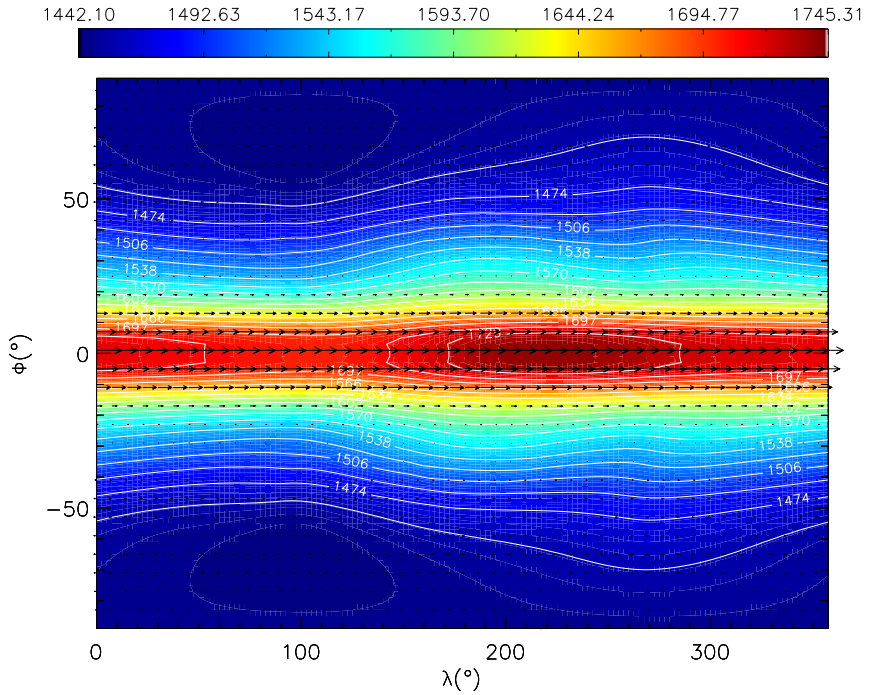

Figure 6.18: Same as Fig. 6.15 but at 1×10^5 Pa.

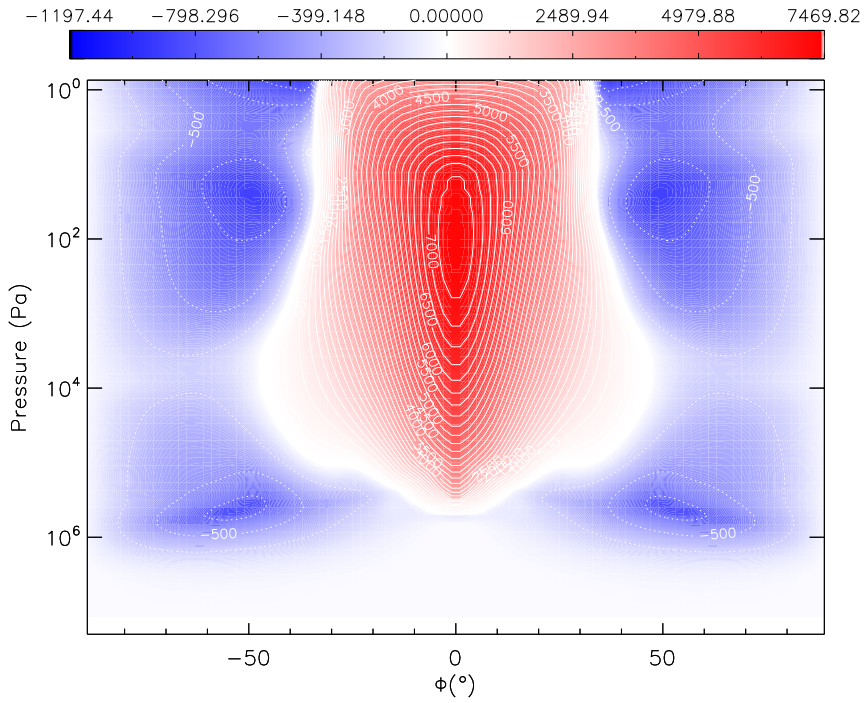

Figure 6.19: The zonal mean of the zonal wind velocity [m/s] after 500 d for the coupled model of HD 209458b discussed in Section 6.2.3. TiO and VO are allowed to form.

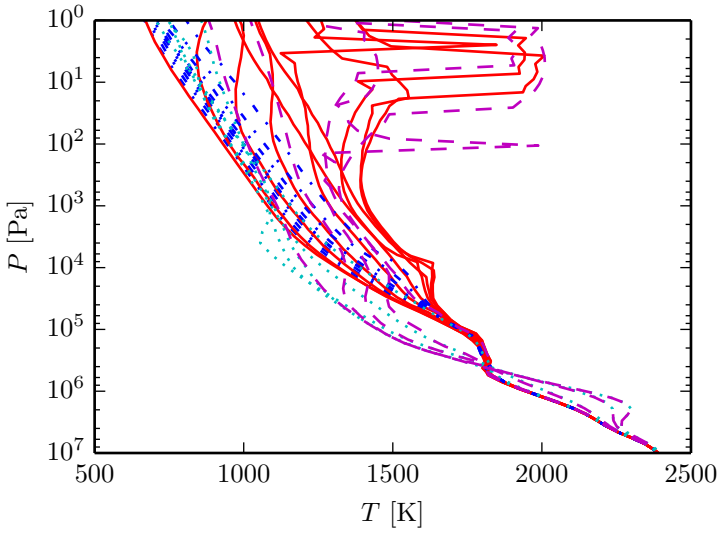

Figure 6.20: P–T profiles around the globe after 500 d for the coupled model of HD 209458b discussed in Section 6.2.3 where TiO and VO are allowed to form. Red solid lines and blue dashed-dotted lines are day and night side profiles, respectively, at 0° latitude. Magenta dashed lines and cyan dotted lines are profiles between 0° and 90° latitude for longitudes 180° and 0°, respectively.

Deeper temperatures are approximately the same as the case without TiO and VO in Fig. 6.13. Horizontal and vertical temperature gradients are very steep in parts of the atmosphere, and they are not well resolved numerically. It is therefore questionable if the numerical solution to the fluid dynamics equations is accurate. The equations solved by the UM dynamical core inherently conserves angular momentum, but the numerical scheme solving these equations is not designed to conserve angular momentum explicitly. The degree of angular momentum conservation should therefore be a good indication of the accuracy of the numerical solution to the fluid dynamics equations. The evolution of angular momentum is plotted in Fig. 6.21, and it is seen to be conserved to an accuracy of $> 99.5\,\%$. We therefore conclude that the UM dynamical core appears to obtain a reasonably accurate solution to the fluid dynamics equations even with such large temperature gradients.

Again we would like to point out that the atmosphere is still evolving after 500 d of simulation time, even more so than in the case without TiO and VO due to the interaction between the hotspot with TiO and VO and the equatorial jet. Whether or not the equatorial jet will cool down the hot spot enough for TiO and VO to disappear completely is unclear, we are in the process of running the model longer to investigate this. It does show, however, that whether or not TiO and VO is present can be very sensitive to the irradiation and redistribution efficiency. It is not possible to assume TiO and VO to be present throughout the whole day side hemisphere, as is often done in 1D models.

It has been suggested that the lack of detection of TiO and VO on these planets could be caused by a cold-trap on the night side, where TiO and VO on the day side would be advected to the night side, condense, and rain out (Showman et al. 2009). Parmentier et al. (2013) found that TiO can be depleted from the day side of HD 209458b if it condenses into particle sizes bigger than a few microns on the planet's night side. For now we point out that whether or not

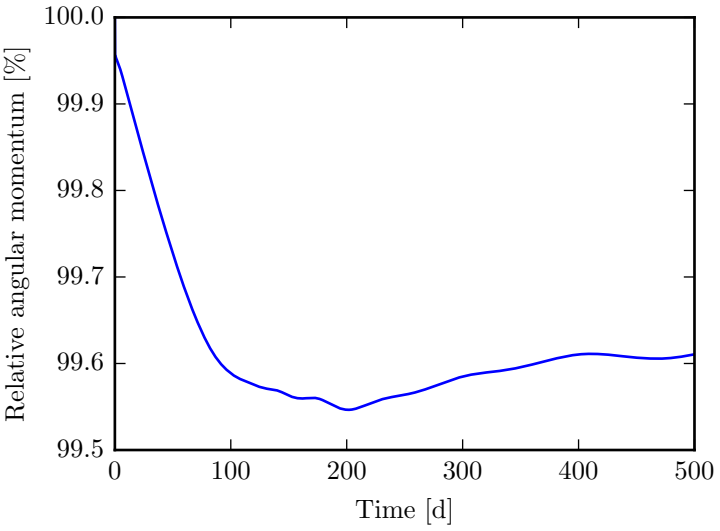

Figure 6.21: Difference in relative angular momentum from the beginning of the simulation for the run where we allow TiO and VO to form, Section 6.2.3. Angular momentum is conserved to an accuracy of $> 99.5\,\%$.

TiO or VO is present in these atmospheres remain highly uncertain, and if they are present on the day side, they may still prove difficult to observe. In the next section we generate synthetic observations from our simulations and compare them to existing observations and the model results from Showman et al. (2009).

6.3 Comparison to observations

Here we calculate observational quantities as described in Section 5.5 from the model output of all our HD 209458b model runs. We begin by considering the transmission spectrum (Section 6.3.1), then the day side emission spectrum (Section 6.3.2), and last the 4.5 µm phase curve recently obtained by Zellem et al. (2014) (Section 6.3.3).

6.3.1 Transmission spectra

We have calculated the transmission spectrum from our models of HD 209458b, and the results are shown in Fig. 6.22 with observational data. We have reduced the transit radius of the temperature-forced model by $0.0138R_*$, the coupled model without TiO and VO by $0.0032R_*$ and the coupled model with TiO and VO by $0.0039R_*$ to match the water feature at 1.4 µm. This is needed as the radius of our lower boundary does not perfectly fit the observations, and should have a small effect on the P–T profiles and the transmission spectrum.

The data around 1.4 µm was presented by Deming et al. (2013) and claim detection of a "muted" water feature. The increase in planet radius at 1.4 µm as seen in the model is due water absorption, and the data does indicate a small increase in radius at this wavelength. The cause of the water feature being muted is unknown. It may be that the observations are not sensitive to planet radii smaller than about $0.120R_*$, on the other hand it may be

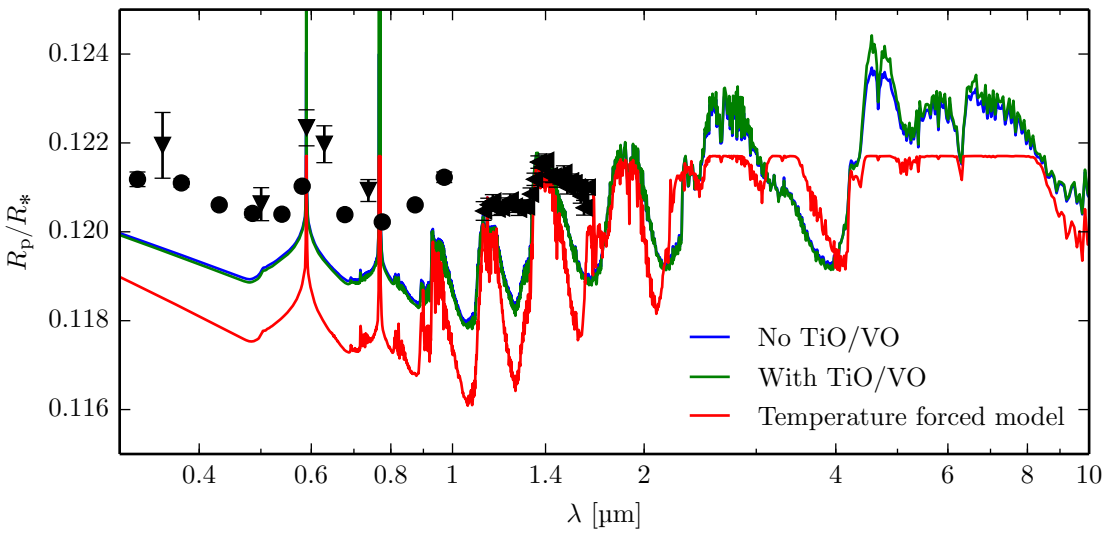

Figure 6.22: Observed (points) and synthetic (lines) transmission spectra for HD 209458b calculated with our coupled and temperature-forced models. Calculated after 600 d for the temperature-forced and coupled model without TiO and VO and 500 d for the model with TiO and VO. The black points are observations from Knutson et al. (2007b) (●), Sing et al. (2008) (▼), Crossfield et al. (2012) (▲) and Deming et al. (2013) (◀). Models have been shifted vertically to fit water feature at 1.4 µm.

caused by an additional scatterer or absorber in the atmosphere of HD 209458b not included in the models as invoked by e.g. Deming et al. (2013). Unfortunately, it is very difficult do distinguish between absorbers and scatterers in a transmission spectrum without recognising specific spectral features. Both absorbers and scatterers have the same effect on the stellar rays going through the planet atmosphere. Another way to mute the water feature is to decrease the scale height of the atmosphere. This can be achieved by increasing the gravity or mean molecular weight, or decreasing the temperature. Due to radial velocity measurements constraining the mass and brightness temperatures derived from day side emission spectra these are considered unlikely causes. The most likely cause is the presence of clouds in the atmosphere of HD 209458b, i.e. scattering particles. Clouds are found throughout the atmospheres of solar system planets (Rossow 1978) and in brown dwarfs (Crossfield et al. 2014), so it would be surprising if they are absent on hot Jupiters. As of yet we do not include clouds in our models, this will be the subject of future work.

Even though TiO and VO are present on the day side of the model where we allow them to form, they are not present in the transmission spectrum. This result is in contrast to Fortney et al. (2010), who calculated transmission spectra from the models of Showman et al. (2009) and found that limb-temperatures were high enough to contain an observable amount of TiO in the transmission spectrum. We would like to point out here that the model of Showman et al. (2009) used interpolation in an opacity database where mixing ratios had already been taken into account, meaning that sharp transitions in opacity due to e.g. condensation will be smeared

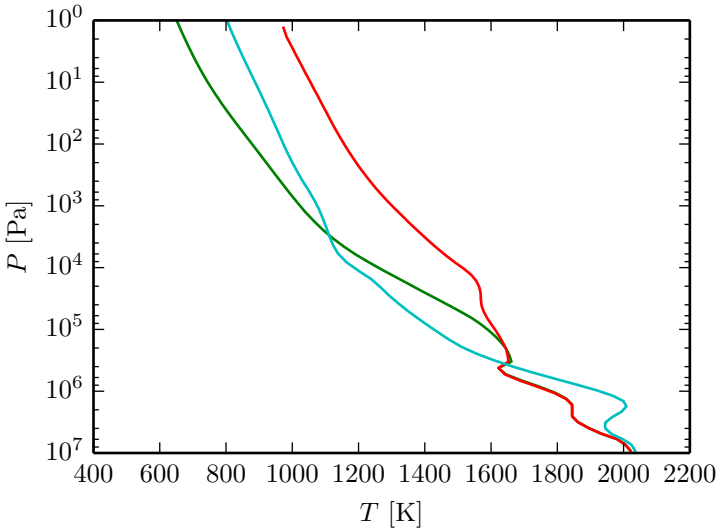

Figure 6.23: P–T profiles for different points along the limb of the planet from our model of HD 209458b without TiO and VO. Note that due to the north-south symmetry longitude 90°, latitude 90° is equivalent to longitude 90°, latitude −90°. Legend can be found in Fig. 6.24.

out as discussed in Chapter 4. As we use equivalent extinction to combine k-coefficients for different gases we are better able to resolve sharp transitions in abundances.

Figure 6.22 indicates that the P–T profile itself has a small impact on the transmission spectrum, but changes in abundances, which are functions of temperature, have a larger impact. To illustrate this further we have plotted the P–T profiles around the limb of the planet from our coupled model without TiO and VO in Fig. 6.23 and 1D transmission spectra calculated from these profiles in Fig. 6.24. At 1.4 µm the planet size is about $0.121 R_*$, and we find that this corresponds to an atmospheric pressure within an order of magnitude of 10^2 Pa depending on the position on the limb. The P–T profiles are quite different, by about 300 K at 10^2 Pa, but the impact on the transmission spectrum is small. The main difference is seen for the hottest profile which has a larger planet radius due to the increased scale height caused by higher temperatures. Shifting the spectra vertically, as is normally done, the differences are smaller than the observational uncertainties. Interestingly, an additional absorption feature appears at about 3.5 µm using the $\lambda = 90°$, $\phi = 0$ profile caused by the increased methane abundance at the lower temperatures in this profile around 10^2 Pa.

6.3.2 Emission spectra

The HD 209458b day side emission spectrum has been measured by several groups, as discussed in Section 6.1. At some wavelengths there are even multiple measurements available. We plot the observed data points with emission spectra calculated for our coupled and temperature-forced models in Fig. 6.25. The disagreement between the original analysis by Knutson et al. (2008) and the reanalysis of Diamond-Lowe et al. (2014) is clearly seen.

Our coupled model without TiO and VO generally underestimates the emission except at 3.6 µm and 24 µm. This means that the model is generally too cold at the optical depth where

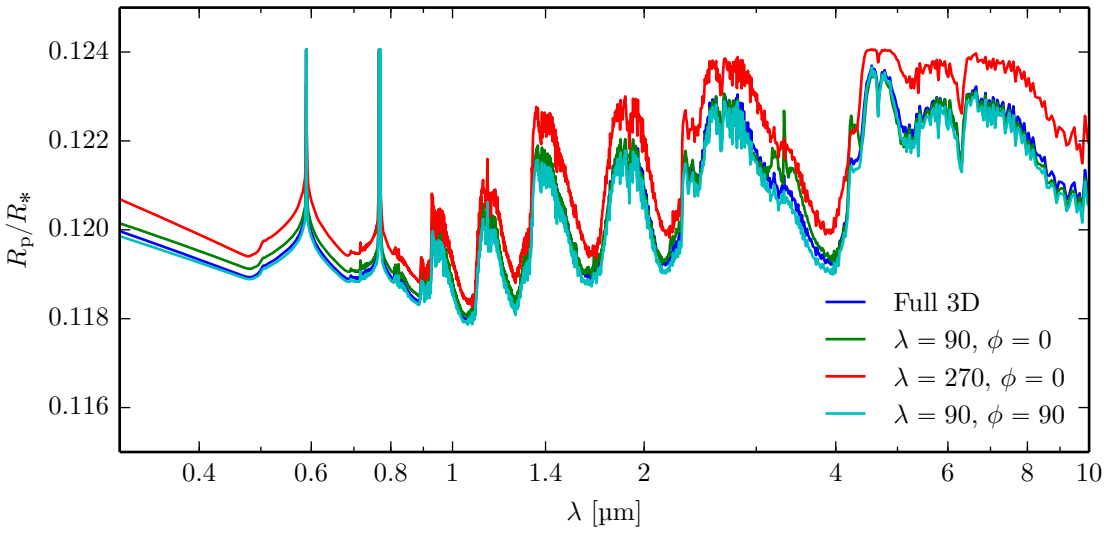

Figure 6.24: Transmission spectra calculated assuming the P–T profiles in Fig. 6.23 apply over the entire planet.

the emission originates. The large decrease in flux at 4.5 µm is due to a CO absorption feature. As CO absorbs strongly at this wavelength, the pressure where the emission originates becomes smaller, causing a lower emission. The temperature-forced model and the coupled model with TiO and VO appear to fit better due to their hotter day sides. The 4.5 µm CO absorption feature in the model without TiO and VO is in the model with TiO and VO turned into a small emission feature. This is due to the temperature inversion, as the lower pressures probed at 4.5 µm has a higher temperature than surrounding wavelengths, causing increased emission.

We do not, however, take this as evidence for TiO and VO in the atmosphere of this planet. We can conclude, however, that without an extra source of opacity our model emission is too low. This can be caused by the presence of TiO and VO or other absorbers of stellar radiation missing from our opacity database, but it can also potentially be caused by clouds. The uncertainty in the observations and the model degeneracy is too large, however, to make definite conclusions.

6.3.3 Phase curves

The 4.5 µm phase curve was measured by Zellem et al. (2014), and in Fig. 6.26 we have plotted their best fit curve together with our synthetic 4.5 µm phase curves. The synthetic phase curves have been integrated over the Spitzer band using the IRAC 4.5 µm filter function. The temperature-forced model fits poorly, with the night side being too cold and the phase offset too small. The coupled model without TiO and VO reproduces the night side flux, but the day side flux is too low, indicating that day side temperatures in the model are too low. The fit could be improved substantially by removing the CO absorption feature at this wavelength, causing an increased emission, but this would mean a significant deviation from chemical equilibrium. The

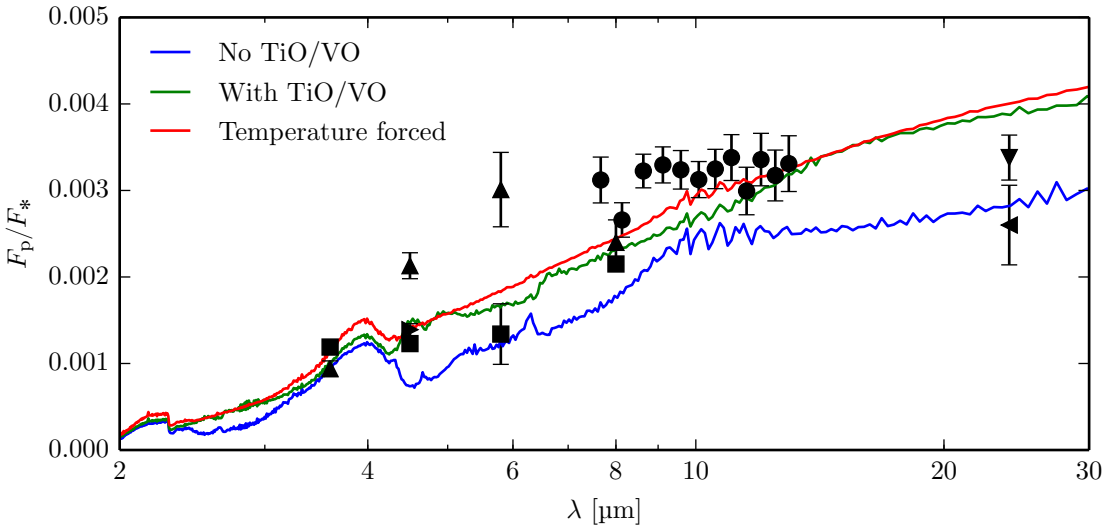

Figure 6.25: Observed (points) and synthetic (lines) emission spectra for HD 209458b calculated with our coupled and temperature-forced models. Calculated after 600 d for the temperature-forced and the coupled model without TiO and VO and 500 d for the model with TiO and VO. The black points are observations from Swain et al. (2008) (●), Crossfield et al. (2012) (▼), Knutson et al. (2008) (▲), Deming et al. (2005) (◀), Zellem et al. (2014) (▶) and Diamond-Lowe et al. (2014) (■).

non-equilibrium calculations by Moses et al. (2011) indicate that the CO abundance is relatively stable, i.e. its abundance is unlikely to be greatly affected by disequilibrium chemistry for the case of HD 209458b. The coupled model with TiO and VO does fit the observations fairly well, reproducing both the day and night side flux, but the flux as the day side comes into view (small orbital phases) is underestimated, meaning that the atmosphere is not hot enough eastward of the substellar point.

The phase offset is slightly underestimated in our coupled models, while the temperature-forced model shows almost no phase offset. The phase offset is essentially determined by the offset of the hotspot from the substellar point, which depends on the balance between the radiative and dynamical timescales. The radiative timescale in the temperature-forced model therefore seems to be underestimated. For the coupled models a lower opacity at 4.5 µm, causing the planet flux to originate at a higher pressure, could potentially increase the phase offset. Interestingly, the models of Showman et al. (2009) seem to have the same problem, slightly underestimating the phase offset. On the other hand they significantly overestimate the night side flux, while we do not, which may be due the older line lists used causing an underestimated opacity at infrared wavelengths.

In Figs. 6.27 to 6.29 we have plotted synthetic phase curves for the four Spitzer IRAC bands from our models, with secondary eclipse data from Diamond-Lowe et al. (2014) and Zellem et al. (2014) at an orbital phase of 180°. The coupled model without TiO and VO generally underestimates the emission, as discussed previously. The temperature-forced model fits the

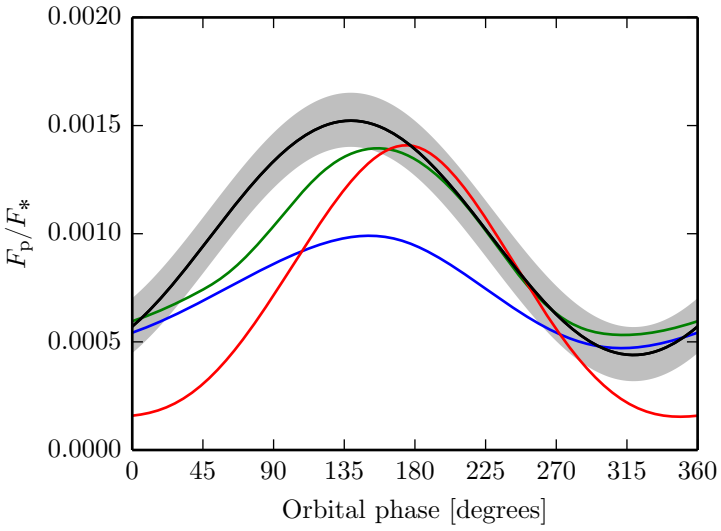

Figure 6.26: Synthetic 4.5 µm phase curves from our models and a the curve fitted to the observational data from Zellem et al. (2014) (black). The model has been integrated over the IRAC bands using the filter functions. The grey shaded area is the 1σ uncertainty for the offset of the observed planet to star flux ratio. Colours are the same as in Fig. 6.25.

data better, but the best fit is obtained with the model including TiO and VO which agrees well with measured fluxes at 4.5 µm, 5.8 µm and 8.0 µm. At 3.6 µm, however, the model emission is too low.

6.4 Summary and conclusions

In summary, we find similar dynamical features in all our models: a broad equatorial jet in the eastward direction and a hotspot shifted slightly eastward of the substellar point. The night side of the temperature-forced model is much colder than in the coupled models, and also much colder than observations indicate. The coupled model without TiO and VO has a warmer night side, which matches the observations at 4.5 µm, but the day side appears to be too cold.

Our coupled model including TiO and VO provides the best fit with observations, with a warmer day side due to the strong absorption of the stellar radiation by these molecules. There are still discrepancies for small to intermediate orbital phases when comparing to the observed 4.5 µm phase curve, indicating that our model is too cool eastward of the substellar point. The phase shift is also slightly underestimated by our model. We do not take the better agreement with observations for our model with TiO and VO as evidence for the presence of these molecules in the atmosphere of HD 209458b, or for evidence of a temperature inversion. We can, however, draw some conclusions from these results:

- A cloud-free model without TiO and VO is too cool to explain the observed thermal emission. This can be caused by the presence of additional visible absorbers or clouds that we do not include.
- Even though TiO and VO are present on the day side they are not seen in the transmission spectrum. This can shed some light on observations that have failed to detect the presence

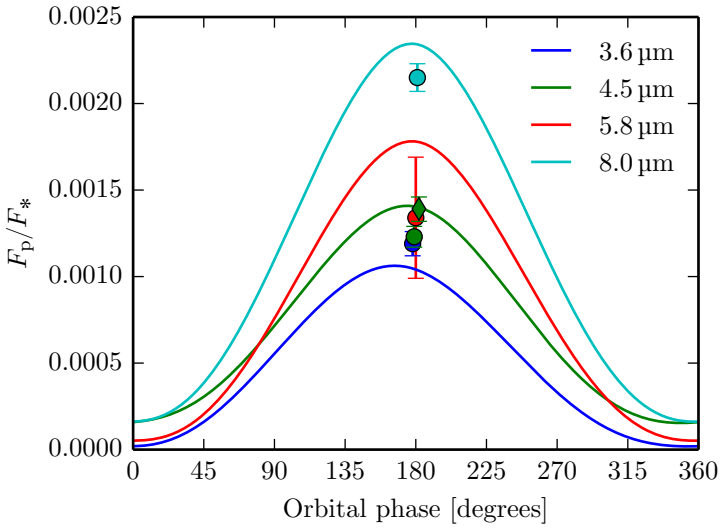

Figure 6.27: Synthetic Spitzer IRAC phase curves from the temperature-forced model. The model has been integrated over the IRAC bands using the filter functions. The data points are from Diamond-Lowe et al. (2014) (circles) and Zellem et al. (2014) (diamond).

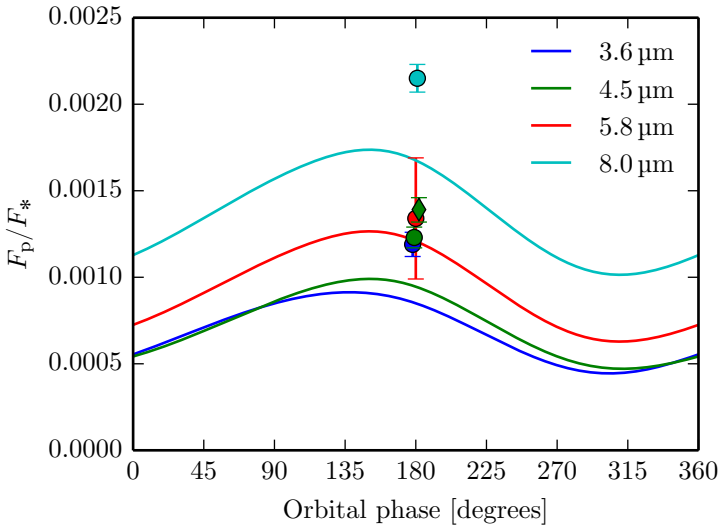

Figure 6.28: Same as Fig. 6.27 from the coupled model without TiO and VO.

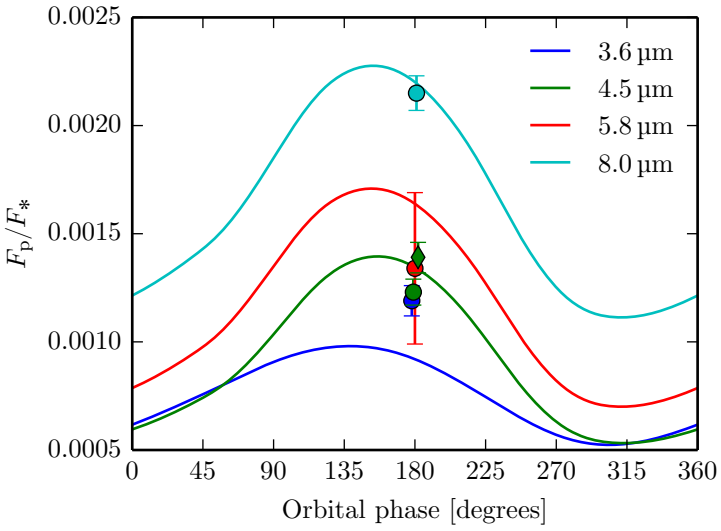

Figure 6.29: Same as Fig. 6.27 from the coupled model allowing for the formation of TiO and VO.

of these molecules in the transmission spectrum of hot Jupiters (Huitson et al. 2013; Sing et al. 2013). The region around the terminator is simply not hot enough to contain TiO and VO, and the transition between a region with TiO and VO and without TiO and VO on the day side, assuming equilibrium chemistry, can be very sharp.

- Significant differences are seen between our models and those of Showman et al. (2009) in transmission spectra and phase curves: our transmission spectra do not contain TiO and VO signatures and our 4.5 µm phase curves underestimate the flux at small orbital phases, while the models of Showman et al. (2009) and Fortney et al. (2010) show TiO and VO signatures in transmission spectra and overestimate the 4.5 µm flux at small orbital phases. In addition, Showman et al. (2009) overestimate the night side emission while we do not. It is not clear what is causing these differences. The approximations made to the dynamical equations in Showman et al. (2009) should have a minor effect on the results presented here and the radiation schemes are very similar. It may partly be due our more sophisticated treatment of TiO and VO condensation or the more extensive opacity database used by Showman et al. (2009), which includes e.g. metal hydrides (Freedman et al. 2008). This is difficult to determine, however, without direct intercomparison of individual model components. Discrepancies are well known for Earth and solar system GCMs (Collins et al. 2006; Lee & Richardson 2010), and they are usually tested against each other through intercomparison projects. Hot Jupiter GCMs are still in their early phase of development, but the discrepancies seen here indicate that such intercomparisons will become crucial in order to interpret models correctly.

In the models discussed here we have set the condensation temperatures of TiO and VO to 1800 K and 1600 K, respectively, which is suitable for pressures around 10^3 Pa (Burrows & Sharp 1999). The condensation temperature is, however, a function of pressure, and at lower

pressures the condensation temperature is also lower. Since we find TiO and VO present at very small pressures (about 10 Pa), we overestimate the condensation temperature here, and consequently underestimate the amount of TiO and VO that would be present according to equilibrium chemistry. Whether or not equilibrium chemistry can be applied to TiO and VO, however, is debated, so we would like to emphasize that even though TiO and VO have not been observed in the atmosphere of HD 209458b yet does not mean it cannot be present. Schwarz et al. (2015) recently obtained and analysed a high resolution emission spectrum of HD 209458b searching for CO emission lines, which if detected would indicate a temperature inversion. They failed to detect a CO signal, which indicates that the atmosphere is close to isothermal at the pressures probed by these measurements. Similar techniques will in the future be able to put better constraints on the abundance of TiO and VO on the day sides of exoplanets.

It should be noted that the analysis of these models has been done using output at given time, usually after a few hundred Earth days of simulation time. The upper atmospheres of these planets, which are completely dominated by the irradiation, will have converged in that time, but for pressures $> 1 \times 10^5$ Pa dynamical and radiative timescales become significantly larger, which means that models will take longer to equilibrate. It is not even certain that such an equilibrium state exists (Liu & Showman 2013; Thrastarson & Cho 2010), which serves to add to the uncertainty in interpreting output from these models.

We have neglected the effects of clouds, as all other GCMs applied to hot Jupiters. Clouds have a non-trivial effect on the climate and are difficult to both model and understand. Depending on their optical properties they may serve to decrease temperatures due to increased scattering of incident radiation, or increase the temperature by trapping thermal radiation. Any cloud scheme will introduce a wealth of additional parameters such as location, optical properties and size distributions. Due to the lack of observational constraints on the composition of clouds in hot Jupiters atmospheres, modelling them in a physically meaningful way becomes difficult. It will be important to use knowledge gained by studying solar system objects and brown dwarfs where observations are of a much higher quality.

Chapter 7

Conclusions and perspectives

In this work we have developed a sophisticated radiation scheme suitable for hot Jupiter atmospheres based on state-of-the-art opacities and the Edwards–Slingo radiation scheme, which can be used to study the atmospheric dynamics of hot Jupiters. Many approximations and assumptions made in previous studies have not been tested for hot Jupiter-like conditions. The primary goal of this work has been to develop a robust and well tested radiation scheme, and to understand the impact of various approximations used in previous modelling works. This will allow for more reliable theoretical analyses in the future, which are needed as the quality of observations continuously improves.

In the last part of this work we have started to apply these developments to study the atmospheric dynamics of hot Jupiters. We will in the future further use the developments presented here to advance our understanding of complex processes in the atmospheres of these exotic planets. In this chapter we summarise our main conclusions and discuss future prospects.

7.1 Conclusions

Calculation of absorption coefficients from high-temperature line lists has been discussed. We present a line profile cut-off scheme that decreases the computation time required to calculate absorption coefficients by a factor of ~ 100 compared to other methods used in the literature, while still giving accurate results. Combining this with parallelisation using OpenMP and MPI makes calculating opacities from high temperature line lists in a reasonable time feasible. We emphasise that pressure broadening parameters are very uncertain and usually extrapolated from room temperature and pressure and small quantum numbers. Improvements in this area will become important as higher accuracy will be required to analyse results from future exoplanet characterisation projects (e.g. JWST, Sphere and ELT). We are currently setting up a collaboration with the ExoMol group at University College London (UCL) and V.E. Zuev Institute of Atmospheric Optics in Tomsk, Russia, to improve these line widths and investigate the effect on model atmospheres and spectra.

The accuracy of radiation schemes used in GCMs has been studied extensively for Earth-like conditions, but detailed analysis for hot Jupiter-like conditions are lacking. We have analysed the accuracy and uncertainties in state-of-the-art radiation schemes used in several GCMs applied to hot Jupiters. Both the two-stream approximation and correlated-k method's applicability to hot Jupiter atmospheres have been analysed by comparing the Edwards–Slingo radiation scheme to discrete ordinate line-by-line calculations. The ES radiation scheme's performance in these tests shows that we have successfully adapted it to hot Jupiter-like atmospheres.

We find that a diffusivity factor of $D = 1.66$, already widely used in both Earth and hot Jupiter GCMs, yields the smallest errors from the two-stream approximation for the thermal component of radiation, although $D = \sqrt{3} \approx 1.73$ is only slightly less accurate. Both the two-stream approximation and the correlated-k method contribute non-negligibly to the total error, with overall heating rate errors $\lesssim 10\,\%$ in regions with significant heating/cooling. Flux errors are similar or smaller. About 10 k-coefficients in each band for molecular line absorption yield satisfactory accuracy. Using ~ 100 k-coefficients per band does improve the overall accuracy, but errors decrease by less than 50 %, while the radiative transfer computation time increases by a factor of 10. We therefore choose to adopt the former as a balance between accuracy and computational cost. Using a mean absorption coefficient in each band, as in Dobbs-Dixon & Agol (2013), yields inaccurate fluxes and heating rates for molecular absorption. Heating rate errors can reach 100 % or more, even in regions with significant heating/cooling. Band-averaged absorption coefficients should thus be used with caution.

Comparing pre-mixed k-coefficients to using the random overlap method we found that, if a P–T profile intersects the condensation curve of TiO and VO, errors in fluxes and heating rates caused by using pre-mixed k-coefficients can become very large, $\gtrsim 50\,\%$. Even for our night side profile, which does not contain TiO and VO, heating rate errors were significant, $\gtrsim 20\,\%$. Pre-mixed k-coefficients should thus be used with care as rapid change in abundances of important absorbers may not be well resolved, which in turn can cause large errors in fluxes and heating rates. We show that errors caused by using equivalent extinction, which is much quicker than a full random overlap treatment, are on the order of the errors caused by the two-stream approximation and correlated-k method, and we consequently adopt this scheme in our GCM runs.

Any radiation scheme applied to hot Jupiters should be checked against the tests we have presented here. These tests, and the detailed descriptions of our methods and approximations, will be useful for future adaptation of radiation schemes in other GCMs. Current observational constraints on exoplanets do not require the level of accuracy we have applied in this work. The field develops at an amazing pace, however, and modellers should now develop the best theoretical and numerical tools to tackle the challenges posed by the increasing accuracy expected from future large observational projects.

We have coupled the adapted Edwards–Slingo radiation scheme to the UM dynamical core ENDGAME. The upper boundary condition was modified to take into account radiation

absorbed above the dynamical domain, while the lower boundary condition was modified to take into account the intrinsic heat flux of the planet. Using uniform irradiation with no rotation, effectively turning the UM into a 1D radiative equilibrium solver, yields good agreement with our 1D radiative-convective equilibrium code `ATMO`, with differences $\lesssim 6\,\%$.

In Chapter 6 we applied our hot Jupiter UM to HD 209458b. The main atmospheric features, such as a broad eastward equatorial jet, are similar to those seen in the temperature-forced model (Mayne et al. 2014a), but night side temperatures are much lower in the temperature-forced model. In addition, day side temperatures are higher compared to our coupled model without TiO and VO, which should be similar to the temperature-forced model. Allowing for the formation of TiO and VO, we observe a small patch around the substellar point that is hot enough to contain TiO and VO in gaseous form, elsewhere the atmosphere is too cold.

Comparing our simulated phase curves, emission and transmission spectra to available observations, we find reasonably good agreement for our model including TiO and VO, while the day side emission appears to be too low for the model without these strong absorbers. We do not take this as evidence for TiO and VO, but rather that there is most likely an extra source of opacity in this atmosphere that we do not include. The observed transmission spectrum does not agree well with our any of our models, or any other cloud-free model in the literature. The presence of clouds has therefore been inferred, which could be a potential source of opacity.

We find significant differences between our models and those of Showman et al. (2009) in transmission spectra and phase curves even though these models use similar assumptions. These discrepancies indicate that intercomparisons will become crucial in order to interpret models correctly.

These planets exhibit a three-dimensional nature that cannot be captured properly by 1D models. As the quality of observations improve, modelling the atmospheric dynamics of hot Jupiters will become crucial to our understanding of hot Jupiter atmospheres. The work presented here provides the basis of future application of the Met Office UM to other planets. In the following section we outline some directions this work could take.

7.2 Future work

There are many different directions the work presented here could take. In Section 7.2.1 we discuss improvements to the radiation scheme that would make it more suitable to hot Jupiter atmospheres. Then, in Section 7.2.2, we discuss the potential future applications of the hot Jupiter UM.

7.2.1 Improvements to the radiation scheme

We would in the future like to further optimise the ES radiation scheme. This would involve completely removing absorbers from bands where the absorption is presumed negligible, and

restrict the wavelength range used by the thermal and stellar components of the radiation scheme. We would also like to reduce the number of bands. Some work has already been done, Kataria et al. (2013) used 11 bands and found that differences compared to using 30 bands were small.

There are several improvements we would like to make to the radiation scheme and the coupling to the dynamical core in order to make it even more suitable to hot Jupiter atmospheres. The Edwards–Slingo radiation scheme assumes a plane-parallel geometry, meaning that effects due to the spherical geometry of the planet are not included in the radiation scheme directly. For planets where the vertical extent of the atmosphere is much smaller than the planet radius, such as the Earth, this is a very good approximation. For hot Jupiters, however, this approximation may be less appropriate as the extent of the atmosphere can be $\sim 10\,\%$ of the planet radius. The accuracy of the plane-parallel approximation should be investigated for hot Jupiter-like atmospheres.

Another aspect of the radiation scheme that could be improved is the assumption of a one-dimensional geometry. This is a valid approximation if horizontal variation in atmospheric conditions are small, but this may not be a good approximation particularly near the terminator of the planet. At latitudes and longitudes on the night side of the planet, but near the terminator, irradiation will not be included in a 1D treatment. In reality, however, the stellar component will be non-zero as some fraction will remain after going through the day side terminator region. Zenith angles at the terminator are very large, however, so this effect should be small.

In addition to investigating the accuracy of the above mentioned approximations, we would like to expand our opacity database. Currently our opacity database includes H_2O, CO, CH_4, NH_3, H2-H2 CIA, and H2-He CIA, which are strong absorbers in the infrared, and Na, K, TiO, VO, which absorbs in the near-infrared and red part of the visible spectrum. If TiO and VO are not present, Na and K will be the dominant absorbers of stellar radiation. Their line wings are broad, but do not extend further than about 0.5 µm towards short wavelengths. For wavelengths shorter than this we only include Rayleigh scattering. Potential absorbers at these short wavelengths are metal hydrides and additional atomic lines, which may become increasingly important for stars with high effective temperatures. This issue may, however, be overshadowed by clouds, which we discuss below.

As the diffuse stellar component of the radiation becomes important, the current formulation of equivalent extinction may have to be modified due to the use of the direct stellar flux at the lower boundary to calculate the equivalent extinction $\bar{K}$ in Eq. (3.60). We plan to implement the random overlap method with reordering and resampling in the ES radiation scheme. Comparing all four different methods of computing k-coefficients for a mixture of gases in the same framework will enable us to evaluate their accuracy and performance, and consequently suitability for use in hot Jupiter GCMs.

The coupled UM has proven to be much more computationally expensive than the temperature-forced model, a combination of the need for a smaller dynamical time step and the additional cost of calculating heating rates from non-grey opacities. For the first issue we would like to

investigate the possibility of implementing adaptive time steps, particularly for the radiation. Due to the physically unrealistic initial conditions used in these models small dynamical and radiative time steps may be required at the beginning of these simulations, but as the atmosphere becomes more stable larger dynamical and radiative time steps may be allowed. A short-term solution is to restart models after the atmosphere has had time to equilibrate with larger dynamical and radiative time steps.

7.2.2 Future research

As discussed in Chapter 4, we found that using an average opacity scheme like that used by Dobbs-Dixon & Agol (2013) can lead to substantial errors in fluxes and heating rates. In the immediate future we plan to investigate the consequences of using this scheme in a GCM, as it would help us understand how sensitive the dynamical processes are to errors in the radiation scheme and the corresponding effect on observables.

Our treatment of abundances have been simple, chemical equilibrium was assumed for all species. We are working on coupling a chemical network to the UM, which will enable us to investigate the effect of non-equilibrium chemistry.

The synthetic phase curves presented here were calculated assuming the planet had achieved a steady-state so that we could use the planet state after, say 600 d, for all orbital phases. This drastically reduces the phase curve computation time as the chemistry and fluxes do not change with time. We have found this to be a valid assumption $\lesssim 1$ bar in the temperature-forced model and the coupled model without TiO and VO. The coupled model with TiO and VO is still evolving slowly, however, and we are currently running longer models to investigate the evolution of the atmosphere beyond 500 d. In addition, this assumption removes all features from the synthetic observations that are caused by time-variability. As observations improve it may become necessary to relax this assumption.

Another issue we would like to investigate is the potential cold-trap of TiO and VO as described in Parmentier et al. (2013). The model of Parmentier et al. (2013) was not self-consistent in that the tracer particles used in the advection scheme were not coupled to the radiation scheme. Thus the feedback on the atmosphere due to a potential change in the abundance of TiO and VO was not considered. The UM has the framework for coupling tracer particle abundances to abundances used in the radiation scheme, which will enable us to study a potential cold-trap more consistently.

The discussion here has focused on the planet HD 209458b, but our model can easily be adapted to other extrasolar planets with H_2- and He-dominated atmospheres. This will enable us to study how the atmospheric circulation, such as the redistribution efficiency and hotspot offset, depends on model parameters such as eccentricity, gravity and metallicity. Work on this has already started in the literature, but the parameter regime is far from understood (Kataria et al. 2014a, 2013; Lewis et al. 2010).

As discussed in Chapter 1 it has become clear from observations that most of these planets are in some way influenced by clouds. No GCM applied to a hot Jupiter, or any exoplanet, includes clouds. The UM has a built-in prognostic cloud scheme (Wilson et al. 2008a,b) that dynamically evolves the cloud particulate properties, including condensation, evaporation and position using tracer particles. Replacing water in this scheme with a generic condensate suitable for the chemistry in hot Jupiter atmospheres will enable us to study the formation and evolution of clouds and their feedback on the atmospheric circulation.

One of the long-term goals of the project is to investigate in more detail the hypothesis suggested by Showman & Guillot (2002) that a vertical transport of kinetic energy into the planet interior can explain the inflated radii of many hot Jupiters. This hypothesis has been difficult to test for several reasons: (i) most models solve the primitive equations which cannot be expected to provide accurate results at high pressures or realistic vertical wind velocities, (ii) deep in the planet's atmosphere dynamical timescales are very long meaning that long simulation timescales are needed, requiring large computational resources, and (iii) these models have an artificial impenetrable bottom boundary which will affect the downward transport of kinetic energy. Since the UM solves the full Euler equations it will be able to realistically model larger vertical domains than models solving the primitive equations. The dynamical core and radiation schemes are also highly optimised in terms of computational cost. These two factors makes the UM well equipped to test this hypothesis. Significant adaptation will be required, however, for the UM to accurately treat large pressures as the equation of state becomes non-ideal and convection becomes the dominant mechanism for energy transport.

In conclusion, the UM provides an excellent base upon which to build a sophisticated GCM applicable to a wide range of atmospheres. The close proximity of the Met Office to the University of Exeter puts us in a unique position to use the UM to study solar system and extrasolar planet atmospheres while at the same time benefiting from using a continuously evolving and improving GCM. The work presented here is only the beginning of an extensive research project aimed at improving our understanding of planetary atmospheres.

Appendix A

Additional derivations

In this appendix we provide useful derivations. Transition probabilities are discussed in Appendix A.1, we provide a derivation of the mean relative velocity between particles as needed by van der Waals broadening in Appendix A.2, in Appendix A.3 we discuss equivalent extinction in more detail, in Appendix A.4 we derive the thermodynamic equation, and in Appendix A.5 we discuss the relationship between velocities measured in an inertial and in a rotating reference frame.

A.1 Transition probabilities

Here we detail different ways of describing transition probabilities between energy levels in atoms and molecules. The definitions and derivations presented here follows that of Šimečková et al. (2006) combined with the notation used in Thomas & Stamnes (2002). Einstein coefficients are defined in Appendix A.1.1, the relationship between Einstein coefficients and the line intensity is given in Appendix A.1.2, and the oscillator strength is discussed in Appendix A.1.3.

A.1.1 Definition of the Einstein coefficients

We introduced the Einstein coefficients in Section 3.1.1. Here we derive the relationship between them, Eq. (3.1). We define the Einstein B-coefficients from the energy density $\mathcal{U}_{\tilde{\nu}}$, i.e. the energy density per unit wavenumber interval. B_{lu} is consequently the number of transitions from the lower to the upper level per unit number density of the species in the lower level per unit energy density $\mathcal{U}_{\tilde{\nu}}$ per unit time. We can therefore write

$$\left(\frac{\mathrm{d}n_{\mathrm{u}}}{\mathrm{d}t}\right)_{\mathrm{abs}} = B_{\mathrm{lu}} n_{\mathrm{l}} \mathcal{U}_{\tilde{\nu}}. \tag{A.1}$$

Similarly for stimulated emission we get

$$\left(\frac{\mathrm{d}n_\mathrm{u}}{\mathrm{d}t}\right)_\mathrm{stim} = -B_\mathrm{ul} n_\mathrm{u} \mathcal{U}_{\tilde{\nu}}, \tag{A.2}$$

where B_ul is the number of induced transitions per unit number density of species in the upper level per unit energy density $\mathcal{U}_{\tilde{\nu}}$ per unit time. The Einstein A_ul-coefficient for spontaneous emission is defined as the number of transitions per unit number density of the species in the upper level per unit time. We can therefore write

$$\left(\frac{\mathrm{d}n_\mathrm{u}}{\mathrm{d}t}\right)_\mathrm{spon} = -A_\mathrm{ul} n_\mathrm{u}. \tag{A.3}$$

Assuming thermodynamic equilibrium (TE) and detailed balance there will be no change in the level populations. We consequently have

$$\left(\frac{\mathrm{d}n_\mathrm{u}^*}{\mathrm{d}t}\right)_\mathrm{spon} + \left(\frac{\mathrm{d}n_\mathrm{u}^*}{\mathrm{d}t}\right)_\mathrm{stim} + \left(\frac{\mathrm{d}n_\mathrm{u}^*}{\mathrm{d}t}\right)_\mathrm{abs} = 0 \quad \Rightarrow \quad A_\mathrm{ul} n_\mathrm{u}^* + B_\mathrm{ul} n_\mathrm{u}^* \mathcal{U}_{\tilde{\nu}} - B_\mathrm{lu} n_\mathrm{l}^* \mathcal{U}_{\tilde{\nu}} = 0, \tag{A.4}$$

where the notation * indicates that n_l^* and n_u^* are the TE number densities. Solving the above equation for $\mathcal{U}_{\tilde{\nu}}$ yields

$$\mathcal{U}_{\tilde{\nu}} = \frac{A_\mathrm{ul}/B_\mathrm{ul}}{n_\mathrm{l}^* B_\mathrm{lu}/n_\mathrm{u}^* B_\mathrm{ul} - 1}. \tag{A.5}$$

In thermodynamic equilibrium $n_\mathrm{l}^*/n_\mathrm{u}^*$ is given by the Boltzmann distribution:

$$\frac{n_\mathrm{l}^*}{n_\mathrm{u}^*} = \frac{g_\mathrm{l}}{g_\mathrm{u}} e^{hc\tilde{\nu}/k_\mathrm{B}T}, \tag{A.6}$$

where g_i is the statistical weight (degeneracy) of level i and $hc\tilde{\nu} = E_\mathrm{u} - E_\mathrm{l}$ is the transition energy. Consequently we have

$$\mathcal{U}_{\tilde{\nu}} = \frac{A_\mathrm{ul}/B_\mathrm{ul}}{(g_\mathrm{l} B_\mathrm{lu}/g_\mathrm{u} B_\mathrm{ul})\, e^{hc\tilde{\nu}/k_\mathrm{B}T} - 1}. \tag{A.7}$$

In TE the energy density is the Planck function,

$$\mathcal{B}_{\tilde{\nu}} = \frac{8\pi hc\tilde{\nu}^3}{e^{hc\tilde{\nu}/k_\mathrm{B}T} - 1}, \tag{2.4}$$

and combining this with Eq. (A.7) we get the Einstein relations

$$A_\mathrm{ul} = 8\pi hc\tilde{\nu}^3 B_\mathrm{ul}, \tag{3.1a}$$

$$g_1 B_\mathrm{lu} = g_\mathrm{u} B_\mathrm{ul}. \tag{3.1b}$$

Since Eq. (3.1) is independent of the state of the gas, i.e. temperature, density etc., it is

also satisfied when the assumption of TE is no longer valid, even in non-local thermodynamic equilibrium (NTLE).

A.1.2 Relationship between the Einstein coefficients and the line intensity

In the following, the subscript $_{\mathrm{lu}}$ for a transition from the lower to the upper level is denoted by i (for transition i) with the corresponding wavenumber $\tilde{\nu}_0$. Treating stimulated emission as negative absorption and using Eqs. (A.1) and (A.2), we have that the change in n_{u} per time due to absorption and stimulated emission is given by

$$\left(\frac{\mathrm{d}n_{\mathrm{u}}}{\mathrm{d}t}\right)_{\mathrm{abs+stim}} = B_{\mathrm{lu}} n_{\mathrm{l}} \mathcal{U}_{\tilde{\nu}} - B_{\mathrm{ul}} n_{\mathrm{u}} \mathcal{U}_{\tilde{\nu}}, \tag{A.9}$$

or equivalently

$$\mathrm{d}n_{\mathrm{u}} = \left(B_{\mathrm{lu}} n_{\mathrm{l}} - B_{\mathrm{ul}} n_{\mathrm{u}}\right) \mathcal{U}_{\tilde{\nu}} \, \mathrm{d}t. \tag{A.10}$$

We introduce the average photon energy per wavenumber, $hc\tilde{\nu}_0 \Phi_i(\tilde{\nu})$, where $\Phi_i(\tilde{\nu})$ is the line profile introduced in Eq. (3.2). Multiplying both sides with $hc\tilde{\nu}_0 \Phi_i(\tilde{\nu})$ yields

$$hc\tilde{\nu}_0 \Phi_i(\tilde{\nu}) \mathrm{d}n_{\mathrm{u}} = hc\tilde{\nu}_0 \Phi_i(\tilde{\nu}) \left(B_{\mathrm{lu}} n_{\mathrm{l}} - B_{\mathrm{ul}} n_{\mathrm{u}}\right) \mathcal{U}_{\tilde{\nu}} \, \mathrm{d}t. \tag{A.11}$$

Note that we have assumed the same line profile for both transitions, usually a good approximation in astrophysics (Rybicki & Lightman 2004).

$\mathrm{d}n_{\mathrm{u}}$ is the number of transitions per unit volume during the time $\mathrm{d}t$, $hc\tilde{\nu}_0 \Phi_i(\tilde{\nu}) \mathrm{d}n_{\mathrm{u}}$ is therefore minus the change in energy density per wavenumber during the time $\mathrm{d}t$. The negative sign is caused by the fact that if $\mathrm{d}n_{\mathrm{u}}$ is positive, energy is being absorbed i.e. the change in energy density is negative. Using $\mathrm{d}t = \mathrm{d}s/c$, where $\mathrm{d}s$ is an infinitesimal distance and c is the speed of light we get

$$\mathrm{d}\mathcal{U}_{\tilde{\nu}} = -hc\tilde{\nu}_0 \Phi_i(\tilde{\nu}) \left(B_{\mathrm{lu}} n_{\mathrm{l}} - B_{\mathrm{ul}} n_{\mathrm{u}}\right) \mathcal{U}_{\tilde{\nu}} \, \mathrm{d}s/c. \tag{A.12}$$

Replacing B_{ul} with B_{lu} using Eq. (3.1b) and for convenience renaming B_{lu} to B_i indicating transition i, we have

$$\mathrm{d}\mathcal{U}_{\tilde{\nu}} = -hc\tilde{\nu}_0 \Phi_i(\tilde{\nu}) \left(B_i n_{\mathrm{l}} - \frac{g_{\mathrm{l}}}{g_{\mathrm{u}}} B_i n_{\mathrm{u}}\right) \mathcal{U}_{\tilde{\nu}} \, \mathrm{d}s/c. \tag{A.13}$$

Equation (A.13) has to be converted to express the change in intensity $\mathrm{d}I_{\tilde{\nu}}$ as a function of the intensity itself $I_{\tilde{\nu}}$. From the definition of intensity, Eq. (2.1), the energy density $\mathcal{U}_{\tilde{\nu}}$ is given by

$$\mathrm{d}\mathcal{U}_{\tilde{\nu}} \equiv \frac{\mathrm{d}^4 E}{\mathrm{d}V \, \mathrm{d}\tilde{\nu}} = \frac{I_{\tilde{\nu}} \cos\theta \, \mathrm{d}A \, \mathrm{d}t \, \mathrm{d}\omega \, \mathrm{d}\tilde{\nu}}{\mathrm{d}A \, \cos\theta \, c \, \mathrm{d}t \, \mathrm{d}\tilde{\nu}} = \frac{I_{\tilde{\nu}}}{c} \mathrm{d}\omega, \tag{A.14}$$

and integrating over all solid angles we get

$$\mathcal{U}_{\tilde{\nu}} = \frac{1}{c}\int_{4\pi} \mathrm{d}\omega\, I_{\tilde{\nu}} = \frac{4\pi}{c}\bar{I}_{\tilde{\nu}} \qquad\qquad \bar{I}_{\tilde{\nu}} \equiv \frac{1}{4\pi}\int_{4\pi} \mathrm{d}\omega\, I_{\tilde{\nu}}. \tag{A.15}$$

Using this result in Eq. (A.13) yields

$$\mathrm{d}\bar{I}_{\tilde{\nu}} = -hc\tilde{\nu}_0 \bar{I}_{\tilde{\nu}} \Phi_i(\tilde{\nu}) \left(B_i n_\mathrm{l} - \frac{g_\mathrm{l}}{g_\mathrm{u}} B_i n_\mathrm{u} \right) \mathrm{d}s/c. \tag{A.16}$$

Since each transition contributes an energy $hc\tilde{\nu}_0$ distributed uniformly over the solid angle 4π, we may use the intensity $I_{\tilde{\nu}}$ instead of the average intensity $\bar{I}_{\tilde{\nu}}$. We therefore have

$$\mathrm{d}I_{\tilde{\nu}} = -hc\tilde{\nu}_0 I_{\tilde{\nu}} \Phi_i(\tilde{\nu}) \left(B_i n_\mathrm{l} - \frac{g_\mathrm{l}}{g_\mathrm{u}} B_i n_\mathrm{u} \right) \mathrm{d}s/c, \tag{A.17}$$

and comparing Eqs. (2.8) and (A.17), we get an expression for the absorption coefficient:

$$\alpha_n(\tilde{\nu}) = h\tilde{\nu}_0 \Phi_i(\tilde{\nu}) \frac{1}{n} \left(B_i n_\mathrm{l} - \frac{g_\mathrm{l}}{g_\mathrm{u}} B_i n_\mathrm{u} \right), \tag{A.18}$$

where n is the number density of the absorber. To get an expression for the line intensity we integrate over all wavenumbers, using that the line profile $\Phi(\tilde{\nu})$ is normalised, and obtain

$$\mathcal{S}_i = h\tilde{\nu}_0 \frac{n_\mathrm{l}}{n} \left(B_i - B_i \frac{g_\mathrm{l} n_\mathrm{u}}{g_\mathrm{u} n_\mathrm{l}} \right). \tag{A.19}$$

Assuming LTE, the level populations n_l and n_u are given by the Boltzmann distribution:

$$\frac{n_\mathrm{l}^*}{n} = \frac{g_\mathrm{l}}{Q(T)} e^{-E_\mathrm{l}/k_\mathrm{B}T}, \qquad \frac{n_\mathrm{u}^*}{n_\mathrm{l}^*} = \frac{g_\mathrm{u}}{g_\mathrm{l}} e^{-hc\tilde{\nu}_0/k_\mathrm{B}T}, \qquad Q(T) = \sum_i g_i e^{-E_i/k_\mathrm{B}T}, \tag{A.20}$$

where $Q(T)$ is the total partition function, and we have

$$\mathcal{S}_i = h\tilde{\nu}_0 \frac{g_\mathrm{l} e^{-E_\mathrm{l}/k_\mathrm{B}T}}{Q(T)} \left(1 - e^{-hc\tilde{\nu}_0/k_\mathrm{B}T} \right) B_i, \tag{A.21}$$

which is the line intensity expressed in terms of the Einstein $B_i = B_\mathrm{lu}$ coefficient. Usually it is more convenient to work with the A_ul-coefficient due to the unambiguity of its definition. Replacing B_i with A_i using Eq. (3.1) we have

$$\mathcal{S}_i = \mathcal{S}_i(T) = \frac{1}{8\pi c\tilde{\nu}_0^2} \frac{g_\mathrm{u} e^{-E_\mathrm{l}/k_\mathrm{B}T}}{Q(T)} \left(1 - e^{-hc\tilde{\nu}_0/k_\mathrm{B}T} \right) A_i. \tag{3.3}$$

A.1.3 Oscillator strength

Some line lists provide a quantity called the oscillator strength f_{lu} of a transition. It is normal to weigh the oscillator strength by the degeneracy of the lower level, i.e. $g_{\mathrm{l}} f_{\mathrm{lu}}$, which is often abbreviated as the gf-value. A detailed quantum-mechanical discussion is outside the scope of this work, see e.g. Rybicki & Lightman (2004) for details.

The oscillator strength is, as the Einstein coefficients, a measure of the probability of a transition. It can be thought of as the correction factor to the total amount of energy extracted from a beam of radiation by a classical harmonic oscillator. In the following we derive an expression relating the Einstein coefficients and the oscillator strength.

The classical damped harmonic oscillator

As a rather crude approximation, an electron can be thought of as trapped in a harmonic potential with natural (angular) frequency ω_0 caused by the nucleus. Treating the inherently quantum mechanical problem of the electron-nucleus interaction using classical physics leads to an expression for the cross section, from which the oscillator strength can be defined.

The oscillations are driven by an external electromagnetic field with frequency ω, and the electron will consequently oscillate. This acceleration of a charge causes dissipation of energy by emitting radiation, and in classical physics it is approximated as being lost through a damping force proportional to the velocity $F = -m_{\mathrm{e}}\gamma\dot{z}$, where m_{e} is the electron mass, $\dot{z}$ the electron velocity and

$$\gamma = \frac{2e^2\omega_0^2}{3m_{\mathrm{e}}c^3}, \tag{A.22}$$

where e is the elementary charge in CGS-Gaussian units. The equation of motion for the electron is

$$m_{\mathrm{e}}\ddot{z} + m_{\mathrm{e}}\gamma\dot{z} + m_{\mathrm{e}}\omega_0^2 z^2 = -eE'\cos(\omega t), \tag{A.23}$$

where z is the position of the electron and E' is the electric field amplitude. It is straight-forward to solve this equation using e.g. the characteristic polynomial. Solving the homogeneous equation first, we have

$$r^2 + \gamma r + \omega_0^2 = 0 \quad \Rightarrow \quad r_{\pm} = \frac{-\gamma \pm \sqrt{\gamma^2 - 4\omega_0^2}}{2}, \tag{A.24}$$

and the solution to the homogeneous equation is given by

$$z^{\mathrm{h}}(t) = Ae^{r_+ t} + Be^{r_- t}. \tag{A.25}$$

Whether or not the oscillations are over-damped, critically damped, or under-damped is irrelevant since we wish to consider the stable solution at $t \to \infty$, where $z^{\mathrm{h}}(t \to \infty) \to 0$. Only the particular solution of Eq. (A.23) is of interest, and we find it by inserting a solution on the form

$z^{\mathrm{p}}(t) = A\cos(\omega t + \phi)$:

$$A(\omega_0^2 - \omega^2)\cos(\omega t + \phi) - A\omega\gamma\sin(\omega t + \phi) = -\frac{eE'}{m_{\mathrm{e}}}\cos(\omega t). \tag{A.26}$$

By using the two identities

$$\cos(\theta_1 + \theta_2) = \cos(\theta_1)\cos(\theta_2) - \sin(\theta_1)\sin(\theta_2), \tag{A.27}$$

$$\sin(\theta_1 + \theta_2) = \sin(\theta_1)\cos(\theta_2) + \cos(\theta_1)\sin(\theta_2), \tag{A.28}$$

we get

$$\left[A(\omega_0^2 - \omega^2)\cos(\phi) - A\omega\gamma\sin(\phi) + \frac{eE'}{m_{\mathrm{e}}}\right]\cos(\omega t) - A\left[(\omega_0^2 - \omega^2)\sin(\phi) + \omega\gamma\cos(\phi)\right]\sin(\omega t) = 0, \tag{A.29}$$

and consequently,

$$A(\omega_0^2 - \omega^2)\cos(\phi) - A\omega\gamma\sin(\phi) + \frac{eE'}{m_{\mathrm{e}}} = 0, \tag{A.30}$$

$$(\omega_0^2 - \omega^2)\sin(\phi) + \omega\gamma\cos(\phi) = 0. \tag{A.31}$$

From Eq. (A.31), we get

$$\tan(\phi) = -\frac{\omega\gamma}{\omega_0^2 - \omega^2}, \tag{A.32}$$

$$\cos(\phi) = \frac{1}{\sqrt{1 + \tan^2(\phi)}} = \frac{\omega_0^2 - \omega^2}{\sqrt{(\omega_0^2 - \omega^2)^2 + \omega^2\gamma^2}} \tag{A.33}$$

$$\sin(\phi) = \frac{\tan(\phi)}{\sqrt{1 + \tan^2(\phi)}} = -\frac{\omega\gamma}{\sqrt{(\omega_0^2 - \omega^2)^2 + \omega^2\gamma^2}}. \tag{A.34}$$

Inserting this into Eq. (A.30) yields

$$A\frac{(\omega_0^2 - \omega^2)^2 + \omega^2\gamma^2}{\sqrt{(\omega_0^2 - \omega^2)^2 + \omega^2\gamma^2}} + \frac{eE'}{m_{\mathrm{e}}} = 0, \tag{A.35}$$

and solving for A:

$$A = -\frac{eE'}{m_{\mathrm{e}}}\frac{1}{\sqrt{(\omega_0^2 - \omega^2)^2 + \omega^2\gamma^2}}. \tag{A.36}$$

An accelerated charge will emit radiation with a power given by the Larmor formula (Rybicki & Lightman 2004), which yields a net energy loss

$$P(\omega, t) = \frac{2}{3}\frac{e^2\ddot{z}^2}{c^3} = \frac{2}{3}\frac{e^2}{c^3}\left[-A\omega^2\cos(\omega t + \phi)\right]^2. \tag{A.37}$$

We are interested in the time averaged emitted power, and averaging the above equation over one period yields

$$P(\omega) \equiv \frac{1}{2\pi}\int_0^{2\pi} P(\omega, t)\,\mathrm{d}t = \frac{e^2A^2\omega^4}{3c^3}, \tag{A.38}$$

since the average of $\cos^2(\omega t + \phi)$ is 1/2. Using Eq. (A.36), we have

$$P(\omega) = \frac{e^4E'^2}{3m_\mathrm{e}^2c^3}\frac{\omega^4}{(\omega_0^2-\omega^2)^2+\omega^2\gamma^2}. \tag{A.39}$$

The energy density in the incident electromagnetic field is $\boldsymbol{E}(t)^2/4\pi$, and the energy transported per unit time per unit area is consequently $cE(t)^2/4\pi$. The time averaged power of the incident electric filed is then given by $cE'^2/8\pi$, and the ratio between the emitted power and incident power per unit area is the scattering cross section

$$\sigma_n(\omega) = \frac{P(\omega)}{cE'^2/8\pi} = \frac{8\pi e^4}{3m_\mathrm{e}^2c^4}\frac{\omega^4}{(\omega_0^2-\omega^2)^2+\omega^2\gamma^2}. \tag{A.40}$$

In the limit where $\delta\omega = \omega_0 - \omega$, $|\delta\omega| \ll \omega$, i.e. the frequency of the incident electromagnetic field is close to the natural oscillation frequency, we can make the following approximation:

$$\omega_0^2 - \omega^2 = (\omega+\delta\omega)^2 - \omega^2 = 2\omega\delta\omega + (\delta\omega)^2 \approx 2\omega\delta\omega = 2\omega\left(\omega_0-\omega\right), \tag{A.41}$$

which yields

$$\sigma_n(\omega) = \frac{8\pi e^4}{3m_\mathrm{e}^2c^4}\frac{\omega^2/4}{(\omega_0-\omega)^2+\gamma^2/4} = \frac{4\pi e^2}{m_\mathrm{e}c}\frac{\gamma/4}{(\omega_0-\omega)^2+(\gamma/2)^2}, \tag{A.42}$$

where on the right-hand side ω has been replaced by ω_0 in the numerator. Changing from angular frequency $\omega = 2\pi\nu = 2\pi c\tilde{\nu}$ to wavenumber $\tilde{\nu}$, we have

$$\sigma_n(\tilde{\nu}) = \frac{\pi e^2}{m_\mathrm{e}c^2}\Phi_\mathrm{L}(\tilde{\nu}), \qquad \Phi_\mathrm{L}(\tilde{\nu}) = \frac{1}{\pi}\frac{\gamma/4\pi c}{(\tilde{\nu}_0-\tilde{\nu})^2+(\gamma/4\pi c)^2}, \tag{A.43}$$

where $\Phi_\mathrm{L}(\tilde{\nu})$ is the Lorentz profile. It is normalised to 1:

$$\int_0^\infty \mathrm{d}\tilde{\nu}\,\Phi_\mathrm{L}(\tilde{\nu}) = 1, \tag{A.44}$$

and the full width at half maximum is given by $\gamma/2\pi c$. The total wavenumber-integrated scattering cross section predicted by this classical model is therefore given by

$$\int_0^\infty \mathrm{d}\tilde{\nu}\,\sigma_n(\tilde{\nu}) = \frac{\pi e^2}{m_\mathrm{e}c^2}. \tag{A.45}$$

Relationship between oscillator strength and Einstein coefficients

The total energy extracted from a beam can be written in terms of a "classical" Einstein $B_{\rm lu}^{\rm cl}$-coefficient in analogy to the discussion above. Using Eq. (A.18), including only the absorption term and setting $n_{\rm l}/n = 1$ we have

$$\sigma_n(\tilde{\nu}) = B_{\rm lu}^{\rm cl} h\tilde{\nu}_0 \Phi_i(\tilde{\nu}) \quad \Rightarrow \quad \int_0^\infty \mathrm{d}\tilde{\nu}\, \sigma_n(\tilde{\nu}) = B_{\rm lu}^{\rm cl} h\tilde{\nu}_0, \tag{A.46}$$

and by comparing Eqs. (A.45) and (A.46) we get the following relation:

$$B_{\rm lu}^{\rm cl} h\tilde{\nu}_0 = \frac{\pi e^2}{m_{\rm e} c^2}. \tag{A.47}$$

The oscillator strength $f_{\rm lu}$ is defined as the correction factor to this expression when quantum mechanical effects are taken into account, i.e.

$$B_{\rm lu} h\tilde{\nu}_0 \equiv \frac{\pi e^2}{m_{\rm e} c^2} f_{\rm lu}, \tag{A.48}$$

where the classical Einstein coefficient has been replaced by its quantum mechanical counterpart. As above, it is more convenient to relate it to the Einstein $A_{\rm ul}$-coefficient, and using Eq. (3.1), we have

$$g_{\rm u} A_{\rm ul} = \frac{8\pi^2 e^2 \tilde{\nu}_0^2}{m_{\rm e} c} g_{\rm l} f_{\rm lu}. \tag{3.7}$$

The quantity $g_{\rm l} f_{\rm lu}$ is often referred to as the gf-value of the transition. Inserting this into Eq. (3.3), we get the line intensity in terms of the gf-value

$$\mathcal{S}_i(T) = \frac{\pi e^2}{m_{\rm e} c^2} \frac{e^{-E_{\rm l}/k_{\rm B}T}}{Q(T)} \left(1 - e^{-hc\tilde{\nu}_0/k_{\rm B}T}\right) g_{\rm l} f_{\rm lu}. \tag{3.8}$$

A.2 The mean relative velocity in van der Waals broadening

Here we derive Eq. (3.26) for the mean relative velocity between particles, $\langle v_{\rm rel} \rangle$. Assuming LTE, the velocity $\boldsymbol{v}_n$ of species n will follow the Maxwell-Boltzmann distribution, Eq. (3.13), and including all three velocity components it is given by

$$\mathcal{D}_n(\boldsymbol{v}_n) = \left(\frac{m_n}{2\pi k_{\rm B} T}\right)^{3/2} e^{-m_n \boldsymbol{v}_n^2 / 2k_{\rm B}T}. \tag{A.49}$$

The average relative velocity between two particles (named 1 and 2 for convenience) is then given by

$$\langle v_{\rm rel} \rangle = \int \mathrm{d}\boldsymbol{v}_1 \int \mathrm{d}\boldsymbol{v}_2\, |\boldsymbol{v}_1 - \boldsymbol{v}_2|\, \mathcal{D}_1(\boldsymbol{v}_1) \mathcal{D}_2(\boldsymbol{v}_2), \tag{A.50}$$

where the integration is over all $\boldsymbol{v}_1$ and $\boldsymbol{v}_2$. It turns out that by introducing two new variables, the integral can be simplified significantly. The centre of mass velocity $\boldsymbol{V}$ and the relative velocity $\boldsymbol{v}$ is defined by

$$\boldsymbol{V} = \frac{m_1\boldsymbol{v}_1 + m_2\boldsymbol{v}_2}{m_1 + m_2}, \qquad\qquad \boldsymbol{v} = \boldsymbol{v}_1 - \boldsymbol{v}_2. \tag{A.51}$$

In order to substitute $\boldsymbol{V}$ and $\boldsymbol{v}$ into Eq. (A.50), an expression for $m_1\boldsymbol{v}_1^2 + m_2\boldsymbol{v}_2^2$ has to be found. By observing that

$$\boldsymbol{v}_1 = \boldsymbol{V} + \frac{m_2}{m_1 + m_2}\boldsymbol{v}, \qquad\qquad \boldsymbol{v}_2 = \boldsymbol{V} - \frac{m_1}{m_1 + m_2}\boldsymbol{v}, \tag{A.52}$$

it is straight-forward to show that

$$m_1\boldsymbol{v}_1^2 + m_2\boldsymbol{v}_2^2 = (m_1 + m_2)\boldsymbol{V}^2 + \frac{m_1 m_2}{m_1 + m_2}\boldsymbol{v}^2. \tag{A.53}$$

Last, the Jacobi-factor for the coordinate transformation must be found. First we replace replace $\boldsymbol{v}_2$ by $\boldsymbol{v}$, and denote the ith component of $\boldsymbol{v}$ by $v^{(i)}$, and similarly for $\boldsymbol{v}_1$ and $\boldsymbol{v}_2$. This yields

$$v^{(i)} = v_1^{(i)} - v_2^{(i)} \qquad\Rightarrow\qquad \frac{\partial v^{(i)}}{\partial v_2^{(i)}} = -1, \tag{A.54}$$

i.e. $\mathrm{d}\boldsymbol{v}_2 = -\mathrm{d}\boldsymbol{v}$, and the integration limits are now from $v^{(i)} \to \infty$ to $v^{(i)} \to -\infty$. Next we replace $\boldsymbol{v}_1$ by $\boldsymbol{V}$, and using Eqs. (A.51) and (A.52), we have

$$\boldsymbol{V} = \boldsymbol{v}_1 - \frac{1}{m_1 + m_2}\boldsymbol{v} \qquad\Rightarrow\qquad \frac{\partial V^{(i)}}{\partial v_1^{(i)}} = 1, \tag{A.55}$$

i.e. $\mathrm{d}\boldsymbol{v}_1 = \mathrm{d}\boldsymbol{V}$. Putting all of this together using Eqs. (A.49), (A.50) and (A.53), and flipping the integration limits on the $\boldsymbol{v}$-integral back to $-\infty$ to ∞, we have

$$\langle v_{\mathrm{rel}}\rangle = \left(\frac{1}{2\pi k_{\mathrm{B}}T}\right)^3 (m_1 m_2)^{3/2} \int_{-\infty}^{\infty}\mathrm{d}\boldsymbol{v}_1 \int_{-\infty}^{\infty}\mathrm{d}\boldsymbol{v}_2\ |\boldsymbol{v}_1 - \boldsymbol{v}_2|\, e^{-(m_1\boldsymbol{v}_1^2 + m_2\boldsymbol{v}_2^2)/2k_{\mathrm{B}}T} \tag{A.56}$$

$$= \left(\frac{1}{2\pi k_{\mathrm{B}}T}\right)^3 (m_1 m_2)^{3/2} \int_{-\infty}^{\infty}\mathrm{d}\boldsymbol{V} e^{-(m_1+m_2)\frac{\boldsymbol{V}^2}{2k_{\mathrm{B}}T}} \int_{-\infty}^{\infty}\mathrm{d}\boldsymbol{v}\, v e^{-\frac{m_1 m_2}{m_1+m_2}\frac{\boldsymbol{v}^2}{2k_{\mathrm{B}}T}} \tag{A.57}$$

Integrating out $\boldsymbol{V}$ using the known integral

$$\int_{-\infty}^{\infty}\mathrm{d}x\, e^{-kx^2} = \sqrt{\frac{\pi}{k}}, \tag{A.58}$$

we have

$$\langle v_{\mathrm{rel}} \rangle = \left(\frac{1}{2\pi k_{\mathrm{B}} T} \right)^3 (m_1 m_2)^{3/2} \left(\frac{2\pi k_{\mathrm{B}} T}{m_1 + m_2} \right)^{3/2} \int_{-\infty}^{\infty} \mathrm{d}\boldsymbol{v}\, v e^{-\frac{m_1 m_2}{m_1 + m_2} \frac{\boldsymbol{v}^2}{2 k_{\mathrm{B}} T}} \tag{A.59}$$

$$= \left(\frac{\tilde{m}}{2\pi k_{\mathrm{B}} T} \right)^{3/2} \int_{-\infty}^{\infty} \mathrm{d}\boldsymbol{v}\, v e^{-\tilde{m}\boldsymbol{v}^2 / k_{\mathrm{B}} T}, \tag{A.60}$$

where the reduced mass $\tilde{m} = m_1 m_2/(m_1 + m_2)$ has been introduced. This integral is identical to the average absolute velocity of a particle with mass $\tilde{m}$. The average relative velocity is therefore given by the average velocity of a particle with mass $\tilde{m}$, i.e.

$$\langle v_{\mathrm{rel}} \rangle = \sqrt{\frac{8 k_{\mathrm{B}} T}{\pi \tilde{m}}} = \sqrt{\frac{8 k_{\mathrm{B}} T}{\pi} \left(\frac{1}{m_1} + \frac{1}{m_2} \right)}, \tag{A.61}$$

where we have used the mean of the Maxwell-Boltzmann distribution.

A.3 Equivalent extinction

Here we derive equivalent extinction following Edwards (1996). Notation of explicit wavenumber dependence has been dropped for convenience. For the thermal component we use the differential upward and downward fluxes introduced in Section 2.2.7,

$$G^{\pm} = \pm \int_{\omega_{\pm}} \mu I' \, \mathrm{d}\omega' = F^{\pm} - \pi B, \tag{A.62}$$

i.e. the the flux less the Planck flux. Using Eq. (2.105b) for the downward flux and substituting for G^- using Eq. (A.62), we get

$$\frac{\mathrm{d}G^-}{\mathrm{d}\tau} + \pi \frac{\mathrm{d}B}{\mathrm{d}\tau} = Dab \left[G^+ + \pi B \right] - D(1 - a(1-b)) \left[G^- + \pi B \right] + D\pi \left[1 - a \right] B_\nu(T), \tag{A.63}$$

which yields

$$\frac{\mathrm{d}G^-}{\mathrm{d}\tau} = DabG^+ - D(1 - a(1-b))G^- - \pi \frac{\mathrm{d}B}{\mathrm{d}\tau}. \tag{A.64}$$

The thermal source term has thus been removed and a new source term $-\pi \mathrm{d}B/\mathrm{d}\tau$ has been introduced accounting for changes in flux due to temperature gradients.

In order to ease the following discussion we go back to a formulation with explicit absorption and scattering coefficients, $\mathrm{d}\tau = -(\alpha + \sigma)\, \mathrm{d}z$, $a = \sigma/(\alpha + \sigma)$. Also introducing $\mathrm{d}u = -D\rho\, \mathrm{d}z$, which yields $\mathrm{d}\tau = (\alpha + \sigma)/(D\rho)\, \mathrm{d}u$, we get

$$\frac{D\rho}{\alpha + \sigma} \frac{\mathrm{d}G^-}{\mathrm{d}u} = DabG^+ - D(1 - a(1-b))G^- - \pi \frac{D\rho}{\alpha + \sigma} \frac{\mathrm{d}B}{\mathrm{d}u}. \tag{A.65}$$

Inserting for a and defining $\alpha = k_\rho^{\mathrm{a}} \rho$, $\sigma = k_\rho^{\mathrm{s}} \rho$, where k_ρ^{a} and k_ρ^{s} are the mass absorption and

scattering coefficients, respectively, we get

$$\frac{\mathrm{d}G^-}{\mathrm{d}u} = k_\rho^{\mathrm{s}} b G^+ - (k_\rho^{\mathrm{a}} + k_\rho^{\mathrm{s}}(1-\tilde{b}))G^- - \pi\frac{\mathrm{d}B}{\mathrm{d}u}, \tag{A.66}$$

where we have introduced the forward scattering coefficient $\tilde{b} = 1 - b$. Equation (A.66) is identical to Eq. (17) in Edwards (1996).

Following Edwards (1996), we let κ_a and κ_s denote mass extinction coefficients for absorption and scattering for all optical processes except one minor gas. We denote the solution exempting the minor gas G_0^-, i.e.

$$\frac{\mathrm{d}G_0^-}{\mathrm{d}u} = \kappa_{\mathrm{s}} b G_0^+ - (\kappa_{\mathrm{a}} + \kappa_{\mathrm{s}}(1-\tilde{b}))G_0^- - \pi\frac{\mathrm{d}B}{\mathrm{d}u}. \tag{A.67}$$

Next, let K_i, $i = 1, 2, \ldots, n_k$ be the k-terms of the minor gas with corresponding weights w_i and $G_i^\pm$ be the solution including the minor gas as well. We get the following equation for the differential flux including k-term K_i for the minor gas:

$$\frac{\mathrm{d}G_i^-}{\mathrm{d}u} = k_\rho^{\mathrm{s}} b G_i^+ - (k_\rho^{\mathrm{a}} + k_\rho^{\mathrm{s}}(1-\tilde{b}) + K_i\zeta)G_i^- - \pi\frac{\mathrm{d}B}{\mathrm{d}u}. \tag{A.68}$$

The total differential flux is consequently

$$G^\pm = \sum_{i=1}^{n_k} w_i G_i^\pm, \tag{A.69}$$

and the equation for the total flux is, using Eqs. (A.66) and (A.68),

$$\begin{aligned}
\frac{\mathrm{d}G^-}{\mathrm{d}u} &= \sum_{i=1}^{n_k} w_i \frac{\mathrm{d}G_i^-}{\mathrm{d}u} && \text{(A.70)}\\
&= \sum_{i=1}^{n_k} w_i \left[k_\rho^{\mathrm{s}} b G_i^+ - (k_\rho^{\mathrm{a}} + k_\rho^{\mathrm{s}}(1-\tilde{b}) + K_i\zeta)G_i^- - \pi\frac{\mathrm{d}B}{\mathrm{d}u} \right] && \text{(A.71)}\\
&= k_\rho^{\mathrm{s}} b G^+ - (k_\rho^{\mathrm{a}} + k_\rho^{\mathrm{s}}(1-\tilde{b}) + \bar{K}^-\zeta)G^- - \pi\frac{\mathrm{d}B}{\mathrm{d}u}, && \text{(A.72)}
\end{aligned}$$

where ζ is the mass mixing ratio of the minor gas and

$$\bar{K}^- = \frac{\sum_{i=1}^{n_k} w_i K_i G_i^-}{\sum_{i=1}^{n_k} w_i G_i^-}. \tag{A.73}$$

This means that the problem can be solved by treating the minor gas as an equivalent grey extinction process through $\bar{K}^-$. Calculating $\bar{K}^-$ requires the full solution to the problem, however, and for this technique to be useful an approximation for $\bar{K}^-$ must be found.

We define

$$\tilde{G}_i^{\pm} = \frac{G_{\mathrm{v},i}^{\pm}}{G_{\mathrm{v}}^{\pm}} G_0^{\pm}, \tag{A.74}$$

where $G_{\mathrm{v},i}^{\pm}$ is the solution including only absorption by the minor gas,

$$\frac{\mathrm{d}G_{\mathrm{v},i}^{\pm}}{\mathrm{d}u} = -K_i \zeta G_{\mathrm{v},i}^{\pm} - \pi \frac{\mathrm{d}B}{\mathrm{d}u}, \tag{A.75}$$

and $G_{\mathrm{v}}^{\pm}$ are the fluxes in vacuum,

$$\frac{\mathrm{d}G_{\mathrm{v}}^{\pm}}{\mathrm{d}u} = -\pi \frac{\mathrm{d}B}{\mathrm{d}u}. \tag{A.76}$$

Using Eq. (A.74), we get

$$\frac{\mathrm{d}\tilde{G}_i^{-}}{\mathrm{d}u} = \kappa_{\mathrm{s}} b \tilde{G}_i^{+} - \left[\kappa_a + \kappa_s(1-\tilde{b}) + K_i\zeta\right] \tilde{G}_i^{-} - \pi \frac{\mathrm{d}B}{\mathrm{d}u} \tag{A.77}$$

$$+ \pi \frac{\mathrm{d}B}{\mathrm{d}u} \left(1 - \frac{G_0^{-}}{G_{\mathrm{v}}^{-}}\right) \left(1 - \frac{G_{\mathrm{v},i}^{-}}{G_{\mathrm{v}}^{-}}\right) - \kappa_s b \tilde{G}^{+} \left(1 - \frac{G_{\mathrm{v},i}^{-} G_{\mathrm{v}}^{+}}{G_{\mathrm{v}}^{-} G_{\mathrm{v},i}^{+}}\right), \tag{A.78}$$

which is identical to Eq. (A.68) except for the last two error terms. Consequently, $\tilde{G}_i^{-} \approx G_i^{-}$ if these two terms are small. We refer to Edwards (1996) for an in-depth discussion, but it turns out that these two terms can be neglected if the minor gas is indeed weakly absorbing.

Thus we can approximate the differential fluxes G_i^{-} in Eq. (A.73) by

$$G_i^{-} \approx \tilde{G}_i^{-} = \frac{G_{\mathrm{v},i}^{-}}{G_{\mathrm{v}}^{-}} G_0^{-}, \tag{A.79}$$

and inserting this back into Eq. (A.73), we get

$$\bar{K}^{-} \approx \frac{\sum_{i=1}^{n_k} w_i K_i G_{\mathrm{v},i}^{-}}{\sum_{i=1}^{n_k} w_i G_{\mathrm{v},i}^{-}}. \tag{A.80}$$

This means that $\bar{K}^{-}$ can be calculated from a calculation involving only the minor gas alone. A similar argument can be applied to the upward fluxes.

The ES radiation scheme uses the net fluxes in Eq. (A.80) instead, i.e.

$$\bar{K} \approx \frac{\sum_{i=1}^{n_k} w_i K_i F_{\mathrm{v},i}}{\sum_{i=1}^{n_k} w_i F_{\mathrm{v},i}}, \tag{3.59}$$

to avoid having different equivalent extinctions in the upward and downward directions.

In the stellar region, assuming random overlap, the direct beam is easily included by calculating transmissions for each gas separately and then taking the product since, assuming random overlap, direct transmissions are multiplicative. For the diffuse beam, which will be non-zero if Rayleigh-scattering is included, an equivalent extinction is defined in the ES scheme

as

$$\bar{K} \approx \frac{\sum_{i=1}^{n_k} w_i K_i F_{\mathrm{s}*,i}}{\sum_{i=1}^{n_k} w_i F_{\mathrm{s}*,i}}, \tag{3.60}$$

where $F_{\mathrm{s}*,i}$ is the direct flux at the lower boundary including absorption only by k-term i.

$\bar{K}$ for each minor gas is obtained by performing n_k calculations involving the minor gas alone. The full fluxes are obtained by representing absorption by each minor gas as an equivalent grey extinction $\bar{K}$ in each band, and performing a full calculation for each k-term of the major gas. Consequently, this calculation scales as $N_{\mathrm{gas}} n_k$, which is much preferable to the $n_k^{N_{\mathrm{gas}}}$ scaling of the random overlap method without reordering and resampling.

Equivalent extinction has been shown to perform satisfactory for the Earth (Edwards 1996), and we tested its applicability to hot Jupiter atmospheres in Chapter 4 and found that errors in fluxes and heating rates are $\lesssim 10\,\%$, about the same as errors caused by the two-stream approximation and correlated-k method. Consequently we adopt equivalent extinction in Chapters 5 and 6 for our GCM simulations.

A.4 The thermodynamic equation

Here we derive and discuss the thermodynamic equation, which couples the heating rate calculated by the radiation scheme to temperature changes in the atmosphere. The Exner pressure and potential temperature, which are two often-used quantities in fluid dynamics are also discussed. The discussion here is based on Vallis (2006).

A.4.1 Thermodynamic identities

The first law of thermodynamics says that the total change in internal energy per mass of fluid, $\mathrm{d}U$ is given by the heat added per mass, $\mathrm{d}Q$, and the work done by the fluid per mass, $\mathrm{d}W$:

$$\mathrm{d}U = \mathrm{d}Q - \mathrm{d}W. \tag{A.81}$$

At the same time, we have the thermodynamic identity

$$\mathrm{d}U = T\,\mathrm{d}\eta - P\,\mathrm{d}\alpha, \tag{A.82}$$

where η is the specific entropy, i.e. entropy per unit mass, and $\alpha = 1/\rho$ is the specific volume. Assume that the fluid element has a pressure P and that its volume changes reversibly/quasistatically by $\mathrm{d}\alpha$, then $\mathrm{d}W = P\,\mathrm{d}\alpha$ and $\mathrm{d}Q = T\,\mathrm{d}\eta$, which yields

$$\mathrm{d}Q = T\,\mathrm{d}\eta = \mathrm{d}U + P\,\mathrm{d}\alpha. \tag{A.83}$$

It is possible to write $\mathrm{d}U$ as

$$\mathrm{d}U = \left(\frac{\partial U}{\partial T}\right)_\alpha \mathrm{d}T + \left(\frac{\partial U}{\partial \alpha}\right)_T \mathrm{d}\alpha, \tag{A.84}$$

and combining Eqs. (A.83) and (A.84) we get a thermodynamic identity for the entropy

$$\mathrm{d}\eta = \frac{1}{T}\left[\mathrm{d}U + P\,\mathrm{d}\alpha\right] = \frac{1}{T}\left(\frac{\partial U}{\partial T}\right)_\alpha \mathrm{d}T + \left[\frac{1}{T}\left(\frac{\partial U}{\partial \alpha}\right)_T + \frac{P}{T}\right]\mathrm{d}\alpha. \tag{A.85}$$

Similar to Eq. (A.84) we can also write

$$\mathrm{d}\eta = \left(\frac{\partial \eta}{\partial T}\right)_\alpha \mathrm{d}T + \left(\frac{\partial \eta}{\partial \alpha}\right)_T \mathrm{d}\alpha, \tag{A.86}$$

and combining Eqs. (A.85) and (A.86), we get

$$\left(\frac{\partial \eta}{\partial T}\right)_\alpha = \frac{1}{T}\left(\frac{\partial U}{\partial T}\right)_\alpha, \qquad \left(\frac{\partial \eta}{\partial \alpha}\right)_T = \frac{1}{T}\left(\frac{\partial U}{\partial \alpha}\right)_T + \frac{P}{T}. \tag{A.87}$$

Using Clairaut's theorem for mixed partials ($\partial^2 f/\partial x \partial y = \partial^2 f/\partial y \partial x$), we have

$$\frac{\partial^2 \eta}{\partial \alpha\, \partial T} = \frac{\partial^2 \eta}{\partial T\, \partial \alpha} \tag{A.88}$$

$$\frac{1}{T}\frac{\partial^2 U}{\partial \alpha\, \partial T} = \frac{1}{T}\frac{\partial^2 U}{\partial T\, \partial \alpha} - \frac{1}{T^2}\left(\frac{\partial U}{\partial \alpha}\right)_T + \left(\frac{\partial}{\partial T}\left(\frac{P}{T}\right)\right)_\alpha \tag{A.89}$$

$$0 = -\frac{1}{T^2}\left(\frac{\partial U}{\partial \alpha}\right)_T + \left(\frac{\partial}{\partial T}\left(\frac{P}{T}\right)\right)_\alpha. \tag{A.90}$$

For an ideal gas, $PV = Nk_\mathrm{B}T$, but in this case it is more convenient to write it in terms of the gas constant for the gas in question, $\mathcal{R} = R/\bar{m}$, where R is the ideal gas constant and $\bar{m}$ is the mean molecular mass in kg/mol. In terms of R, the equation of state is $P = nRT$, where n is the number density in mol/m^3. Inserting $\mathcal{R}\bar{m}$ for R, we get $P = n\bar{m}\mathcal{R}T = \rho\mathcal{R}T$.

We consequently have $P/T = \rho\mathcal{R} = \mathcal{R}/\alpha$, and looking back to Eq. (A.90) the second term on the right-hand side is zero for an ideal gas. This yields

$$\left(\frac{\partial U}{\partial \alpha}\right)_T = 0 \qquad \text{ideal gas}, \tag{A.91}$$

i.e. the total energy of a fluid parcel does not depend on its volume given that it satisfies the ideal gas equation. Using the above result in Eq. (A.84) and inserting this into Eq. (A.83) yield

$$\mathrm{d}Q = T\,\mathrm{d}\eta = \mathrm{d}U + P\,\mathrm{d}\alpha = \left(\frac{\partial U}{\partial T}\right)_\alpha \mathrm{d}T + P\,\mathrm{d}V = c_V\,\mathrm{d}T + P\,\mathrm{d}\alpha, \tag{A.92}$$

where we have introduced the specific heat capacity at constant volume:

$$c_V \equiv \left(\frac{\mathrm{d}U}{\mathrm{d}T}\right)_\alpha. \tag{A.93}$$

The specific heat capacity at constant pressure is defined as

$$c_P \equiv \left(\frac{\partial H}{\partial T}\right)_P = \left(\frac{\partial U}{\partial T}\right)_P + P\left(\frac{\partial \alpha}{\partial T}\right)_P, \tag{A.94}$$

where we have introduced the (specific) enthalpy $H = U + P\alpha$, $\mathrm{d}H = \mathrm{d}U + \mathrm{d}(P\alpha)$, which can be interpreted as the total energy of the system, U, plus the energy needed to make room for it at constant pressure, $P\alpha$. For an ideal gas $P\alpha = \mathcal{R}T$, which yields $\mathrm{d}H = c_V\,\mathrm{d}T + \mathrm{d}(P\alpha) = c_V\,\mathrm{d}T + \mathrm{d}(\mathcal{R}T) = (c_V + \mathcal{R})\,\mathrm{d}T$, i.e.

$$c_P = \left(\frac{\partial H}{\partial T}\right)_P = c_V + \mathcal{R}. \tag{A.95}$$

This can be used to replace c_V by c_P in Eq. (A.92):

$$\mathrm{d}Q = T\,\mathrm{d}\eta = c_V\,\mathrm{d}T + P\,\mathrm{d}\alpha = c_P\,\mathrm{d}T - \mathcal{R}\,\mathrm{d}T + P\,\mathrm{d}\alpha, \tag{A.96}$$

and again using $\mathcal{R}\,\mathrm{d}T = \mathrm{d}(P\alpha) = \alpha\,\mathrm{d}P + P\,\mathrm{d}\alpha$, we have

$$\mathrm{d}Q = T\,\mathrm{d}\eta = c_P\,\mathrm{d}T - \alpha\,\mathrm{d}P. \tag{A.97}$$

A.4.2 Exner pressure and potential temperature

The potential temperature, θ, is defined as the temperature that a fluid would have if moved adiabatically (without any heat exchange) to a reference pressure, P_0. We now need to relate θ to the other thermodynamic variables. Using Eq. (A.97) and the ideal gas equation, we get

$$\mathrm{d}\eta = c_P\frac{\mathrm{d}T}{T} - \alpha\frac{\mathrm{d}P}{T} = c_P\frac{\mathrm{d}T}{T} - \mathcal{R}\frac{\mathrm{d}P}{P} = c_P\,\mathrm{d}\ln T - \mathcal{R}\,\mathrm{d}\ln P. \tag{A.98}$$

No heat exchange implies $\mathrm{d}\eta = 0$, and integrating the resulting separable differential equation from P, T to P_0, θ yields

$$c_P\int_T^\theta \mathrm{d}\ln T = R\int_P^{P_0}\mathrm{d}\ln P, \tag{A.99}$$

integrating, we have

$$c_P\ln\left(\frac{\theta}{T}\right) = R\ln\left(\frac{P_0}{P}\right), \tag{A.100}$$

which yields the final expression for the potential temperature:

$$\theta = T\left(\frac{P_0}{P}\right)^{\mathcal{R}/c_P}. \tag{5.4}$$

Another useful quantity is the Exner pressure (or function), which is defined as

$$\Pi = \left(\frac{P}{P_0}\right)^{\mathcal{R}/c_P} = \frac{T}{\theta}, \tag{5.5}$$

i.e. $T = \Pi\theta$. The temperature and pressure can consequently be replaced by the potential temperature and Exner pressure, respectively. The fluid dynamics equations solved by the UM dynamical core ENDGAME use potential temperature and Exner pressure, see Eq. (5.10).

A.4.3 The thermodynamic equation

The thermodynamic identities in Appendix A.4.1 apply to individual fluid parcels, and we can therefore apply the material derivative, Eq. (5.3), to these identities. There are, however, two assumptions involved:

(i) The fluid is LTE, i.e. we apply the thermodynamic identities locally and expect quantities like temperature and pressure to vary locally.

(ii) Macroscopic fluid motion is reversible and not a source of entropy, i.e. we do not have to consider this contribution to the local entropy η.

Taking Eq. (A.97) and forming the material derivative, we get

$$\dot{Q} \equiv \frac{\mathrm{D}Q}{\mathrm{D}t} = c_P\frac{\mathrm{D}T}{\mathrm{D}t} - \alpha\frac{\mathrm{D}P}{\mathrm{D}t}, \tag{A.101}$$

where $\dot{Q}$ is the total added heat per unit mass per unit time. Using Eq. (5.4) to express the temperature in terms of the potential temperature, $T = \theta\,(P/P_0)^{\mathcal{R}/c_P}$, and inserting this into Eq. (A.101), yields

$$\dot{Q} = c_P\frac{\mathrm{D}}{\mathrm{D}t}\left(\theta\left(\frac{P}{P_0}\right)^{\mathcal{R}/c_P}\right) - \alpha\frac{\mathrm{D}P}{\mathrm{D}t} \tag{A.102}$$

$$= c_P\left(\frac{P}{P_0}\right)^{\mathcal{R}/c_P}\frac{\mathrm{D}\theta}{\mathrm{D}t} + c_P\theta\frac{\mathrm{D}}{\mathrm{D}t}\left(\left(\frac{P}{P_0}\right)^{\mathcal{R}/c_P}\right) - \alpha\frac{\mathrm{D}P}{\mathrm{D}t} \tag{A.103}$$

$$= \frac{c_PT}{\theta}\frac{\mathrm{D}\theta}{\mathrm{D}t} + \frac{c_P\mathcal{R}}{c_PP}\theta\left(\frac{P}{P_0}\right)^{\mathcal{R}/c_P}\frac{\mathrm{D}P}{\mathrm{D}t} - \alpha\frac{\mathrm{D}P}{\mathrm{D}t} \tag{A.104}$$

$$= \frac{c_PT}{\theta}\frac{\mathrm{D}\theta}{\mathrm{D}t} + \alpha\frac{\mathrm{D}P}{\mathrm{D}t} - \alpha\frac{\mathrm{D}P}{\mathrm{D}t} \tag{A.105}$$

$$= \frac{c_PT}{\theta}\frac{\mathrm{D}\theta}{\mathrm{D}t}. \tag{A.106}$$

This is the thermodynamic equation relating the added heat to the increase in temperature taking into account the work done on the environment due the increase in pressure:

$$\frac{\mathrm{D}\theta}{\mathrm{D}t} = \frac{\theta}{T}\frac{\dot{Q}}{c_P}. \tag{5.6}$$

A.5 Vectors in rotating reference frames

Here we briefly go through the relation between vectors in interial frames and rotating reference frames. The discussion is based in Vallis (2006).

A.5.1 Rate of change of a vector

Consider a vector $\boldsymbol{C}$ rotating with a constant angular velocity $\boldsymbol{\Omega}$ in an inertial frame. The change in $\boldsymbol{C}$ is given by

$$\delta\boldsymbol{C} = |\boldsymbol{C}| \sin\vartheta \, \delta\lambda \, \boldsymbol{m}, \tag{A.107}$$

where ϑ is the angle between $\boldsymbol{\Omega}$ and $\boldsymbol{C}$, $\delta\lambda$ is the angle of the rotation and $\boldsymbol{m}$ is a unit vector in the direction of change. By definition $\delta\lambda = |\boldsymbol{\Omega}|\delta t$ and we get

$$\delta\boldsymbol{C} = |\boldsymbol{C}| \, |\boldsymbol{\Omega}| \sin\vartheta \, \boldsymbol{m} \, \delta t = \boldsymbol{\Omega} \times \boldsymbol{C} \, \delta t, \tag{A.108}$$

and which yields

$$\left(\frac{\mathrm{d}\boldsymbol{C}}{\mathrm{d}t}\right)_{\mathrm{I}} = \boldsymbol{\Omega} \times \boldsymbol{C}, \tag{A.109}$$

where we have used the subscript 'I' to indicate that it is the rate of change of $\boldsymbol{C}$ in the inertial frame.

For a vector $\boldsymbol{B}$ that changes in a rotating reference frame, the change in the inertial frame is given by

$$(\delta\boldsymbol{B})_{\mathrm{I}} = (\delta\boldsymbol{B})_{\mathrm{R}} + (\delta\boldsymbol{B})_{\mathrm{rot}}\,, \tag{A.110}$$

where the subscript 'R' indicates that the quantity is measured in the rotating reference frame. Using Eq. (A.109) we get

$$\left(\frac{\mathrm{d}\boldsymbol{B}}{\mathrm{d}t}\right)_{\mathrm{I}} = \left(\frac{\mathrm{d}\boldsymbol{B}}{\mathrm{d}t}\right)_{\mathrm{R}} + \boldsymbol{\Omega} \times \boldsymbol{B}, \tag{A.111}$$

which relates the rate of change of a vector $\boldsymbol{B}$ in an inertial reference frame to that in a rotating reference frame.

A.5.2 Velocity and acceleration in a rotating frame

In order to derive a relation between the velocity as measured in a rotating reference frame and the velocity as measured in the inertial frame, we apply Eq. (A.111) to the position $\boldsymbol{r}$:

$$\boldsymbol{v}_{\mathrm{I}} = \boldsymbol{v}_{\mathrm{R}} + \boldsymbol{\omega} \times \boldsymbol{r}. \tag{A.112}$$

The velocities $\boldsymbol{v}_{\mathrm{I}}$ and $\boldsymbol{v}_{\mathrm{R}}$ are referred to as the inertial and relative velocity, respectively. We then apply Eq. (A.111) to $\boldsymbol{v}_{\mathrm{R}}$ which yields

$$\left(\frac{\mathrm{d}\boldsymbol{v}_{\mathrm{R}}}{\mathrm{d}t}\right)_{\mathrm{I}} = \left(\frac{\mathrm{d}\boldsymbol{v}_{\mathrm{R}}}{\mathrm{d}t}\right)_{\mathrm{R}} + \boldsymbol{\Omega} \times \boldsymbol{v}_{\mathrm{R}}, \tag{A.113}$$

and using Eq. (A.112) yields

$$\left(\frac{\mathrm{d}\boldsymbol{v}_{\mathrm{I}}}{\mathrm{d}t}\right)_{\mathrm{I}} = \left(\frac{\mathrm{d}\boldsymbol{v}_{\mathrm{R}}}{\mathrm{d}t}\right)_{\mathrm{R}} + \boldsymbol{\Omega} \times \boldsymbol{v}_{\mathrm{R}} + \frac{\mathrm{d}\boldsymbol{\Omega}}{\mathrm{d}t} \times \boldsymbol{r} + \boldsymbol{\Omega} \times \left(\frac{\mathrm{d}\boldsymbol{r}}{\mathrm{d}t}\right)_{\mathrm{I}}. \tag{A.114}$$

Using Eq. (A.112) to replace $(\mathrm{d}\boldsymbol{r}/\mathrm{d}t)_{\mathrm{I}}$ this gives us the final relation between the acceleration in the rotating and inertial reference frames:

$$\left(\frac{\mathrm{d}\boldsymbol{v}_{\mathrm{R}}}{\mathrm{d}t}\right)_{\mathrm{R}} = \left(\frac{\mathrm{d}\boldsymbol{v}_{\mathrm{I}}}{\mathrm{d}t}\right)_{\mathrm{I}} - 2\boldsymbol{\Omega} \times \boldsymbol{v}_{\mathrm{R}} - \boldsymbol{\Omega} \times (\boldsymbol{\Omega} \times \boldsymbol{r}). \tag{5.8}$$

Bibliography

Allard, N. F., Allard, F., Hauschildt, P. H., Kielkopf, J. F., & Machin, L. 2003, A&A, 411, L473

Allard, N. F., Royer, A., Kielkopf, J. F., & Feautrier, N. 1999, Phys. Rev. A, 60, 1021

Allard, N. F., Spiegelman, F., & Kielkopf, J. F. 2007, A&A, 465, 1085

Amundsen, D. S., Baraffe, I., Tremblin, P., et al. 2014, A&A, 564, A59

Asplund, M., Grevesse, N., Sauval, A. J., & Scott, P. 2009, ARA&A, 47, 481

Bailey, J. & Kedziora-Chudczer, L. 2012, MNRAS, 419, 1913

Baraffe, I., Chabrier, G., & Barman, T. 2008, A&A, 482, 315

Baraffe, I., Chabrier, G., & Barman, T. 2010, Reports on Progress in Physics, 73, 016901

Barber, R. J., Tennyson, J., Harris, G. J., & Tolchenov, R. N. 2006, MNRAS, 368, 1087

Barman, T. S., Hauschildt, P. H., & Allard, F. 2001, ApJ, 556, 885

Barman, T. S., Hauschildt, P. H., & Allard, F. 2005, ApJ, 632, 1132

Barman, T. S., Hauschildt, P. H., Schweitzer, A., et al. 2002, ApJ, 569, L51

Barstow, J. K., Aigrain, S., Irwin, P. G. J., et al. 2014, ApJ, 786, 154

Barstow, J. K., Tsang, C. C. C., Wilson, C. F., et al. 2012, Icarus, 217, 542

Batygin, K. & Stevenson, D. J. 2010, ApJ, 714, L238

Beaulieu, J.-P., Bennett, D. P., Fouqué, P., et al. 2006, Nature, 439, 437

BelBruno, J. J., Gelfand, J., Radigan, W., & Verges, K. 1982, Journal of Molecular Spectroscopy, 94, 336

Birkby, J. L., de Kok, R. J., Brogi, M., et al. 2013, MNRAS, 436, L35

Bonfils, X., Delfosse, X., Udry, S., et al. 2013, A&A, 549, A109

Borucki, W. J., Koch, D., Basri, G., et al. 2010, Science, 327, 977

Brogi, M., Snellen, I. A. G., de Kok, R. J., et al. 2012, Nature, 486, 502

Burrows, A., Hubeny, I., Budaj, J., Knutson, H. A., & Charbonneau, D. 2007, ApJ, 668, L171

Burrows, A., Marley, M., Hubbard, W. B., et al. 1997, ApJ, 491, 856

Burrows, A., Marley, M. S., & Sharp, C. M. 2000, ApJ, 531, 438

Burrows, A. & Orton, G. 2009, ArXiv e-prints

Burrows, A. & Sharp, C. M. 1999, ApJ, 512, 843

Burrows, A., Sudarsky, D., & Hubeny, I. 2006, ApJ, 650, 1140

Burrows, A. & Volobuyev, M. 2003, ApJ, 583, 985

Butler, R. P., Marcy, G. W., Fischer, D. A., et al. 1999, ApJ, 526, 916

Butler, R. P., Wright, J. T., Marcy, G. W., et al. 2006, ApJ, 646, 505

Charbonneau, D., Brown, T. M., Latham, D. W., & Mayor, M. 2000, ApJ, 529, L45

Charbonneau, D., Brown, T. M., Noyes, R. W., & Gilliland, R. L. 2002, ApJ, 568, 377

Cho, J. Y.-K., Menou, K., Hansen, B. M. S., & Seager, S. 2003, ApJ, 587, L117

Cho, J. Y.-K., Menou, K., Hansen, B. M. S., & Seager, S. 2008, ApJ, 675, 817

Clough, S. A., Kneizys, F. X., & Davies, R. W. 1989, Atmospheric Research, 23, 229

Collins, W. D., Ramaswamy, V., Schwarzkopf, M. D., et al. 2006, Journal of Geophysical Research (Atmospheres), 111, 14317

Cooper, C. S. & Showman, A. P. 2005, ApJ, 629, L45

Crossfield, I. J. M., Biller, B., Schlieder, J. E., et al. 2014, Nature, 505, 654

Crossfield, I. J. M., Knutson, H., Fortney, J., et al. 2012, ApJ, 752, 81

Deming, D., Seager, S., Richardson, L. J., & Harrington, J. 2005, Nature, 434, 740

Deming, D., Wilkins, A., McCullough, P., et al. 2013, ApJ, 774, 95

Demory, B.-O., de Wit, J., Lewis, N., et al. 2013, ApJ, 776, L25

Désert, J.-M., Lecavelier des Etangs, A., Hébrard, G., et al. 2009, ApJ, 699, 478

Diamond-Lowe, H., Stevenson, K. B., Bean, J. L., Line, M. R., & Fortney, J. J. 2014, ApJ, 796, 66

Dobbs-Dixon, I. & Agol, E. 2013, MNRAS, 435, 3159

Dobbs-Dixon, I., Cumming, A., & Lin, D. N. C. 2010, ApJ, 710, 1395

Dobbs-Dixon, I. & Lin, D. N. C. 2008, ApJ, 673, 513

Edwards, J. M. 1996, Journal of Atmospheric Sciences, 53, 1921

Edwards, J. M., Manners, J., Thelen, J.-C., Ingram, W. J., & Hill, P. G. 2012, UM Documentation

Edwards, J. M. & Slingo, A. 1996, Quarterly Journal of the Royal Meteorological Society, 122, 689

Elasser, W. M. 1942, Heat transfer by infrared radiation in the atmosphere No. 6 (Harvard Meteorological Studies), 107

Ellingson, R. G., Ellis, J., & Fels, S. 1991, J. Geophys. Res., 96, 8929

Fischer, D. A., Marcy, G. W., Butler, R. P., et al. 2003, ApJ, 586, 1394

Fortney, J. J., Cooper, C. S., Showman, A. P., Marley, M. S., & Freedman, R. S. 2006a, ApJ, 652, 746

Fortney, J. J., Lodders, K., Marley, M. S., & Freedman, R. S. 2008a, ApJ, 678, 1419

Fortney, J. J., Marley, M. S., Lodders, K., Saumon, D., & Freedman, R. 2005, ApJ, 627, L69

Fortney, J. J., Marley, M. S., Saumon, D., & Lodders, K. 2008b, ApJ, 683, 1104

Fortney, J. J., Saumon, D., Marley, M. S., Lodders, K., & Freedman, R. S. 2006b, ApJ, 642, 495

Fortney, J. J., Shabram, M., Showman, A. P., et al. 2010, ApJ, 709, 1396

Freedman, R. S., Marley, M. S., & Lodders, K. 2008, ApJS, 174, 504

Freytag, B., Allard, F., Ludwig, H.-G., Homeier, D., & Steffen, M. 2010, A&A, 513, A19

Gamache, R. R., Lynch, R., & Brown, L. R. 1996, J. Quant. Spec. Radiat. Transf., 56, 471

Gibson, N. P., Aigrain, S., Barstow, J. K., et al. 2013, MNRAS, 436, 2974

Goldblatt, C., Lenton, T. M., & Watson, A. J. 2009, Quarterly Journal of the Royal Meteorological Society, 135, 619

Goody, R., West, R., Chen, L., & Crisp, D. 1989, J. Quant. Spec. Radiat. Transf., 42, 539

Goorvitch, D. 1994, ApJS, 95, 535

Gray, D. F. 2005, The Observation and Analysis of Stellar Photospheres, 3rd edn. (Cambridge University Press)

Gustafsson, B., Edvardsson, B., Eriksson, K., et al. 2008, A&A, 486, 951

Hadded, S., Aroui, H., Orphal, J., Bouanich, J.-P., & Hartmann, J.-M. 2001, Journal of Molecular Spectroscopy, 210, 275

Han, E., Wang, S. X., Wright, J. T., et al. 2014, PASP, 126, 827

Hansen, C. J., Schwartz, J. C., & Cowan, N. B. 2014, MNRAS, 444, 3632

Hauschildt, P. H. & Baron, E. 1999, Journal of Computational and Applied Mathematics, 109, 41

Heiter, U., Barklem, P., Fossati, L., et al. 2008, Journal of Physics Conference Series, 130, 012011

Heller, W. 1965, The Journal of Physical Chemistry, 69, 1123

Heng, K. 2012, ApJ, 748, L17

Heng, K., Menou, K., & Phillipps, P. J. 2011, MNRAS, 413, 2380

Heng, K. & Showman, A. P. 2014, ArXiv e-prints

Henry, G. W., Marcy, G. W., Butler, R. P., & Vogt, S. S. 2000, ApJ, 529, L41

Hoeijmakers, H. J., de Kok, R. J., Snellen, I. A. G., et al. 2014, ArXiv e-prints

Hogan, R. J. 2010, Journal of Atmospheric Sciences, 67, 2086

Hollingsworth, J. L. & Kahre, M. A. 2010, Geophys. Res. Lett., 37, 22202

Homeier, D. 2005, Memorie della Societa Astronomica Italiana Supplementi, 7, 157

Huang, X. & Cumming, A. 2012, ApJ, 757, 47

Huber, K. P. & Herzberg, G. 1979, Constants of Diatomic Molecules, 1st edn., Molecular Spectra and Molecular Structure, v. 4 (Van Nostrand Reinhold), 716

Huitson, C. M., Sing, D. K., Pont, F., et al. 2013, MNRAS, 434, 3252

Humlícek, J. 1982, J. Quant. Spec. Radiat. Transf., 27, 437

Iro, N., Bézard, B., & Guillot, T. 2005, A&A, 436, 719

Irwin, P. G. J., Teanby, N. A., de Kok, R., et al. 2008, J. Quant. Spec. Radiat. Transf., 109, 1136

Kataria, T., Showman, A. P., Fortney, J. J., Marley, M. S., & Freedman, R. S. 2014a, ApJ, 785, 92

Kataria, T., Showman, A. P., Fortney, J. J., et al. 2014b, ArXiv e-prints

Kataria, T., Showman, A. P., Lewis, N. K., et al. 2013, ApJ, 767, 76

Knutson, H. A., Charbonneau, D., Allen, L. E., Burrows, A., & Megeath, S. T. 2008, ApJ, 673, 526

Knutson, H. A., Charbonneau, D., Allen, L. E., et al. 2007a, Nature, 447, 183

Knutson, H. A., Charbonneau, D., Cowan, N. B., et al. 2009, ApJ, 690, 822

Knutson, H. A., Charbonneau, D., Noyes, R. W., Brown, T. M., & Gilliland, R. L. 2007b, ApJ, 655, 564

Knutson, H. A., Lewis, N., Fortney, J. J., et al. 2012, ApJ, 754, 22

Kurucz, R. L. 2012, Robert L. Kurucz on-line database of observed and predicted atomic transitions

Lacis, A. A. & Oinas, V. 1991, J. Geophys. Res., 96, 9027

Le Moal, M. F. & Severin, F. 1986, J. Quant. Spec. Radiat. Transf., 35, 145

Lebonnois, S., Lee, C., Yamamoto, M., et al. 2011, in EPSC-DPS Joint Meeting 2011, 144

Lee, C., Lewis, S. R., & Read, P. L. 2005, Advances in Space Research, 36, 2142

Lee, C. & Richardson, M. I. 2010, Journal of Geophysical Research (Planets), 115, 4002

Lee, J.-M., Fletcher, L. N., & Irwin, P. G. J. 2012, MNRAS, 420, 170

Lee, J.-M., Irwin, P. G. J., Fletcher, L. N., Heng, K., & Barstow, J. K. 2014, ApJ, 789, 14

Leonard, P. J. 1974, Atomic Data and Nuclear Data Tables, 14, 21

Lewis, N. K., Showman, A. P., Fortney, J. J., et al. 2010, ApJ, 720, 344

Liang, M.-C., Parkinson, C. D., Lee, A. Y.-T., Yung, Y. L., & Seager, S. 2003, ApJ, 596, L247

Lide, D. R., ed. 1995, CRC Handbook of Chemistry and Physics, 76th edn. (CRC Press)

Line, M. R., Liang, M. C., & Yung, Y. L. 2010, ApJ, 717, 496

Line, M. R., Wolf, A. S., Zhang, X., et al. 2013, ApJ, 775, 137

Liou, K. N. 1980, An introduction to atmospheric radiation., 2nd edn. (Academic Press)

Liu, B. & Showman, A. P. 2013, ApJ, 770, 42

Madhusudhan, N., Knutson, H., Fortney, J. J., & Barman, T. 2014, Protostars and Planets VI, 739

Madhusudhan, N. & Seager, S. 2009, ApJ, 707, 24

Majeau, C., Agol, E., & Cowan, N. B. 2012, ApJ, 747, L20

Mansfield, C. R. & Peck, E. R. 1969, Journal of the Optical Society of America (1917-1983), 59, 199

Mantz, A. W., Malathy Devi, V., Chris Benner, D., et al. 2005, Journal of Molecular Structure, 742, 99

Margolis, J. S. 1993, J. Quant. Spec. Radiat. Transf., 50, 431

Marley, M. S., Ackerman, A. S., Cuzzi, J. N., & Kitzmann, D. 2013, Clouds and Hazes in Exoplanet Atmospheres, ed. S. J. Mackwell, A. A. Simon-Miller, J. W. Harder, & M. A. Bullock (University of Arizona Press), 367–391

Marley, M. S. & Robinson, T. D. 2014, ArXiv e-prints

Marois, C., Macintosh, B., Barman, T., et al. 2008, Science, 322, 1348

Maxted, P. F. L., Anderson, D. R., Doyle, A. P., et al. 2013, MNRAS, 428, 2645

Mayne, N. J., Baraffe, I., Acreman, D. M., et al. 2014a, A&A, 561, A1

Mayne, N. J., Baraffe, I., Acreman, D. M., et al. 2014b, Geoscientific Model Development, 7, 3059

Mayor, M. & Queloz, D. 1995, Nature, 378, 355

Mazeh, T., Naef, D., Torres, G., et al. 2000, ApJ, 532, L55

McCullough, P. R., Crouzet, N., Deming, D., & Madhusudhan, N. 2014, ApJ, 791, 55

Meador, W. E. & Weaver, W. R. 1980, Journal of Atmospheric Sciences, 37, 630

Menou, K. & Rauscher, E. 2009, ApJ, 700, 887

Mlawer, E. J., Taubman, S. J., Brown, P. D., Iacono, M. J., & Clough, S. A. 1997, J. Geophys. Res., 102, 16663

Moses, J. I., Visscher, C., Fortney, J. J., et al. 2011, ApJ, 737, 15

Müller-Wodarg, I. C. F., Mendillo, M., Yelle, R. V., & Aylward, A. D. 2006, Icarus, 180, 147

Nikolov, N., Sing, D. K., Pont, F., et al. 2014, MNRAS, 437, 46

Nordlund, A. 1982, A&A, 107, 1

Nouri, S., Orphal, J., Aroui, H., & Hartmann, J.-M. 2004, Journal of Molecular Spectroscopy, 227, 60

Nymeyer, S., Harrington, J., Hardy, R. A., et al. 2011, ApJ, 742, 35

Oreopoulos, L., Mlawer, E., Delamere, J., et al. 2012, Journal of Geophysical Research (Atmospheres), 117, 6118

Padmanabhan, A., Tzanetakis, T., Chanda, A., & Thomson, M. J. 2014, J. Quant. Spec. Radiat. Transf., 133, 81

Parmentier, V., Showman, A. P., & Lian, Y. 2013, A&A, 558, A91

Penndorf, R. 1957, Journal of the Optical Society of America (1917-1983), 47, 176

Pine, A. S. 1992, J. Chem. Phys., 97, 773

Pine, A. S., Markov, V. N., Buffa, G., & Tarrini, O. 1993, J. Quant. Spec. Radiat. Transf., 50, 337

Plez, B. 1998, A&A, 337, 495

Polichtchouk, I., Cho, J. Y.-K., Watkins, C., et al. 2014, Icarus, 229, 355

Pollacco, D. L., Skillen, I., Collier Cameron, A., et al. 2006, PASP, 118, 1407

Pont, F., Knutson, H., Gilliland, R. L., Moutou, C., & Charbonneau, D. 2008, MNRAS, 385, 109

Pont, F., Sing, D. K., Gibson, N. P., et al. 2013, MNRAS, 432, 2917

Ralchenko, Y., Kramida, A., Reader, J., & NIST ASD Team. 2010, NIST Atomic Spectra Database (ver. 4.0.0), [Online].

Rauscher, E. & Menou, K. 2010, ApJ, 714, 1334

Rauscher, E. & Menou, K. 2012, ApJ, 750, 96

Rauscher, E. & Menou, K. 2013, ApJ, 764, 103

Redfield, S., Endl, M., Cochran, W. D., & Koesterke, L. 2008, ApJ, 673, L87

Régalia-Jarlot, L., Thomas, X., von der Heyden, P., & Barbe, A. 2005, J. Quant. Spec. Radiat. Transf., 91, 121

Richard, C., Gordon, I. E., Rothman, L. S., et al. 2012, J. Quant. Spec. Radiat. Transf., 113, 1276

Rogers, T. M. & Komacek, T. D. 2014, ApJ, 794, 132

Rogers, T. M. & Showman, A. P. 2014, ApJ, 782, L4

Rossow, W. B. 1978, Icarus, 36, 1

Rothman, L. S., Gordon, I. E., Babikov, Y., et al. 2013, J. Quant. Spec. Radiat. Transf., 130, 4

Rothman, L. S., Gordon, I. E., Barbe, A., et al. 2009, J. Quant. Spec. Radiat. Transf., 110, 533

Rothman, L. S., Gordon, I. E., Barber, R. J., et al. 2010, J. Quant. Spec. Radiat. Transf., 111, 2139

Rutten, R. J. 2003, Radiative Transfer in Stellar Atmospheres, eighth edn. (Sterrekundig Instituut Utrecht, Institute of Theoretical Astrophysics Oslo)

Rybicki, G. B. & Lightman, A. P. 2004, Radiative Processes in Astrophysics (John Wiley & Sons)

Sauval, A. J. & Tatum, J. B. 1984, ApJS, 56, 193

Schreier, F. 1992, J. Quant. Spec. Radiat. Transf., 48, 743

Schwarz, H., Brogi, M., de Kok, R., Birkby, J., & Snellen, I. 2015, ArXiv e-prints

Schweitzer, A. & Hauschildt, P. H. 2004, in American Institute of Physics Conference Series, Vol. 730, American Institute of Physics Conference Series, ed. J. S. Cohen, D. P. Kilcrease, & S. Mazavet, 111–116

Schweitzer, A., Hauschildt, P. H., Allard, F., & Basri, G. 1996, MNRAS, 283, 821

Schwenke, D. W. 1998, Faraday Discussions, 109, 321

Seager, S. 2010, Exoplanet Atmospheres: Physical Processes (Princeton University Press)

Seager, S. & Deming, D. 2010, ARA&A, 48, 631

Seager, S. & Sasselov, D. D. 2000, ApJ, 537, 916

Sharp, C. M. & Burrows, A. 2007, ApJS, 168, 140

Showman, A. P., Cho, J. Y.-K., & Menou, K. 2011, Atmospheric Circulation of Exoplanets, ed. S. Seager (University of Arizona Press), 471–516

Showman, A. P., Cooper, C. S., Fortney, J. J., & Marley, M. S. 2008, ApJ, 682, 559

Showman, A. P., Fortney, J. J., Lian, Y., et al. 2009, ApJ, 699, 564

Showman, A. P. & Guillot, T. 2002, A&A, 385, 166

Shporer, A., O'Rourke, J. G., Knutson, H. A., et al. 2014, ApJ, 788, 92

Sing, D. K., Désert, J.-M., Fortney, J. J., et al. 2011, A&A, 527, A73

Sing, D. K., Désert, J.-M., Lecavelier Des Etangs, A., et al. 2009, A&A, 505, 891

Sing, D. K., Huitson, C. M., Lopez-Morales, M., et al. 2012, MNRAS, 426, 1663

Sing, D. K., Lecavelier des Etangs, A., Fortney, J. J., et al. 2013, MNRAS

Sing, D. K., Vidal-Madjar, A., Désert, J.-M., Lecavelier des Etangs, A., & Ballester, G. 2008, ApJ, 686, 658

Sing, D. K., Wakeford, H. R., Showman, A. P., et al. 2015, MNRAS, 446, 2428

Skartlien, R. 2000, ApJ, 536, 465

Snellen, I. A. G., Albrecht, S., de Mooij, E. J. W., & Le Poole, R. S. 2008, A&A, 487, 357

Snellen, I. A. G., de Kok, R. J., de Mooij, E. J. W., & Albrecht, S. 2010, Nature, 465, 1049

Solodov, A. M. & Starikov, V. I. 2009, Molecular Physics, 107, 43

Stevenson, K. B., Désert, J.-M., Line, M. R., et al. 2014, Science, 346, 838

Steyert, D. W., Wang, W. F., Sirota, J. M., Donahue, N. M., & Reuter, D. C. 2004, J. Quant. Spec. Radiat. Transf., 83, 183

Sudarsky, D., Burrows, A., & Hubeny, I. 2003, ApJ, 588, 1121

Swain, M. R., Bouwman, J., Akeson, R. L., Lawler, S., & Beichman, C. A. 2008, ApJ, 674, 482

Swain, M. R., Tinetti, G., Vasisht, G., et al. 2009, ApJ, 704, 1616

Tashkun, S. A. & Perevalov, V. I. 2011, J. Quant. Spec. Radiat. Transf., 112, 1403

Tennyson, J. & Yurchenko, S. N. 2012, MNRAS, 425, 21

Thibault, F., Boissoles, J., Le Doucen, R., et al. 1992, J. Chem. Phys., 96, 4945

Thibault, F., Calil, B., Boissoles, J., & Launay, J. M. 2000, Physical Chemistry Chemical Physics (Incorporating Faraday Transactions), 2, 5404

Thomas, G. E. & Stamnes, K. 2002, Radiative Transfer in the Atmosphere and Ocean (Cambridge University Press)

Thrastarson, H. T. & Cho, J. Y. 2010, ApJ, 716, 144

Tinetti, G., Vidal-Madjar, A., Liang, M.-C., et al. 2007, Nature, 448, 169

Toon, O. B., McKay, C. P., Ackerman, T. P., & Santhanam, K. 1989, J. Geophys. Res., 94, 16287

Torres, G., Winn, J. N., & Holman, M. J. 2008, ApJ, 677, 1324

Tremblin, P., Amundsen, D. S., Mourier, P., et al. 2015, ApJ, 804, L17

Unsöld, A. 1955, Physik der Sternatmopshären: Mit Besonderer Berucksichtigung der Sonne, 2nd edn. (Springer)

Šimečková, M., Jacquemart, D., Rothman, L. S., Gamache, R. R., & Goldman, A. 2006, J. Quant. Spec. Radiat. Transf., 98, 130

Vallis, G. K. 2006, Atmospheric and Oceanic Fluid Dynamics (Cambridge University Press)

Varanasi, P. & Chudamani, S. 1990, J. Quant. Spec. Radiat. Transf., 43, 1

Venot, O., Hébrard, E., Agúndez, M., et al. 2012, A&A, 546, A43

Voronin, B. A., Lavrentieva, N. N., Mishina, T. P., et al. 2010, J. Quant. Spec. Radiat. Transf., 111, 2308

Wakeford, H. R., Sing, D. K., Deming, D., et al. 2013, MNRAS, 435, 3481

Waldmann, I. P., Tinetti, G., Drossart, P., et al. 2012, ApJ, 744, 35

Weiss, L. M., Marcy, G. W., Rowe, J. F., et al. 2013, ApJ, 768, 14

Wenger, C. & Champion, J. P. 1998, J. Quant. Spec. Radiat. Transf., 59, 471

Wenger, C., Champion, J. P., & Boudon, V. 2008, J. Quant. Spec. Radiat. Transf., 109, 2697

Wilson, D. R., Bushell, A. C., Kerr-Munslow, A. M., Price, J. D., & Morcrette, C. J. 2008a, Quarterly Journal of the Royal Meteorological Society, 134, 2093

Wilson, D. R., Bushell, A. C., Kerr-Munslow, A. M., et al. 2008b, Quarterly Journal of the Royal Meteorological Society, 134, 2109

Wiscombe, W. J. & Evans, J. W. 1977, Journal of Computational Physics, 24, 416

Wood, N., Staniforth, A., White, A., et al. 2014, Q. J. R. Meteorol. Soc., 140, 1505

Wright, J. T. & Gaudi, B. S. 2013, Exoplanet Detection Methods, ed. T. D. Oswalt, L. M. French, & P. Kalas (Springer Netherlands), 489

Wu, Y. & Lithwick, Y. 2013, ApJ, 763, 13

Yamazaki, Y. H., Skeet, D. R., & Read, P. L. 2004, Planet. Space Sci., 52, 423

Yurchenko, S. N., Barber, R. J., & Tennyson, J. 2011, MNRAS, 413, 1828

Yurchenko, S. N. & Tennyson, J. 2014, MNRAS, 440, 1649

Zahnle, K., Marley, M. S., Freedman, R. S., Lodders, K., & Fortney, J. J. 2009, ApJ, 701, L20

Zdunkowski, W. G. & Korb, G. J. 1985, Promet, 2/3, 26

Zdunkowski, W. G., Panhans, W.-G., Welch, R. M., & Korb, G. J. 1982, Beiträge zur Physik der Atmosphäre, 55, 215

Zdunkowski, W. G., Welch, R. M., & Korb, G. 1980, Beiträge zur Physik der Atmosphäre, 53, 147

Zellem, R. T., Lewis, N. K., Knutson, H. A., et al. 2014, ApJ, 790, 53

Zhu, C., Babb, J. F., & Dalgarno, A. 2006, Phys. Rev. A, 73, 012506